

VOLUME 10, ISSUES 1-2, 2005

ISSN 1463-5003

OCEAN MODELLING

<http://www.elsevier.com/locate/ocemod>

Editor-in-Chief: **Peter Killworth**,
Southampton Oceanography Centre, UK

Special Issue

The Second International Workshop on
Unstructured Mesh Numerical Modelling
of Coastal, Shelf and Ocean Flows

Guest Editors

J. Pietrzak
E. Deleersnijder
J. Schröter

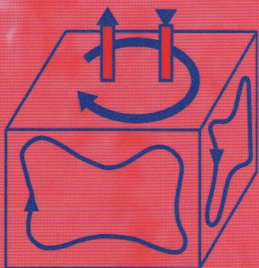


Table of Contents

- Pietrzak J., E. Deleersnijder and J. Schröter, 2005, Preface, *Ocean Modelling*, 10, 1-3
- Pain C.C., M.D. Piggott, A.J.H. Goddard, F. Fang, G.J. Gorman, D.P. Marshall, M.D. Eaton, P.W. Power, C.R.E. de Oliveira, 2005, Three-dimensional unstructured mesh ocean modelling, *Ocean Modelling*, 10, 5-33
- Danilov S., G. Kivman and J. Schröter, 2005, Evaluation of an eddy-permitting finite-element ocean model in the North Atlantic, *Ocean Modelling*, 10, 35-49
- Labeur R.J. and J.D. Pietrzak, 2005, A fully three dimensional unstructured grid non-hydrostatic finite element coastal model, *Ocean Modelling*, 10, 51-67
- Myers P.G., S. Grey and K. Haines, 2005, A diagnostic study of interpentadal variability in the North Atlantic Ocean using a finite element model, *Ocean Modelling*, 10, 69-81
- Le Roux D.Y., A. Sène, V. Rostand and E. Hanert, 2005, On some spurious mode issues in shallow-water models using a linear algebra approach, *Ocean Modelling*, 10, 83-94
- Piggott M.D., C.C. Pain, G.J. Gorman, P.W. Power and A.J.H. Goddard, 2005, *h*, *r*, and *hr* adaptivity with applications in numerical ocean modelling, *Ocean Modelling*, 10, 95-113
- Hanert E., D.Y. Le Roux, V. Legat and E. Deleersnijder, 2005, An efficient Eulerian finite element method for the shallow water equations, *Ocean Modelling*, 10, 115-136
- Casulli V. and P. Zanolli, 2005, High resolution methods for multidimensional advection-diffusion problems in free-surface hydrodynamics, *Ocean Modelling*, 10, 137-151
- Ham D.A., J. Pietrzak and G.S. Stelling, 2005, A scalable unstructured grid 3-dimensional finite volume model for the shallow water equations, *Ocean Modelling*, 10, 153-169
- Behrens J., N. Rakowsky, W. Hiller, D. Handorf, M. Läuter, J. Pöpke and K. Dethloff, 2005, amatos: Parallel adaptive mesh generator for atmospheric and oceanic simulation, *Ocean Modelling*, 10, 171-183
- Frickenhaus S., W. Hiller and M. Best, 2005, FoSSI: the family of simplified solver interfaces for the rapid development of parallel numerical atmosphere and ocean models, *Ocean Modelling*, 10, 185-191
- Hall P. and A.M. Davies, 2005, The influence of an irregular grid upon internal wave propagation, *Ocean Modelling*, 10, 193-209
- Greenberg D.A., J.A. Shore, F.H. Page and M. Dowd, 2005, A finite element circulation model for embayments with drying intertidal areas and its application to the Quoddy region of the Bay of Fundy, *Ocean Modelling*, 10, 211-231
- Iskandarani M., J.C. Levin, B.-J. Choi and D.B. Haidvogel, 2005, Comparison of advection schemes for high-order h-p finite element and finite volume methods, *Ocean Modelling*, 10, 233-252



Preface

Special Issue:
**The second international workshop on unstructured mesh
numerical modelling of coastal, shelf and ocean flows
Delft, The Netherlands, September 23–September 25, 2003**

While traditional structured mesh ocean models are now well established they are restricted in their ability to fit domains with arbitrary geometries and there has been no fundamental change to the techniques employed since their development in the sixties. In the meantime numerical techniques have evolved, as have computer resources. The potential advantages of unstructured grid methods are significant, islands and complex bathymetry can easily be handled, resolution can be placed in boundary layers in an optimal manner, the problem of stair casing near land boundaries can be avoided by having a mesh aligned with the boundary and adaptive grids with dynamically changing resolution are possible. The time is right for a change of direction and introduction of new methods into both oceanography and coastal engineering.

A series of now annual workshops on unstructured mesh numerical modelling of coastal, shelf and ocean flows was initiated by Jens Schröter, Eric Deleersnijder and Florent Lyard in September 2002. The first workshop took place in Louvain-la-Neuve, the second in Delft and the third in Toulouse. The workshops were initiated due to the growing interest in unstructured mesh methods in oceanography and coastal engineering. The idea behind the workshops is to promote open discussion, focussing on numerical issues as well as applications. The interest in this area of flow modelling attests to the importance of this emerging field for both oceanographers and engineers.

This volume publishes 14 papers presented at the Delft workshop. The diversity of approaches and the enthusiasm of the groups made for a successful meeting. At the meeting 33 talks and 7 posters were presented, with substantial time set aside for general discussions on finite element and finite volume techniques as well as the physical processes that need to be resolved in the future generation of coastal and ocean models. In addition more specialised discussions took place on topics such as basis functions, stabilisation, advection schemes, solvers and grid generators.

The collection of papers presented here represents only some of the topics covered by the workshop, see <http://fluidmechanics.tudelft.nl/unstructured/workshop/> for further details. The first

paper in the special issue by Pain et al. is an excellent introduction to the subject and also reflects the research being undertaken by the Imperial College group; see also work by Piggott et al. which is one of the first applications of adaptive finite elements in oceanography. The papers by Danilov et al. and Labeur and Pietrzak present two models using a fully unstructured grid approach with tetrahedral elements. The former model has been developed with large scale ocean applications in mind, the latter for coastal ocean applications in which non-hydrostatic effects are important. Myers et al. use a finite element model to investigate the interpentadal variability in the North Atlantic Ocean. LeRoux et al. present a linear algebra approach for the investigation of spurious modes in shallow water models. Hanert et al. presented work carried out on Eulerian and semi-Lagrangian methods. Casulli and Zanolli presented further developments to the UnTrim model which is widely used in the coastal ocean and engineering communities. Ham et al. presented a new finite volume shallow water model, that builds upon the UnTrim approach. Behrens et al. and Frickenhaus et al. cover some important technical issues dealing with adaptive mesh generators and interfaces to parallel sparse solvers respectively. Hall and Davies presentation addresses the effects of irregular grids on the quality of internal wave simulations. Greenberg et al. present an application of Quoddy to the Bay of Fundy, addressing the important coastal ocean modelling issue of flooding and drying. The issue concludes with a paper by Iskandarani et al. on high order advection schemes to improve the family of spectral element ocean models originally developed at Rutgers.

It is clear that there is much activity in this area of research which is likely to lead to accurate and well tested unstructured mesh models available to the ocean and coastal modelling communities. For further information on our activities please see <http://wessex.eas.ualberta.ca/~myers/FE/fe-page.html>.

We would like to thank Ocean Modelling for the opportunity to publish a set of related papers in a special issue. Also we wish to thank the authors and the many referees for their excellent and time consuming work. We hope that this special issue will stimulate further progress in this exciting area of ocean modelling.

Guest editors

Julie Pietrzak

*Environmental Fluid Mechanics Section
Faculty of Civil Engineering and Geosciences*

Technical University of Delft

P.O. Box 5048, 2600 GA Delft

The Netherlands

E-mail address: J.Pietrzak@citg.tudelft.nl

Eric Deleersnijder

*G. Lemaître Institute of Astronomy and Geophysics (ASTR) & Centre for Systems
Engineering and Applied Mechanics (CESAME)*

Université Catholique de Louvain

*4 Avenue G. Lemaître, B-1348 Louvain-la-Neuve
Belgium*

E-mail address: ericd@astr.ucl.ac.be

Jens Schröter
Alfred-Wegener-Institute for Polar- and Marine Research
Postfach 12 01 61, 27515 Bremerhaven
Germany
E-mail address: jschroeter@awi-bremerhaven.de

Available online 2 November 2004



Three-dimensional unstructured mesh ocean modelling

C.C. Pain^{a,*}, M.D. Piggott^{a,*}, A.J.H. Goddard^a, F. Fang^a, G.J. Gorman^a,
D.P. Marshall^b, M.D. Eaton^a, P.W. Power^a, C.R.E. de Oliveira^c

^a *Applied Modelling and Computation Group, Department of Earth Science and Engineering, Imperial College,
Prince Consort Road, London SW7 2BP, UK*

^b *Department of Meteorology, University of Reading, PO Box 243, Reading RG6 6BB, UK*

^c *Nuclear and Radiological Engineering Program, The George W. Woodruff School of Mechanical Engineering,
Georgia Institute of Technology, Atlanta, GA 30332-0405, USA*

Received in revised form 8 July 2004; accepted 22 July 2004

Available online 2 November 2004

Abstract

In this article the advantages and current status of unstructured mesh ocean modelling are reviewed. Future challenges are discussed along with the potential of resulting methods to make a significant impact on ocean modelling over the next decade. These methods are important because they are the only techniques that can simultaneously resolve both small and large scale ocean flows while smoothly varying resolution and conforming to complex coastlines and bathymetry. Realising the full potential of such methods will necessitate the use of dynamic mesh adaptivity. A number of techniques need to be combined and developed from different numerical modelling and geophysical fluid dynamics disciplines in order to create a powerful unstructured mesh ocean model. These are: accurate and robust methods for the discretisation and advection of tracers, density and momentum; the choice of element/cell and satisfaction of the LBB stability condition; representation of hydrostatic and geostrophic balance; the ability to deal with sigma coordinate-like errors associated with the use of unstructured meshes; initial mesh generation to follow complex bathymetry and coastlines; sub-grid scale modelling on unstructured and possibly solution adaptive meshes; scalable solvers and parallel computing. A good solution to each problem is required, and thus

* Corresponding authors. Tel.: +44 207 5949322; fax: +44 207 5947444 (M.D. Piggott).

E-mail addresses: c.pain@imperial.ac.uk (C.C. Pain), m.d.piggott@imperial.ac.uk (M.D. Piggott).

the resulting model may be argued to be considerably more complex than traditionally used structured mesh models. It is these topics that are addressed here.

© 2004 Elsevier Ltd. All rights reserved.

1. Introduction

Traditional ocean models (for background material, see [Haidvogel and Beckmann, 1999](#); [Griffies et al., 2000](#)) are extremely sophisticated with hundreds of person-years invested in all aspects of their development. However, the fundamental techniques used to solve the momentum and continuity equations have remained largely unchanged since their original development ([Bryan, 1969](#); [Bryan and Cox, 1967](#)). They have typically evolved to a high degree of sophistication (e.g. the MIT model; [Marshall et al., 1997](#)), with a range of methods for parameterising the various unresolved physical processes, as well as the use of hybrid meshes (although still structured) for example. However, evolution does not always result in optimality since current models only reflect the methods and computing resources that used to be available. Thus it seems timely to investigate the possibility of changing some of the fundamental aspects of these models; the use of an unstructured mesh with the option for dynamically changing resolution seems a natural next step.

The first work on the use of finite elements and unstructured meshes in the field of ocean modelling was probably by [Fix \(1975\)](#). Examples of other important early work may be found in [Lynch and Gray \(1979\)](#), [Haidvogel et al. \(1980\)](#), [Platzman \(1981\)](#), [Dumas et al. \(1982\)](#) and [Le Provost and Vincent \(1986\)](#). Subsequent work concentrated mainly on diagnostic models (e.g. [Myers and Weaver, 1995](#); [Greenberg et al., 1998](#); [Nechaev et al., 2003](#)), and models based upon shallow water systems (e.g. [Lynch and Werner, 1987](#); [Ma, 1993](#); [Iskandarani et al., 1995](#)). More recently models which compute solutions with three-dimensional (3-D) hydrostatic ([Lynch et al., 1996](#); [Iskandarani et al., 2003](#); [Danilov et al., 2004](#)) and non-hydrostatic ([Ford et al., in press-a](#); [Labeur and Pietrzak, 2004](#)), dynamics have been developed.

There is currently a fairly wide range of approaches and techniques employed by the ‘unstructured-mesh’ community. For example, the Spectral Element Ocean Model (SEOM) of [Iskandarani et al. \(1995\)](#) uses an unstructured mesh of rectangles in the horizontal, sigma coordinates in the vertical, and is very accurate with the typical use of sixth degree or higher Legendre polynomials. The model of [Lynch et al. \(1996\)](#) uses an unstructured mesh of triangles in the horizontal, with sigma coordinates in the vertical. Buoyancy forces are evaluated by interpolating density onto a structured background mesh. The FEOM model ([Danilov et al., 2004](#)) uses a Galerkin least squares approach to stabilise and remove spurious modes, as well as a finite difference treatment of buoyancy forces on nodes stacked one on top of another in the vertical. The MIT model, although using a structured mesh, can use shaved cells ([Adcroft et al., 1997](#)) to conform to bathymetry, and can use modified z coordinates to adjust the coordinate system to follow a free surface ([Adcroft and Campin, 2004](#)).

New to unstructured mesh models is the need to obtain a suitable coastline and bathymetry conforming mesh ([Legrand et al., 2000](#); [Gorman et al., submitted for publication](#)). Another important aspect of an unstructured mesh ocean model is the choice of element, i.e. how the various solution variables are represented on the mesh. This can be viewed as the analogue of

Arakawa grid staggering in structured mesh models. Work on analysing these choices with regards their impact on spurious computational modes and the representation of states close to geostrophic balance in shallow water models may be found in Le Roux et al. (1998), Hanert et al. (2002) and Le Roux et al. (2004).

The potential advantages of an unstructured mesh ocean model are significant. For example, there are issues relating to boundary conditions when bathymetry and coastlines are represented by a ‘staircase’ regular structured mesh. The result can be an inadvertent application of no-slip boundary conditions, and consequent problems with the transport of dense fluids along slopes. This process must be parameterised for staircase topography, for example using enhanced diffusion in the cells adjacent to the ocean floor. Having the mesh aligned with the bathymetry avoids many of these problems (Adcroft and Marshall, 1998) and allows the fluid to slide over bathymetry, as described by a frictional model for example. Unstructured meshes also enable the use of greater mesh resolution in the direction normal to the coastline than tangential to it where typically boundary layers develop (e.g. western and frictional). Resolving developing flow features (e.g. fronts, eddies, overflows) whose positions are not necessarily known *a priori* requires the use of adaptive mesh resolution. Thus ideally mesh adaptivity techniques would be employed which can dynamically change model resolution to optimally resolve such flows.

The aims of future unstructured mesh ocean models are to:

- be accurate and robust in ocean flow conditions (e.g. accurate noise-free representation of hydrostatic and geostrophic balance);
- be non-hydrostatic but without the additional computational overhead when the flow is close to hydrostatic;
- exploit nonlinear advection methods on unstructured meshes so that both accuracy and robustness may be combined;
- use sub-grid scale modelling designed for unstructured (inhomogeneous and anisotropic meshes) and possibly dynamically changing meshes;
- be conservative;
- possess a free surface and accurately resolve barotropic and baroclinic modes;
- be implicit, or semi-implicit, so that time-step sizes are not necessarily restricted by grid size (i.e. allow large Courant numbers associated with the various physical processes present);
- have an unstructured mesh in the vertical as well as the horizontal to optimise efficiency gains;
- use anisotropic mesh adaptivity with resolution controlled through error measures, or to better resolve areas of socio-economic importance, and also to include mesh movement to allow the model to follow isopycnal layers or coherent structures;
- make use of parallel computing with load-balanced domain decompositions methods;
- be able to assimilate data into a predictive model and exploit natural grid hierarchies to accelerate inversion and obtain sensitivity information.

The remainder of this article addresses these issues with a number of modelling demonstrations using the model under development as part of this work (Ford et al., in press-a). The next section describes numerical advection methods, and highlights the relative merits of a wide range of approaches. In Section 3 the closely related topic of sub-grid scale modelling on unstructured evolving meshes is discussed. In Section 4 the important issue of element choice and its links with

Arakwawa grid staggering is reviewed. Section 5 covers the topics of mesh adaptivity, mesh movement and error measures, which are crucial in many ways for reaping the full benefits of unstructured mesh modelling. This is followed in Section 6 by a discussion on the links between adaptivity and the choice of vertical coordinate which has proved to be so important for traditional ocean models. Section 7 covers initial mesh generation and draws heavily on the previous two sections. Finally, in Section 8 the importance of the accurate representation of balance, solvers and scientific computing issues are discussed.

2. Advection

This section presents numerical methods for resolving on unstructured meshes the transport of density, tracers, momentum, free surface height, and sets of coupled advection equations.

The accurate numerical modelling of advection (or transport) remains a central problem in many areas of fluid dynamics such as oceanography (Pietrzak, 1998; Smolarkiewicz and Margolin, 1998; Hanert et al., 2004; Iskandarani et al., 2004). This is mainly due to the conflicting demands of accuracy and the requirement for stability and boundedness of the numerical discretisation scheme (Darwish, 1993). First-order discretisation schemes, although stable, are highly numerically diffusive. Conversely high-order schemes, although accurate, tend to give rise to numerical oscillations in regions where there are large solution gradients. In the field of fluid dynamics it was realised quite early on (for background see Hirsch, 1990), that the only way to achieve a high-order bounded scheme free from numerical oscillations was to introduce nonlinearity into the discretised equations, even if the original differential equations are linear. This is a consequence of Gudonov's theorem (Toro, 1997) which states that there are no linear monotone high-order schemes for hyperbolic systems of equations.

2.1. Petrov–Galerkin methods

While Bubnov–Galerkin (using the same weighting/test functions as expansion functions) discretisations of transport equations are dispersive, generalised least squares discretisations (Ackroyd, 1997) represent an alternative approach which tend in general to be quite dissipative. If the least squares error is minimised using finite elements as basis functions, a discrete system with a symmetric-positive-definite matrix results. To overcome the problems related to each approach for advection processes, it is popular to combine the dissipative least squares methods with non-dissipative Galerkin methods to produce an attractive compromise in the Galerkin-least-squares (GLS) method (Hughes et al., 1989). These methods are all Petrov–Galerkin in nature (a weighted residual method) and typically applied using finite elements. They have the advantage that they attempt to reduce explicitly the residuals of the governing equations. The consistency of the approach (being a residual based formulation) leads to robustness and accuracy advantages. For example, usually (depending on the element choice) all mass matrices have the property that they are distributed (i.e. non-diagonal).

Similar to GLS is the typical Petrov–Galerkin (PG) weighting; that is, using a weighting function which puts more emphasis on what is happening in the upstream direction. It is a popular choice and the weighting is almost universally chosen for scalar equations as $N_i + \frac{1}{2} \frac{h}{|\mathbf{u}|} \mathbf{u} \cdot \nabla N_i$,

in which N_i is the finite element basis function associated with node i and u is the transport velocity for the scalar being solved for. The element width h depends on the element choice, e.g. h is the width of an element for linear interpolants and half that width for quadratic interpolants. However, these methods are still prone to oscillate in the direction normal to the flow as their dissipation is streamline based. The common cure is to introduce additional nonlinearity (Hughes et al., 1986; Oñate et al., 1997; Almeida and Silva, 1997). This usually takes the form of diffusing away large equation residuals, often in the direction of largest spatial gradients (Masud and Hughes, 1997; Hughes and Mallet, 1986b; Codina, 1993). Although these methods can be shown to be non-oscillatory and satisfy a maximum principle (the maximum and minimum values of the solution variable are on the boundaries of the space–time domain for a scalar advection/diffusion equation with a divergence free advecting velocity field), they tend to be more dissipative than nonlinear finite volume (FV) or control volume (CV) methods. Nonlinear CV methods are well developed and certainly the most widely used transport methods and thus this advantage does not seem surprising.

More recently, discontinuous finite element methods (DFEM) in both the space and time domains have been applied to the time-dependent transport equation (Wareing et al., 1999). Although linear discontinuous representations are more robust than other time-stepping schemes such as Crank–Nicolson, they still lack sufficient numerical stability. Also, variational principles for the time-dependent form of the transport equation have been derived (Donea and Huerta, 2003; Ackroyd, 1997). These variational finite element schemes use continuous finite elements for both the space and time domains. The variational principle can also be recast as a weighted residual formulation with an appropriate spacetime PG weighting. The advantages of these schemes are that their stability properties are potentially better than the linear discontinuous formulations employing Bubnov–Galerkin weightings due to the dissipation introduced from the PG weighting. However, due to the linearity of the scheme it does not preclude the possibility that oscillations may occur in the space–time solution (since this can only be achieved using methods which introduce nonlinearity).

Space–time Petrov–Galerkin methods have found widespread application for solving advection–diffusion-type problems. Space–time finite element methods use either continuous or discontinuous finite elements for both the space and time domains; the time domain is simply treated as another dimension over which transport takes place. The most crucial issue in most space–time formulations is the distance over which numerical dissipation is applied. For linear space–time formulations, typically this has meant a choice between using either the spatial or temporal meshes to determine these distances, or alternatively, using the distance across the space–time elements. If the spatial mesh is used to determine the element length scales, this introduces the correct amount of numerical dissipation for steady-state cases (Eriksson et al., 1996). If the temporal mesh is used to determine the element length scales, this assumes that the spatial dimension is largely invariant. Examples of this approach include the Lax–Wendroff (Lax and Wendroff, 1960) and Taylor–Galerkin (Donea, 1984) methods. A disadvantage of this approach is that the time-step size needs to be tuned in order to represent a typical element length scale associated with a spatial mesh. Thus this approach can become computationally inefficient as steady-state is approached.

None of these methods used to calculate representative distances are entirely satisfactory. A more appropriate way of calculating the distance is to use the variation of the solution in

space–time. Therefore the space–time methods must in general introduce nonlinearity and use the local solution gradients in order to calculate representative distances. For instance, if the steepest gradients in the solution are in the time dimension then the time-step size (or a multiple of it) should act as the representative distance over which numerical dissipation is introduced, see Pain et al. (in press-a).

In addition to the calculation of the representative distance over which numerical dissipation is introduced, the angle between the gradient of the solution and the streamline direction is important and is used in most nonlinear Petrov–Galerkin methods.

2.2. Control volume methods

Control volume (CV) methods involve integrating the transport terms over surfaces of CVs in order to gauge the quantity of incoming and outgoing information. Thus the accuracy of this approach is limited by the accuracy of the information evaluated at the CV boundaries. High-order schemes are typically realised by placing polynomials through local CV values in order that accurate values on the CV boundaries can be established. These high-order polynomials can put more emphasis on interpolating upstream CV cell values such as in the QUICK (Leonard, 1979, 1991) scheme for example. Other possible methods involve constructing a local Taylor series expansion through nearby CV values (Ackroyd, 1997), fitting a plane (which defines a gradient) through nearby CV values in a least squares fashion, or using finite element/spectral element interpolation (Karniadakis and Sherwin, 1999).

These CV methods can easily switch to a non-oscillatory method when a solution extrema is detected, and thus preserve the non-oscillatory (in N-dimensions), and even the Total Variation Diminishing (TVD) property in 1-D. The Sweby diagram approach (Sweby, 1984), is particularly successful at this and typically switches between a number of schemes such as QUICK and a central method as defined by a curve on the Sweby diagram. This curve can be changed to optimise the compressive properties of the scheme (e.g. sharp interface preserving properties) as in the superbee approach (Roe, 1985), or a compromise which does not act to make sine waves square such as in the van Leer approach (van Leer, 1974, 1977).

The Normalised Variable Diagram (NVD) (Leonard, 1988) approach to flux limiting produces equivalent schemes to the Sweby diagram approach, at least in 1-D. However, it acts on more fundamental extrema detecting variables and as such is the approach adopted in the multi-dimensional unstructured mesh formulations employed here. It is the method used to obtain the high fidelity density solutions in the gravity current simulation presented in Fig. 1. The domain here is 20 km long and 5 km wide, with a linearly varying bathymetry of maximum depth 1 km and minimum depth 0.2 km. A column of dense water 5 °C cooler than the surrounding water is released in the shallower part of the domain (cf. Özgökmen and Chassignet, 2002). The Kelvin–Helmholtz instability resulting in vertical mixing and entrainment, and the lobe and cleft structure of the gravity current head can clearly be seen. See Pain et al. (in press) for a full description of the advection method that uses an implicit approach with temporal limiting as well as spatial limiting to avoid oscillations introduced by high-order interpolants used in the time domain, especially when large time-steps are used (the maximum local Courant number for this simulation was 15). The Barton scheme (Centrella and Wilson, 1984) is an effective alternative to other

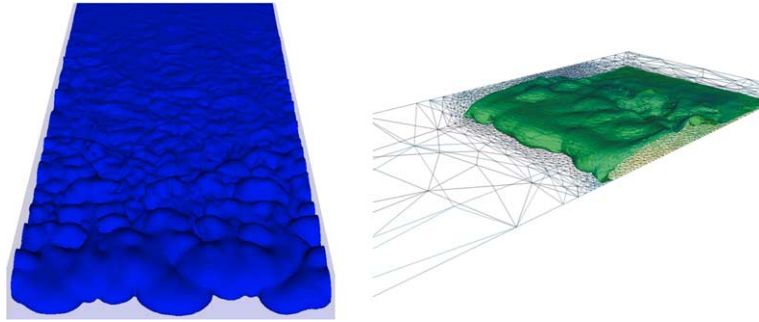


Fig. 1. Density field in a gravity current simulation as described in Section 2.2. Left: an isosurface of density obtained on a fixed hexahedral mesh of approximately 1.5 M nodes, and utilising control volume based high-resolution advection of density. Right: result obtained with standard discontinuity capturing SUPG for the advection of density (an isosurface of which is shown) on an adaptive unstructured mesh of approximately 80000 nodes and 200000 elements.

approaches for unstructured meshes and uses a combination of a number of schemes to evaluate fluxes on CV boundaries.

The DFEM is a combination of CV and FEM methods and typically (as in the Discontinuous Galerkin (DG) method) uses a Galerkin discretisation within each element and CV-like fluxes for incoming/outgoing element information. Attempts have been made to suppress oscillations occurring in DFEM solutions. For example in Kershaw et al. (1998) linear and quadratic elements were used, as well as a nonlinear programming approach, to suppress the oscillations and alter the solution in a minimal way. Since it is a hybrid approach it is especially complex to design a DFEM scheme that satisfies the maximum principle.

2.3. Coupled systems of equations

For coupled systems of hyperbolic equations, such as the shallow water equations, it is possible to determine the incoming/outgoing information to each control volume by looking at eigenstructure of the resulting equations (Brunner and Holloway, 2001a,b). The eigenstructure is spatially variant in many fluid flow problems (e.g. in the compressible inviscid and shallow water systems), but fortunately analytical expressions for the eigenvalues and eigenvectors exist (Toro, 1997, 2001). Multi-dimensional Riemann methods typically form a 1-D Riemann decomposition normal to each face of a control volume. The most accurate approach (also used to form the basis of a residual formulation) is to use the same upwind bias used to discretise the fluxes to discretise the sources in the equations normal to a face. In addition, since this approach allows one to determine the quantity of incoming and outgoing information for coupled systems of hyperbolic equations, it allows the easy application of limiting methods (limiting the fluxes on the control volume boundaries to avoid oscillations). The limiting functions should ideally take into account sources in the differential equations when calculating extrema detecting functions (Hubbard and Garcia-Navarro, 2000).

Least squares methods are also an effective means of dealing with coupled systems of equations. When dealing with equation sets with different dimensions (e.g. momentum and continuity equations) it can be advisable to multiply one of these equation sets by a certain dimensional number,

or equivalently solve the equations in non-dimensional form. However, one of the main problems with this approach is that it is not always clear what number to multiply one or more of the equation sets by, and this can vastly affect the performance of the least squares discretisation. In addition, practitioners are often disturbed to find the discretised momentum equation within the discretised continuity equation and vice-versa. On the positive side this approach can eliminate spurious modes (e.g. pressure modes), making it possible to use shared pressure–velocity–free surface meshes. It will also suppress spurious numerical oscillations near sharp gradients. However, as with other dissipative discretisation schemes, care must be taken when combining it with sub-grid scale models such as Large Eddy Simulation (LES) methods, since the dissipative discretisation method is in effect providing much of the sub-grid scale modelling (Hughes et al., 2000). Similarly, least squares methods and coupled equation PG methods share all the above attributes with GLS methods.

A diffusion based approach of introducing nonlinearity into PG methods for solving strongly coupled systems of equations is reported by Shakib et al. (1991), the magnitude of the diffusion is proportional to the magnitude of the equation residuals. Thus the method acts to diffuse out equation residuals. Nonlinear discontinuity capturing PG schemes applied to coupled systems use a rank-one weighting matrix for the application of isotropic diffusion (Hughes and Mallet, 1986a,b; Shakib et al., 1991). The streamline up-wind Petrov–Galerkin (SUPG) method of Pain et al. (in press-b) uses a nonlinear PG formulation with diffusion introduced only in the streamline direction, and for time-dependent problems this diffusion acts in space–time using DFEM in time, see Pain et al. (in press-a).

To avoid equation coupling issues the momentum and continuity equations are most often treated separately. Moreover, this approach can guarantee to result in bounded densities and tracers when solving the coupled momentum and incompressible continuity equations using a piecewise constant basis function for the density, and the same basis functions for pressure and for the weighting of the continuity equations. For a bounded scheme the fact that the discretised continuity equation is embedded in the discretised advection equation presents additional issues that can be addressed with CV methods. Unless the discretised continuity equation is actually the discretised continuity equation satisfied by the solution to the momentum/continuity equations, then sources/sinks of the advected quantity will result affecting the boundedness and accuracy of the solution. This consistency was achieved in the high-resolution method results shown in Fig. 1, and is the main reason why control volume methods are applied in situations where the solution must be bounded.

3. Sub-grid scale modelling on unstructured meshes

Sub-grid scale (SGS) modelling has many links with, and is strongly related to, the topic of accurate and robust advection methods. This is because much of the sub-grid scale processes requiring modelling (e.g. various turbulent effects) are processes described by transport, but usually on a scale much smaller than the mesh size (Sagaut, 1998). Thus it is not surprising that transport methods themselves have often been used as turbulence models (e.g. Denbo and Skyllingstad, 1996; Hoffman and Johnson, 2004). See also Hughes et al. (2000) for a discussion of the links between the Smagorinsky LES and the variational multiscale approach to numerical stabilisation

when modelling turbulent flows. In fact sub-grid scale modelling techniques have been shown in many ways to be equivalent to some of the stabilisation techniques discussed in the previous section (Hughes, 1995; Brezzi et al., 1997).

Since the error (deviation of the numerical solution from the exact solution) satisfies a transport equation set similar to the original (Donea and Huerta, 2003), it is not surprising that sub-grid scale processes often involve the use of transported variables e.g. turbulent kinetic energies in dynamic Large Eddy Simulation (LES) models. As far as this work is concerned the main issues are the design of sub-grid scale models on variable resolution unstructured meshes, and how they interact with dynamically changing anisotropic resolution (Figs. 1 and 2), right up to the point where the processes become explicitly resolved by the mesh. Bearing in mind that the sub-grid scale model typically depends strongly on resolution, the interaction of sub-grid scale modelling with dynamically changing meshes provides additional nonlinearities that need to be understood. In fact this may provide an entirely new field of endeavour. For example, there is a requirement to include both the discretisation and the modelling errors, e.g. model errors from LES (Hoffman and Johnson, 2004). Goal based mesh optimisation methods, in which the mesh is adapted to optimally represent the goal, e.g. the drag past an obstruction or a measure of the dynamics of the flow, may be constructed to take into account the additional nonlinearities associated with these SGS models, see Hoffman and Johnson (2004) for further discussion on goal based mesh adaptivity. See Bentham et al. (in press) for a discussion on how anisotropic and inhomogenous mesh resolution may be reflected in the sub-grid scale model.

An alternative modelling approach can be derived by averaging the fluid quantities along fluid particle trajectories, i.e. Lagrangian averaging. The advantage is that fluid structures, such as



Fig. 2. Adapted unstructured mesh for a barotropic wind driven gyre circulation on a beta-plane. Anisotropic resolution has automatically been focused in the western boundary current region and subsequent nonlinear eddies, and changes in response to the evolving flow fields.

overturning billows and vortices, remain more coherent and are not smoothed to such an extent. One such model, the LANS-alpha model (Foias et al., 2001), changes the momentum equations so that the fluid is advected by a smoothed velocity field (the smoothing may be designed to match the variable numerical resolution). This filtering has been demonstrated to yield very attractive results including, for isotropic turbulence, an improved adherence to Kolmogorov's $-5/3$ energy-wavenumber scaling-law, up to the length scale set by the filter. For an oceanographic application see (Holm and Nadiga, 2003).

Another example of sub-grid scale modelling is that given by the wind forcing which generates waves and imparts momentum into the ocean depending on the wave amplitude and whether they break (Cavaleri and Bertotti, 2003). This type of sub-grid scale model typically discretises the probability density function of the waves into their frequency (wavelength) and direction, resulting in a large set of coupled differential equations—the coupling is via nonlinear wave interactions. The discretisation of wave direction (as well as frequency) is strongly related to mesh resolution. Not taking into account the spatial resolution can lead to ray effects (spurious numerical rays due to the truncation of direction discretisation). Similar models must also be developed for the interaction with the atmosphere through heat fluxes, and in an analogous way internal waves and diapycnal mixing. Ice modelling also provides additional sub-grid scale challenges.

Various further phenomena, such as overturning and mixing, need parameterisation. They typically range from the use of infinite diffusion in the vertical when an inversion of the stratification occurs, to 2.5 equation approaches to vertical mixing (Mellor and Yamada, 1982). Whereas with attempts at resolving the turbulent 2-D (horizontal) structures via simple eddy parameterisation, e.g. bi-harmonic dissipation (which is difficult to treat implicitly because of large stencils) and LES methods, often no attempt is made at modelling the turbulent fluctuations in the vertical and second moment closure methods are thus frequently used (Mellor and Yamada, 1982). See also Gent and McWilliams (1990) for a popular and successful approach to parameterising isopycnic mixing by geostrophic eddies. Additional parameterisations are required for vertical mixing and entrainment due to fluid moving over inclined bathymetry; effects due to the roughness of the bathymetry and coastlines are typically modelled in the form of Rayleigh friction or viscosity models. For example the friction required in coastal shallow water models is typically a vertical average of the bottom Rayleigh friction.

Numerous other sub-grid scale processes need parameterising, and the models employed need amendment to work on unstructured meshes with potentially fine mesh resolution, right up to the point where the processes become explicitly resolved by the mesh.

4. Mixed finite elements

In an analogous manner to structured A, B, C, D, and E grids (Arakawa and Lamb, 1977) (which respectively consist of a shared velocity/pressure mesh; velocity nodes at the corners and pressure nodes at the centre of elements; velocity normal to a face at the element faces and pressure at the element centre; velocity tangential to a face at the element faces and pressure at the element centre; and the velocity at the faces and pressures at the element centre), there exist many possible finite element pairs which have varying capabilities in resolving inertia-gravity

and Rossby waves for example. For background related to standard structured mesh methods see Haidvogel and Beckmann (1999) and Griffies et al. (2000) and the references therein, and for unstructured meshes see Le Roux et al. (1998), Hanert et al. (2002) and Le Roux et al. (2004), and see also Section 8.4. Some of the simplest and most popular choices are now briefly discussed.

Using the notation of Gresho and Sani (1998), the hexahedral (Q_1P_0) element with tri-linear velocity and piecewise-constant pressure is equivalent to the B-grid and thus has the property of representing well internal waves when the Rossby deformation radius is large in comparison to the local mesh resolution. It is however plagued by singular pressure modes which seem largely not to affect the accuracy of velocity, especially with the limited use of Dirichlet velocity boundary conditions. It is stabilised typically with piecewise-constant shock functions (Gresho and Sani, 1998; Norburn and Silvester, 1998).

The hexahedral (Q_1Q_1) and tetrahedral (P_1P_1) elements employ a shared mesh and have similarities with the A-grid. Again this choice needs stabilising which typically takes the form of a second or fourth-order dissipation term introduced into the right-hand side of the continuity equation. When a pressure equation is formed in its continuous representation a fourth-order stabilisation term is effectively introduced into the continuity equation (Sotiropoulos and Abdallah, 1991) which explains in part its success. However, this approach is plagued by difficulties in achieving continuity satisfaction locally or globally. Introducing bubble functions to the approximation of velocity (the result is often termed the MINI element) can also cure the stability issues (e.g. Fortin and Fortin, 1985) and has been shown to produce identical discretisations to certain Petrov–Galerkin weightings—yet another form of stabilisation (Hughes, 1995). Recently there has been the realisation that subtracting a more accurate first-order operator from a less accurate representation of the first-order operator has very nice dissipative properties that can eliminate spurious pressure or free surface modes (Codina and Blasco, 2000). This is also true of second-order operators and has been used in ocean modelling for many years by subtracting out one rotated (less accurate) discretisation using a five point stencil from a second five point stencil discretisation of diffusion to eliminate spurious free surface height modes.

The hexahedral (Q_2Q_1) Taylor–Hood element with a linear variation in pressure, a quadratic variation in velocity, and simple continuity between elements is LBB (Ladyzhenskaya, 1969; Babuška, 1971; Brezzi, 1974) stable but has many more velocity nodes than continuity equations. The result can be surprisingly poor accuracy with forcing of the momentum equations, as in, for example, buoyancy-driven flows. The cure seems to be to project the forcing onto the pressure basis functions. The introduction of an additional piecewise-constant pressure component can also be an effective cure. The closely related 20 node serendipity element does not have such problems, but it is considerably less accurate and the resulting mass matrices are not easily lumped (which can be important for solvers). The tetrahedral (P_2P_1) Taylor–Hood element has similar properties to the corresponding hexahedral element.

The lowest-order Raviart–Thomas element ($P_1^1Q_0$) consists of a piecewise-linear basis function centred on element edges and used to represent the normal component of velocity, along with a piecewise-constant pressure. It is the analogue of the C-grid and seems particularly useful, for example in Legrand et al. (2000) it was shown not to exhibit spurious free surface pressure modes.

The lowest order Crouzeix–Raviart element ($P_1^{NC}Q_0$) consists of a piecewise-linear basis function centred on element edges and used to represent velocity components, and a piecewise-constant pressure. It may be considered to be the analogue of the E-grid. It was shown by Le

Roux et al. (1998), along with many other low-order pairs, to have problems representing geostrophic balance accurately.

Other possibilities include using a piecewise-linear discontinuous velocity within each element and a continuous piecewise-quadratic pressure. This has the advantage that the mass matrices are block diagonal (each block being associated with an individual element) and is LBB stable, but its lack of inter-element continuity requires careful treatment of second-order terms generally resulting in large stencils. The choice of quadratic velocity and quadratic pressure can be stabilised with a pressure dissipation term in the continuity equation. Often this term is matched by a corresponding alteration to the discretisation of the pressure in the momentum equations. An alternative form of dissipation is to add a term which penalises the deviation of the pressure from a linear variation. This will manifest itself as supplementary edge equations in quadratic elements; when the value of dissipation is large the result is a linear variation of pressure through each element. Again, introducing a cubic bubble function for velocity can make quadratic elements LBB stable. To allow for the use of equal order interpolants for the representation of velocity and pressure in incompressible Navier–Stokes solvers the constraint may be modified through the inclusion of a ‘filter term’. The pressure gradient projection technique constructs this term by introducing a new unknown — the projection of the pressure gradient onto the velocity space, the term added to incompressibility is then the divergence of the difference between the pressure gradient and its projection, multiplied by a suitable parameter ideally defined element-wise (Cordina and Blasco, 2000).

For further discussions on the crucial matter of element choice, see Fortin and Fortin (1985), Gunzburger (1989), Brezzi and Fortin (1991), Girault and Raviart (1986), Gresho and Sani (1998), Le Roux et al. (1998) and the references therein.

5. Mesh adaptivity/node movement

A common problem encountered by model users is that the computational grid or mesh used in a numerical simulation has to be generated a priori to the solution procedure. It is therefore difficult to resolve adequately the local physical features at a first attempt, and the mesh often needs to be adapted to enable the solution procedure to satisfy resolution requirements. Importantly, this also allows for a reduction in computational effort which is crucial for complex applications. As an example see Fig. 2 where an adapted mesh from a simulation of wind driven barotropic circulation in a box is presented. Further discussions on the application of adaptive methods in ocean modelling, including mesh movement techniques, is given in (Piggott et al., 2004).

Many adaptivity techniques make use of a hierarchy of meshes where de-refinement involves rolling back a hierarchy of elements in the mesh (e.g. Jimack, 1998; Olliver et al., 2000). While hierarchical adaptive methods are anisotropic to a degree, it is not possible to form long thin elements aligned with the solution as elements are restricted by their *ancestors* in the hierarchy. An alternative anisotropic mesh optimisation technique is used in the authors’ ocean model and was developed by Pain et al. (2001). A tetrahedral mesh is improved through edge collapsing and splitting, edge swapping, face to edge swapping, and smoothing in a fashion similar to Freitag and Ollivier-Gooch (1997) and Buscaglia and Dari (1997).

5.1. Error measures for mesh adaptivity

Mesh adaptivity or optimisation relies on the derivation of appropriate error measures which dictate how the mesh is to be modified. Several error measures which serve as a criterion for mesh modification have been proposed. These range from interpolation-based a priori error measures (Löhner et al., 1985; Peraire et al., 1987; Wu et al., 1990), to a posteriori error measures (Strouboulis and Oden, 1990; Ainsworth and Oden, 1997) which can take into account the physics of the problem by, for example, applying an implicit equation residual technique and often involve the solution of an associated dual problem. A priori error measures tend only to give an indication of the solution complexity at the current time. Conversely, since they take more account of the underlying problem being solved, a posteriori error measures are able to quantify the accumulation and propagation of the error through the mesh. Another approach is to optimise the mesh so as to optimally resolve a quantity or goal of interest. This goal could be configured to be an oceanographically relevant quantity, see Power et al. (2004) and the references therein. An additional consideration when adapting the mesh is that not only node density, but also the alignment of the mesh relative to the solution is important. For example, in boundary layers or fronts the mesh may need to be refined in one direction only e.g. normal to a western boundary current. Hessian-based error measures (derived from interpolation theory) are capable of fulfilling this requirement (Piggott et al., 2004). They have additional attractive features, such as simplicity and ease of evaluation, they also enable the use of a non-Euclidean metric allowing the meshes to be anisotropically adapted truly automatically.

5.2. Methods of adapting a mesh

Once an error measure has been derived the nodes may be re-distributed according to this measure. This step in an adaptive procedure is quite complex algorithmically, and is intrinsically dependent on the initial mesh generation method and geometrical and material boundary conforming requirements (e.g. kinetic energy absorbing sponge layers near domain boundaries). Unstructured tessellation methods can deal with geometries of arbitrary complexity and they lend themselves naturally to adaptivity. There are three main approaches to the generation of unstructured tetrahedral meshes: the Delaunay triangulation scheme (George, 1998); the Advancing Front technique (Löhner and Parikh, 1988; Moller and Hansbo, 1995); and the Quadtree/Octree approach (Kallinderis and Vijaya, 1993). Delaunay tessellation is a procedure for forming optimal tessellations using an appropriate metric for measuring distances. It leads to robust algorithms which can easily incorporate adaptivity. Region-wise coarsening/refinement can be achieved with the Advancing Front technique in which both new nodes and triangles are regenerated in the region (Kallinderis and Vijaya, 1993). The main drawback of this technique is the fact that the mesh has to be regenerated at every mesh adaptation, which can be computationally expensive for large problems. Octree methods by nature do not offer scope for aligning the mesh anisotropically with the solution.

In general 2-D Delaunay meshes are of good quality and can lead to useful mesh adapting schemes for triangular (Xu et al., 1998) and quadrilateral (Borouchaki and Frey, 1998) elements. However, in 3-D when nodes are evenly distributed, the element aspect ratio can

become very large (George, 1998), despite all the edge lengths of an element being approximately equal with respect to the desired metric. Local mesh connectivity transformations have been used by Joe (1989) to obtain a mesh that satisfies the Delaunay property, along with a modification to optimise the interior dihedral angle of the resulting tetrahedral elements and discourage thin ‘slivers’. Further work on 3-D Delaunay meshing can be found in Borouchaki and Lo (1995), Borouchaki and George (1996), Castro-Diaz et al. (1997) and Weatherill (1994).

The fact that the Delaunay kernel permits element ‘slivers’ has provided the motivation to discard it in favour of mesh optimisation methods here. Such optimisation methods are guaranteed to converge and have proved relatively insensitive to computational roundoff error which can be an issue with Delaunay methods (Xu et al., 1998). For example, Freitag and Ollivier-Gooch (1997) demonstrated successful mesh optimisation involving swapping (mesh connectivity adjustments) and smoothing (node position adjustments) of a mesh, and also showed that using either of these independently leads to severely reduced mesh quality. In particular, interior element angles are highly sub-optimal with node movement alone. Also, it was demonstrated that purely optimisation-based node movement is CPU-expensive when compared with simpler methods such as Laplacian-based smoothing, and with little gain in mesh quality over the latter. This has motivated the use of approximate optimisation techniques for mesh smoothing (node movement) based on minimising an energy norm. The quality of the poorest element (as defined by some objective functional) is used as a measure of the overall mesh quality. This quantity is calculated via a Riemannian metric based here on the combination of solution field Hessian matrices. Appropriate scaling of the metric (Castro-Diaz et al., 1997) enables the resolution of multi-scale phenomena as encountered in oceanic flows.

5.3. Mesh movement

Whilst the methods described above represents a major increase in power for numerical models, further important developments are possible. In fluids applications the ability of the mesh to move in a quasi-Lagrangian manner is a considerable benefit. For example, if mesh points were moving approximately with the flow velocity this would effectively result in a much reduced transport velocity (relative to the moving mesh), and hence the possibility of accurately using larger time-steps, cf. the properties of semi-Lagrangian methods (Staniforth and Côté, 1991). A major disadvantage of Lagrangian-like schemes is that mesh tangling may occur. This may be mitigated, and robustness restored, through the combined use of mesh movement and mesh adaptivity or optimisation as introduced in previous sections. This combined approach offers the advantages of each method, without many of the drawbacks, it may be viewed as a generalization of the popular arbitrary Lagrangian–Eulerian (ALE) methods (Donea and Huerta, 2003). Additional advantages of using a moving mesh to account for a large proportion of the mesh resolution change is that the use of mesh-to-mesh interpolation may be minimized (indeed this requirement could be included in the definition of a controlling error measure), and load-imbalances (see Section 8.6) in parallel computations will occur at a reduced rate. Current research is revolving around the issue of using moving variable resolution in the vertical to mimic the properties of isopycnal models in the ocean interior. See Piggott et al. (2004) for further details and discussions.

5.4. Wetting and drying

The 3-D modelling of flood propagation in river and floodplain systems can use existing numerical formulations, but significant developments are needed to include wetting and drying processes and appropriate mesh adaptivity criteria for a moving waterline. An irregular waterline and land geometry, and the appearance and disappearance of isolated dry areas, makes the modelling of wetting and drying a significant challenge. There exists no purely Lagrangian method that can deal with this situation. However the volume of fluid (VOF) approach (as is often used in highly convoluted free surface problems), in which a volume fraction function is used to represent the fraction of each mixed cell occupied by fluid, can represent arbitrarily complex wetting and drying geometries. The wetting/drying interface can be tracked with a volume tracking method with a geometric evaluation of the volume fluxes across the interface. For example, in the new mixed marker and VOF method (Aulisa et al., 2003) the reconstruction and advection of the waterline during wetting and drying processes is modelled. Among numerous algorithms, Aulisa's method combines mass conservation and an accurate representation of the coastline curvature. In order to best represent the movement in the wetting and drying process, meshes near the waterline can be refined and/or mesh adaptivity used as suggested by Tchamen and Kawahita (1998), Horritt (2002) and Bates (2000). Some of the accuracy of Lagrangian wetting and drying methods can be regained with the VOF approach when it is combined with mesh adaptivity and node movement.

6. Coordinate systems and comparison with unstructured mesh methods

In many respects the coordinate system is the most fundamental choice for any ocean model (Haidvogel and Beckmann, 1999; Griffies et al., 2000). It defines the way that the discretisation is performed in the vertical. The three most commonly used choices are: z coordinates (regularly spaced cells/elements in the vertical with cells on the same horizontal level); sigma coordinates which follow the bathymetry and stretch the mesh in the vertical linearly up to the free surface; and isopycnal coordinates which follow surfaces of constant density. Each has its own advantages and disadvantages, the only current certainty being that no single approach is ideal for general wide-ranging oceanic application. z coordinates have the advantages of simplicity and the ability to resolve pressure gradients accurately, however they are poor at representing bathymetry in a smooth and accurate manner (Adcroft et al., 1997). Isopycnal methods, which in effect align the mesh in the vertical with isopycnals and move with them in a Lagrangian manner (see previous section), may result in improved levels of diapycnal mixing which can be very poorly resolved with other methods, although problems may arise when layer thickness vanishes (Bleck, 1998). Sigma coordinates are well suited to accurately follow bathymetry and allow the application of appropriate boundary conditions on the sea floor, but they are prone to large pressure gradients errors in the presence of steep bathymetry (Haney, 1991).

Hybrid methods are used to combine the advantages of more than one approach. For example, isopycnal coordinates may be used in the interior of stratified ocean basins, with z coordinates in the surface mixed layer and on the shelf, and sigma coordinates near the ocean floor (Griffies et al., 2000). There are obviously interfacing issues where the coordinate systems or mesh changes.

In Bleck (2002), isopycnal coordinates are used which relax to Cartesian coordinates as the thickness of cells in the vertical vanishes—one of the major disadvantages of purely isopycnal methods.

However, there is a growing realisation that a 3-D unstructured mesh method can provide an alternative hybrid approach, with a combination of mesh optimisation and node movement in the vertical in a Lagrangian-like manner to follow the free surface and isopycnals, and to improve levels of diapycnal mixing, for example. Mesh adaptive techniques may also be used to re-distribute the mesh resolution locally or more globally, for example in response to the convergence of isopycnal layers, or to optimally represent sections of the bathymetry of most importance to the resulting solution dynamics. The use of an unstructured mesh in the vertical can yield problems analogous to the pressure gradient errors encountered with the use of sigma coordinates. A possible solution to this is described in Ford et al. (in press-a, in press-b).

As previously discussed, an unstructured mesh in the horizontal has the advantage of being able to focus resolution in order to resolve what is of interest, and not be restricted to the resolution dictated by any singular points (e.g. spherical poles) present in the coordinate system used in the horizontal. Although it may seem that finite elements have no problems with singularities (perhaps with the underlying coordinate being arbitrarily chosen as Cartesian coordinates), there may be issues when there is a need to resolve turbulent mixing with anisotropic diffusion/viscosity tensors (e.g. small diffusion in the vertical whilst relatively large in the horizontal). There is still a need to define this and singularities seem unavoidable in its definition (although they are perhaps easier to deal with).

7. Bathymetry and coastline conforming mesh generation

The accurate simulation of various oceanic processes requires not only an appropriate model of the physical forces that drive the system, but also a sufficiently accurate representation of the domain of interest, i.e. here a domain defined by the bathymetry and coastline. Inadequate representation of the coastline may lead to problems such as spurious stresses (e.g. Adcroft and Marshall, 1998), while poor representation of bathymetry can lead to problems modelling internal waves or separation of boundary currents (e.g. Özgökmen et al., 1997; Stern, 1998; Tansley and Marshall, 2000; Munday and Marshall, submitted for publication). In practice there is a trade off between how close the discretised domain is to reality and how appropriate it is for numerical modelling with finite computational resources. Therefore, a computational mesh representing the geometry should be optimised everywhere with respect to this trade off by representing the geometry to a specified error, with a minimum number of mesh elements or nodes.

The majority of ocean models, whether they use regular cell spacing or curvilinear grids, represent the domain with a structured mesh. The curvilinear grid lines yield a mesh of quadrilateral computational cells in the horizontal which may be fitted to the coastal geometry. Typically, this horizontal structure is then maintained throughout the vertical levels. Unstructured mesh models offer an alternative approach. Their flexibility means that a far more accurate and efficient representation of domain geometries is possible. The number of nodes/elements used to represent the boundary will limit the minimum cost of the entire simulation. It is suggested that this representation should not be altered during the course of a simulation; that is, the original surface should not be coarsened during a mesh adaptive simulation to avoid changing the integrity of the domain and associated conservation issues. In an adaptive simulation the mesh may of course be refined

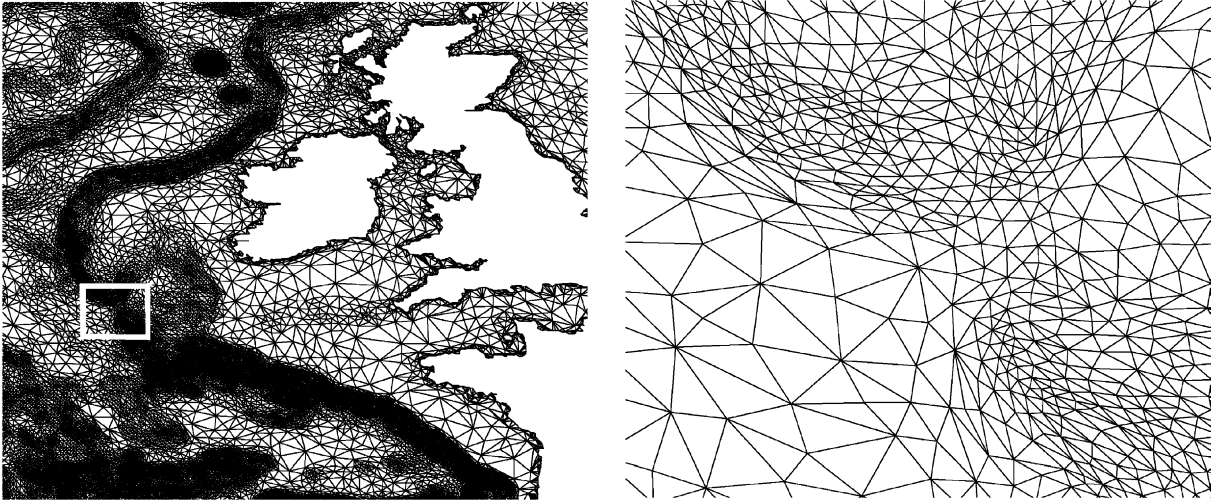


Fig. 3. Section of a mesh constructed for the North Atlantic. The panel on the right is a blow-up of a region of the Celtic Shelf break given by the white box in the left panel.

without changing the bathymetry representation where/when necessary to follow the flow. Thus it is desirable to represent a given geometry to a prescribed accuracy with the minimal number of nodes/elements to avoid excessive resolution in the eventual simulations.

Unstructured grid generators are typically based upon a Delaunay algorithm, for example as used by codes such as TriGrid (Henry and Walters, 1993) and Triangle (Shewchuk, 2003). This approach has been used in oceanographic applications on the sphere by Legrand et al. (2000). Many of these methods provide techniques for inserting extra nodes in regions where there is a steep gradient or curvature. In addition to this, since a Delaunay mesh is the aim, the quality of an element in the mesh is judged more on its geometrical quality in the Euclidean sense, rather than on its accuracy at representing bathymetry.

A typical bathymetry conforming unstructured mesh is presented in Fig. 3. This (sea floor) surface is a section of a mesh constructed for the North Atlantic, and a blow-up is shown to demonstrate the ability to construct a mesh which aligns itself, for efficiency, with bathymetry variations. The mesh generation approach taken here for robustness employs similar anisotropic mesh adaptivity methods as described in Section 5. To conform to the bathymetry the field whose accuracy is being optimised is the depth of the ocean. Thus the quality of elements is measured with respect to a metric constructed from the curvature of the bathymetry. This, combined with appropriate coastline recovery, results in a 3-D anisotropic mesh which focuses resolution where it is required to optimally represent the bathymetry of the domain. For further details and examples, see Gorman et al. (submitted for publication).

8. Solving the linear equations

The main issue in this section is the solution of the coupled momentum and continuity equations, with the incompressibility constraint being enforced through pressure in a similar manner

to a Lagrange multiplier. Due to problems with scalability, direct solvers are not generally used for large scale ocean modelling and so only iterative solution methods are considered in this section. Other important issues include coupling with the free surface through perhaps a supplementary free surface equation, and internal waves through the evolution of the density field. Ultimately, this requires the solution of a large matrix equation which couples velocity, pressure and density, and is formed after linearisation of the equations. Usually Picard iteration is used to linearise the system of equations; Quasi-Newton-type methods are generally not used as their radius of convergence is smaller, resulting in less stable schemes. Most often the coupled pressure/velocity equations are solved together implicitly or semi-implicitly; this allows for the use of larger time-steps than those permitted with explicit methods. Using large time steps (as measured by the local Courant number) may be especially important when an adaptive algorithm provides a wide variation in element sizes.

8.1. Coupled solvers

Standard techniques for solving the coupled systems either solve the equations as they are (Brezzi and Fortin, 1991; Girault and Raviart, 1986; Gresho and Sani, 1998), typically with GMRES (Saad and Schultz, 1986) and a suitable preconditioner (these preconditioners often mimic the actions of projection based methods, see below), or they eliminate velocity and solve for pressure separately. This requires matrix inner and outer iterations. The outer iteration may be of gradient type e.g. FGMRES (Frayssé et al., 1998) and solves the system for pressure. For Stokes flow the result is a symmetric positive definite matrix for pressure, and the method is referred to as the Uzawa method. The inner iteration is required to perform a matrix vector multiplication, as this requires the solution of the discretised momentum matrix. When Coriolis forcing is dominant this provides a good representation of balance not polluted by time truncation operator splitting errors associated with segregated velocity-pressure solution methods.

8.2. Projection methods

Many current ocean models opt for a semi-implicit approach which involves the segregated solution for velocity and pressure, but is still implicit in each individually. These are derived from the SIMPLE family of methods (Patanaker and Spalding, 1970) for obtaining pressure, in which one typically solves the momentum equations with a best guess for pressure, and then projects the resulting velocity field into a continuity satisfying space such that the vorticity remains invariant, see also Gresho (1990) and Ford et al. (in press-a). These systems of equations are repeatedly solved until convergence. Often in time-stepping methods one or two steps of this procedure are used. This approach can also be used with an inconsistent method of solving for pressure, for example solving a second-order equation for pressure. Care must be taken when using mass lumping inconsistently for the scheme to remain stable. This results in a mixed mass method (i.e. lumped mass for pressure and consistent mass for momentum), see Gresho and Sani (1998).

Typically the CFL condition is not violated by orders of magnitude (fluid particles do not travel right across the domain) and thus the resulting matrices that are solved for momentum and tracers are well-conditioned (although mesh quality can play an important role here, see Piggott et al. (2004)) and can easily be solved. However, the elliptic ‘pressure’ equation that is solved in incom-

pressible flows is not as well-conditioned, since this reflects the global spread of information right across the domain to ensure continuity satisfaction. This is the most difficult case, whereas for compressible flows the matrices become better conditioned. With free surface flows much of the pressure changes can be absorbed by the free surface and so the information is not spread so far in a single time-step.

8.3. Operator splitting to resolve waves

The momentum equation can be depth averaged, either algebraically or by integration, and the result combined with the kinematic free surface equation to obtain a wave equation for the free surface height. Care must be taken to achieve a level of consistency between this approach and the full 3-D equations, particularly when the barotropic and baroclinic modes are solved for separately. For example, the barotropic mode with a free surface may have a much smaller time-step (to resolve the fast surface gravity waves) than the 3-D baroclinic mode which is far more expensive. Uncoupling these can vastly improve computational efficiency, but presents issues when bringing these modes back together, see for example Killworth et al. (1991). How to effectively do this remains an unsolved problem with an unstructured mesh model; for some work towards this goal in a restricted case, see Danilov et al. (2004).

8.4. Balance

As well as relying on the element type to allow the accurate representation of states close to hydrostatic and geostrophic balance (cf. Section 4), there are methods of subtracting out these effects from the governing equations. Released from the constraints of representing balance well, far greater flexibility in the choice of element results. For example, the choice may be made on the grounds of efficiency and accuracy, or in the elements ability to represent other solution characteristics.

LBB stable element choices generally have problems accurately approximating hydrostatic balance $\partial p/\partial z = -\rho g$ on unstructured meshes. Thus it is convenient to split the pressure p into hydrostatic p_h and non-hydrostatic parts p_{nh} and solve for these separately. In Lynch et al. (1996) ρ is interpolated onto a regular background mesh and from this p_h is calculated by integration. In the finite element model FEOM (Danilov et al., 2004) the mesh is constructed such that nodes are aligned one on top of the other in the vertical, and p_h is solved for using a 1-D finite difference method. Alternatively, in the non-hydrostatic code of Ford et al. (in press-a) p_{nh} is dealt with in the same manner as the pressure is in standard Navier–Stokes solvers (cf. Sections 8.1 and 8.2), whilst the effects of the hydrostatic pressure gradient are calculated by differentiating the expression $\partial p_h/\partial z = -\rho g$ in the horizontal, and then integrating down from the free surface to obtain $\partial p_h/\partial x$ and $\partial p_h/\partial y$. These are then placed directly into the horizontal momentum equations as additional source terms. This is one of the most accurate ways of dealing with hydrostatic balance for a given polynomial expansion. On a non-uniform unstructured mesh this procedure is not straightforward and discontinuous linear elements are used to represent these derivatives in Ford et al. (in press-a) which allows for an arbitrary mesh structure in the vertical, see Fig. 4 (centre) for the resulting pressure field following the special treatment of buoyancy. In addition, the gravity currents in Fig. 1 were modelled using this approach.

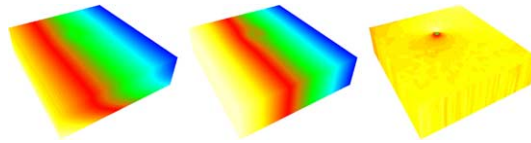


Fig. 4. Pressure field in simulation of stratified flow past a Gaussian seamount on an f -plane. Left: the computed ‘full’ pressure without any special treatment of the ‘hydrostatic’ and ‘geostrophic’ terms. Centre: remaining pressure following the subtraction of the ‘hydrostatic’ term, as explained in Section 8.4. Right: remaining pressure following the subtraction of both the ‘hydrostatic’ and ‘geostrophic’ terms, as explained in Section 8.4.

In an analogous manner, states close to geostrophic balance cause problems for finite element discretisations on unstructured meshes. Again, the appropriate choice of element pair can reduce this issue (Le Roux et al., 1998). See also Adcroft et al. (1999) where a combination of Arakawa staggered grids is suggested for use in grid point schemes. Alternatively, geostrophic balance may be dealt with by forming an elliptic equation for the effect of Coriolis acceleration by first forming a Helmholtz decomposition of the Coriolis term into divergence-free and curl-free components. It is worth mentioning that this can also be done for hydrostatic balance. Since there are no restrictions in the choice of elements used to resolve this expression, for example linear elements can be used with a Q1 (or P1) representation of velocity, it may be solved to a high accuracy to minimise spurious noise effects. Also, since the resulting discretisation matrix is formed in the continuum, the stencil for a given order of pressure approximation is reduced. This makes it cheaper to solve, and since it removes the largest parts of pressure from the governing equations the non-geostrophic/non-hydrostatic parts of pressure can be quickly solved for, using an elliptic equation solver. This combination also enables local continuity satisfaction and in principle, a higher-order polynomial expansion can be used to achieve balance far more accurately. See Fig. 4 (right) for the resulting pressure field following the special treatment of the Coriolis (or ‘geostrophic’) term.

8.5. Elliptic equation solvers

Solving for pressure or free surface height can often be done by solving a symmetric-positive definite system of equations. The most natural solver is Preconditioned Conjugate Gradients (PCG) and thus the choice of preconditioner is critical (Golub and van Loan, 1989). Incomplete Cholesky factorisation, Symmetric Successive Over Relaxation (SSOR) or Parameterised Forward Backward Gauss-Siedel (FBGS) (Adams, 1983) have often been used, but as the system of equations becomes large, multi-grid type methods or hierarchical preconditioners can become more effective (Stüben, 2000). These have optimal convergence properties but require a series of increasingly finer meshes or solutions. For an unstructured mesh often the only practical choice is an algebraically formed series of coarser problems. These are typically realised by a suitable mapping from a nodal to hierarchical basis, and a corresponding mapping of the matrix to form a coarser representation of it. In practice a series of increasingly coarse matrices are used; this rapidly spreads solution information across the domain and is particularly important for large problems with great horizontal resolution, although perhaps not such a large number of cells/elements in the vertical. When the flow is nearly hydrostatic this method can be encouraged to rapidly coarsen the mesh in the vertical, and then move on to perform coarsening in the horizontal where most

of the work needs to be done. See Stüben (2000) where preferential coarsening in different directions is used based upon graph colouring techniques. Parallel implementations of these methods in an oceanographic context are currently under investigation.

8.6. Parallel computing

Regardless of gains in computational efficiency from advanced numerical methods, there is always going to be a need for parallel computing when a solution cannot be obtained within a reasonable timescale on a serial computer, and/or where there is a limit on local resources such as memory. This is certainly true of ocean modelling, where the desired level of detail and sophistication in the model required for realism will generally far exceed the computational resources available, even when parallelism has been achieved. Because of this, efficient parallel algorithms for ocean modelling are of the utmost importance to reduce the serial bottle-neck. In the case of computational grids, whether they be structured or unstructured, parallelism is achieved through domain decomposition methods (DDM). Fundamental to DDM is the requirement to solve a graph-partitioning problem, the graph being derived from the computational mesh. The graph partitioning problem involves an equal partitioning of the graph nodes into sub-domains which are distributed among processors, thus balancing the computational load across the processors.

The graph partitioning solution is constrained by the need to minimise the number of graph edges dividing the partitions (sub-domains) because the cost of interprocessor communication in a parallel simulation increases with the edge-cut. The most successful methods developed for obtaining good quality graph partitions are k -way multi-level techniques. These techniques typically generate a hierarchy of coarsened graphs where the coarsest level is readily partitioned into k subdomains. This partitioning is then projected up through the hierarchy of meshes where a refinement step is carried out at each step. Partition refinement can be done using neutral network optimisation methods (Pain et al., 1999a) or Fiduccia–Mattheyses type heuristics (Fiduccia and Mattheyses, 1982), as implemented in codes such as Metis (Karypis, 2003) and Jostle (Walshaw, 2003). These methods are themselves parallelised so graph re-partitioning can be calculated in parallel, which is necessary for improving existing graph partitions or addressing the computational load-imbalances which may occur. For parallel machines with heterogeneous communication between processors, the cost of interprocess communication arising from the domain decomposition may be further minimised by mapping domains to processors in some optimal way (Pain et al., 1999b). In the case of a Beowulf cluster using dual processor nodes for example, this would seek to maximise the amount of interprocess communication within the dual node while minimising that over the network.

For solving a set of equations in parallel on a partitioned mesh, a multi-block explicit procedure is commonly used as a preconditioner combined with a gradient based method e.g. PCG or FGMRES. Relaxation methods such as SSOR within each subdomain may form the basis of the preconditioner. So-called chaotic preconditioners (see Dertsekas and Tsitsiklis, 1991; Tai and Tseng, 2002) use these same methods but have no-synchronisation step and collect information from neighbouring subdomains when and where they are available to speed up the parallel solution. Again parallel hierarchical preconditioners (Stüben, 2000) provide a way of rapidly spreading solver information across the domain. However, typical multi-grid or hierarchical solvers can be

communication intensive and consequently may be less attractive on slow communicating parallel machines.

The application of mesh adaptivity or optimisation to partitioned meshes (for parallel solutions using DDM) presents a new set of challenges. The central issues with parallel mesh adaptivity are mesh conformity across subdomain boundaries and the treatment of load-imbalance. There are important differences between the mesh adaptivity method applied in this work (cf. Fig. 2) and hierarchical mesh adaptivity methods (e.g. Jimack, 1998) when it comes to parallelisation. Perhaps the most important of these differences is how the elements are adapted to a given error norm. Hierarchical based adaptivity methods use a two-stage process where first elements are coarsened or refined within a single ancestral tree, in effective isolation from neighbouring elements, followed by a sweep over all elements to identify element edges which must be split to obtain a conformal mesh. This allows the mesh adaptation process to be carried out in parallel with little communication. Load-balancing is addressed by partitioning the mesh at the coarsest level (Jimack, 1998; Touheed et al., 1998).

In contrast to this, the anisotropic mesh optimisation technique employed here is iterative in nature. This requires each element to change its size and shape in response to local changes in the mesh and solution as the procedure progresses, which could lead to a high number of short communications between domains when adapting elements on or near domain boundaries. To overcome this problem, elements on boundaries between sub-domains are first locked in place. The serial mesh optimisation method is then applied to each domain, disallowing any change to these locked elements. Mesh conformity is maintained because the elements shared between domains are not allowed to change. When the serial optimisation method is finished there may be elements on or near the domain boundary which are still suboptimal. In addition to this a load-imbalance will have invariably occurred due to coarsening and refinement of the mesh in different domains. Both of these issues are addressed simultaneously by re-partitioning the mesh, constraining the graph-partition using edge-weights inversely proportional to the quality of elements connected to the edge. This application of edge-weights discourages the graph partition from cutting across poor quality elements. Once the mesh has been re-distributed to processors according to the new partitioning, the mesh optimisation method can be reapplied to finish adapting the mesh.

Special consideration must be given to mixed element formulations (cf. Section 4) with typically a different polynomial expansion for different variables. The method used here for solving incompressible fluid flow requires a larger stencil size for pressure than for velocity. Thus a second layer of halo (or ghost) nodes is required for the pressure solution; essentially this is an extended halo which includes all elements that share a node with any element cut by the graph partition. Fig. 5 shows how the subdomains dynamically adjust to balance the load in a simulation of incompressible flow past a cylinder at a moderate Reynolds number using the ocean model. In this simulation a diffusive re-partitioning method was predominantly used to reduce the amount of information migrating between processors (Schloegel et al., 1997), however it was found that a re-partition–re-map operation (Karypis et al., 2002) was required periodically to counter degradation in the edge-cut. In this simulation the subdomains may actually be seen to move downstream with the produced von Karman vortex street.

The success of parallel computation in ocean modelling brings its own challenges. Once a large simulation has been performed it then becomes a non-trivial problem to visualise and analyse the

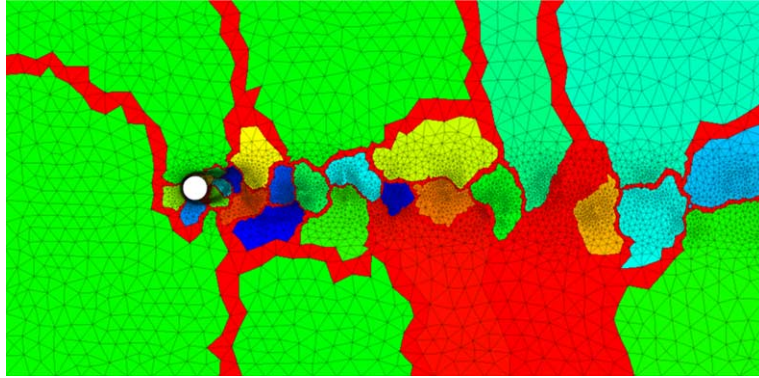


Fig. 5. A demonstration of parallel mesh adaptivity—32 subdomains shown which dynamically adjust to balance the load in the adapting mesh. The mesh here is resolving the von Karman vortex street in a simulation of flow past a cylinder.

results. This in itself requires distributed computing resources for both parallel visualisation and the application of diagnostic tools, for example see [GODIVA \(2003\)](#).

9. Concluding remarks

In this paper the advantages of unstructured mesh ocean models have been discussed. These include the ability to accurately represent coastlines and bathymetry, and the application of appropriate boundary conditions; the ability to choose arbitrarily the mesh resolution (not depending on the coordinate system used), and make this highly non-uniform to match modelling requirements. Also, the use of meshes which dynamically adapt to the solution fields has been discussed. There however remain a number of issues to be addressed in this relatively new field. For example the conservation of key variables; sub-grid scale modelling on changing anisotropic meshes; the optimal representation of balance; and optimal exploitation of node movement and mesh adaptivity. However, the benefits over traditionally used ocean models are immense and justify the substantial amount of work necessary to construct such a model over and above that necessary to produce a traditional model. With more appropriately focused numerical resolution ocean dynamics may be better predicted, as can be events such as climate change. The result would be a single model that can be used efficiently for both coastal and global ocean modelling. It remains to be seen the extent to which such a model will supersede traditional models, but clearly this approach will play an important role in the future of ocean modelling.

References

- Ackroyd, R.T., 1997. *Finite Element Methods for Particle Transport: Applications to Reactor and Radiation Physics*. Research Studies Press, Taunton, Somerset, England.
- Adams, L.M., 1983. An m -step preconditioned conjugate gradient method for parallel computations. *IEEE Parallel Computation Proceedings*, IEEE, Bellare, MI, pp. 36–43.

- Adcroft, A., Campin, J.M., 2004. Rescaled height coordinates for accurate representation of free-surface flows in ocean circulation models. *Ocean Modell.* 7, 269–284.
- Adcroft, A., Hill, C., Marshall, J., 1997. Representation of topography by shaved cells in a height coordinate ocean model. *Mon. Weath. Rev.* 125, 2293–2315.
- Adcroft, A., Marshall, D., 1998. How slippery are piecewise-constant coastlines in numerical ocean models? *Tellus A* 50, 95–108.
- Adcroft, A.J., Hill, C.N., Marshall, J.C., 1999. A new treatment of the Coriolis term in C-grid models at both high and low resolutions. *Mon. Weath. Rev.* 127, 1928–1936.
- Ainsworth, M., Oden, J.T., 1997. A posteriori error estimation in finite element analysis. *Comput. Methods Appl. Mech. Engrg.* 142, 1–88.
- Almeida, R.C., Silva, R.S., 1997. A stable Petrov–Galerkin method for convection-dominated problems. *Comput. Methods Appl. Mech. Engrg.* 140, 291–304.
- Arakawa, A., Lamb, V.R., 1977. Computational design of the basic dynamical processes of the UCLA general circulation model. *Methods Comput. Phys.* 17, 174–267.
- Aulisa, E., Manservigi, S., Scardovelli, R., 2003. A mixed markers and volume-of-fluid method for the reconstruction and advection of interfaces in two-phase and free-boundary flows. *J. Comput. Phys.* 188, 611–639.
- Babuška, I., 1971. Error-bounds for finite element method. *Numer. Math.* 16, 322–333.
- Bates, P.D., 2000. Development and testing of a subgrid-scale moving for moving-boundary hydrodynamic problems in shallow water. *Hydrol. Process.* 14, 2073–2088.
- Bentham, T., Pain, C.C., Colville, R.N., in press. Large-eddy simulations in complex geometries using anisotropic mesh adaptivity. *Internat. J. Numer. Methods Fluids*.
- Bleck, R., 1998. Ocean modeling in isopycnic coordinates. In: Chassignet, E.P., Verron, J. (Eds.), *Ocean Modeling and Parameterization*, pp. 423–448.
- Bleck, R., 2002. An oceanic general circulation model framed in hybrid isopycnic-Cartesian co-ordinates. *Ocean Modell.* 4, 55–88.
- Borouchaki, H., Frey, P.J., 1998. Adaptive triangular-quadrilateral mesh generation. *Internat. J. Numer. Methods Engrg.* 41, 915–934.
- Borouchaki, H., George, P.L., 1996. Optimal delaunay point insertion. *Internat. J. Numer. Methods Engrg.* 39, 3407–3437.
- Borouchaki, H., Lo, S.H., 1995. Fast delaunay triangulation in three dimensions. *Comput. Methods Appl. Mech. Engrg.* 128, 153–167.
- Brezzi, F., 1974. On the existence, uniqueness and approximation of saddle-point problems arising from Lagrange multipliers. *RAIRO Ser. Rouge Anal. Numer.* 8 (R-2), 129–151.
- Brezzi, F., Fortin, M., 1991. *Mixed and Hybrid Finite Element Methods*. Springer-Verlag.
- Brezzi, F., Franca, L.P., Hughes, T.J.R., Russo, A., 1997. $b = \int g$. *Comput. Methods Appl. Mech. Engrg.* 145, 329–339.
- Brunner, T.A., Holloway, J.P., 2001a. One-dimensional Riemann solvers and the maximum entropy closure. *J. Quant. Spectrosc. Radiat. Transfer.* 69, 543–566.
- Brunner, T.A., Holloway, J.P., 2001. Two-dimensional time-dependent Riemann solvers for neutron transport. M&C Salt Lake City, UT, USA, September 2001.
- Bryan, K., 1969. A numerical method for the study of the circulation of the world ocean. *J. Comput. Phys.* 4, 347–376.
- Bryan, K., Cox, M.D., 1967. A numerical investigation of the oceanic general circulation. *Tellus* 19, 54–80.
- Buscaglia, G.C., Dari, E.A., 1997. Anisotropic mesh optimization and its application in adaptivity. *Internat. J. Numer. Methods Engrg.* 40, 4119–4136.
- Castro-Diaz, M.J., Hecht, F., Mohammadi, B., Pironneau, O., 1997. Anisotropic unstructured mesh adaption for flow simulations. *Internat. J. Numer. Methods Fluids* 25, 475–491.
- Cavaleri, L., Bertotti, L., 2003. The characteristics of wind and wave fields modelled with different resolutions. *Quart. J. Roy. Met. Soc.* 129, 1647–1662.
- Centrella, J., Wilson, J.R., 1984. Planar numerical cosmology II: The finite difference equations and numerical tests. *Astrophys. J. Suppl. Ser.* 54, 229–249.

- Codina, R., 1993. A discontinuity-capturing crosswind-dissipation for the finite element solution of the convection–diffusion equation. *Comput. Methods Appl. Mech. Engrg.* 110, 325–342.
- Codina, R., Blasco, J., 2000. Stabilised finite element method for the transient Navier–Stokes equations based upon a pressure gradient projection. *Comput. Methods Appl. Mech. Engrg.* 182, 277–300.
- Danilov, S., Kivman, G., Schröter, J., 2004. A finite element ocean model: principles and evaluation. *Ocean Modell.* 6, 125–150.
- Darwish, M.S., 1993. A new high-resolution scheme based on the normalised variable formulation. *Numer. Heat. Transfer B* 24, 353–371.
- Denbo, D.W., Skyllingstad, E.D., 1996. An ocean large-eddy simulation model with application to deep convection in the Greenland Sea. *J. Geophys. Res.* 101 (C1), 1095–1110.
- Dertsekas, D.P., Tsitsiklis, J.N., 1991. Some aspects of parallel and distributed iterative algorithms—a survey. *Automatica* 27, 3–41.
- Donea, J., 1984. A Taylor–Galerkin method for convective transport problems. *Internat. J. Numer. Methods Engrg.* 20, 101–120.
- Donea, J., Huerta, A., 2003. *Finite Element Methods for Flow Problems*. John Wiley.
- Dumas, E., Le Provost, C., Poncet, A., 1982. Feasibility of finite element methods for oceanic general circulation modelling. In: *Proc. Fourth Internat. Conf. on Finite Elements in Water Resources*, Hanover, Germany, pp. 5,43–5,55.
- Eriksson, K., Estep, W., Hansbo, P., Johnson, C., 1996. *Computation Differential Equations*. Cambridge University Press.
- Fiduccia, C.M., Mattheyses, R.M., 1982. A linear time heuristic for improving network partitions. In: *Proceedings in the 19th IEEE Design Automation Conference*, pp. 175–181.
- Fix, G.J., 1975. Finite element models for ocean circulation problems. *SIAM J. Appl. Math.* 29, 371–387.
- Foias, C., Holm, D.D., Titi, E.S., 2001. The Navier–Stokes-alpha model of fluid turbulence. *Physica D* 152, 505–5119.
- Ford, R., Pain, C.C., Piggott, M.D., Goddard, A.J.H., de Oliveira, C.R.E., Umbleby, A.P., in press-a. A non-hydrostatic finite element model for three-dimensional stratified oceanic flows. Part I: Model formulation. *Mon. Weath. Rev.*
- Ford, R., Pain, C.C., Piggott, M.D., Goddard, A.J.H., de Oliveira, C.R.E., Umbleby, A.P., in press-a. A non-hydrostatic finite element model for three-dimensional stratified oceanic flows. Part II: Model validation. *Mon. Weath. Rev.*
- Fortin, M., Fortin, A., 1985. Newer and newer elements for incompressible flow. In: *Gallagher, R.H., Carey, G.F., Oden, J.T., Zienkiewicz, O.C. (Eds.), Finite Elements in Fluids—Volume 6*, pp. 171–187.
- Frayssé, V., Giraud, L., Gratton, S., 1998. A set of Flexible-GMRES routines for real and complex arithmetics. *Technical Report TR/PA/98/20, CERFACS, Toulouse, France.*
- Freitag, L.A., Ollivier-Gooch, C., 1997. Tetrahedral mesh improvement using swapping and smoothing. *Internat. J. Numer. Methods Engrg.* 40, 3979–4002.
- Gent, P.R., McWilliams, J.C., 1990. Isopycnal mixing in ocean circulation models. *J. Phys. Oceanogr.* 20, 150–155.
- George, P.L., 1998. *Delaunay Triangulation and Meshing: Application to Finite Elements*. HERMES, Paris.
- Girault, V., Raviart, P.A., 1986. *Finite Element Methods for Navier–Stokes Equations. Theory and Algorithms*. Springer-Verlag.
- GODIVA, 2003. *Grid based Diagnostics, Interactive Visualisation and Data Analysis*. <<http://www.e-science.clrc.ac.uk/web/projects/godiva>>.
- Golub, G.H., van Loan, C.F., 1989. *Matrix Computations*, second ed. Johns Hopkins University Press.
- Gorman, G.J., Piggott, M.D., Pain, C.C., de Oliveira, C., Umbleby, A., Goddard, A.J.H., submitted for publication. Optimal bathymetric representation through constrained unstructured mesh adaptivity. *Ocean Modell.*
- Greenberg, D.A., Werner, F.E., Lynch, D.R., 1998. A diagnostic finite-element ocean circulation model in spherical-polar coordinates. *J. Atmos. Oceanic Tech.* 15, 942–958.
- Gresho, P.M., 1990. On the theory of semi-implicit projection methods for viscous incompressible flow and its implementation via a finite element method that also introduces a nearly consistent mass matrix. Part I: Theory. *Internat. J. Numer. Methods Fluids* 11, 587–620.
- Gresho, P.M., Sani, R.L., 1998. *Incompressible Flow and the Finite Element Method*. John Wiley.

- Griffies, S.M., Böning, C., Bryan, F.O., Chassignet, E.P., Gerdes, R., Hasumi, H., Hirst, A., Treguier, A.M., Webb, D., 2000. Developments in ocean climate modelling. *Ocean Modell.* 2, 123–192.
- Gunzburger, M., 1989. *Finite Element Methods for Viscous Incompressible Flows: A Guide to Theory, Practice, and Algorithms*. Academic Press.
- Haidvogel, D.B., Beckmann, A., 1999. *Numerical Ocean Circulation Modeling*. Imperial College Press.
- Haidvogel, D.B., Robinson, A.R., Schulman, E.E., 1980. The accuracy, efficiency, and stability of three numerical models with application to open ocean problems. *J. Comput. Phys.* 34, 1–53.
- Hanert, E., Le Roux, D.Y., Legat, V., Deleersnijder, E., 2004. Advection schemes for unstructured grid ocean modelling. *Ocean Modell.* 7, 39–58.
- Hanert, E., Legat, V., Deleersnijder, E., 2002. A comparison of three finite elements to solve the linear shallow water equations. *Ocean Modell.* 5, 17–35.
- Haney, R.L., 1991. On the pressure gradient force over steep topography in sigma coordinate models. *J. Phys. Oceanogr.* 21, 610–619.
- Henry, R., Walters, R., 1993. Geometrically based, automatic generator for irregular triangular networks. *Commun. Numer. Math. Engrg.* 9, 555–566.
- Hirsch, C., 1990. *Numerical Computation of Internal and External Flows—Volume 2: Computational Methods for Inviscid and Viscous Flows*. John Wiley.
- Hoffman, J., Johnson, C., 2004. A new approach to computational turbulence modeling. *Comput. Methods Appl. Mech. Engrg.*
- Holm, D.D., Nadiga, B.T., 2003. Modeling mesoscale turbulence in the barotropic double-gyre circulation. *J. Phys. Oceanogr.* 33, 2355–2365.
- Horritt, M.S., 2002. Evaluating wetting and drying algorithms for finite element models of shallow water flow. *Internat. J. Numer. Methods Engrg.* 85, 835–851.
- Hubbard, M.E., Garcia-Navarro, P., 2000. Flux difference splitting and the balancing of source terms and flux gradients. *J. Comput. Phys.* 165, 89–125.
- Hughes, T.J.R., 1995. Multiscale phenomena: Green's functions, the Dirichlet-to-Neumann formulation, subgrid scale models, bubbles and the origins of stabilized methods. *Comput. Methods Appl. Mech. Engrg.* 127, 387–401.
- Hughes, T.J.R., Franca, L.P., Hulbert, G.M., 1989. A new finite element formulation for computational fluid dynamics: VIII. The Galerkin/least-squares method for advective–diffusive equations. *Comput. Methods Appl. Mech. Engrg.* 73, 173–189.
- Hughes, T.J.R., Mallet, M., 1986a. A new finite element formulation for computational fluid dynamics: III. The generalized streamline operator for multidimensional advective–diffusive systems. *Comput. Methods Appl. Mech. Engrg.* 58, 305–328.
- Hughes, T.J.R., Mallet, M., 1986b. A new finite element formulation for computational fluid dynamics: IV. A discontinuity-capturing operator for multidimensional advective–diffusion systems. *Comput. Methods Appl. Mech. Engrg.* 58, 329–336.
- Hughes, T.J.R., Mallet, M., Mizukami, A., 1986. A new finite element formulation for computational fluid dynamics: II. Beyond SUPG. *Comput. Methods Appl. Mech. Engrg.* 54, 341–355.
- Hughes, T.J.R., Mazzei, L., Jansen, K.E., 2000. Large eddy simulation and the variational multiscale method. *Comput. Visual Sci.* 3, 47–59.
- Iskandarani, M., Haidvogel, D.B., Boyd, J.P., 1995. A staggered spectral element model with application to the oceanic shallow water equation. *Internat. J. Numer. Methods Fluids* 20, 393–414.
- Iskandarani, M., Haidvogel, D.B., Levin, J.C., 2003. A three-dimensional spectral element method for the solution of the hydrostatic primitive equations. *J. Comput. Phys.* 186, 397–425.
- Iskandarani, M., Levin, J.C., Choi, B.-J., Haidvogel, D.B., 2004. Comparison of advection schemes for high-order h - p finite element and finite volume methods. *Ocean Modell.* (this volume).
- Jimack, P.K., 1998. Techniques for parallel adaptivity. In: Topping, B.H.V. (Ed.), *Parallel and Distributed Processing for Computational Mechanics II*. Saxe-Coburg Publications.
- Joe, B., 1989. Three-dimensional triangulations from local transformations. *SIAM J. Sci. Statist. Comput.* 10, 718–741.
- Kallinderis, Y., Vijaya, P., 1993. Adaptive refinement-coarsening scheme for three-dimensional unstructured meshes. *AIAA J.* 31, 1440–1447.

- Karniadakis, G.E., Sherwin, S.J., 1999. *Spectral/hp Element Methods for Computational Fluid Dynamics*. Oxford University Press.
- Karypis, G., 2003. Metis. <<http://www.users.cs.umn.edu/~karypis/metis/>>.
- Karypis, G., Schloegel, K., Kumar, V., 2002. Parmetis: Parallel graph partitioning and sparse matrix ordering library. <<http://www.users.cs.umn.edu/~karypis/metis/>>.
- Kershaw, D.S., Prasad, M.K., Shaw, M.J., Milovich, J.L., 1998. 3D unstructured mesh ALE hydrodynamics with the upwind discontinuous finite element method. *Comput. Methods Appl. Mech. Engrg.* 158, 81–116.
- Killworth, P.D., Stainforth, D., Webb, D.J., Peterson, S.M., 1991. The development of a free surface Bryan–Cox–Semtner model. *J. Phys. Oceanogr.* 21, 1333–1348.
- Labeur, R.J., Pietrzak, J., 2004. A fully three dimensional unstructured grid non-hydrostatic finite element coastal model. *Ocean Modell.* (this volume).
- Ladyzhenskaya, O., 1969. *Mathematical Theory of Viscous Incompressible Flows*. Gordon and Breach Science Publishers.
- Lax, P.D., Wendroff, B., 1960. Systems of conservation laws. *Comm. Pure Appl. Math.* 13, 217–237.
- Le Provost, C., Vincent, P., 1986. Some tests of precision for a finite element model of ocean tides. *J. Comput. Phys.* 110, 273–291.
- Le Roux, D.Y., Sene, A., Rostand, V., Hanert, E., 2004. On some spurious mode issues in shallow-water models using a linear algebra approach. *Ocean Modell.* (this volume).
- Le Roux, D.Y., Staniforth, A., Lin, C.A., 1998. Finite elements for shallow-water equation ocean models. *Mon. Weath. Rev.* 126, 1931–1951.
- Legrand, S., Legat, V., Deleersnijder, E., 2000. Delaunay mesh generation for an unstructured-grid ocean general circulation model. *Ocean Modell.* 2, 17–28.
- Leonard, B.P., 1979. A stable and accurate convection modeling procedure based on quadratic upstream interpolation. *Comput. Methods Appl. Mech. Engrg.* 19, 59–98.
- Leonard, B.P., 1988. Simple high accuracy resolution program for convective modeling of discontinuities. *Internat. J. Numer. Methods Fluids* 8, 1291–1318.
- Leonard, B.P., 1991. The ULTIMATE conservative difference scheme applied to unsteady one-dimensional advection. *Comput. Methods Appl. Mech. Engrg.* 88, 17–74.
- Löhner, R., Morgan, K., Zienkiewicz, K.O., 1985. An adaptive finite element procedure for compressible high speed flows. *Comput. Methods Appl. Mech. Engrg.* 51, 441–465.
- Löhner, R., Parikh, P., 1988. Generation of three-dimensional unstructured grids by the advancing-front method. *Internat. J. Numer. Methods Fluids* 8, 1135–1149.
- Lynch, D.R., Gray, W.R., 1979. A wave equation model for finite element tidal computations. *Comput. Fluids* 7, 207–228.
- Lynch, D.R., Ip, J.T.C., Naimie, C.E., Werner, F.E., 1996. Comprehensive coastal circulation model with application to the Gulf of Maine. *Contin. Shelf Res.* 16, 875–906.
- Lynch, D.R., Werner, F.E., 1987. Three-dimensional hydrodynamics on finite elements. Part I: Linearized harmonic model. *Internat. J. Numer. Methods Fluids* 7, 871–909.
- Ma, H., 1993. A spectral element basin model for the shallow water equations. *J. Comput. Phys.* 109, 133–149.
- Marshall, J., Adcroft, A., Hill, C., Perelman, L., Heisey, C., 1997. A finite-volume, incompressible Navier–Stokes model for studies of the ocean on parallel computers. *J. Geophys. Res.* 102 (C3), 5753–5766.
- Masud, A., Hughes, T.J.R., 1997. A space–time Galerkin/least-squares finite element formulation of the Navier–Stokes equations for moving domain problems. *Comput. Methods Appl. Mech. Engrg.* 146, 91–126.
- Mellor, G.L., Yamada, T., 1982. Development of turbulence closure model fro geophysical fluid problems. *Rev. Geophys. Space Phys.* 20, 851–875.
- Moller, P., Hansbo, P., 1995. On advancing front mesh generation in three dimensions. *Internat. J. Numer. Methods Engrg.* 38, 3551–3569.
- Munday, D.R., Marshall, D.P., 2004. On the separation of a barotropic western boundary current from a cape. *J. Phys. Oceanogr.*
- Myers, P.G., Weaver, A.J., 1995. A diagnostic barotropic finite-element ocean circulation model. *J. Atmos. Oceanic Tech.* 12, 511–526.

- Nechaev, D., Schröter, J., Yaremchuk, M., 2003. A diagnostic stabilized finite-element ocean circulation model. *Ocean Modell.* 5, 37–63.
- Norburn, S., Silvester, D., 1998. Stabilised vs. stable mixed methods for incompressible flow. *Comput. Methods Appl. Mech. Engrg.* 166, 131–141.
- Oliker, L., Biswas, R., Gabow, H.N., 2000. Parallel tetrahedral mesh adaptation with dynamic load balancing. *Parallel Comput.* 26 (12), 1583–1608.
- Oñate, E., García, J., Idelsohn, S., 1997. Computation of the stabilization parameter for the finite element solution of advective–diffusive problems. *Internat. J. Numer. Methods Fluids* 25, 1385–1407.
- Özgökmen, T.M., Chassignet, E.P., 2002. Dynamics of two-dimensional turbulent bottom gravity currents. *J. Phys. Oceanogr.* 32, 1460–1478.
- Özgökmen, T.M., Chassignet, E.P., Paiva, A.M., 1997. Impact of wind forcing, bottom topography, and inertia on midlatitude jet separation in a quasigeostrophic model. *J. Phys. Oceanogr.* 27, 2460–2476.
- Pain, C.C., de Oliveira, C.R.E., Goddard, A.J.H., 1999a. A neural network graph partitioning procedure for grid-based domain decomposition. *Internat. J. Numer. Methods Engrg.*, 593–613.
- Pain, C.C., de Oliveira, C.R.E., Goddard, A.J.H., 1999b. Simulated annealing task to processor mapping for domain decomposition methods on distributed parallel computers. *Concurrency: Practice and Experience* 11, 155–165.
- Pain, C.C., Eaton, M.D., Smedley-Stevenson, R.P., Goddard, A.J.H., Piggott, M.D., de Oliveira, C.R.E., in press-a. Space–time streamline upwind Petrov–Galerkin methods for the Boltzmann transport equation. *Comput. Methods Appl. Mech. Engrg.*
- Pain, C.C., Eaton, M.D., Smedley-Stevenson, R.P., Goddard, A.J.H., Piggott, M.D., de Oliveira, C.R.E., in press-b. Streamline upwind Petrov–Galerkin methods for the steady-state Boltzmann transport equation. *Comput. Methods Appl. Mech. Engrg.*
- Pain, C.C., Gomes, J.L.M.A., Eaton, M.D., de Oliveira, C.R.E., Goddard, A.J.H., in press. Numerical transport methods for multi-phase fluid flow and radiation modelling. *Internat. J. Numer. Methods Fluids*.
- Pain, C.C., Umpleby, A.P., de Oliveira, C.R.E., Goddard, A.J.H., 2001. Tetrahedral mesh optimisation and adaptivity for steady-state and transient finite element calculations. *Comput. Methods Appl. Mech. Engrg.* 190, 3771–3796.
- Patanaker, S.V., Spalding, D.B., 1970. *Heat and Mass Transfer in Boundary Layers*, second ed. Intertext, London.
- Peraire, J., Vahdati, M., Morgan, K., Zienkiewicz, O.C., 1987. Adaptive remeshing for compressible flow computations. *J. Comput. Phys.* 72, 449–466.
- Pietrzak, J., 1998. The use of TVD limiters for forward-in-time upstream-biased advection schemes in ocean modeling. *Mon. Weath. Rev.* 126, 812–830.
- Piggott, M.D., Pain, C.C., Gorman, G.J., Power, P.W., Goddard, A.J.H., 2004. *h*, *r* and *hr* adaptivity in ocean modelling. *Ocean Modell.* (this volume).
- Platzman, G.W., 1981. Some response characteristics of finite element tidal models. *J. Comput. Phys.* 40, 36–63.
- Power, P., Pain, C.C., Piggott, M.D., Gorman, G., Marshall, D., Goddard, A., 2004. Sensitivity based error norms for adaptive mesh ocean modelling. *Ocean Modell.* (this volume).
- Roe, P.L., 1985. Large scale computations in fluid mechanics: Part 2 Lectures in Applied Mechanics, vol. 22. American Mathematical Society, Providence, RI.
- Saad, Y., Schultz, M.H., 1986. GMRES, a generalised minimum residual algorithm for solving nonsymmetric linear systems. *SIAM J. Sci. Statist. Comput.* 7, 856–869.
- Sagaut, P., 1998. *Large Eddy Simulation for Incompressible Flows*. Springer.
- Schloegel, K., Karypis, G., Kumar, V., 1997. Multilevel diffusion schemes for repartitioning of adaptive meshes. *J. Parallel Distributed Comput.* 47 (2), 109–124.
- Shakib, F., Hughes, T.J.R., Johan, Z., 1991. A new finite element formulation for computational fluid dynamics: X. Te compressible Euler and Navier–Stokes equations. *Comput. Methods Appl. Mech. Engrg.* 89, 141–219.
- Shewchuk, J., 2003. Triangle. <<http://www.2.cs.cmu.edu/~quake/triangle.html>>.
- Smolarkiewicz, P.K., Margolin, L.G., 1998. MPDATA: A finite-difference solver for geophysical flows. *J. Comput. Phys.* 140, 459–480.
- Sotiropoulos, F., Abdallah, S., 1991. The discrete continuity equation in primitive variable solutions of incompressible flow. *J. Comput. Phys.* 95, 212–227.

- Staniforth, A., Côté, J., 1991. Semi-Lagrangian integration methods for atmospheric models: a review. *Mon. Weath. Rev.* 119, 2206–2223.
- Stern, M.E., 1998. Separation of a density current from the bottom of a continental shelf. *J. Phys. Oceanogr.* 28, 2040–2049.
- Strouboulis, T., Oden, J.T., 1990. A posteriori error estimation of finite element approximations in fluid mechanics. *Comput. Methods Appl. Mech. Engrg.* 78, 201–242.
- Stüben, K., 2000. An introduction to algebraic multigrid. In: Trottenberg, U., Oosterlee, C.W., Schüller, A. (Eds.), *Multigrid*. Academic Press, London, pp. 413–532.
- Sweby, P.K., 1984. High resolution schemes using flux limiters for hyperbolic conservation laws. *SIAM J. Numer. Anal.* 21, 995–1011.
- Tai, X., Tseng, P., 2002. Convergence rate analysis of an asynchronous space decomposition method for convex minimization. *Math. Comput.* 71 (239), 1105–1135.
- Tansley, C.E., Marshall, D.P., 2000. On the influence of bottom topography and the deep western boundary current on Gulf Stream separation. *J. Mar. Res.* 58, 297–325.
- Tchamen, G.W., Kawahita, R.A., 1998. Modelling wetting and drying effects over complex topography. *Hydrol. Process.* 12, 1151–1182.
- Toro, E.F., 1997. *Riemann Solvers and Numerical Methods for Fluid Dynamics*. Springer.
- Toro, E.F., 2001. *Shock-Capturing Methods for Free-Surface Shallow Flows*. John Wiley.
- Touheed, N., Selwood, P., Jimack, P.K., Berzins, M., 1998. A comparisons of some dynamic load-balancing algorithms for a parallel adaptive flow solver. In: Topping, B.H.V. (Ed.), *Parallel and Distributed Processing for Computational Mechanics II*. Saxe-Coburg Publications.
- van Leer, B., 1974. Towards the ultimate conservative differencing scheme. II: Monotonicity and conservation combined in a second order scheme. *J. Comput. Phys.* 14, 361–370.
- van Leer, B., 1977. Towards the ultimate conservative difference scheme. V: A second-order sequel to Godunov's method. *J. Comput. Phys.* 32, 101–136.
- Walshaw, C.H., 2003. JOSTLE. <<http://www.gre.ac.uk/~c.walshaw/jostle/>>.
- Wareing, T.A., Morel, J.E., McGhee, J.M., 1999. A diffusion synthetic acceleration method for the S_N equations with discontinuous finite element space and time differencing. Los Alamos Report, LA-UR-99-1224.
- Weatherill, N.P., 1994. Efficient three-dimensional Delaunay triangulation with automatic point creation and imposed boundary constraints. *Internat. J. Numer. Methods Engrg.* 37, 2005–2039.
- Wu, J., Zhu, J.Z., Szmelter, J., Zienkiewicz, O.C., 1990. Error estimation and adaptivity in Navier–Stokes incompressible flows. *Comput. Mech.* 6, 259–270.
- Xu, X., Pain, C.C., Goddard, A.J.H., de Oliveria, C.R.E., 1998. An automatic adaptivity meshing techniques for Delaunay triangulations. *Comput. Methods Appl. Mech. Engrg.* 161, 297–303.



ELSEVIER

Available online at www.sciencedirect.com

SCIENCE @ DIRECT®

Ocean Modelling 10 (2005) 35–49

**Ocean
Modelling**

www.elsevier.com/locate/ocemod

Evaluation of an eddy-permitting finite-element ocean model in the North Atlantic

Sergey Danilov *, Gennady Kivman, Jens Schröter

Alfred Wegener Institute for Polar and Marine Research, Postfach 12-01-61, 27515 Bremerhaven, Germany

Received 28 November 2003; received in revised form 1 July 2004; accepted 30 July 2004

Available online 2 November 2004

Abstract

A new version of the 3D finite-element primitive-equation ocean model (FEOM) based on tetrahedron partitioning of the computational domain is applied to simulate the North Atlantic circulation at eddy-permitting resolution ($1/15^{\circ}$ – 2°). It relies on a horizontally refined mesh in regions of steep topography and allows the sloping bottom to be represented within the z -coordinate vertical discretization, similar to the so-called shaved-cell approach. It is the first time this approach is used to model large-scale ocean circulation. The FEOM performance in the North Atlantic is compared with that of the finite-difference models of similar resolution of the DYNAMO project. The meridional overturning circulation and heat transport of FEOM agree well with those of the DYNAMO project models, while the mean sea surface height demonstrates the presence of the Gulf Stream recirculation reproduced only by the ISOPYCNIC model of DYNAMO. The annual mean transports of the Gulf Stream and Deep Western Boundary Current at 27°N are of 37Sv and 17Sv with core velocities of about 1 m/s and 12 cm/s respectively. Due to flexibility in mesh refinement the FEOM provides a tool for modelling the influence of small-scale phenomena unresolved by current climate models on large-scale ocean circulation.

© 2004 Elsevier Ltd. All rights reserved.

Keywords: North Atlantic circulation; Finite elements; Ocean modelling

* Corresponding author.

E-mail addresses: sdanilov@awi-bremerhaven.de (S. Danilov), gkivman@awi-bremerhaven.de (G. Kivman), jschroeter@awi-bremerhaven.de (J. Schröter).

1. Introduction

There is a widespread perception in the ocean modelling community that finite-element methods (FEM) are unfit for the modelling of the general circulation of the ocean. The obvious success of FEM is regarded to be limited to tidal modelling and regional/coastal or engineering applications. It is the purpose of this article to demonstrate new developments for the modelling of basin-scale circulation with finite elements.

Ocean circulation models are distinguished by the processes they include, e.g., eddy dynamics. A further classification is the treatment of the vertical coordinate (Griffies et al., 2000). Although the latter seems to be a minor numerical detail it has a major impact on the solution. This impact was studied rigorously for z , σ and isopycnic models in the DYNAMO project (Willebrand et al., 2001) in the context of eddy-permitting models of the North Atlantic. There is ongoing effort in designing models which overcome some of the deficiencies of the traditional approaches (such as HYCOM which uses a hybrid coordinate, or extensions of POM that use a generalized coordinate). Here we add another alternative and show how finite elements can be used to combine the advantages of different techniques. To point out the advantages and weaknesses of our approach we compare our results mainly with those presented in detail in the DYNAMO project.

One of the main conclusion of the DYNAMO intercomparison project of eddy-permitting ocean circulation models was that many features of ocean circulation are controlled by localized processes (such as overflows) and details of the bathymetry in key regions (e.g., around Flemish Cap) (Willebrand et al., 2001). They can be adequately described at the eddy-resolving grids which is too costly to be used in climate studies. An alternative could be employing a model based on an unstructured grid and providing flexibility in local mesh refinement.

In a previous paper (Danilov et al., 2004; hereafter referred to as DKS04) we have presented a three-dimensional finite-element ocean model (FEOM) based on the primitive equations and designed for climatic studies. The model used a 3D tetrahedral mesh based on a 2D unstructured surface triangular mesh, and stratified in the vertical direction. It combined terrain-following coordinate in deep regions with z -levels in upper 200m. We tested the model performance on the North Atlantic mesh covering the basin from 7°N to 80°N with mean resolution of 0.8°, and showed the model to be capable of reproducing the mean heat transport and meridional overturning with realism typical of coarse-resolution models.

This paper continues DKS04 and presents an eddy-permitting version of the FEOM, which differs from the coarse-resolution version of DKS04 in two important aspects. First, the new version solves the equations for barotropic mode separately and uses the sea surface height to calculate the three-dimensional flow field. This provides a considerable gain in performance. Second, it uses the z -coordinate framework (which avoids pressure gradient errors), and resolves the sloping bottom by refining the horizontal resolution locally in regions of steep bathymetry. Our approach is similar to the shaved cells (Adcroft et al., 1997) used with finite volume discretization and is a natural feature of FEOM due to its tetrahedral mesh.

The sensitivity of ocean general circulation models (OGCMs) to the vertical discretization became a central issue in the late 1990s and was studied thoroughly in several intercomparison projects such as DYNAMO (Willebrand et al., 2001) and DAMÉE-NAB (Chassignet et al., 2000). Despite numerous efforts, accurate representation of the bottom topography still presents a challenge for most OGCMs. Difficulties of z - and σ -coordinate models are well known and thoroughly

discussed in the literature. The partial cell approach is an improvement over the standard stepwise bathymetry of z -coordinate (Maier-Reimer et al., 1993; Adcroft et al., 1997; Pacanowski and Gnanadesikan, 1998). Yet the most general way of accounting for sloping bathymetry in z -coordinate models is the concept of shaved cells (Adcroft et al., 1997) that has been applied for years in engineering. Though partial and shaved cells seem to be quite promising, there is only limited experience of using partial cells (see, i.e., Myers and Deacu, 2004) while no results of using shaved cells in real ocean simulation exist to our knowledge.

The goal of this paper is twofold. First, it briefly describes further steps in the FEOM development compared to the initial setup of DKS04. Second, it presents results of testing the FEOM in the eddy-permitting regime on the North Atlantic mesh against other North Atlantic models. Our main focus is on the DYNAMO models (see Willebrand et al., 2001). On the one hand, these models have finer resolution than the mean resolution of FEOM, yet still are in the eddy-permitting regime. On the other hand, the main goal of the DYNAMO project was systematic intercomparison of models belonging to three main classes (based on z , σ , and isopycnic vertical coordinate) to get “an improved understanding of dependence of the simulated North Atlantic circulation . . . on various aspects of the model formulation” (Willebrand et al., 2001). Comparing FEOM and DYNAMO project results is then natural as FEOM’s vertical discretization combines advantages of z - and σ -coordinates.

The paper is organised as follows. We begin with describing the model configuration and highlighting new features in Section 2. Section 3 contains analysis of a 10-year simulation and comparison with a set of other North Atlantic models. Summary and conclusions are presented in Section 4.

2. Model design

The numerics of the model used in this study were mostly described in DKS04 and are not repeated here. The model solves the 3D primitive equations together with advection–diffusion equations for potential temperature and salinity discretized by finite elements. For the prognostic fields, we use piecewise linear representation with basis functions defined on a tetrahedral partitioning of the computational domain. As in DKS04, the mesh is structured vertically and unstructured horizontally. Each surface triangle defines a 3D column that is then cut into prisms with prescribed levels. At the second step of mesh generation, each prism is divided into tetrahedra. The time stepping is backward Euler as in DKS04 but done with a different solver (see below).

2.1. New features of the FEOM

The main new feature adopted in the current version is splitting the dynamic equations into barotropic/baroclinic subproblems. On coarse grids ($<10^5$ 3D nodes), the computational cost of solving 3D unsplit equations is affordable and solver convergence is easy to achieve with reasonably large time steps (in excess of several hours). On the eddy-permitting mesh of the North Atlantic employed here, the solver convergence becomes broken at time steps around 1h due to non-banded part of the problem’s stiffness matrix (see DKS04), and the numerical cost becomes prohibitive.

The version described in DKS04 solved unsplit set of the 3D primitive equations for 3D velocity \mathbf{v} and sea surface height (SSH) ζ . Although it was costly in terms of CPU time it involved less approximations. The problem with splitting lies in the implicit treatment of the horizontal viscosity operator in the FEOM. It cannot be written in terms of the barotropic velocity or transport in barotropic (depth integrated) equations (see DKS04 for details).

To separate the barotropic subproblem out of the full problem we admit small inconsistency and write the horizontal viscosity operator in the barotropic subproblem as acting on the barotropic velocity. As long as the viscosity is small the inconsistency between the barotropic and full problems introduced by this approximation is only minor. The SSH obtained by solving the barotropic subproblem is used in the 3D equations which are then solved for the full horizontal velocity. Velocity correction procedure is applied to the horizontal velocity at every time step to eliminate spurious divergence introduced by using stabilization and the approximation of horizontal viscosity.

Another new feature of the model is a mixing parameterization that was absent in the previous version. We utilize a scheme by Gent (1991) that computes the vertical mixing coefficients (for tracers and momentum) as a function of the local Richardson number. The horizontal viscosity uses the Smagorinsky formula as in DKS04, but with smaller lower and upper threshold values of $25 \text{ m}^2/\text{s}$ and $10^3 \text{ m}^2/\text{s}$ respectively. Our experience is that the Smagorinsky viscosity is at its lower limit for almost entire ocean.

2.2. Mesh

A novel strategy of surface mesh generation is now employed. Given the set of geopotential (z) layers and topography one first computes the number of layers as a function of horizontal coordinates. Next, one tries to arrange the nodes in accordance with the gradient of that function such that the difference in the number of layers between two neighbouring nodes does not exceed one. The depth of the bottom nodes is allowed to deviate from the level positions so that bottom tetrahedra could have nodes on three different depths. The approach ensures that the bottom is represented as a continuous piecewise linear surface without vertical segments after partitioning into tetrahedra is made. It is analogous to the shaved-cell approach known for z -coordinate finite volume models. This flexibility is the main advantage of using tetrahedral FE discretization. The bottom tetrahedra with nodes on three levels introduce some pressure gradient errors however they are localized to the bottom-most layer. Since the affordable number of 2D nodes is always limited, the procedure also imposes limitation on the steepness of the bathymetry that could be resolved. We used the ETOPO5 bathymetry averaged over 0.25° cells as an initial approximation and further smoothed it in a procedure that penalizes both the deviation from the data and the slope of the bottom.

In addition to sloping bottom regions, the nodal density is also increased in coastal and dynamically important areas. Fig. 1 depicts the spatially varying horizontal resolution of the model defined as a mean over neighbouring triangles. It is much finer along the continental slope (there are triangles measuring $1/15^\circ$) than in the interior. The mesh covers an area from 7°N to 80°N as in DKS04 and consist of approximately 16000 surface nodes and 220000 3D nodes arranged on 23 vertical levels. The layer thicknesses are 10, 20(2), 25(6), 50(2), 125, 175, 400, 500(5), 750(3)m, with the number of layers given in brackets.

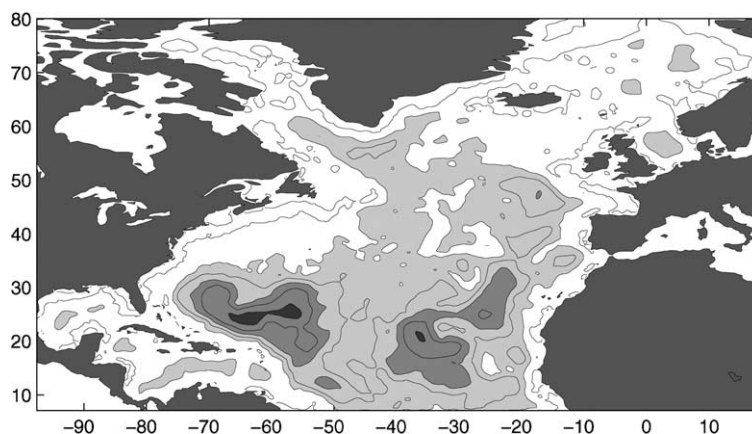


Fig. 1. Resolution in degrees of the North Atlantic mesh averaged over triangles with a common node. The contour interval is 0.3° , and the boundaries of shaded zones correspond to 0.6° , 1.2° and 1.8° (from light to dark).

2.3. Boundary conditions and forcing

Artificial boundaries at 7°N and 80°N were considered as closed for the velocities. For the temperature and salinity, sponge zones were introduced with relaxation to seasonal Levitus climatology (Levitus et al., 1994; Levitus and Boyer, 1994). The relaxation coefficient is $1/(5\text{ days})$ at the boundary and decreases with the distance from it. The southern buffer zone occupies a 5° belt while the north-eastern one extends to 60°N . This was done to ‘parameterize’ overflow processes in the Denmark Strait still unresolved at the present mesh and compensate for deficiency in surface forcing in this area. Otherwise too warm and salty water brought northward by the North Atlantic Current penetrates into the Labrador Sea and makes it too warm and salty after about 1 year of simulation. Temperature and salinity were also relaxed to climatology in a 3° belt in the Bay of Cadiz.

At the surface, the model was forced by the monthly NCEP wind stress for 1990–1999. The surface temperature and salinity were relaxed to the seasonal Levitus climatology with the relaxation time of 30 days.

2.4. Computational cost

An important characteristic of any ocean model is its computational efficiency. The total CPU cost of FEOM in the current setup is about 4 h on 32 processors per one model year on IBM pSeries 690 with the speedup of about 15. This cost is affordable for studies of processes on the decadal scale.

The cost is higher than that of finite-difference models of the FEOM mean resolution (about 0.5°). This is essentially linked to the use of unstructured grids, which makes computing right hand sides (RHSs) more expensive. Indeed, to compute a derivative at a node all neighbouring nodes are used on unstructured grids. Since their typical number is 20 in the FEOM, computing RHSs could be a factor of 10 slower than on structured grids. Using implicit time stepping and thus solvers (see below) also influences the CPU cost directly by time spent in the solution phase,

and indirectly through the need to assemble the stiffness matrices. However, the solution phase takes less than half of the total time in the current setup, and expensive computations are partly compensated by employing large time steps. The current version runs with 2 h time step for dynamics and 1 h for tracers.

In total, the computational expense of the model presented here is comparable with that of the DYNAMO models. While on structured grids only a fraction of nodes is in the dynamically important areas (such as the continental slope), almost half of FEOM nodes have mean resolution better than $1/3^\circ$ and are located where this resolution is needed. Thus despite its higher CPU cost per node the FEOM could produce finer effective resolution in dynamically important areas with much smaller total number of nodes.

2.5. Solvers

Using solvers for time stepping is very uncommon for the OGCMs which are almost exclusively based on explicit time stepping (except for the implicit free surface used with some models) and avoid using solvers whenever possible.

Here we would like to reiterate (cf. DKS04) that there are reasons in favour of solvers. First, discretizing time derivative with finite elements produces the so-called mass matrix. It is composed of L_2 scalar products of basis functions and links time derivatives over neighbouring nodes. As such, any scheme of time stepping needs a solver to invert the mass matrix every time step unless it is lumped (replaced by its diagonal approximation). Although computationally much cheaper, lumping reduces accuracy and increases dispersion, as we have shown in DKS04 on the example of the advection scheme. FEOM uses consistent mass matrices.

Second, computing derivatives of the solution could lead to a noise, especially on unstructured grids, if there is no control over their norm. This control is guaranteed by including viscosity or diffusivity terms into the operator part if the variational formulation is used. Then, to enhance the stability of the scheme (and make larger time steps possible), the Coriolis term in the momentum equation and advection term in the tracer equation are also included into the operator part. This last step makes the stiffness matrices of the dynamic and tracer problem non-symmetric and in this way renders the choice of the solver much more critical (yet tractable).

Griffies et al. (2000) express some concern about solver performance. The basic points stressed by them are: (i) difficulties in finding a good first guess, (ii) poor convergence, and (iii) bad scalability on parallel computers. The first two points actually depend on the quality of the preconditioner and are never a problem with iterative solvers used in the FEOM (Frickenhaus, 2003). The third point is indeed of concern and requires careful design of the storage and communication structure (efficient node numbering, node partition between the processors and distribution of stiffness matrices are among the important factors), and experimenting with solvers.

We investigated the performance of different solvers when increasing the model size from the coarse to current resolution. PILUT, PETSC and HYPRE solvers used here (see Frickenhaus, 2003) scale linearly with the size of the tracer and full velocity problems (which implies that the number of iterations remains the same). The number of iterations increases with size for the barotropic subproblem, yet this would be the case with finite-difference models too. Of the three solvers tested, PETSC scales best on parallel computers. We hope that optimizing preconditioners to particular problems solved in the FEOM would help to reduce the cost of the solution phase.

3. Results

The results presented below were obtained in a 10-year run initialized with the Levitus climatology (Levitus et al., 1994; Levitus and Boyer, 1994). This time span is still insufficient for the initial conditions to lose influence, yet no significant trends in SSH are seen at the final stage of integration. The last three years were used for the analysis.

3.1. Mean sea surface height and variability

Fig. 2 depicts the mean sea surface height computed over the last three years of the run. The Gulf Stream separates somewhat north of Cape Hatteras at about 38° . The model resolution in this region is only about 0.3° (see Fig. 1) which is typically considered insufficient according to the experience gained with other eddy-permitting models of comparable $1/3^\circ$ resolution (see for example, summary of the DYNAMO Group results in Willebrand et al., 2001; we will refer to the models described there as LEVEL, SIGMA and ISOPYCNIC thereafter). Even models of finer resolutions such as $1/4^\circ$ POP (Maltrud et al., 1998), 15–20km POM (Ezer and Mellor, 2000), $1/6^\circ$ POP (Chao et al., 1996) still locate the separation point further to the north. Only very fine resolution models ($1/10^\circ$ POP of Smith et al., 2000, and $1/12^\circ$ MICOM of Paiva et al., 1999) perform better. The exception to this rule is a $3/4^\circ$ version of ROMS (Haidvogel et al., 2000) which even locates the separation point slightly to the south of Cape Hatteras.

Surprisingly the overall structure of the SSH produced by FEOM is very similar to that of ISOPYCNIC, see Fig. 2. Both show Gulf Stream recirculation. Similar to ISOPYCNIC, one branch of the recirculation turns to the east and in spite of the coarse resolution used in the central North Atlantic forms a front at about 35°N which is related to the Azores Current. Two other DYNAMO models failed in reproducing this current. It is interesting to note that even a gyre near the Portugal coast is present in both FEOM and ISOPYCNIC.

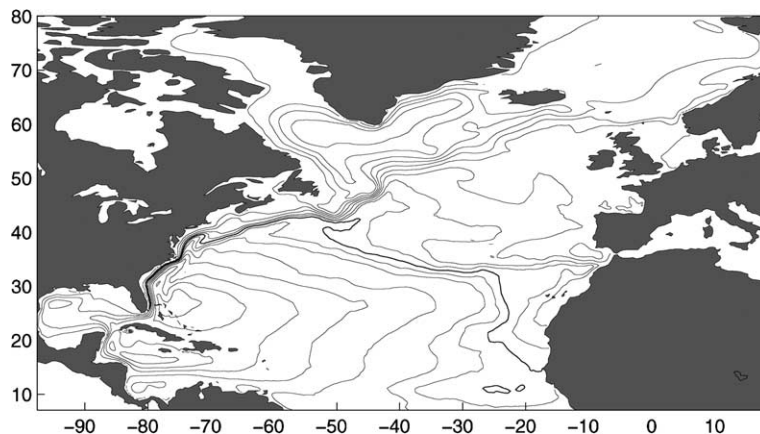


Fig. 2. Three-year mean SSH. Contour intervals are 0.1 m except for two intervals on both sides of the zero line (thick contour) which are 0.05 m.

Similarly, the shapes of the subpolar gyre in the FEOM and ISOPYCNIC are close to each other and follow the same pattern as in eddy-resolving simulations of Smith et al. (2000). That is because the North Atlantic Current (NAC) in these models separates from the Grand Banks at about 50°N and a branch of the NAC turns to the northwest and penetrates deep into the Labrador Sea. SIGMA shows the NAC going further to the northwest while LEVEL separates it from the Grand Banks far to the south.

Reproducing the correct pathway of the NAC in this area is a common problem for z -coordinate models at eddy-permitting resolution noted in Böning et al. (1996) and Willebrand et al. (2001) (see also Treguier et al., 2001). Even a 1/12° version of FLAME is imperfect in simulating the penetration of warm subtropical water into the Labrador Sea along the Grand Banks (see Fig. 4d of Eden et al., 2004), although it is significantly better than the 1/3° version. In contrast, the pattern of mean temperature in FEOM at 50m depth (see Fig. 3) is in good agreement with observed temperature in this area except for warming close to the coast and 15°C isotherm going too far north.

Seemingly, the path of the NAC along the Grand Banks is strongly affected by topographic effects as it is relatively well reproduced by models dealing with smooth topography. Some support to this conclusion could be found in results of Myers and Deacu (2004) who show that approximating the bottom with partial cells makes this feature closer to observations.

The FEOM SSH variability is presented in Fig. 4. In the Gulf Stream region it is mainly concentrated around the separation point where its standard deviation exceeds 20cm. In the remaining part of the Gulf Stream it is of the order of 3cm which is lower than the lowest variability in DYNAMO shown by ISOPYCNIC. However, it is worth to remember that the horizontal reso-

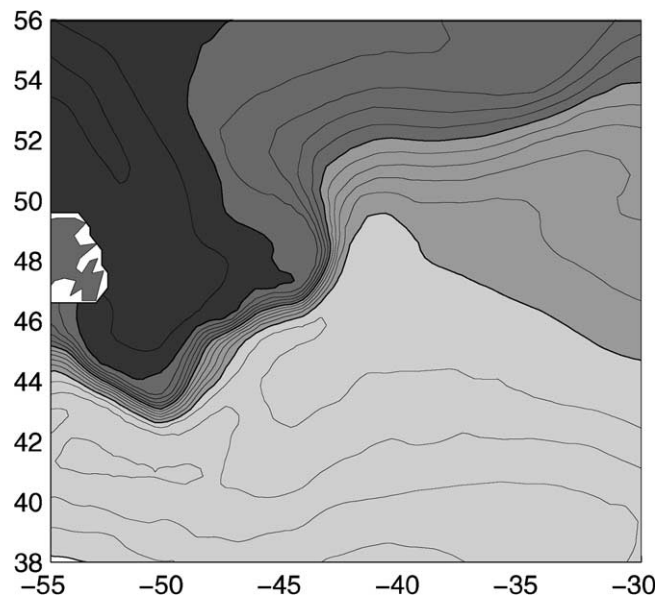


Fig. 3. Three-year mean temperature at 50m depth east of Newfoundland. The contour interval is 1°C, and the boundaries between the shaded zones are at 5, 10 and 15°C beginning from the darkest one.

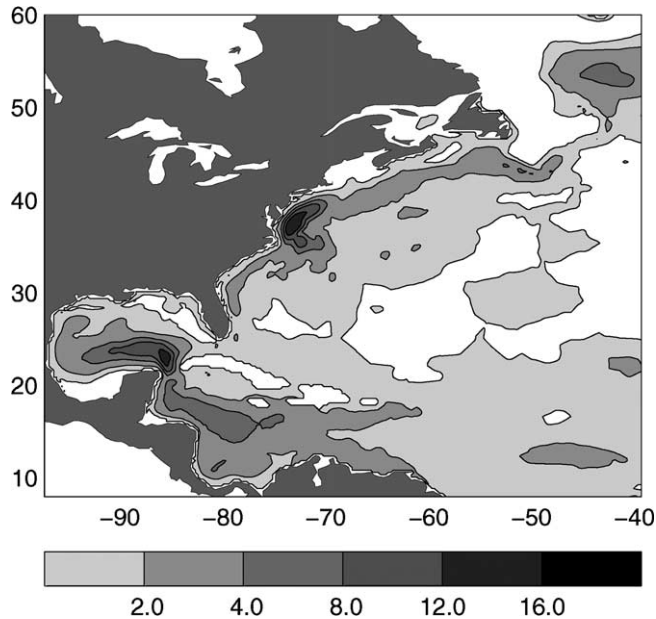


Fig. 4. Standard deviation of SSH in the Western North Atlantic over the last three years of integration (cm).

lution of FEOM in this area is only about 0.5° , and that it uses large implicit time steps both resulting in weaker variability. Yet it is generally comparable with typical values obtained in the DAMÉE-NAB intercomparison project (Chassignet et al., 2000).

The model exhibits strong SSH variability in the Caribbean and Gulf of Mexico which could be attributed to finer spatial resolution there. The standard deviation reaches 12 cm in the Caribbean Sea and 20 cm in the Gulf of Mexico which is notably higher than in a $1/3^\circ$ MOM and comparable to a $1/9^\circ$ version (Oschlies, 2002). However the subtle features of circulation are not reproduced properly as they may be sensitive to the detail of spatial resolution (still rather coarse at about 0.6° in the Central part of the Gulf of Mexico) and local bathymetry (Chassignet, personal communication, 2003). Problems include the direction of eddy propagation in the Gulf of Mexico. Once eddies enter the Yucatan Channel they turn to the west in FEOM instead of moving in the north-west direction as regional simulations reveal (Morey et al., 2003).

3.2. Meridional overturning and heat transport

The mean meridional overturning stream function of FEOM is presented in Fig. 5. The maximum transport value is 14.5 Sv which agrees well with LEVEL but is slightly lower than in ISO-PYCNIC and SIGMA. The position of the maximum is located at 35°N and 1200 m depth. Compared to the DYNAMO models, this is in better agreement with the position of the maximum obtained in Smith et al. (2000). The FEOM also exhibits the spurious upwelling around 35°N which is associated with the Gulf Stream separation and is traditional to level coordinate models if the Gent and McWilliams (1990) parameterization of mixing is not used (Böning et al., 1995).

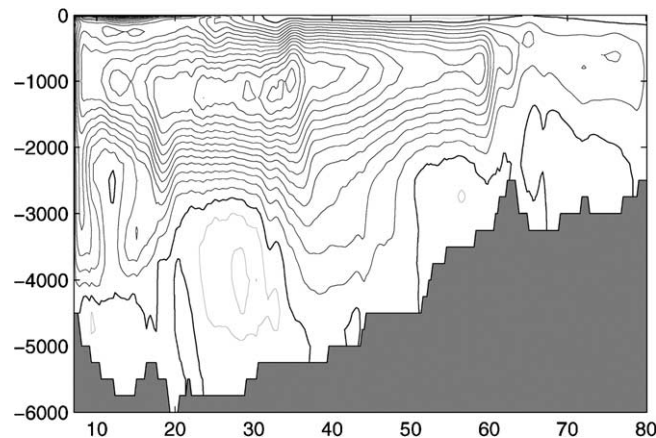


Fig. 5. Meridional overturning stream function (Sv) averaged over the last three years of integration. The maximum value is 14Sv and is located at 35°N and 1200m depth. Spurious circulation cells at the south are due to treating the open boundary as closed. Contours are drawn through 1 Sv, and the thick contour corresponds to zero transport. Notice the gradual deepening towards the equator between 60°N and 35°N.

The Denmark Strait overflow of the North Atlantic Deep Water (NADW) is relatively weak compared to all three DYNAMO models. This can be explained by relaxation to Levitus climatology considered too poor to represent the East Greenland Current (Willebrand et al., 2001). For this reason, the DYNAMO project used another data set in the northern buffer zone. However, contrary to ISOPYCNIC and SIGMA, FEOM is able to produce strong sinking in the subpolar gyre of 7Sv at about 60°N which is in agreement with LEVEL and is also supported by Smith et al. (2000).

Another feature of the overturning circulation present in FEOM is sinking of the NADW from 60°N to about 42°N. This sinking is clearly seen in Smith et al. (2000) and ISOPYCNIC, less visible but still present in SIGMA and is absent in LEVEL. FEOM also exhibits deep reverse cells which are also present in LEVEL, SIGMA and Smith et al. (2000).

The mean meridional heat transport at 24°N equals 0.95 PW which is slightly lower than in SIGMA and ISOPYCNIC and the estimate of Macdonald (1998) but higher than in LEVEL. At 36°N and 48°N the heat transport is notably underestimated compared to SIGMA and ISOPYCNIC but is almost identical with that of LEVEL and stays within error bars of Macdonald (1998).

Note once again that we relaxed model surface temperature and salinity to the Levitus seasonal climatology, while all DYNAMO models were forced by a surface heat flux computed according to Barnier et al. (1995). The latter is shown (Maltrud et al., 1998) to produce notably higher values of the meridional heat flux and overturning.

3.3. Deep Western Boundary Current

A distinct feature of the North Atlantic circulation is a narrow Deep Western Boundary Current associated with the major part of the thermohaline circulation. Its realistic representation is a crucial test for the model performance. Fig. 6 shows that the Deep Western Boundary Current

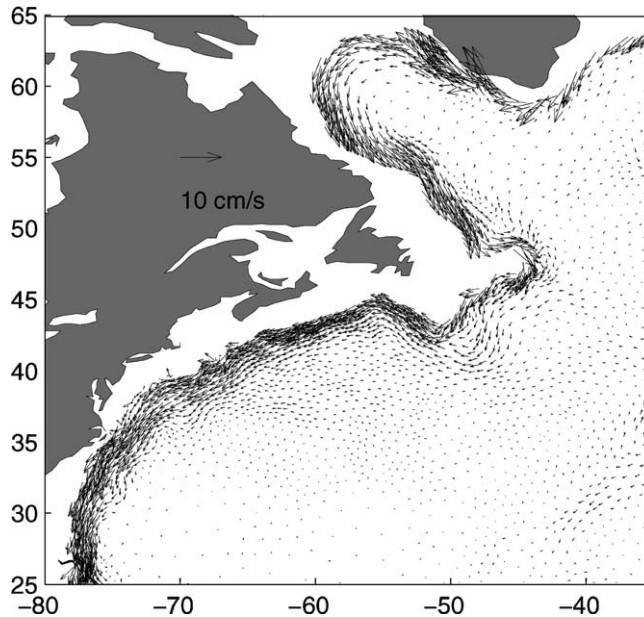


Fig. 6. Three-year mean horizontal velocity at 1625 m.

(DWBC) remains attached to the shelf break in the FEOM similar to ISOPYCNIC and SIGMA while in LEVEL it extends far into the open ocean.

Fig. 7 depicts a section of the meridional velocity in the vicinity of the western boundary at 27°N. Due to still insufficient horizontal resolution at the continental shelfbreak which results in oversmoothed bathymetry the FEOM, similar to SIGMA, joins the Florida and Antilles Currents. However, the northward transport appears to be narrower and stronger. Maximum northward velocities are about 1 m/s which is twice as high as in SIGMA and corresponds well to LEVEL which produced the strongest Florida Current among the DYNAMO models. The volume northward transport between the coast and 78°W is 37 Sv in the FEOM which agrees well with all DYNAMO models.

The structure of the DWBC is largely similar to that produced by SIGMA. As in this model, the core located at the 2000 m depth is well attached to the continental slope and the deep southward transport has some signature at the surface. Though FEOM has a coarser local resolution in this area than the DYNAMO models, the DWBC has the same horizontal extension of 1° though still being too wide compared to observations (Lee et al., 1996). The maximum southward velocity at the core of DWBC is 12 cm/s which coincides with LEVEL but is slightly lower than 15 cm/s observed (Lee et al., 1996) and obtained in SIGMA. The southward volume transport is 17 Sv which is also in agreement with the DYNAMO models.

3.4. Azores Current

The DYNAMO models are of different skills in reproducing the Azores Current which crosses the North Atlantic in the eastward direction at about 35°N and possibly plays an important role in the ventilation of the North Atlantic subtropical gyre (New et al., 2001). It was very well

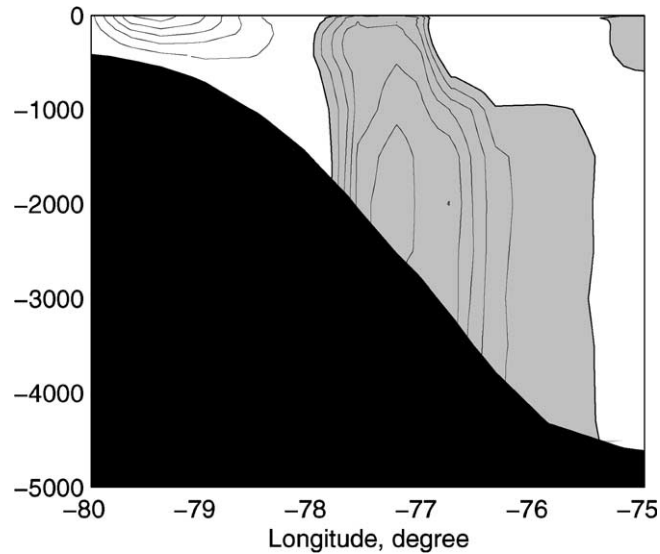


Fig. 7. Meridional velocity cross-section (cm/s) along 27°N averaged over the last three years of integration. The maximum northward and southward velocities are about 1 m/s and 12 cm/s respectively. The core of the Deep Western Boundary Current is located at the depth of 2000m. Contour intervals are 0.2m/s for northward velocities and 2 cm/s for southward ones. The area of southward transport is shaded.

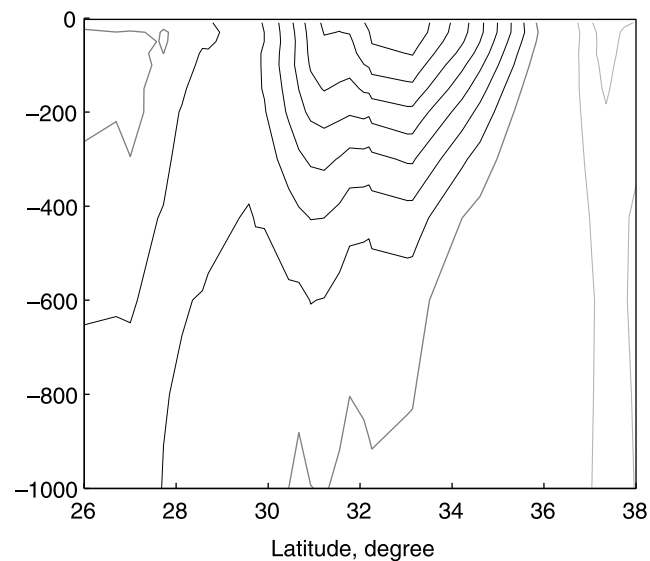


Fig. 8. Three-year mean zonal velocity at 30°W . The contour interval is 1 cm/s, the thick gray line corresponds to zero velocity, and black contours correspond to eastward velocities.

pronounced in ISOPYCNIC, less visible in SIGMA and absent in LEVEL. It is worth mentioning that this problem is also persistent in other z -coordinate models like POP (Smith et al., 2000) and

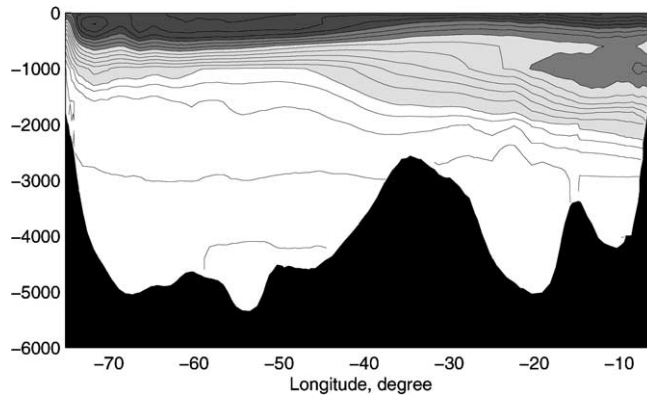


Fig. 9. Salinity at the zonal cross-section at 35°N averaged over the last three years of integration. The boundaries between the shaded zones correspond to 35.1, 35.7 and 36 psu. Contours are drawn through 0.05 psu in the white zone and 0.1 psu above.

OPA (Treguier et al., 2001) on non-eddy-resolving grids, and is improved only at the eddy-resolving grids (Smith et al., 2000).

As it is seen from Fig. 8 that presents a zonal velocity cross-section, FEOM is able to reproduce the Azores Current. Its strength of 8 cm/s and structure is quite similar to that of ISOPYCNIC (compare to Fig. 2 of New et al., 2001). This model capability could be related to the fact that FEOM maintains the Mediterranean salinity tongue (see Fig. 9) which is clearly seen in the Levitus climatology and the WOCE hydrographic section A03. It is also worth mentioning that finite-difference models of the DAMÉE-NAB intercomparison project (Chassignet et al., 2000) were unable to reproduce this observed feature although their resolution and the mean resolution of FEOM are similar.

4. Summary and conclusions

The results of a 10-year simulation of the North Atlantic circulation with FEOM show that the model is capable of reproducing the main features of the circulation with a skill comparable to that of regular-grid models of finer resolution. We have shown that its mean SSH, meridional overturning and heat flux agree reasonably well with those of 1/3° resolution models. Some details of the North Atlantic circulation such as, for example the pathways of the NAC and DWBC are reproduced by FEOM with more realism than by LEVEL. The sloping topography of the FEOM could be partly responsible for this improvement yet this question requires further investigation. Of course, the skill of z -coordinate models at finer resolution (Smith et al., 2000) becomes superior to both LEVEL and the current version of FEOM but at the expense of much higher CPU cost.

Given that the FEOM mesh combines z -levels with sloping bottom one would have guessed that the solution produced by FEOM shares the features of LEVEL and SIGMA. Surprisingly, in many respects (such as the SSH structure, the SSH variability, the Azores Current etc.) FEOM's circulation appears to be similar to that of ISOPYCNIC. The reason for this similarity is unclear to us.

The CPU cost of the model divided per node number is significantly higher than that of the structured-grid finite-difference models, which comes more from the unstructured character of the FEOM grid than from using solvers. Yet the efficiency of the model should be estimated by its ability to reproduce the ocean circulation in dynamically important areas and in most cases depends on local resolution and topography representation. In terms of efficient resolution, FEOM has an affordable CPU cost.

The main conclusion drawn from the DYNAMO intercomparison project is that the large-scale ocean thermohaline circulation in the North Atlantic is strongly influenced by processes occurring on a local scale and is rather sensitive to small-scale details of the bathymetry the role of which is not fully understood (Willebrand et al., 2001). Due to the freedom in representing bathymetry and the possibility of mesh refinement in areas of interest (which was not fully explored in the current version), FEOM could serve as a tool for investigating this issue. Our future work will go along this line. Another promising direction of applying the FEOM is modelling regional circulations by a global model with local mesh refinement. It would eliminate both open boundary and nesting problems.

Acknowledgments

We thank Paul Myers and an anonymous reviewer for their comments which were helpful for improving the manuscript. The computations were performed on the IBM pSeries 690 Supercomputer of the HLRN-systems in Berlin and Hannover within the project hbk00010.

References

- Adcroft, A., Hill, C., Marshall, J., 1997. Representation of topography by shaved cells in a height coordinate ocean model. *Mon. Weath. Rev.* 125, 2293–2315.
- Barnier, B., Siefridt, L., Marchesiello, P., 1995. Thermal forcing of a global ocean circulation model using a three-year climatology of ECMWF analyses. *J. Mar. Sys.* 6, 363–380.
- Böning, C.W., Holland, W.R., Bryan, F.O., Danasoglu, G., McWilliams, J.C., 1995. An overlooked problem in model simulations of the thermohaline circulation and heat transport in the Atlantic Ocean. *J. Climate* 8, 515–523.
- Böning, C.W., Bryan, F.O., Holland, W.R., Döscher, R., 1996. Deep-water formation and meridional overturning in a high-resolution model of the North Atlantic. *J. Phys. Oceanogr.* 26, 1142–1164.
- Chao, Y., Gangopadhyay, A., Bryan, F.O., Holland, W.R., 1996. Modeling the Gulf Stream system: How far from reality? *Geophys. Res. Lett.* 23, 3155–3158.
- Chassignet, E.P., Arango, H., Dietrich, D., Ezer, T., Ghil, M., Haidvogel, D.B., Ma, C.-C., Mehra, A., Paiva, A., Sirkes, Z., 2000. DAMÉE-NAB: the base experiment. *Dyn. Atmos. Oceans* 32, 155–183.
- Danilov, S., Kivman, G., Schröter, J., 2004. A finite element ocean model: principles and evaluation. *Ocean Modell.* 6, 125–150.
- Eden, C., Greatbatch, R.J., Böning, C.W., 2004. Adiabatically correcting an eddy-permitting model using large-scale hydrographic data: application to the Gulf Stream and the North Atlantic Current. *J. Phys. Oceanogr.* 34, 701–719.
- Ezer, T., Mellor, G.L., 2000. Sensitivity studies with the North Atlantic sigma coordinate Princeton Model. *Dyn. Atmos. Oceans* 32, 185–208.
- Frickenhaus, S., 2003. Parallel Solvers for Irregular Sparse Linear Systems. Available from <<http://www.awipotsdam.de/InfoCenter/IT/WorkingGroups/SciComp/SSolversUG.html>>.
- Gent, P.G., McWilliams, J.C., 1990. Isopycnal mixing in ocean circulation models. *J. Phys. Oceanogr.* 20, 150–155.

- Gent, P.R., 1991. The heat budget of the TOGA-COARE domain in an ocean model. *J. Geophys. Res.* 96, 3323–3330.
- Griffies, S.M., Böning, Bryan, F.O., Chassignet, E.P., Gerdes, R., Hasumi, H., Hirst, A., Treguier, A.-M., Webb, D., 2000. Developments in ocean climate modeling. *Ocean Modell.* 2, 123–192.
- Haidvogel, D.B., Arango, H.G., Hedstrom, K., Beckmann, A., Malanotte-Rizzoli, P., Shchepetkin, A.F., 2000. Model evaluation experiments in the North Atlantic Basin: simulations in nonlinear terrain-following coordinates. *Dyn. Atmos. Oceans* 32, 239–281.
- Lee, T.N., Johns, W., Zantopp, R., Fillenbaum, E., 1996. Moored observations of western boundary current variability and thermohaline circulation at 26.5°N in the subtropical North Atlantic. *J. Phys. Oceanogr.* 26, 962–983.
- Levitus, S., Boyer, T.P., 1994. *World Ocean Atlas Temperature*, vol. 4. NOAA, Washington, DC.
- Levitus, S., Burgett, R., Boyer, T.P., 1994. *World Ocean Atlas Salinity*, vol. 3. NOAA, Washington, DC.
- Macdonald, A.M., 1998. The global ocean circulation: a hydrographic estimate and regional analysis. *Progr. Oceanogr.* 41, 281–382.
- Maier-Reimer, E., Mikolajewicz, U., Hasselmann, K., 1993. Mean circulation of the Hamburg LSG OGCM and its sensitivity of to the thermohaline surface forcing. *J. Phys. Oceanogr.* 23, 731–757.
- Maltrud, M.E., Smith, R.D., Semtner, A.J., Malone, R.C., 1998. Global eddy-resolving ocean simulation driven by 1985–1995 atmospheric winds. *J. Geophys. Res.* 103, 30825–30853.
- Morey, S.L., Zavala-Hidalgo, O'Brien, J.J., 2003. Impact of vertical resolution on a numerical model of the Gulf of Mexico. *Oceans Extended Abstract*, 1234–1237.
- Myers, P.G., Deacu, D., 2004. Labrador sea freshwater content in a model with a partial cell topographic representation. *Ocean Modell.* 6, 359–377.
- New, A.L., Jia, Y., Coulibaly, M., Dengg, J., 2001. On the role of the Azores Current in the ventilation of the North Atlantic Ocean. *Progr. Oceanogr.* 48, 163–194.
- Oschlies, A., 2002. Improved representation of upper-ocean dynamics and mixed layer depths in a model of the North Atlantic on switching from eddy-permitting to eddy-resolving grid resolution. *J. Phys. Ocean.* 32, 2277–2298.
- Pacanowski, R.C., Gnanadesikan, A., 1998. Transient response in a z-level ocean model that resolves topography with partial cells. *Monthly Weather Rev.* 126, 3248–3270.
- Paiva, A.M., Hargrove, J.T., Chassignet, E.P., Bleck, R., 1999. Turbulent behavior of a fine mesh (1/12°) numerical simulation of the North Atlantic. *J. Mar. Sys.* 21, 307–320.
- Smith, R.D., Maltrud, M.E., Bryan, F.O., Hecht, M.W., 2000. Numerical simulation of the North Atlantic Ocean at 1/10°. *J. Phys. Ocean.* 32, 1532–1561.
- Treguier, A.M., Barnier, B., de Miranda, A.P., Molines, J.M., Grima, N., Imbard, M., Madec, G., Messenger, C., Reynand, T., Michel, S., 2001. An eddy-permitting model of the Atlantic circulation: evaluating open boundary conditions. *J. Geophys. Res.* 106, 22115–22129.
- Willebrand, J., Barnier, B., Böning, C., Dietrich, C., Killworth, P.D., Le Provost, C., Jia, Y., Molines, J.-M., New, A.L., 2001. Circulation characteristics in three eddy-permitting models of the North Atlantic. *Progr. Oceanogr.* 48, 123–161.



A fully three dimensional unstructured grid non-hydrostatic finite element coastal model

Robert Jan Labeur *, Julie D. Pietrzak

*Environmental Hydraulics Section, Faculty of Civil Engineering and Geosciences,
Technical University of Delft, P.O. Box 5048, Stevinweg 1, 2600 GA Delft, The Netherlands*

Received 1 December 2003; received in revised form 8 June 2004; accepted 14 June 2004

Available online 10 November 2004

Abstract

The non-hydrostatic model FINEL3D is based on the finite element method. In the model no approximations to the non-hydrostatic equations have been made. The model uses a 3-D fully unstructured grid and tetrahedral elements. The calculations presented here use the so called mini-element. In this paper the models capability to simulate internal flow and internal wave formation over small scale topography are considered. The flow of a stratified fluid over small scale topographic features in an estuary may generate considerable non-hydrostatic internal wave activity. The model is shown to accurately simulate internal trapped waves and internal lee waves. Differences between the analytical solutions and the model results are shown to be due to numerical diffusion.

© 2004 Elsevier Ltd. All rights reserved.

Keywords: Stratified flow; Non-hydrostatic; Internal waves; Finite element method

1. Introduction

A new three-dimensional non-hydrostatic finite element numerical model, FINEL3D is presented. FINEL3D was developed for simulating non-hydrostatic flows in estuarine and coastal

* Corresponding author. Tel.: +31 15 2785069; fax: +31 15 2784842.

E-mail address: r.j.labeur@citg.tudelft.nl (R.J. Labeur).

locations. In particular much attention has been paid recently to accurately resolving internal waves. Internal waves are a widespread feature of coastal seas and oceans. They are known to play an important role in the transfer of mass and momentum. Consequently they may exert a strong influence on the vertical structure of a stratified flow (Pietrzak et al., 1991). Kranenburg and Pietrzak (1989) in a series of laboratory experiments demonstrated that internal waves could significantly increase the local production of turbulence.

In recent years a number of numerical models have been developed to simulate non-hydrostatic coastal and ocean flows. Many of these models have made some sort of approximation to the non-hydrostatic equations, see for example, Marshall et al. (1997), Casulli and Stelling (1998), Stansby and Zhou (1998), Casulli (1999), Hodges and Street (1999), Stelling and Busnelli (2001), Kanarska and Maderich (2002), Casulli and Zanolli (2002). Typically the approximations involve separating the solution into hydrostatic and non-hydrostatic components and sequentially solving for them. In the first step one neglects contributions from the non-hydrostatic pressure and velocity. While at the second step the velocities are corrected by including non-hydrostatic pressure terms. Since these approaches split the solution they can introduce splitting errors. Stelling and Zijlema (2003) recently introduced a new method based on a pressure correction method which does not introduce a splitting error. However, in contrast to the above the approach adopted here is to solve the complete non-hydrostatic equations. This approach was adopted because it was considered important to resolve small scale non-hydrostatic coastal flows.

The model, FINEL3D, is also different to many others in the literature in that it is a fully unstructured grid three dimensional model. Many of the newer hydrostatic unstructured grid flow models follow the philosophy of being unstructured (either finite element or finite volume) in the horizontal but structured in the vertical. For example, a geopotential, z -level coordinate is adopted in the UnTrim model (Casulli and Walters, 2000) and the ELCIRC model (Zhang and Baptista, in press), which uses a similar formulation to the UnTrim approach. While a sigma (terrain following) co-ordinate system was adopted in the finite element models Quoddy (Lynch et al., 1996) and a generalised terrain following mapping was adopted by Iskandarani et al. (2003). Recently a non-hydrostatic version of the UnTrim model has been developed by Casulli and Zanolli (2002). They demonstrated that splitting the solution procedure into a hydrostatic and non-hydrostatic part, in combination with a z -level co-ordinate in the vertical gave efficient results in the case of quasi-hydrostatic flows. However, in the case where the flow is non-hydrostatic and one is dealing with complex geometries it can be advantageous to use a fully three dimensional approach.

Using tetrahedral elements the vertical alignment of the grid can be chosen arbitrarily. To our knowledge the only other ocean model to adopt this philosophy is the model of Danilov et al. (2004). The main reason for adopting this approach is that it allows topographic features to be accurately resolved. It allows a lot of flexibility in the specification of the vertical grid location, i.e. clustering near features of interest without having to resort to hybrid coordinates, see for example, Pietrzak et al. (2001). To our knowledge FINEL3D is one of the few fully three dimensional, finite element, non-hydrostatic flow models. The model has been tested and validated in a number of studies concerned with flow in complex coastal engineering works, see Svašek (2001) for a study of current induced forces on ships in stratified flow conditions, where the clear advantages of the finite element approach are demonstrated. Recently the model has been used to simulate internal waves in the Rotterdam Waterway (Pietrzak and Labeur, 2004). Here we present the model formulation and provide a number of linear internal wave test cases and laboratory data

against which to validate the model. The final objective is a coastal flow model capable of accurately simulating a range of complex stratified flow problems.

Internal waves may be generated by various mechanisms, but most notably by stratified tidal flow over topography. Starting with the pioneering work of Long (1953) numerous studies have been carried out of topographically generated internal waves. Many studies have focused on internal wave generation by isolated large amplitude topographic features and the associated upstream propagation of solitons, see the review by Baines (1995). Internal solitons can be described with hydrostatic theory and Boussinesq approximations. However, this approach lacks generality. Observations in the Rotterdam Waterway showed large amplitude trapped internal waves and lee waves, Pietrzak et al. (1990) and Kranenburg et al. (1991). The non-hydrostatic waves were generated by the tidal flow of stratified fluid over small scale bed features with amplitudes of the order 0.1–1 m in a typical water depth of 16 m and wavelengths of the order 30–80 m. Shallow seas, such as the North Sea are often covered in such bed features, sand waves with wavelengths of a few hundred metres and heights about 10% of the depth are observed. Mega ripples with heights up to a meter and wavelengths of the order tens of meters are typically superposed on such sand waves. What is of particular interest is that internal waves are generated by typical tidal flow conditions over low amplitude bed topography such as sand waves and mega ripples. Since small scale topographic features are present in most estuaries and coastal seas, internal waves are expected to occur in many situations. Consequently, the need for accurate non-hydrostatic models that can simulate stratified flows has gained importance in recent years. Hence we consider the accurate modelling of such types of non-hydrostatic flow.

First, the numerical model, FINEL3D, is described in detail in Section 2. Then a summary of linear internal trapped wave theory and internal lee wave theory is provided in Section 3. The results of some test computations are described in Section 4. Finally conclusions are presented in Section 5.

2. Numerical model

2.1. Equations

In this section, the numerical flow model is described. The model employed here is FINEL3D which is based on the Navier–Stokes equations (2.1) and (2.2), with transport equation (2.4) for the relative density. In vector form the incompressible Navier–Stokes equations read:

$$\frac{\partial \bar{\mathbf{u}}}{\partial t} + \bar{\mathbf{u}} \cdot \nabla \bar{\mathbf{u}} - \nu \nabla^2 \bar{\mathbf{u}} = \frac{1}{\rho} (\bar{\mathbf{F}}_{\text{res}} - \nabla p) \quad (2.1)$$

$$\nabla \cdot \bar{\mathbf{u}} = 0 \quad (2.2)$$

The momentum equation (2.1) expresses that water particles are accelerated due to a pressure gradient and external forces, while momentum may also be dissipated by internal friction. The left-hand side of (2.1) is the advection–diffusion part of the momentum equation, with velocity vector $\bar{\mathbf{u}}$ [m/s] and (turbulent) kinematic viscosity ν [m²/s]. The right-hand side of (2.1) contains the gradient of the pressure p [N/m²] and the sum of the external forces per unit volume $\bar{\mathbf{F}}_{\text{res}}$ [N/m³], both

divided by the density ρ [kg/m³]. Eq. (2.2) is the incompressibility constraint. Incompressibility of the fluid is maintained by the pressure gradient through the momentum equation. In this way the incompressibility of the fluid implicitly determines the pressure distribution. Density differences in the fluid contribute to the resulting force \bar{F}_{res} . A constant temperature and small changes of pressure and salinity are assumed so that a linearised equation of state may be used to calculate the density from the salinity distribution. Invoking the Boussinesq approximation, which states that density differences $\Delta\rho = \rho - \rho_0$ are also small with respect to the average density ρ_0 , the right-hand side of (2.1) may be approximated as:

$$\frac{1}{\rho}(\bar{F}_{\text{res}} - \nabla p) \approx \frac{1}{\rho_0}(-\rho g \bar{e}_z - \rho_0 g \nabla(h - z)) = -g(\tilde{\rho} \bar{e}_z + \nabla h) \quad (2.3)$$

Here, g [m/s²] is the gravitational acceleration and h [m] is the piezometric level with respect to the average density, implicitly defined by the relation $p = \rho_0 g(h - z)$. For the relative density difference $\tilde{\rho} = (\rho - \rho_0)/\rho_0$ [-] a transport equation holds:

$$\frac{\partial \tilde{\rho}}{\partial t} + \bar{u} \cdot \nabla \tilde{\rho} - \kappa \nabla^2 \tilde{\rho} = 0 \quad (2.4)$$

where κ [m²/s] is the (turbulent) diffusivity. Eqs. (2.3) and (2.4) result in a coupling of the flow and the advected density field.

2.2. Discretisation

The model is based on the finite element method. In the finite element approach the continuous fields of \bar{u} and h are approximated in a computational domain Ω with boundary Γ by finite dimensional function spaces V_h and Q_h respectively. These function spaces are spanned by N_u basis functions v_h and N_q basis functions q_h thus forming a subspace of the respective continuous fields. In this way the continuous fields \bar{u} and h are approximated by

$$\bar{u} \approx \bar{u}_h = \sum_{i=1}^{N_u} \bar{u}_i v_{h,i} \quad \text{and} \quad h \approx h_h = \sum_{i=1}^{N_q} h_i q_{h,i} \quad (2.5)$$

The function spaces V_h and Q_h have to satisfy certain integrability conditions, e.g. some norms should be well defined. Next, the discrete form of the equations is found by considering the weak form of the discrete solution in the discrete function spaces V_h and Q_h (Galerkin method). The discrete form of the momentum equation becomes:

$$\begin{aligned} \forall \bar{v}_h \in V_h \int_{\Omega} \left\{ \left(\frac{\partial \bar{u}_h}{\partial t} + \bar{a}_h \cdot \nabla \bar{u}_h + g \nabla h_h + g \tilde{\rho}_h \bar{e}_z \right) \bar{v}_h + \nu \nabla \bar{u}_h \cdot \nabla \bar{v}_h \right\} d\Omega \\ + \oint_{\Gamma_{\bar{u}}} \left\{ (\bar{a}_h \cdot \bar{n})^- [\bar{u}_0 - \bar{u}_h] - \nu \frac{\partial \bar{u}}{\partial n} \Big|_0 \right\} \bar{v}_h d\Gamma \\ + \oint_{\Gamma_h} \left\{ g[h_0 - h_h] \bar{n} + (\bar{a}_h \cdot \bar{n})^- [\bar{u}_{\tau,0} - \bar{u}_{\tau,h}] - \nu \frac{\partial \bar{u}_{\tau}}{\partial n} \Big|_0 \right\} v_h d\Gamma = 0 \end{aligned} \quad (2.6)$$

which implies projection of the momentum equation on each of the basis functions \bar{v}_h belonging to V_h . The vector \bar{a}_h appearing in Eq. (2.6) is the advective velocity relative to the grid movement (see

comments below). The viscous term is integrated by parts giving rise to a boundary integral on $\Gamma_{\bar{u}}$ specifying the viscous shear stresses. This integral also has a contribution from the inward advective transport of momentum by the inward advective velocity component $(\bar{a}_h \cdot \bar{n})^-$, with \bar{n} being the outward pointing unit normal vector along the boundary. In both the advective and viscous parts subscript zero indicates quantities to be specified along the boundary. Alternatively, the velocity components themselves may be specified along $\Gamma_{\bar{u}}$ thus restricting the space V_h . Along Γ_h the external piezometric level h_0 has to be specified, resulting in a normal stress. In addition the tangential velocity $\bar{u}_{\tau,0}$ or tangential stresses have to be specified along Γ_h . Omitting the advective and diffusive momentum transfer terms from these boundary integrals simply implies that the associated stresses are zero (free slip boundary).

The weak form of the discrete continuity equation follows from a projection of the incompressibility constraint on all functions belonging to Q_h yielding:

$$\forall_{q_h \in Q_h} \int_{\Omega} \bar{u}_h \cdot \nabla q_h \, d\Omega - \oint_{\Gamma_h} \bar{u}_h \cdot \bar{n} q_h \, d\Gamma - \oint_{\Gamma_{\bar{u}}} \bar{u}_0 \cdot \bar{n} q_h \, d\Gamma - \oint_{\Gamma_{\text{free surface}}} \frac{\partial h}{\partial t} n_z q_h \, d\Gamma = 0 \quad (2.7)$$

Integration by parts in this case leads to a boundary integral containing the normal velocity. Along $\Gamma_{\bar{u}}$ the normal velocity must be prescribed while along Γ_h the discrete (interior) normal velocity should be substituted instead. Omitting this boundary condition simply implies a closed wall (normal velocity equal to zero). At the free surface the integrated normal velocity is related to the movement of the piezometric level h , as expressed by the third boundary integral in which n_z is the vertical component of the unit normal vector to the free surface. The piezometric level h in the entire fluid is implicitly defined through coupling of the momentum equation and the continuity equation. Therefore h may also be regarded as a Lagrange multiplier for the incompressibility constraint.

The function spaces V_h and Q_h follow from the spatial discretisation of the computational domain Ω . Typically, a 2-dimensional spatial discretisation will consist of triangles or quadrilaterals (tetrahedrons or hexahedrons in 3 dimensions). The discrete function spaces V_h and Q_h may not be chosen independently but have to obey certain compatibility requirements in order to guarantee stability of the discrete solution. A number of allowable combinations are known, see for instance Gunzburger (1989). The model uses the so-called MINI-element illustrated in Fig. 1. The q_h are piecewise linear on triangles (or tetrahedrons in 3D). In addition the \bar{v}_h space is enriched by piecewise linear functions that have value one in the element centre and vanish on the element boundaries, also referred to as ‘bubble-functions’. The velocities associated with these bubble functions can be eliminated from the discrete system of equations reducing it to a coupled system in the nodal degrees of freedom only. This ‘static condensation’ in effect leads to a pressure-Poisson equation being added to the continuity equation which stabilizes the pressure-velocity coupling. After solving for the nodal velocities, the bubble-velocities are found by back substitution. The resulting computational grid is unstructured.

The discrete relative density difference $\tilde{\rho}_h$ is approximated in the same space V_h as are the velocities. This is a prerequisite for stability of the density–velocity coupling (Gunzburger, 1989). The discrete transport equation therefore has a form similar to the discrete momentum equation (2.6):

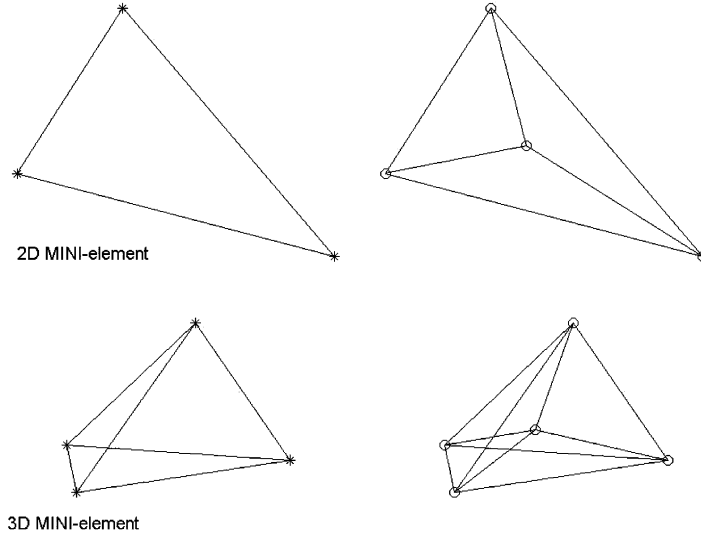


Fig. 1. Distribution of pressure nodes (*) and velocity nodes (O) in the 2- and 3-dimensional MINI-element.

$$\begin{aligned} \forall v_h \in V_h \int_{\Omega} \left\{ \left(\frac{\partial \tilde{\rho}_h}{\partial t} + \bar{a}_h \cdot \nabla \tilde{\rho}_h \right) v_h + \kappa \nabla \tilde{\rho}_h \cdot \nabla v_h \right\} d\Omega \\ + \oint_{\Gamma_{\tilde{\rho}}} \left\{ (\bar{a}_h \cdot \bar{n})^- [\tilde{\rho}_0 - \tilde{\rho}_h] - \kappa \frac{\partial \tilde{\rho}}{\partial n} \Big|_0 \right\} v_h d\Gamma = 0 \end{aligned} \quad (2.8)$$

In domains with a free surface the computational grid is continuously adapted to the position of the free surface. The resulting motion of the grid points is incorporated in the advective speed \bar{a}_h which is the flow velocity relative to the grid movement. It is well known that for relatively high velocities (large element Péclet-numbers) numerical treatment of the advection term as in Eqs. (2.6) and (2.8) may give rise to instabilities. These instabilities are already suppressed by the use of the bubble-functions, but the resulting stabilization is not always optimal in advection dominated cases (Simo et al., 1995). Some additional stabilization by upstream differencing may therefore be necessary. In this model the Streamline Upwind Petrov Galerkin (SUPG) method is used for this purpose where in each element e the associated weighting functions $v_{h,e}$ are locally replaced by modified functions $v_{h,e}^*$ according to:

$$v_{h,e}^* = v_{h,e} + \tau_e \bar{a}_{h,e} \cdot \nabla v_{h,e} \quad (2.9)$$

where τ_e is an elementwise parameter with the dimension of time (Hughes, 1987). The τ_e can be computed in several ways, giving the modeller some freedom. Here τ_e is related to the mean residence time of fluid particles in each element:

$$\tau_e = \frac{\int d\Omega_e}{\oint |\bar{a} \cdot \bar{n}| d\Gamma_e} \zeta(Pe) \quad (2.10)$$

where $\zeta(Pe)$ is a Péclet-number dependent function which tends to one for pure advection ($v = 0$) and tends to zero in case of diffusion dominated problems ($Pe = 0$). For stationary 1-dimensional

problems an optimal expression for $\zeta(Pe)$ is known giving nodally exact solutions. For general cases a number of alternative expressions are proposed in the literature (see for instance [Heinrich and Pepper, 1999](#)). In the inviscid simulations presented here $\zeta(Pe)$ is equal to one. The resulting formulation effectively controls spurious oscillations near sharp gradients such as jump discontinuities and (outflow) boundary layers ([Johnson, 1990](#)). It is important to note that the modified test functions should be used in all terms of the discrete equations, in order to maintain consistency of weak form, yielding an accuracy of order $1\frac{1}{2}$ in advection-dominated cases ([Hughes, 1987](#)). In the computations reported here however, the consistent approach did not result in stable stationary solutions and the stabilization had to be applied on the advection terms only. This adds some artificial diffusion to the equations (along streamlines only, with diffusion tensor $\tilde{\nu}_a = \tau_e \bar{a}_h \bar{a}_h^T$) reducing the accuracy of the advection terms to first order. Finally, the equations are discretised in time using the implicit θ -method, in which the discrete equations for the velocity and piezometric level remain coupled.

2.3. Solution algorithm

The resulting system of equations for the increments $\Delta \bar{u}_h$ and Δh_h of the discrete solution has the following block matrix structure:

$$\begin{bmatrix} A & D \\ E & B \end{bmatrix} \begin{pmatrix} \Delta \bar{u}_h \\ \Delta h_h \end{pmatrix} = \begin{pmatrix} r_{\bar{u}} \\ r_h \end{pmatrix} \quad (2.11)$$

where A , D and E are sparse matrix blocks for the advection–diffusion, gradient and divergence operators respectively, while B includes the free surface condition and the pressure–Poisson terms for the piezometric level h_h . The right-hand side vector contains the explicit parts $r_{\bar{u}}$ and r_h . The coupled system is solved as a whole using the BiCGSTAB algorithm as an iterative solver ([van der Vorst, 1992](#)). The performance of the BiCGSTAB algorithm heavily relies on the quality of the preconditioner that is used. Here the approach of [van der Ploeg \(1994\)](#) is followed where an approximate lower-upper (LU) block decomposition is constructed after pre-multiplying the last row of system (2.11) by the advection–diffusion operator A , in order to improve the condition number. Therefore, instead of (2.11) the following system is solved:

$$\begin{bmatrix} I & 0 \\ 0 & A \end{bmatrix} \begin{bmatrix} A & D \\ E & B \end{bmatrix} \begin{pmatrix} \Delta \bar{u}_h \\ \Delta h_h \end{pmatrix} = \begin{bmatrix} I & 0 \\ 0 & A \end{bmatrix} \begin{pmatrix} r_{\bar{u}} \\ r_h \end{pmatrix} \quad (2.12)$$

As preconditioner an approximate inverse of this block system is constructed by means of an approximate LU block-decomposition as follows:

$$\begin{bmatrix} A & D \\ AE & AB \end{bmatrix}^{-1} \approx \begin{bmatrix} A & D \\ 0 & AB - ED \end{bmatrix}^{-1} \begin{bmatrix} I & 0 \\ E & I \end{bmatrix}^{-1} \approx \begin{bmatrix} L_1 U_1 & D \\ 0 & L_2 U_2 \end{bmatrix}^{-1} \begin{bmatrix} I & 0 \\ E & I \end{bmatrix}^{-1} \quad (2.13)$$

in which $L_1 U_1$ and $L_2 U_2$ are incomplete decompositions of the convection–diffusion matrix A and the Schur-complement $AB - ED$ respectively. Before its decomposition the Schur-complement is constructed in an approximate way by multiplication of A with B and E with D at the element level. In our applications the resulting iterative method is stable and robust. Due to non-linearity of the system the system matrix has to be assembled at every time step.

The transport equation for the relative density difference (2.8) is also solved iteratively, using BiCGSTAB with the inverse of the incomplete decomposition $L_1 U_1$ as a preconditioner. Leap-frog time stepping of the coupled flow and density transport equations is necessary because of the presence of the following subsystem in the velocity–density coupling:

$$\frac{\partial}{\partial t} \begin{pmatrix} \tilde{\rho} \\ w \end{pmatrix} + \begin{bmatrix} 0 & \frac{\partial \tilde{\rho}}{\partial z} \\ g & 0 \end{bmatrix} \begin{pmatrix} \tilde{\rho} \\ w \end{pmatrix} = 0 \quad (2.14)$$

where w [m/s] is the vertical velocity component. In a stable stratification system (2.14) has imaginary eigenvalues leading to vertical oscillations by the relative buoyancy (with Nyquist-frequency). Leap-frog treatment of the coupled flow-density equations makes time integration of system (2.14) conditionally stable. As the classical leap-frog scheme has no damping a slightly modified scheme is used where in the vertical momentum equation instead of the relative density at the present time level $\tilde{\rho}^n$ an extrapolated value $\tilde{\rho}^{n+\gamma}$ is used:

$$\tilde{\rho}^{n+\gamma} = \tilde{\rho}^n + \gamma(\tilde{\rho}^n - \tilde{\rho}^{n-1}) \quad (2.15)$$

The damping parameter $\gamma \in [0; 1]$ can be adjusted in order to avoid unphysical transients, while steady solutions remain unchanged. Still, in flows with dominant buoyant forcing, vertical spurious modes of velocities and density may appear as, in general, the discrete buoyant forcing term $\tilde{\rho}_h g \bar{e}_z$ in the momentum equation for the vertical velocity is not entirely within the space of gradients of the discrete piezometric level ∇h_h (Pelletier et al., 1989). These spurious modes can be avoided by projecting the buoyancy term on the vertical gradient of a discrete buoyant potential $\varphi_h \in q_h$ as follows:

$$\forall_{\varphi_h \in q_h} \int_{\Omega} \frac{\partial \varphi_h^{n+\gamma}}{\partial z} \frac{\partial q_h}{\partial z} d\Omega = \int_{\Omega} \tilde{\rho}_h^{n+\gamma} \frac{\partial q_h}{\partial z} d\Omega \quad (2.16)$$

The vertical gradient of the buoyant potential $\varphi_h^{n+\gamma}$ is then used in the vertical momentum equation instead of the relative density $\tilde{\rho}_h^{n+\gamma}$ itself. This projection removes the incompatible modes from the buoyant forcing term, and is used in all computations described in this paper.

The resulting model is second order accurate except for the advective terms, which are of first order accurate only when using the upstream option. A simple turbulence model, based on mixing length theory and Richardson number dependent damping functions, can be employed to include the effects of turbulence. The wall shear stress is in that case computed by a conventional wall function with a prescribed value of the Nikuradse roughness height. See for example, Rodi (1984). In this paper however, only inviscid simulations are presented.

3. Internal waves

In this section we present a number of applications, paying particular attention to the models ability to resolve non-hydrostatic flows of particular relevance to coastal flows. Therefore, we consider the generation and propagation of internal waves by small scale bottom topography. Many previous studies of internal waves have tended to deal with (long) internal solitary waves which are generated by stratified tidal flow interaction with large scale topography. Whereas internal

solitary waves can be described with hydrostatic theory and Boussinesq approximations we are interested in short internal waves that in general need to be described with the full 3D equations. Of particular interest to us are the studies by Pietrzak et al. (1990) and Kranenburg et al. (1991). They focused on the generation of internal waves by small scale bed features as observed in the Rotterdam Waterway, a partially mixed estuary. Both trapped internal waves as well as internal lee waves were observed. These non-hydrostatic internal waves were generated by the tidal flow of stratified fluid over small scale rhythmic bed features with amplitudes of the order 0.1–1 m in a typical water depth of 16m and topographic wavelengths of the order 30–80m. A series of 11 bed waves were observed over an approximately 1 km section of the bed.

Two types of response were observed to dominate the echo-soundings. The first consisted of large amplitude waves located over the rhythmic bed features. These were interpreted as resonant trapped internal waves. The internal wave wavelengths were of the same order as the topographic wavelengths. Additionally they had amplitudes that were three to four times larger than the topography generating them. The wave height of the largest internal wave was approximately equal to half the water depth. The waves were recorded on the ebbing tide. Initially longer wavelength trapped internal waves were excited with shorter wavelength components being excited as the background tidal flow decelerated. In this case a resonant forcing occurred when the current speed was coincident with the phase speed of a free (short) internal wave mode. The second type of response consisted of internal lee waves downstream of a topographic bed feature. Kranenburg and Pietrzak (1989) further explored the lee wave response through laboratory and analytical studies. The laboratory experiments consisted of two layer flow of stratified fluid over an isolated topographic feature. The latter data set includes measurements of wave amplitude and turbulent intensity at a number of positions downstream in a steady lee wave train as a function of internal Froude number.

In the following section we describe elements of trapped internal wave theory and internal lee wave theory. We then present results showing that FINEL3D can simulate both trapped internal waves and lee waves. In addition, the laboratory data set allow us to further validate the fully non-hydrostatic three-dimensional model.

3.1. Summary of trapped internal wave and internal lee wave theory

Here we summarise relevant elements of internal wave theory. Fig. 2 shows a stably stratified fluid flowing over a series of bed features. Fluid particles are displaced vertically as they flow over the topography and due to buoyant restoring forces internal waves are generated.

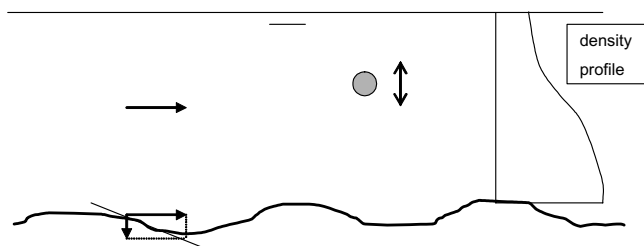


Fig. 2. Sketch of stratified flow over topography.

Pietrzak and Labeur (2004) include a derivation of the trapped internal wave solutions. Here some analytical solutions are briefly discussed. Assuming linear theory and under the Boussinesq approximation, the vertical velocity w satisfies the Taylor–Goldstein equation, see for example Baines (1995). Assuming a rigid lid at the surface and the bottom boundary condition to be given by $\hat{w} = U_0 \frac{dh}{dx} = k_T U_0 h_0 \cos(k_T x)$ where U_0 is the horizontal velocity at the bed, h_0 is the amplitude of the topography, x is the horizontal co-ordinate and k_T is the topographic wavenumber, the vertical velocity is assumed to have the form $w(x, z, t) = \hat{w}(z) e^{ik(x-ct)}$ with z the vertical co-ordinate assumed positive in a direction away from the bed and t is time. In the case of stationary internal waves trapped to the topography the phase speed c of the internal waves with respect to the topography is zero. Assuming the undisturbed horizontal mean shear flow $U(z)$ and the buoyancy frequency $N(z)$ are independent of depth, the solution to the Taylor–Goldstein equation is given by

$$w(x, z) = \frac{U_0 k_T h_0 \sin[(l^2 - k^2)^{1/2}(H - z)] \cos(k_T x)}{\sin[(l^2 - k^2)^{1/2} H]} \quad (3.1)$$

with $l^2(z) = \frac{N^2}{U^2} - \frac{1}{U} \frac{d^2 U}{dz^2}$ and k is the wavenumber of the trapped internal wave. Here we consider solutions of the above equation which have the same wavelength as the bottom topography. It is worth noting that the solution is singular for values of the wavenumber of $k = [l^2 - n^2 \pi^2 / H^2]^{1/2}$. The conditions for resonance are therefore satisfied whenever $|c_r|_{\lambda=\lambda_T} = |U|$, where c_r is the relative phase speed with respect to the fluid.

In contrast a train of internal lee waves is formed on the downstream side of the topography generating them. Lee waves are also stationary with respect to the topography generating them, $c = 0$. The waves propagate against the flow so that the relative phase speed matches the mean velocity of the flowing water, $|c_r| = |U|$. Lee waves can form in subcritical flow, but not in supercritical flow. Increasing the water velocity the relative phase speed must also increase, which is associated with a corresponding increase in the wavelength. In general, the group velocity decreases as the phase speed and the wavelength increase.

Kranenburg and Pietrzak (1989) developed a Boussinesq type theory of internal lee waves in a two-layer flow. To obtain different group and phase velocities Boussinesq equations were adopted. This is still an approximate way to account for non-hydrostatic effects. A requirement is that the horizontal length scale is large with respect to the total depth. Kranenburg and Pietrzak (1989) also carried out two-layer internal lee wave experiments. The laboratory results compared favorably with their theoretical solutions provided an effective length of the topography including the separation zone was included in the theoretical calculations. Their equations are suited to model near critical flow over topography, which have relatively long lee waves. It was found that above an internal Froude number of 0.9 large amplitude and unsteady behaviour resulted which is not accounted for by their steady, linear Boussinesq theory.

4. Results

Here we consider stationary inviscid flow over small amplitude bed topography in order to compare the model results with linear internal trapped wave and internal lee wave theory. In addition a comparison is made against laboratory data. A more detailed study of trapped internal

wave generation can be found in [Pietrzak and Labeur \(2004\)](#). Here we further investigate certain aspects of the model verification, paying particular attention to the laboratory data described in [Kranenburg and Pietrzak \(1989\)](#).

4.1. *Trapped internal waves*

Two trapped internal wave runs are described here. In Run A the focus is on the models ability to reproduce the linear internal wave modes and the influence of numerical viscosity on the resulting solutions. In Run B the models ability to reproduce the same response but this time with a distorted mesh is explored. In both examples, the model domain is 740 m in length, extending from $-187.5 \leq x \leq 187.5$ m with a depth of 15 m. In the centre of the domain a series of six bed waves with a wavelength of 50 m and an amplitude of 0.15 m are present and to either side a flat bed region of 35 m exists. The horizontal grid spacing was 2.5 m, which is 20 nodes per wavelength, and the vertical grid spacing was 0.5 m, which amounts to 31 nodes in each vertical. A time step of 2 s was used. The initial conditions are of a linear density profile throughout the domain with a density difference over the vertical of 10 kg m^{-3} . The same linear density profile was also specified at the open boundaries during the simulation. A constant vertically uniform velocity was specified on either side of the flow domain. The kinematic viscosity ν and diffusivity κ are both set to zero. In order to minimise boundary reflections, a flow relaxation scheme was used at the open boundaries. In these runs the flow relaxation zone was 12.5 m wide. Run B was identical to Run A except that a distorted finite element mesh was used, [Fig. 3](#). It is clear that many of the triangles are far from equilateral in this case.

[Fig. 4](#) shows the theoretical and computed vertical velocity for a range of successive stationary wave modes. Shown is a 100 m section in the middle of the domain. While the model results are in good agreement with the theoretical solutions of the Taylor–Goldstein equation, the model response shows a somewhat smaller horizontal phase shift and slightly larger amplitudes that is worse for higher wave modes. The same figure shows the effect of a highly distorted mesh. The higher modes are poorly resolved but the mode 1 response is still reasonable.

In order to investigate the skewness in the phase shift of the computed solutions, the theoretical solutions with an amount of upwind diffusion equivalent to that in the SUPG scheme using [Eqs. \(2.9\) and \(2.10\)](#), which for background velocities of 0.40 m/s, 0.15 m/s and 0.085 m/s amounts to about $0.16 \text{ m}^2/\text{s}$, $0.062 \text{ m}^2/\text{s}$ and $0.035 \text{ m}^2/\text{s}$ respectively, are also included in [Fig. 4](#). The numerical diffusion associated with the upwind scheme appears to be the cause of the differences at higher mode numbers. However, we are primarily interested in resolving low mode internal waves and the model gives good agreement in this case.

4.2. *Internal lee waves*

[Fig. 5](#) shows the results from the internal lee wave simulation. This test case is compared against linear wave theory as well as against laboratory data. The laboratory data and the theory are described in [Kranenburg and Pietrzak \(1989\)](#). The experiments were designed to study near critical internal lee waves generated by the flow of a turbulent two layer fluid over a topographic feature. A two layer stationary flow was set up in the 130 m long Delft Hydraulics tidal flume. The working section of the flume used in these experiments was 64 m long and 1 m wide and 0.4 m

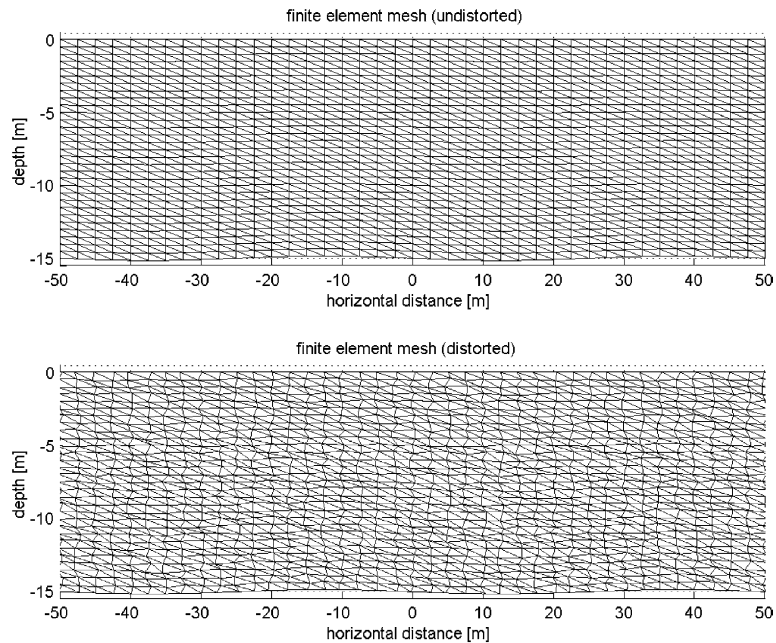


Fig. 3. The finite element meshes used in Run A (above) and Run B (below). Note the distorted mesh used in Run B.

deep. Layer Reynolds numbers of 20,000 were used. The fixed obstacle had a height of 4 cm or 1/10 the total water depth. Small amplitude topography was selected so that internal lee waves could be studied. Large scale topography typically leads to the formation of internal hydraulic jumps and generally leads to significant upstream influence, see [Baines \(1995\)](#) and references therein. A density difference of 25 kg m^{-3} was used. Density profiles were recorded 1 m upstream of the topography.

Here we focus on the numerical simulations along the axis of the tidal flume. The numerical model domain was 6 m long, the topography had a half sinusoidal shape of length 20 cm and height 4 cm. The topography was located 1.0 m downstream of the inflow boundary. A two layer flow was specified with layer depths of 16 cm in the upper layer and 24 cm in the lower layer, a constant discharge in each layer of $0.0245 \text{ m}^3 \text{ s}^{-1}$, as in agreement with Test 1 of the laboratory experiments, see [Kranenburg and Pietrzak \(1989\)](#) for details. The kinematic viscosity and diffusivity in the (inviscid) simulations were both zero. Three hundred grid cells (triangles) were used in the horizontal direction and 30 grid cells in the vertical. A time step of 0.05 s was used. In order to make the comparison with the two layer theory the velocity and density were uniform within each layer. The model was initialised with a two-layer system as described and constant discharges were specified at the upstream boundary. The flow relaxation zones were not necessary in these lee wave simulations.

The internal Froude number (F) for this test case was 0.9. In the laboratory test cases it was found that the flow was steady for a Froude number of 0.9. However for higher Froude numbers the flow became more unsteady and eventually formed a hydraulic jump as critical conditions were approached. The theory only applied to steady flow, so we take $F = 0.9$. In order to have

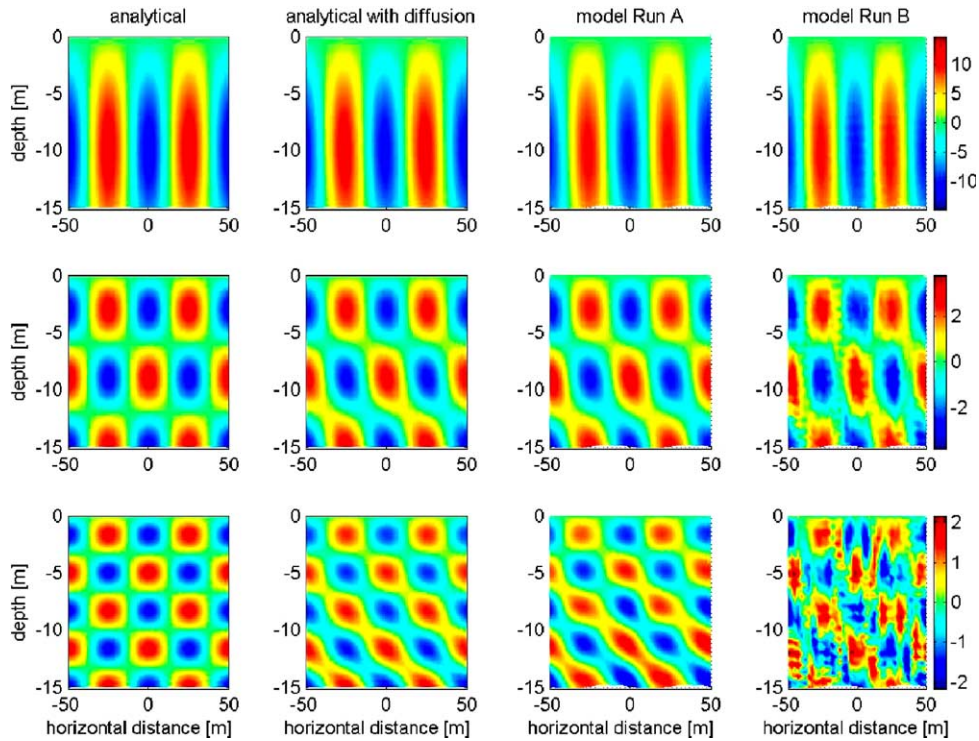


Fig. 4. From top to bottom trapped internal wave modes 1, 3 and 5. Shown are vertical velocities calculated from the analytical solution (left), the analytical solution including an equivalent amount of horizontal diffusion due to upwinding (middle left), and from the numerical solutions Run A (middle right) and Run B (right); and background velocities of $u_0 = 0.40, 0.15$ and 0.085 ms^{-1} . The scale of the vertical velocities is given in mms^{-1} .

a similar model configuration the domain was setup as described above. The simulations were carried out for 5 min, at which time the flow was stationary. Transients from the start up of the simulation had died out.

Fig. 5 shows the mode 1 internal lee wave response. The internal Froude number in this test case is 0.9. A lee wave train is seen downstream from the topography with a wavelength of 1.25 m. The lee wave has an amplitude of 2 cm which is half the amplitude of the bed topography. Downstream the lee wave is seen to decay. Fig. 6 shows the results from the model simulation, as well as from inviscid Boussinesq theory. For this test case, referred to as Test 1 in Kranenburg and Pietrzak (1989), the amplitude of the internal lee wave was 0.2 cm and the wavelength was about 1.25 m. It is seen that the amplitude just downstream of the topography is about 0.2 cm and the wavelength is of the order 1.25 m. The model appears to reproduce the main features of the internal lee wave response. Fig. 6 shows analytical two layer internal wave solutions and FINEL3D model results. Shown is a comparison of the model results against Boussinesq theory, using an effective obstacle length of $L = 34 \text{ cm}$. This calculation uses the flow separation length as observed in the laboratory data. If instead we compare the model results to the Boussinesq theory and use the actual obstacle length of $L = 20 \text{ cm}$ the analytical theory under predicts the amplitude of the internal lee wave. This result was also found in the laboratory data, where it was found that the

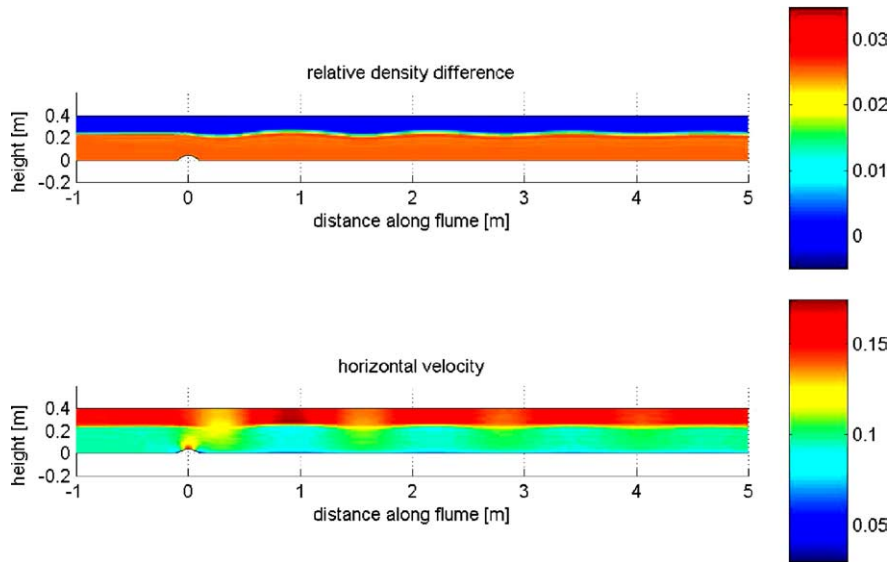


Fig. 5. Simulated internal lee wave train downstream of small amplitude half sinusoidal topography. The axes are relative density (above) and horizontal velocity (below) in units of m s^{-1} .

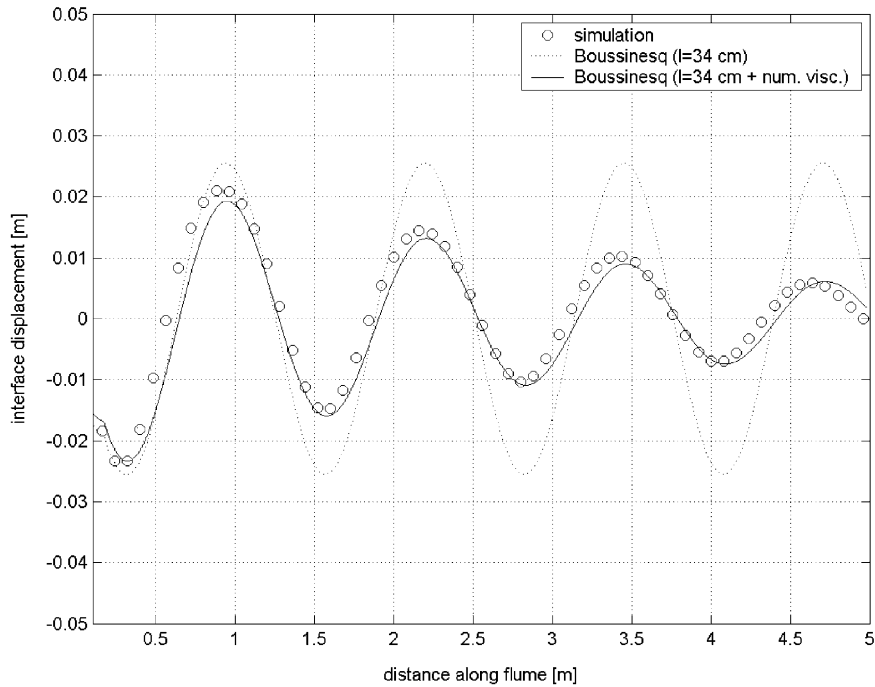


Fig. 6. Analytical two layer internal wave solutions and FINEL3D model results. Shown is a comparison of the model results against Boussinesq theory, using an effective obstacle length of $L = 34\text{ cm}$. This calculation uses the flow separation length as observed in the laboratory data. In addition a theoretical curve is included which also accounts for the numerical diffusion.

flow separation region needed to be accounted for to get good agreement with theory. In addition a theoretical curve is included which also accounts for the numerical diffusion, which in this simulation had a magnitude of $8 \times 10^{-4} \text{ m}^2/\text{s}$. Good agreement is found between the model and theory if the numerical diffusion is accounted for.

5. Conclusions

In this paper the new model FINEL3D has been presented. The model is a non-hydrostatic, finite element, fully 3D unstructured flow model. In recent years a number of numerical models have been developed to simulate non-hydrostatic coastal and ocean flows. The model presented here is to our knowledge unique in that it is a non-hydrostatic fully three dimensional finite element model in which no approximations were made to the non-hydrostatic equations. One of the main reasons for adopting this solution strategy was that the model was originally developed for complex stratified flows both through and around small scale engineering structures. Here grid flexibility and the ability of the grid to adapt to complex boundaries is extremely important. However, this is also true for many estuarine and coastal flow fields. Therefore the model is currently being developed and tested to ensure that it can accurately simulate stratified flows in estuaries and coastal seas. Because the model employs a fully 3D unstructured grid, the model employs linear finite elements. This simplifies the solution procedure and helps to reduce the computational cost.

The model has been shown to simulate internal waves. A number of numerical tests were performed for which the theoretical solutions are known from either the Taylor–Goldstein equation or from two layer Boussinesq theory. The model was shown to reproduce the Mode 1–3 trapped internal waves with a high level of accuracy. Phase errors became apparent at higher wave modes. These were shown to be due to numerical diffusion associated with the use of the SUPG scheme. The model was also found to reproduce the two layer internal lee wave response. Accurate results were obtained if the flow separation distance was included in the analytical solution. The original comparison between the laboratory data and the Boussinesq theory also concluded that an effective obstacle length accounting for the flow separation region, had to be used in order to get good agreement between the laboratory solution and the theoretical solution. It is encouraging that the FINEL3D simulation also demonstrated the same behaviour.

However, it was also shown that the SUPG scheme introduces numerical diffusion into the numerical simulations. If diffusion equal in magnitude to that of the numerical scheme is added to the theoretical linear trapped wave solutions and the lee wave solutions, then the internal wave response is shown to agree well with theory. Consistent use of the SUPG scheme would not necessarily introduce these errors as the stabilization is then applied to all terms of the momentum equation. In this case however only the advection terms were stabilized as the consistent approach did not result in a stationary internal wave response. This is the subject of future investigations. Current research also addresses the use of alternative linear elements with lower diffusion. Nevertheless, discrepancies resulting from the first order discretisation of the advective terms are considered small. FINEL3D has been shown to be suitable for modelling non-hydrostatic stratified flows as typically occur in estuaries and coastal seas. In particular the flow of a stratified fluid over small scale topographic features in an estuary may generate trapped internal

waves and internal lee waves. FINEL3D was found to accurately reproduce these types of internal waves.

Acknowledgments

FINEL3D was developed by the first author while at Svašek Hydraulics and has been further developed through funding from Delft University of Technology. We thank Svašek Hydraulics for allowing us to use the model.

References

- Baines, P.G., 1995. *Topographic Effects in Stratified Flows*. Cambridge University Press, p. 482.
- Casulli, V., 1999. A semi-implicit finite difference method for non-hydrostatic, free-surface flows. *International Journal for Numerical Methods in Fluids* 30, 425–440.
- Casulli, V., Stelling, G.S., 1998. Numerical simulation of 3D quasi-hydrostatic, free-surface flows. *Journal of Hydraulic Engineering* 124, 678–686.
- Casulli, V., Walters, R., 2000. An unstructured grid three dimensional model based on the shallow water equations. *International Journal for Numerical Methods in Fluids* 32, 331–348.
- Casulli, V., Zanolli, P., 2002. Semi-implicit numerical modelling of nonhydrostatic free-surface flows for environmental problems. *Mathematical and Computer Modelling* 36, 1131–1149.
- Danilov, S., Kivman, G., Schröter, J., 2004. A finite element ocean model: principles and evaluation. *Ocean Modelling* 6, 125–150.
- Gunzburger, M.D., 1989. *Finite Element Methods for Viscous Incompressible Flows*. Boston Academic Press.
- Heinrich, J.C., Pepper, D.W., 1999. *Intermediate Finite Element Method—Fluid Flow and Heat Transfer Applications*. Hamilton Printing Co.
- Hodges, B.R., Street, R.L., 1999. On simulation of turbulent nonlinear free-surface flows. *Journal of Computational Physics* 151, 425–457.
- Hughes, T.J.R., 1987. Recent progress in the development and understanding of SUPG methods with special reference to the compressible Euler and Navier–Stokes equations. *International Journal for Numerical Methods in Fluids* 7, 1261–1275.
- Iskandarani, M., Haidvogel, D.B., Levin, J.C., 2003. A three dimensional spectral element model for the solution of the hydrostatic primitive equations. *Journal of Computational Physics* 186, 397–425.
- Johnson, C., 1990. *Numerical Solution of Partial Differential Equations by the Finite Element Method*. Cambridge University Press.
- Kanarska, Y.V., Maderich, V.S., 2002. Non-hydrostatic model for stratified flows with free-surface. *Applied Hydromechanics* 4 (76), 280–289.
- Kranenburg, C., Pietrzak, J.D., 1989. Internal lee waves in turbulent two-layer flow. *Journal of Hydraulic Engineering, ASCE* 115, 1352–1370.
- Kranenburg, C., Pietrzak, J.D., Abraham, G., 1991. Trapped internal waves over undular topography. *Journal of Fluid Mechanics* 226, 205–217.
- Long, R.R., 1953. Some aspects of the flow of stratified fluids. I. A theoretical investigation. *Tellus* 5, 1–42.
- Lynch, D.R., Ip, J.T.C., Namie, C.E., Werner, F.E., 1996. Comprehensive coastal circulation model with application to the Gulf of Maine. *Continental Shelf Research* 16 (7), 875–906.
- Marshall, J., Adcroft, A., Hill, C., Perelman, L., Heisey, C., 1997. A finite-volume, incompressible Navier–Stokes model for studies of the ocean on parallel computers. *Journal of Geophysical Research* 102, 5753–5766.
- Pelletier, D., Fortin, A., Camarero, 1989. Are FEM solutions of incompressible flows really incompressible? (or how simple flows can cause headaches!). *International Journal for Numerical Methods in Fluids* 9, 99–112.

- Pietrzak, J.D., Kranenburg, C., Abraham, G., 1990. Resonant internal waves in fluid flow. *Nature* 344, 844–847.
- Pietrzak, J.D., Kranenburg, C., Abraham, G., Kranenburg, B., van der Wekken, A., 1991. Internal wave activity in Rotterdam Waterway. *Journal of Hydraulic Engineering, ASCE* 117, 738–757.
- Pietrzak, J.D., Jakobsen, J., Burchard, H., Vested, H.J., Petersen, O., 2001. A three-dimensional hydrostatic model for coastal and ocean modelling using a generalised topography following co-ordinate system. *Ocean Modelling* 4, 173–205.
- Pietrzak, J., Labeur, R.J., 2004. Trapped internal waves over undular topography in a partially mixed estuary. *Ocean Dynamics* 54, 315–323.
- Rodi, W., 1984. *Turbulence Models and their Application in Hydraulics*. IAHR, Delft.
- Simo, J.C., Armero, F., Taylor, C.A., 1995. Stable and time-dissipative finite element methods for the incompressible Navier–Stokes equations in advection dominated flows. *International Journal for Numerical Methods in Engineering* 38, 1475–1506.
- Stansby, P.K., Zhou, J.G., 1998. Shallow-water solver with non-hydrostatic pressure: 2D vertical plane problems. *International Journal for Numerical Methods in Fluids* 28, 541–563.
- Stelling, G.S., Busnelli, M.M., 2001. Numerical simulation of the vertical structure of discontinuous flows. *International Journal for Numerical Methods in Fluids* 37, 23–43.
- Stelling, G.S., Zijlema, M., 2003. An accurate and efficient finite difference algorithm for non-hydrostatic free-surface flow with application to wave propagation. *International Journal for Numerical Methods in Fluids* 43, 1–23.
- Svašek, b.v., 2001. Hydraulic Research Beerkanaal phase 1—step I.2, technical report 01311/1166 (in Dutch).
- van der Vorst, H.A., 1992. Bi-CGSTAB: a fast and smoothly converging variant of Bi-CG for the solution of nonsymmetric linear systems. *SIAM Journal on Scientific and Statistical Computing* 13 (2), 631–644.
- van der Ploeg, A., 1994. Preconditioning for sparse matrices with applications. Ph.D. thesis, Rijksuniversiteit Groningen.
- Zhang, J., Baptista, A., in press. A cross-scale model for 3D baroclinic circulation in estuary-plum-shelf systems: I. Formulation and skill assessment. *Continental Shelf Research*.



A diagnostic study of interpentadal variability in the North Atlantic Ocean using a finite element model

Paul G. Myers^{a,*}, Steve Grey^b, Keith Haines^b

^a *Department of Earth and Atmospheric Sciences, University of Alberta, Edmonton, Alberta, Canada T6G 2E3*

^b *Environmental Systems Science Centre, Reading University, 3 Earley Gate Reading RG6 6AL, UK*

Received 12 February 2003; received in revised form 29 March 2004; accepted 15 July 2004

Available online 10 November 2004

Abstract

Previous work has shown that major changes to the thermohaline structure of the North Atlantic occurred between the pentads 1955–1959 and 1970–1974 and that these changes led to significant changes in the transport of the Gulf Stream system. Here we expand on these results by examining the changes in North Atlantic transports for the entire period 1950–1994. Based on temperature and salinity data from the Lozier climatology, and the deviations from this during different periods since 1950, the thermohaline densities are reconstructed. The circulations associated with these different periods are then derived using a diagnostic finite element model. The results show significant decadal variability in transports in both the sub-tropical and sub-polar gyres.

© 2004 Elsevier Ltd. All rights reserved.

1. Introduction

Modelling of the ocean and the climate system has now been going on for a number of decades. The ocean models that are presently used in most modeling studies are largely based on traditional finite-difference (FD) techniques. Although possessing advantages in terms of simplicity and ease of use, these techniques often have difficulty in resolving land boundaries, straits and

* Corresponding author. Tel.: +1 780 492 6706; fax: +1 780 492 2030.

E-mail addresses: pmyers@ualberta.ca (P.G. Myers), kh@mail.nerc-essc.ac.uk (K. Haines).

narrow active regions such as boundary currents. The nature of the differencing can also lead to difficulties near the poles.

An alternative numerical technique is the finite element (FE) method, which has recently attracted increasing interest from the oceanographic community (e.g. [Le Provost, 1986](#); [Myers and Weaver, 1995](#)). The piecewise nature of the FE approach means that it can provide much more flexible representations of irregular real world coastlines than traditional FD grids. This piecewise formulation also means that grid refinement in regions of interest can be simply done without loss of accuracy. This allows for western boundary currents, the shelf break, narrow straits, etc. to be properly resolved with the necessary resolution, without requiring unnecessarily high resolution everywhere in the domain. Other advantages include a natural treatment of boundary conditions and avoidance of some high latitude/pole problems.

The FE method has been widely used in tidal and coastal modelling applications. Coastal uses range from barotropic studies of tidal residual currents (e.g. [Foreman et al., 1993](#)) to the 3-dimensional prognostic advanced-turbulence model QUODDY ([Lynch et al., 1992](#); [Lynch et al., 1996](#)) used, for example, to study the Gulf of Maine and the Scotian Shelf (e.g. [Hannah et al., 2001](#)). Regional or global scale applications have been less common, ranging from the global tidal model of [Le Provost et al. \(1995\)](#) to basin scale diagnostic calculations ([Iskandarani et al., 1993](#); [Myers et al., 1996](#); [Myers and Weaver, 1997](#); [Greenberg et al., 1998](#)).

The interest in this method has picked up significantly over the last few years, as can be seen with the successes of a number of new models in this field ([SEOM-Iskandarani et al., 2003](#); [FEOM-Danilov et al., in press](#)), and as highlighted in this special issue. One promising area for applications of this method is the Canadian Arctic archipelago, where the unstructured nature of finite element meshes is potentially ideal for the narrow and complex geometries of that region. [Kliem and Greenberg \(2003\)](#) used a diagnostic finite element model to examine the circulation in the Arctic archipelago.

One of the main aims of the World Ocean Circulation Experiment (WOCE) was to collect a global data set. Although the number of direct current measurements is still limited, a large number of measurements exist for temperature and salinity and hence density. From the density field and its gradients, a number of techniques exist to determine the velocity, or volume transport fields.

Simple diagnostic models have been used for a number of years to help us understand the ocean's circulation. Estimates of wind-driven transport by integrating characteristics (along lines of constant f/H) have been performed using observed wind fields (e.g. [Welander, 1959](#); [Godfrey, 1989](#)). Including the effects of stratification through the Joint Effect of Baroclinicity and Relief (JEBAR), [Mellor et al. \(1982\)](#) and [Greatbatch et al. \(1991\)](#) examined the mean climatological state of the circulation in the Atlantic Ocean. Using a more refined finite element model, [Myers et al. \(1996\)](#) found very good correspondence between model diagnosed and observed transports in the North Atlantic, and in the North Pacific ([Myers and Weaver, 1997](#)). They ([Myers et al., 1996](#)) also found that the presence of the JEBAR term was crucial in developing realistic circulations in diagnostic models.

[Levitus \(1989a,b,c, 1990\)](#) showed that the thermohaline structure of the North Atlantic underwent significant changes between 1955–1959 and 1970–1974. Using the density fields from these pentads, [Greatbatch et al. \(1991\)](#) showed that these changes were associated with large scale changes in the transport of the Gulf Stream, with much larger transports in 1955–1959 than

1970–1974. Grey et al. (2000) used XBT data to study the thermocline structure in all pentads from 1950 and inferred that circulation changes in the sub-tropical gyre played a major role in the variability. Curry and McCartney (2001) derived a transport index for the North Atlantic, representing the upper 2000-db eastward baroclinic mass transport between the sub-polar and sub-tropical gyres and noted a gradual weakening during the low NAO period of the 1960s and then an intensification over the next 25 years of a persistently high NAO. Here we first use the data of Grey et al. (1999) to investigate the circulation changes that have occurred since 1950 and show that changes in the diagnosed volume transport for the sub-tropical and sub-polar gyres show similar variability to the thermohaline structure. We then extend the study to consider all 5 year running pentads between 1945 and 1996, based upon temperature anomaly data contained in the World Ocean Atlas 1998 (WOA98), finding similar thermohaline variability.

2. Finite element model

The diagnostic model used in this paper is based upon the work of Myers and Weaver (1995). Although simple compared to the many newly developed state-of-the-art finite element models (as described in this volume), and using basic numerical techniques, the model is still a very good tool for diagnostic studies of ocean transport. The diagnostic model solves the vertically integrated, steady-state, linearized barotropic vorticity equation in spherical co-ordinates, with the higher order metric terms dropped. Note that although the model equation is linear, non-linear effects will be implicitly included through the observed density fields.

These density effects are brought in through the JEBAR term. The importance of this term was shown in the pioneering studies of Sarkisyan and Ivanov (1971) and Holland and Hirschman (1972). This term represents a correction to the topographic steering term in the vorticity equation. Through pressure gradients (set up by the density field), it provides a significant term in the calculation of oceanic transports in diagnostic models (Mertz and Wright, 1992).

A more detailed description of the model, including the complete form of the barotropic vorticity equation used is given in Myers and Weaver (1995). The same FE grid as from that previous study is also used. Although that grid contains excess resolution in areas where it is not needed, a decision was made to use the same grid as in Myers et al. (1996) to facilitate comparisons with that earlier work.

3. Climatological data

Lozier et al. (1995) is an annual mean climatology of the North Atlantic, based on 143,879 hydro-graphic stations. Temperature and salinity are recorded on a $1^\circ \times 1^\circ$ resolution grid, and depth levels with maximum thickness of 100m. The original data set had large gaps where station data were sparse and the averaging was not sufficient to overcome natural variability, giving the data set a noise-like appearance as it attempts to resolve the mesoscale signal.

These difficulties of missing data and noise had to be resolved before the hydrography could be used. Each missing point is given the mean value of temperature and salinity of the immediate surrounding points on an isopycnal plane (following Lozier et al., 1995) if there are five or more

good data points. If there are less than five valid surrounding points then the missing point is left blank. This procedure is repeated several times until no more can be filled. When this happens and there are still some obviously missing grid-points, the interpolation method is passed over once with a limit of four surrounding points contributing to filling in a point. Further five point average passes are then performed.

The TS properties and the depth of each isopycnal were smoothed on isopycnal surfaces using a small scale, $3^\circ \times 3^\circ$, boxcar filter. The depth filtering helps to produce smoother fields and can be done independently of TS filtering without distorting those properties. A second pass only filters the depth of the isopycnal surfaces without further smoothing of the TS properties. The resulting fields are then converted back to depth surfaces. The end product is smooth in appearance but because the smoothing is much smaller scale than that used by Levitus, the large gradients are preserved better and small features are not lost. Henceforth we will refer to this climatology as the Gridded Lozier Climatology, which is complete and regularly gridded. Figures comparing temperature and salinity fields between the Gridded Lozier climatology, the original Lozier et al. (1995) and the Levitus climatology (1982) can be found in Grey et al. (1999).

One of the main differences between this climatology and that of Levitus (1982) is the scale that they have been smoothed over. Levitus (1982) chose an influence radius based on the amount of smoothing required for remote, poorly observed regions, such as the southern ocean. The resulting smallest influence radius of 771 km therefore produces significant smoothing in regions with abundant observations and large property gradients. Lozier et al. (1995) examined the North Atlantic with its higher density of observations and thus were able to smooth on much smaller scales, only averaging data within a one-degree square around a grid-point. The gridded data were then smoothed but nowhere on a scale greater than 3 degrees. Furthermore, all processing was performed on potential density surfaces. The resultant climatology thus has improved resolution of small scale features and preserves steep gradients.

These differences in the density field will lead to different calculated transports based on the JEBAR relation. The calculation of the Levitus (1982) climatology has been performed previously and was described by Myers et al. (1996). The transports based on the isopycnal data are given in Fig. 1. Both climatologies reproduce the observed overall structure of the North Atlantic circulation but some interesting differences exist.

The Gulf Stream and Gulf Stream Extension are tighter in the Gridded Lozier experiments, with the maximum transport spread out over a band of only $2\text{--}3^\circ$. This is a direct consequence of the smaller smoothing scales used in the Gridded Lozier climatology. Larger transports are found in the cyclonic recirculation gyres in the mid-Atlantic Bight, similar to the $\sim 40\text{Sv}$ in the western gyre suggested by Johns et al. (1995). There is a stronger and more distinct jet penetrating well into the Atlantic, until 45°W , with transports of between 80 and 100Sv (compared with Levitus $60\text{--}70\text{Sv}$) at 55°W . At this longitude, Richardson (1985) suggests 93Sv , while Hogg (1992) gives a maximum total of 147Sv , although suggesting the possibility of lower results. This is consistent with the findings of Lozier et al. (1995) and Grey et al., 1999 who describe a better representation of the Gulf Stream front and other such features in the isopycnal climatology.

In the Lozier based transport figure, there is a low in the southern Labrador Sea, near 52°N and 45°W . Associated with this is an anticyclonic countercurrent flowing north into the Labrador Sea. This low and the countercurrent have been seen in both the recent observational float studies of Lavender et al. (2000) and the modelling studies of Kase et al. (2001) and Myers (2002).

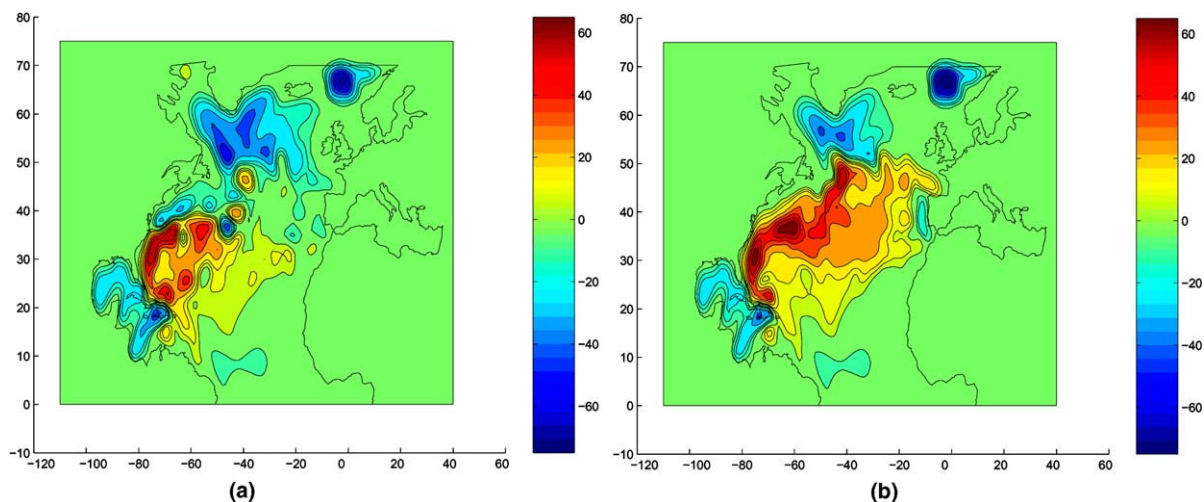


Fig. 1. Diagnosed transports calculated using the FE model, with the JEBAR term calculated using the density data from the: (a) the Gridded Lozier climatology; (b) the Levitus 1994 Atlas. Values are given in Sv and the difference in magnitude between any two locations indicates the transport between those points.

The same calculation was also ran using the data from the Levitus 94 Atlas (Fig. 2b). The transports in the sub-polar gyre are very similar to that from the older Levitus (1982) data, but the differences are surprisingly large in the sub-tropical gyre. The Gulf Stream transport is significantly weaker (60 Sv), with the jet being significantly broader. The separation is also poorly represented here, with the cyclonic recirculation in the mid-Atlantic Bight nearly non-existent, consistent with previous work implying the importance of these gyres for Gulf Stream separation at Cape Hatteras. Chang and Chao (2000) compared the 1° World Ocean Atlas (WOA) with the Lozier et al. (1995) and noted artifacts in the WOA data, as well as serious weakening of fronts from the large smoothing scale used.

4.1. Constructing the pentadal hydrography

The climatological hydrography, with information on temperature and salinity can be used to produce ocean currents and transports. However, the climatology represents a mean state of the ocean based on irregular and non-uniform measurements taken throughout the century. Sub-surface observations of temperature and salinity, both of which are needed to calculate density fields and hence transports, such as CTD casts and Nansen bottles are sparse so compilation of hydrographies to represent shorter time periods is more difficult.

Expendable bathythermograph observations, particularly in the North Atlantic, are much more widespread but only give information on subsurface temperatures and only in the upper water column. The method used here combines the comprehensive data of the climatological hydrography with pentads of XBTs to produce complete pentadal hydrographies based on thermocline and halocline displacements. Climatological temperature-salinity relationships are retained, consistent with previous research on interdecadal variability (Levitus, 1989a; Reverdin et al., 1997).

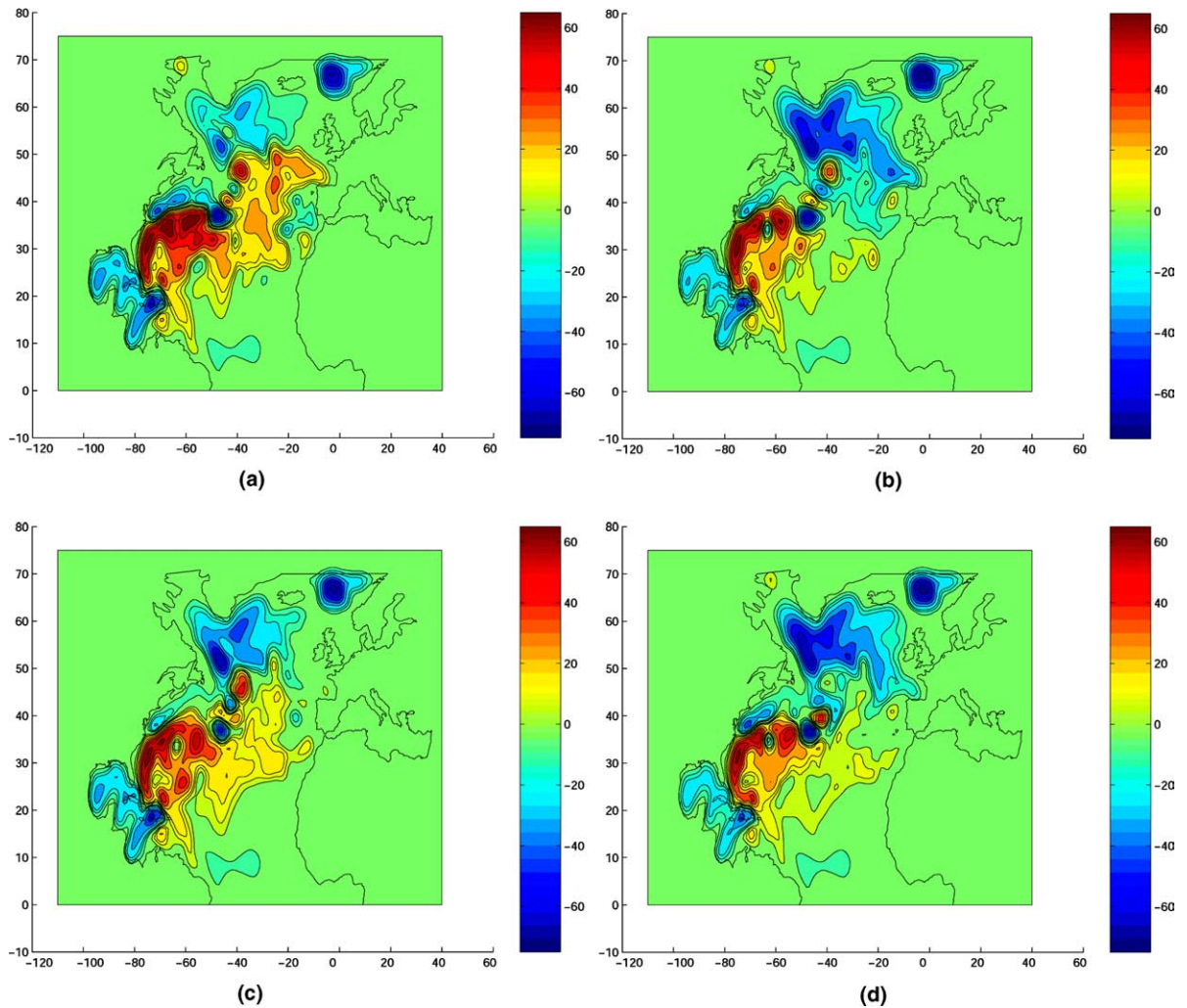


Fig. 2. Transport Streamfunctions (in Sv) for the pentad: (a) 1960–1964; (b) 1970–1974; (c) 1980–1984 and (d) 1990–1994. Calculations performed using the diagnostic finite element model, with climatological winds and the density fields associated with each pentad.

The Gridded Lozier climatology for the pentads is based on vertical displacement to fit with XBT profiles. For each XBT, the nearest temperature profile from the climatology is vertically displaced until the sum mean-square temperature anomalies at all depths are minimized. The displacements required to match all XBTs in the pentad are recorded and then mapped to produce a field of mean displacements. The temperature and salinity profiles of the Gridded Lozier climatology are then displaced according to this field to produce the new hydrographic estimate of the North Atlantic for the pentadal period. The thermocline displacements are consistent with the thermal anomalies at ~ 400 m (Grey et al., 2000). Assimilation studies (Troccoli and Haines, 1999; Troccoli et al., 2002) suggest that a vertical displacement to match the XBT profiles is a bet-

ter solution than grafting on a shallow hydro-graphic observation onto a deep climatology. Numerical models have been shown to respond better to this approach (Troccoli et al., 2002).

4.2. Pentadal circulation and transports

Here we extend the transport analysis of Greatbatch et al. (1991) to each pentad from 1950–1954 to 1990–1994. We use the vertically displaced fields to provide pentadal density data. We use the same climatological winds (Hellerman and Rosenstein, 1983) for all pentads, as Myers et al. (1996) showed that the main transports in the diagnostic model are predominantly produced through the JEBAR term (the effect of the winds show up implicitly in the density data used).

The diagnosed barotropic transports for selected pentads are shown in Fig. 2. The transports in all periods, but especially the early ones (e.g. 1950s), are very noisy, with some potentially unrealistically large transports associated with eddy like features. In the later periods, with more data available, the structures become smoother. However, in all cases, there are still a number of ‘eddies’ and bullseye type features, probably associated with the lifting or lowering of the density fields in localized regions, which are probably not realistic. However, there are also large scale features which are consistent in appearance and whose changes can be realistically examined.

In both the sub-tropical and sub-polar gyres, there are significant changes in the transports over time. For the Gulf Stream near Gape Hatteras, high transports are to be found in 1950–1954 and 1960–1964 while below average transports are seen in 1955–1959 and 1965–1969. The transports are close to the climatological average (Fig. 1a) for 1970–1984, while higher transports are again seen in 1985–1989 and 1990–1994. Changes to the shape of the sub-tropical gyre and the tightness of the recirculations are also present. Strong variability is seen in the eddy train downstream from the Gulf Stream separation, including the Mann Eddy off Flemish Cap. In some pentads (1955–1959 and 1990–1994), the eddy has almost disappeared.

Greater sensitivity to temporal change than for the actual Gulf Stream can be seen in the cyclonic recirculation gyres in the mid-Atlantic Bight. From the late 1960s through to the late 1970s (and potentially the early 1980s), transports are low (20 Sv maximum) and the gyres are very constrained spatially, for the most part isolated from the main cyclonic sub-polar gyre. At other times, the transport increases and the gyres are directly connected with a down-shelf branch of the Labrador Current.

In general, this connection between the slope water gyres and the Labrador Current occurs in pentads with strong Labrador Current transport (early 1950s, and the 1980s and 1990s). The Labrador Current is also strong in the mid-1970s, a time when the slope water gyre is weaker. There is an out of phase relationship between the eastern parts of the sub-tropical and sub-polar gyres, with the edge of the sub-polar gyre reaching farther east and south when the sub-tropical gyre’s eastern penetration is curtailed.

The results are suggestive of the commonly held hypothesis that North Atlantic transports vary with the NAO. Largest sub-tropical gyre transports are found during and after the warm phases of the NAO, while low transports are associated with persistent cold phases. Table 1 shows the net transport from the core of the Labrador Sea to the central Sargasso Sea, for each pentad (similar to the Curry and McCartney, 2001, diagnostic), showing this variability.

The total transports from Table 1 for the 1990–1994 period were the largest of any we calculated, although large transports are also indicated from 1980 onwards. The very strong transports,

Table 1

Transport for each pentad (and the climatologies) across the North Atlantic Stream, in Sv, from the core of the Labrador Sea, to the central Sargasso Sea

Pentad	Transport (Sv)
1950–1954	119
1955–1959	67
1960–1964	72
1965–1969	99
1970–1974	93
1975–1979	96
1980–1984	118
1985–1989	115
1990–1994	123
Lozier climatology	102
Levitus climatology	83

which are also present upstream near the Gulf Stream separation, are consistent with the results of Grey et al. (2000), who suggest that these enhanced transports, especially in the sub-tropical gyre, increase the transport of warm near-surface waters northwards throughout the period. Further investigations are needed to identify any sequence of events which might indicate a cause for the observed changes.

One limitation of the above analysis is that the timing of the pentads was chosen to be each half decade (e.g. 1960–1964) and these do not necessarily catch any specific physical events (such as a high or low phase of the NAO). The World Ocean Atlas (NODC, 1998) provides temperature anomalies on a 1-degree grid for each 5 year running pentad from 1945–1949 up to 1992–1996, as well as climatological values of temperature and salinity. For each pentad, the pentadal temperature anomalies were added to the climatological temperature. Then, these modified temperature values, combined with the climatological salinity, were used to calculate densities. The calculated density was then used in the JEBAR relation and the diagnostic model was run for each of the overlapping pentads.

The pentadal transport plots for the pentads that match those in the previous analysis are consistent with, and as noisy as, those from the previous analysis. Rather than show transport plots from each pentad, we will focus on transport time series from a number of interesting locations in the North Atlantic: the Iceland Basin, the eastern/central Labrador Sea, along the path of the North Atlantic Current, within the recirculation gyres of the mid-Atlantic Bight and along the path of the separated Gulf Stream. Fig. 3 shows the locations of these points and the transport time series from each location. The time series for the Gulf Stream is shown separately from the other four as its scale overwhelms the transport variations at the other locations where the transports are smaller. Our diagnosed Gulf Stream transport varies between 60 and 150 Sv over the time period analyzed. Although some of the variability may be associated with meandering and other changes in the jet path, a clear quasi-decadal signal in strength also seems to be present. The same signal phase is also seen in the recirculation gyres to the north of the Gulf Stream, with diagnosed transports ranging from 5–30 Sv. Downstream, the North Atlantic Current transports also indicate significant transport variability (5–25 Sv), but other than in the 1950s, this variability

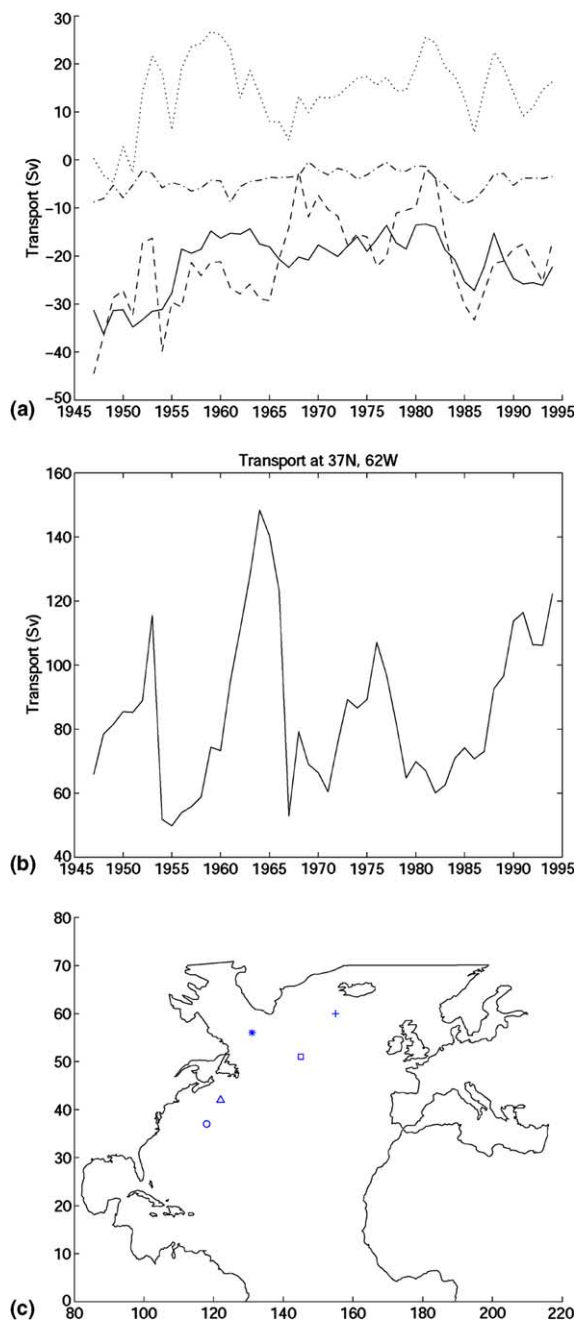


Fig. 3. Time series of Gulf Stream transport (Sv) at 37N, 62W for each 5 year running pentad between 1945 and 1996; (a) for the Iceland Basin at 60 N 25 W (dash dot line), the eastern/central Labrador Sea at 56N 49W (solid line), along the path of the North Atlantic Current at 51N 35W (dotted line) and within the recirculation gyres of the mid-Atlantic Bight at 42N 58W (dashed line); (b) Time series of transport (Sv) for the same 5 year running pentads as in; (c) Map of North Atlantic, indicating the location of five points where the diagnosed time series for each overlapping 5 year pentad between 1945 and 1996 are given; circle—Gulf Stream, triangle—recirculation gyres, square—North Atlantic Current, star—Labrador Sea and plus—Iceland Basin.

is not in phase with the Gulf Stream transports. Instead, it is much more in phase with the diagnosed transports in the eastern Labrador Sea, except in the 1950s when the North Atlantic Current transports are weak and the Labrador Sea transports are strong. The Labrador Sea transports are also high in the early 1990s.

5. Summary and discussion

A diagnostic finite element model is used to examine the transports in the North Atlantic Ocean. Although basic, the model is still able to accurately diagnose the large scale North Atlantic transport structure. Improved transport estimates and Gulf Stream structure are found when the Gridded Lozier isopycnal climatology is used for the density terms in the JEBAR relation. The isopycnal climatology also improves the diagnosed transport structure in the sub-polar gyre and leads to a representation of the recently discovered countercurrent structure in the Labrador Sea (Lavender et al., 2000).

To examine interdecadal variability, the large number of XBT observations available are used. For each pentad between 1950–1954 and 1990–1994 the climatology is modified based on a vertical displacement to fit XBT profiles. A mean displacement field for each time period is produced and then used to create new thermohaline density climatologies. These pentadal climatologies are then used to calculate the density gradients for the diagnostic model, leading to transport estimates for each pentad. To further this analysis, temperature anomaly data from the World Ocean Atlas were used for each 5 year running pentad between 1945 and 1996. Although the transport plots from the pentadal data are noisy due to localized changes in the density data, they still show clear signals in the behavior of the gyres and major currents over time.

Changes in the structure and magnitudes of the sub-tropical and sub-polar transports are found through the time period. Gulf Stream transports and especially the slope water recirculation gyres, are low through the late 1960s and 1970s and high in the 1950s and from the 1980s onwards. Strong transports in the slope water gyres are normally consistent with these circulation features being connected to (and in phase with) transport changes in the Labrador Current. Rossby and Benway (2000) showed that slow interannual variations in the path of the separated Gulf Stream may be governed by the outflow of waters from the Labrador Shelf region. Our study suggests that indeed the magnitude of the slope water recirculations is very sensitive to a potential connection with the Labrador Current and flow across the Newfoundland Shelf. Consistent with this idea, we also find that the path and northward extent of the Gulf Stream, in these diagnostic calculations, varies with the strength and horizontal extent of the slope water gyres. As an additional example of this, if we use the thermohaline densities from the 1994 World Ocean Atlas (Levitus and Boyer, 1994), which poorly represent the slope water gyres, to calculate the JEBAR term, we get a much more northern Gulf Stream path (with poor separation) and a truncated southern extent to the sub-polar gyre.

A large variability in the baroclinic transport between the sub-tropical and sub-polar gyres is found, of the order of ± 23 Sv. This is significantly larger than the $\pm 17\%$ variability found by Curry and McCartney (2001), and may be related to strong gradients and small scale features produced by the lifting and lowering used in constructing the pentadal densities. Such small scale features would be most prevalent when data is sparse, such as in the earlier period of our analysis. If we

examine only the pentads since 1965–1969, we find a smaller variability of $\pm 16\text{Sv}$, which is 15% of the mean for that period. Larger transport signals would also be expected here, since with the inclusion of the JEBAR term in our calculations, we are estimating more than just the flat-bottom Sverdrup relation. Despite the greater variance, the transports variations found here are in phase with the index of [Curry and McCartney \(2001\)](#), which is in turn related to the NAO index (at a lag), although without a direct high correlation.

Acknowledgments

PGM would like to thank Megan Vickerd and Shoshana Goldstein for their assistance with the transport calculations and plotting. The authors would also like to thank the two anonymous reviewers for their comments that helped improve the manuscript. This work was funded by NSERC and CFCAS grants awarded to PGM. This work was also supported by a Natural Environmental Research Council Studentship GT4/94/335/P and a WOCE Grant from the Southampton Oceanography Centre, awarded to SG.

References

- Chang, C.J., Chao, Y., 2000. A comparison between the World Ocean Atlas and Hydrobase climatology. *Geophysical Research Letters* 27, 1191–1194.
- Curry, R.G., McCartney, M.S., 2001. Ocean gyre circulation changes associated with the North Atlantic Oscillation. *Journal of Physical Oceanography* 31, 3374–3400.
- Danilov, S., Kivman, G., Schroter, J., in press. A finite element ocean model: principles and evaluation. *Ocean Modelling*.
- Foreman, M.G.G., Henry, R.F., Walters, R.A., Ballantyne, V.A., 1993. A finite element model for tides and resonance along the north coast of British Columbia. *Journal of Geophysical Research* 98, 2509–2531.
- Godfrey, J.S., 1989. A Sverdrup model of the depth-integrated flow for the world ocean allowing for island circulations. *Geophysical and Astrophysical Fluid Dynamics* 45, 89–112.
- Greatbatch, R.J., Fanning, A.F., Goulding, A.D., Levitus, S., 1991. A diagnosis of interpentadal circulation changes in the North Atlantic. *Journal of Geophysical Research* 96, 22009–22023.
- Greenberg, D., Werner, F., Lynch, D., 1998. A diagnostic finite-element ocean circulation model in spherical-polar coordinates. *Journal of Atmospheric and Oceanic Technology* 15, 942–958.
- Grey, S.M., Haines, K., Macdonald, A.M., 1999. Climatological hydrography of the North Atlantic. *International WOCE Newsletter* 36, 23–25.
- Grey, S., Haines, K., Troccoli, A., 2000. A study of temperature changes in the upper N. Atlantic 1950–94. *Journal of Climate* 13, 2697–2711.
- Hannah, C.G., Shore, J., Loder, J.W., Naimie, C.E., 2001. Seasonal circulation on the western and central Scotian Shelf. *Journal of Physical Oceanography* 31, 591–615.
- Hellerman, S., Rosenstein, M., 1983. Normal monthly wind stress over the world ocean with error estimates. *Journal of Physical Oceanography* 13, 1093–1104.
- Hogg, N.G., 1992. On the transport of the Gulf Stream between Cape Hatteras and the Grand Banks. *Deep Sea Research* 39, 1231–1246.
- Holland, W.R., Hirschman, A., 1972. A numerical calculation of the circulation in the North Atlantic Ocean. *Journal of Physical Oceanography* 2, 336–354.
- Iskandarani, M., Haidvogel, D.B., Boyd, J.P., 1993. A staggered spectral finite element model with application to the oceanic shallow water equations. *International Journal of Numerical Methods in Fluids* 20, 393–414.

- Iskandarani, M., Haidvogel, D.B., Levin, J., 2003. A three-dimensional spectral element model for the solution of the hydrostatic primitive equations. *Journal of Computational Physics* 186, 397–425.
- Johns, W.E., Shay, T.J., Bane, J.M., Watts, D.R., 1995. Gulf stream structure, transport and recirculation near 68° W. *Journal of Geophysical Research* 100, 817–838.
- Kase, R.H., Biastoch, A., Stammer, D.B., 2001. On the mid-depth circulation in the Labrador and Irminger Seas. *Geophysical Research Letters* 28, 3433–3436.
- Kliem, N., Greenberg, D.A., 2003. Diagnostic simulations of the summer circulation in the Canadian Arctic Archipelago. *Atmosphere-Ocean* 41, 273–289.
- Lavender, K.L., Davis, R.E., Owens, W.B., 2000. Mid-depth recirculation observed in the interior Labrador and Irminger seas by direct velocity measurements. *Nature* 407, 66–69.
- Le Provost, C., 1986. On the use of finite element methods for ocean modelling. In: O'Brien, J.J. (Ed.), *Advanced Physical Oceanographic Numerical Modelling*. D. Reidel Publishing Company, pp. 557–580.
- Le Provost, C., Genco, M., Lyard, F., 1995. Modeling and predicting tides over the world ocean. In: Lynch, D., Davies, A. (Eds.), *Quantitative Skill Assessment for Coastal Ocean Models*. Amer. Geophys. Union.
- Levitus, S., 1982. *Climatological Atlas of the World Ocean*. Tech. Rep. 13, U.S. Department of Commerce, National Oceanographic and Atmospheric Administration.
- Levitus, S., 1989a. Interpentadal variability of temperature and salinity at intermediate depths of the North Atlantic Ocean, 1970–1974 versus 1955–1959. *Journal of Geophysical Research* 94, 6091–6131.
- Levitus, S., 1989b. Interpentadal variability of temperature and salinity in the deep North Atlantic Ocean, 1970–1974 versus 1955–1959. *Journal of Geophysical Research* 94, 16125–16131.
- Levitus, S., 1989c. Interpentadal variability of temperature and salinity in the upper 150m of the North Atlantic Ocean, 1970–1974 versus 1955–1959. *Journal of Geophysical Research* 94, 9679–9685.
- Levitus, S., 1990. Interpentadal variability of steric sea level and geopotential thickness of the North Atlantic Ocean, 1970–1974 versus 1955–1959. *Journal of Geophysical Research* 95, 5233–5238.
- Levitus, S., Boyer, T.P., 1994. *World Ocean Atlas 1994. Temperature*, vol. 4. Tech. Rep. 4, U.S. Department of Commerce, National Oceanographic and Atmospheric Administration.
- Lozier, M.S., Owens, W.B., Curry, R.G., 1995. The climatology of the North Atlantic. *Progress in Oceanography* 36, 1–44.
- Lynch, D., Ip, J., Naimie, C., Werner, F., 1996. Comprehensive coastal circulation model with application to the Gulf of Maine. *Continental Shelf Research* 16, 875–906.
- Lynch, D., Werner, F., Greenberg, D., Loder, J., 1992. Diagnostic model for baroclinic and wind-driven circulation in shallow seas. *Continental Shelf Research* 12, 37–64.
- Mellor, G.L., Mechoso, C.R., Keto, E., 1982. A diagnostic calculation of the general circulation of the Atlantic Ocean. *Deep Sea Research* 29, 1171–1192.
- Mertz, G., Wright, D.G., 1992. Interpretations of the JEBAR term. *Journal of Physical Oceanography* 22, 301–305.
- Myers, P.G., 2002. SPOM: A regional model of the sub-polar North Atlantic. *Atmosphere-Ocean* 40, 445–463.
- Myers, P.G., Weaver, A.J., 1995. A diagnostic barotropic finite-element ocean circulation model. *Journal of Atmospheric and Oceanic Technology* 12, 511–526.
- Myers, P.G., Weaver, A.J., 1997. On the circulation of the North Pacific Ocean: Climatology, seasonal cycle and interpentadal variability. *Progress in Oceanography* 38, 1–49.
- Myers, P.G., Fanning, A.F., Weaver, A.J., 1996. JEBAR, bottom pressure torque and Gulf Stream separation. *Journal of Physical Oceanography* 26, 671–683.
- NODC, 1998. *World Ocean Atlas 1998*. Tech. Rep., NOAA, U.S. Department of Commerce.
- Reverdin, G., Cayan, D., Kushnir, Y., 1997. Decadal variability of hydrography in the upper northern North Atlantic in 1948–1990. *Journal of Geophysical Research* 10, 8505–8531.
- Richardson, P.L., 1985. Average velocity and transport of the Gulf Stream near 55°W. *Journal of Marine Research* 43, 83–111.
- Rosby, T., Benway, R.L., 2000. Slow variations in mean path of the Gulf Stream east of Cape Hatteras. *Geophysical Research Letters* 27, 117–120.

- Sarkisyan, A.S., Ivanov, V.F., 1971. Joint effect of baroclinicity and bottom relief as an important factor in the dynamics of sea currents. *Izvestiya Akademii Nauk Science USSR Atmospheric and Oceanic Physics (English Translation)* 7, 173–178.
- Troccoli, A., Balmaseda, M., Segschneider, J., Vialard, J., Andersen, D.L.T., Haines, K., Stockdale, T., Vitart, F., Fox, A.D., 2002. Salinity adjustments in the presence of temperature data assimilation. *Monthly Weather Review* 130, 89–102.
- Troccoli, A., Haines, K., 1999. Use of the temperature–salinity relation in a data assimilation context. *Journal of Atmospheric and Oceanic Technology* 16, 2011–2025.
- Welander, P., 1959. On the vertically integrated mass transport in the oceans. In: Bolin, B. (Ed.), *The Atmosphere and the Sea in Motion*. The Rockefeller Press and the Oxford University Press, pp. 95–101.



On some spurious mode issues in shallow-water models using a linear algebra approach

D.Y. Le Roux ^{a,*}, A. Sène ^b, V. Rostand ^a, E. Hanert ^c

^a *Département de Mathématiques et de Statistique, Université Laval, Québec, QC, Canada G1K 7P4*

^b *Département de Mathématiques Appliquées, Université Gaston Berger, UFR SAT, BP 234, Saint Louis, Senegal*

^c *Institut d'Astronomie et de Géophysique G. Lemaître, Université Catholique de Louvain, 2 Chemin du Cyclotron, B-1348 Louvain-la-Neuve, Belgium*

Received 10 December 2003; received in revised form 5 April 2004; accepted 1 July 2004

Available online 2 November 2004

Abstract

Numerical methods that are usually employed in ocean modelling are typically finite-difference, finite and spectral-element techniques. For most of these methods the coupling between the momentum and continuity equations is a delicate problem and it usually leads to spurious solutions in the representation of inertia-gravity waves. The spurious modes have a wide range of characteristics and may take the form of pressure (surface-elevation), velocity and/or Coriolis modes. The modes usually cause aliasing and an accumulation of energy in the smallest-resolvable scale, leading to noisy solutions. The Fourier analysis has proven practical and beneficial to describe the spurious solutions of several classical schemes. However it is restricted to uniform meshes on which the variables are regularly distributed. In this paper, a linear algebra approach is proposed to study the existence and the behaviour of stationary spurious modes associated with zero frequency, for some popular finite-difference and finite-element grids. The present approach is performed on uniform meshes but it applies equally well to regular as well as unstructured meshes with irregular geometry for the finite-element schemes.

© 2004 Elsevier Ltd. All rights reserved.

* Corresponding author. Tel.: +1 418 656 7348; fax: +1 418 656 2817.
E-mail address: dlroux@mat.ulaval.ca (D.Y. Le Roux).

Keywords: Ocean modelling; Shallow-water equations; Spurious computational modes; Finite-difference method; Finite-element method

1. Introduction

The shallow-water equations are of considerable importance for a variety of problems of coastal and environmental engineering, including oceanic, atmospheric and groundwater flows. Oceanic models typically employ gridpoint, finite and spectral-element techniques. However, most of these methods may lead to spurious solutions in the representation of inertia-gravity waves (Batteen and Han, 1981; Williams, 1981), when solving the shallow-water and Navier–Stokes equations.

Walters and Carey (1983) investigated the nature of spurious pressure modes by means of a one-dimensional Fourier analysis of the linearized shallow-water equations. They found that spurious solutions may arise from the coupling of the momentum and continuity equations when representing inertia-gravity waves. This problem is encountered in both finite-difference and finite-element formulations. Its severity depends upon the placement of velocity and surface-elevation (or pressure) variables on a mesh, and upon the choice of appropriate basis functions for finite-element discretizations.

The spurious modes usually take the form of surface-elevation, velocity and/or Coriolis modes. They are small-scale artifacts introduced by the spatial discretization scheme which do not propagate but are trapped within the model grid, and associated with zero frequency. If the spurious solutions are left undamped, they can cause an accumulation of energy in the smallest-resolvable scale, leading to noisy solutions.

For example, subject to the no-slip boundary condition the B-grid (Mesinger and Arakawa, 1976) exhibits surface-elevation modes and hence a checkerboard pattern of noise in both the gravity wave and inertial limits, while the C-grid (Mesinger and Arakawa, 1976) is prone to Coriolis modes in the inertial limit only, provided the grid resolution is low relative to the Rossby radius of deformation (Walters and Carey, 1984). The finite-element pairs P_1 – P_1 and P_1 – P_0 (Brezzi and Fortin, 1991) suffer from surface-elevation modes in a similar manner as for the A- and B-finite-difference grids (Walters and Carey, 1983; Le Roux et al., 1998). The B- and C-grids and the P_1 – P_1 and P_1 – P_0 pairs are described later in Section 3.

Attention has been focused almost exclusively on the spurious surface-elevation modes since these were argued to be the most troublesome (Walters and Carey, 1983). A number of arguments have been advanced to explain their origin and to provide a basis for selecting grids that perform well. This has resulted in several strategies using the following methods: mixed-order finite-element interpolation (Walters and Cheng, 1980; Walters, 1983), equal-order elements with variables carried at sets of points staggered in space (Williams, 1981; Hua and Thomasset, 1984), vorticity and divergence instead of velocity in the momentum equations (Staniforth and Mitchell, 1977) and wave-equation (Lynch and Gray, 1979) and Petrov–Galerkin (Hughes et al., 1986) formulations.

The Fourier analysis has proven practical and beneficial to describe the spurious solutions of several classical finite-difference and finite-element schemes (Walters and Carey, 1983). However, it is restricted to uniform meshes on which the variables are regularly distributed.

Triangular finite-elements are attractive for ocean modelling due to their inherent flexibility for representing irregular boundaries and for local mesh refinement. However, the finite-element method has not been widely used in ocean modelling to date. This is because the ocean modelling community has been using finite-difference techniques for a long time and did not invest significant efforts to develop finite-element approaches.

For most of existing finite-element schemes the occurrence of spurious solutions is implicitly linked to an imbalance in the number of degrees of freedom between the discrete surface-elevation and the two components of the discrete velocity vector (Le Roux et al., 1998). It is then crucial to describe the behaviour of the spurious modes and their impact on the quality of the numerical solution, and possibly try to cure them. On structured meshes, macro element techniques (Brezzi and Fortin, 1991) may permit to “eliminate” the spurious modes. On unstructured meshes this is usually more difficult, and appropriate filtering techniques or the use of artificial dissipation are usually employed.

This paper is a first step towards the understanding of the behaviour of spurious solutions that may arise on unstructured grids. In order to do so, a linear algebra approach is proposed to study the existence and the behaviour of stationary spurious modes associated with zero frequency, for some popular finite-difference and finite-element grids. The present approach is performed on uniform meshes but it applies equally well to regular as well as unstructured meshes with irregular geometry for the finite-element schemes. The two-dimensional linearized form of the shallow-water equations are used in their inviscid and viscous forms, with appropriate boundary conditions, including the Coriolis terms.

The paper is organized as follows. The model equations are presented in Section 2. The discrete spurious modes are then examined in Section 3 for several popular finite-difference and finite-element schemes, in both inviscid and viscous cases. In Section 4, some concluding remarks complete the study.

2. The shallow-water model

2.1. Governing equations

Let Ω be the model domain with boundary Γ . The inviscid linear shallow-water equations are expressed in Cartesian coordinates (LeBlond and Mysak, 1978) as

$$\mathbf{u}_t + f\mathbf{k} \times \mathbf{u} + g\nabla\eta = 0, \quad (1)$$

$$\eta_t + H\nabla \cdot \mathbf{u} = 0, \quad (2)$$

where $\mathbf{u} = (u, v)$ is the horizontal velocity field, η is the surface-elevation with respect to the reference level $z = 0$, f and g are the Coriolis parameter and gravitational acceleration, respectively; \mathbf{k} is a unit vector in the vertical and the mean depth H is assumed constant. Note that η plays the role that pressure plays in the Navier–Stokes equations. For a contained flow, Eqs. (1) and (2) are solved subject to the no-normal flow boundary condition

$$\mathbf{u} \cdot \mathbf{n} = 0 \quad \text{on } \Gamma, \quad (3)$$

where \mathbf{n} is the outward pointing normal at the boundary.

2.2. The free modes

In the continuum case the free modes of (1) and (2) are examined by perturbing about the basic state $u = v = \eta = 0$. We seek solutions of (1) and (2) of the form $(u, v, \eta) = (\tilde{u}, \tilde{v}, \tilde{\eta})e^{i(kx+ly+\omega t)}$, where k and l are the wave numbers in the x - and y -directions, respectively, and ω is the angular frequency. Substitution into (1) and (2) then leads to a square matrix system for the Fourier amplitudes $\tilde{u}, \tilde{v}, \tilde{\eta}$. For a non-trivial solution to exist, the determinant of the matrix must equal zero, and this constraint leads to the following dispersion relation for the frequency

$$\omega(\omega^2 - f^2 - gH(k^2 + l^2)) = 0. \quad (4)$$

The first solution $\omega = 0$ is the geostrophic mode and it would correspond to the slow Rossby mode on a β -plane, while the other two solutions $\omega = \pm (f^2 + gH(k^2 + l^2))^{1/2}$ correspond to the free-surface gravitational modes with rotational correction. Since ω is purely real, all modes are neutrally stable and neither amplify nor decay.

3. Examination of the spurious discrete modes

3.1. A Fourier approach

Walters and Carey (1983) examined the numerical dispersion relations of the shallow-water and the compressible Navier–Stokes equations using a Fourier approach. For a given spatial scheme, in which the velocity and surface-elevation variables are uniformly distributed on a regular mesh, a set of selected discretized equations is obtained. Solutions of the form $(u, v, \eta) = (\tilde{u}, \tilde{v}, \tilde{\eta})e^{i(kx+ly+\omega t)}$ are again sought. Substitution into the selected discretized equations leads to a square matrix system for the Fourier amplitudes $\tilde{u}, \tilde{v}, \tilde{\eta}$. For a non-trivial solution to exist, the determinant of the matrix must equal zero. This constraint leads to a dispersion relation for the frequency, from which the eigensolutions may then be obtained analytically using appropriate boundary data. In their study, where the Coriolis effects are not considered, Walters and Carey (1983) described two basic sets of spurious modes.

For the first set, the velocity field is zero and non-constant elevation/pressure functions lie in the null space of the discrete gradient operator. Solution uniqueness is then lost since any multiple of a spurious mode can be added to any solution of the discrete equations and still satisfy them. It was also noted that this family of spurious modes is common to discretizations of both the shallow-water and the (compressible or incompressible) Navier–Stokes equations. For solution uniqueness, the null space of the discrete gradient operator must only contain constant surface-elevation functions, reflecting the fact that surface elevation is only determined to within an arbitrary additive constant, determined by fixing the surface-elevation reference level.

The second set of possible modes are those for which the elevation is zero and the velocity field is in the null space of the discrete divergence operator. Having noted their possible existence, little else is said about them in Walters and Carey (1983). Attention is focused almost exclusively on the spurious elevation modes of zero velocity, since these are argued to be the most troublesome. The occurrence of such spurious elevation solutions has been observed in a variety of finite-difference

(Walters and Carey, 1984) and finite-element (Walters, 1983; Le Roux, 2001) approximations to the shallow-water equations.

The Fourier analysis is restricted to uniform meshes on which the variables are regularly distributed. As a first step towards the understanding of the behaviour of spurious solutions on unstructured meshes, a linear algebra approach is now investigated, including the Coriolis effects.

3.2. A linear algebra approach

The linear algebra approach described herein is based on the study of the discrete operators (e.g. gradient, divergence, Coriolis) obtained by discretizing (1) and (2) in time and space. The velocity and surface-elevation components of the spurious solutions, if they exist, are then searched in the null space of these discrete operators. As previously mentioned, such a study applies equally well to uniform as well as unstructured meshes with irregular geometry. As a first step, only uniform meshes will be considered in the following.

For a given time step $\Delta t = t^{n+1} - t^n$ we introduce a general time discretization scheme of the form

$$\frac{\mathbf{u}^{n+1} - \mathbf{u}^n}{\Delta t} + f\mathbf{k} \times (\gamma\mathbf{u}^{n+1} + [1 - \gamma]\mathbf{u}^n) + g(\alpha\nabla\eta^{n+1} + [1 - \alpha]\nabla\eta^n) = 0, \quad (5)$$

$$\frac{\eta^{n+1} - \eta^n}{\Delta t} + H(\alpha\nabla \cdot \mathbf{u}^{n+1} + [1 - \alpha]\nabla \cdot \mathbf{u}^n) = 0 \quad (6)$$

with $0 \leq \alpha \leq 1$ and $0 \leq \gamma \leq 1$. Observe that $\alpha = \gamma = 0, 1/2, 1$ yield the respective forward Euler, Crank–Nicolson and backward Euler type schemes.

Eqs. (5) and (6) are then discretized in space and rewritten in matrix form as

$$\mathbf{A}\mathbf{X}^{n+1} = \mathbf{B}\mathbf{X}^n \quad (7)$$

with $\mathbf{X}^n = (\mathbf{u}_1^n, \dots, \mathbf{u}_N^n, \eta_1^n, \dots, \eta_M^n)$ at time t^n and

$$A = \begin{pmatrix} \mathbf{M}^u + \gamma\mathbf{C} & \alpha\mathbf{G} \\ \alpha\mathbf{D} & \mathbf{M}^\eta \end{pmatrix} \quad \text{and} \quad B = \begin{pmatrix} \mathbf{M}^u + (\gamma - 1)\mathbf{C} & (\alpha - 1)\mathbf{G} \\ (\alpha - 1)\mathbf{D} & \mathbf{M}^\eta \end{pmatrix},$$

where $\mathbf{M}^u, \mathbf{M}^\eta$ are the velocity and surface-elevation mass matrices, respectively, and $\mathbf{C}, \mathbf{G}, \mathbf{D}$ are the Coriolis, gradient and divergence discrete operators, respectively.

The surface-elevation, velocity and Coriolis spurious modes are specific eigenmodes associated with zero frequency. Hence, those modes have a zero phase speed, they do not propagate but are trapped within the model grid. We thus search for stationary eigenvectors $\mathbf{X} = (u_1, \dots, u_N, \eta_1, \dots, \eta_M)$, such that $\mathbf{X}^{n+1} = \mathbf{X}^n$, associated with the generalized eigenvalue problem

$$\mathbf{A}\mathbf{X} = \lambda\mathbf{B}\mathbf{X}, \quad (8)$$

where $\lambda = 1$. Eq. (8) then leads to

$$\mathbf{A}\mathbf{X} = \mathbf{B}\mathbf{X}, \quad \text{i.e.} \quad (\mathbf{A} - \mathbf{B})\mathbf{X} = \mathbf{0}, \quad (9)$$

or, equivalently

$$\begin{pmatrix} C_{N,N} & G_{N,M} \\ D_{M,N} & 0_{M,M} \end{pmatrix} \begin{pmatrix} \mathbf{u}_i \\ \eta_j \end{pmatrix} = \begin{pmatrix} 0 \\ 0 \end{pmatrix} \tag{10}$$

with $i = 1, \dots, N$ and $j = 1, \dots, M$, independently of the parameters α and γ and the mass matrices M^u and M^η .

We also let $E = (CD)'$.

We now introduce the schemes that are used for the spatial discretization. Eight candidate finite-element pairs and finite-difference grids (shown in Fig. 1) for representing velocity and surface-elevation are described and evaluated in the remainder of this paper. In particular, their ability to approximate the shallow-water system in a spurious mode-free manner is investigated using structured meshes. The grids employed correspond to biased right isocetes triangles for the finite-element pairs and regular squares for the finite-difference grids.

The two candidate finite-difference grids are the classical B- and C-grids of Mesinger and Arakawa (1976). For both schemes the elevation field is carried at the center of the computational cells, and the elevation and velocity variables are staggered in space. For the B-grid the two components of the velocity field are located at the cell corners, while the normal velocities are carried at cell edge midpoints for the C-grid.

Conventional finite-element terminology is adopted to describe the six candidate triangular finite-element pairs of this study. The nomenclature P_m-P_n means that velocity components and surface elevation are, respectively, represented as piecewise-defined polynomials of degree m and n . Enhancements of this basic terminology are introduced as needed. Five finite-element velocity/surface-elevation pairs denoted P_1-P_1 , $P_1^{NC}-P_1$, P_1 iso P_2-P_1 , P_2-P_1 and MINI are first described. Common to all five is a piecewise-linear continuous representation of surface-elevation and they differ from one another in their representation of velocity.

The P_1-P_1 pair has velocity and surface-elevation nodes co-located at triangle vertices and the corresponding basis functions are piecewise-linear. The $P_1^{NC}-P_1$ pair (Hua and Thomasset, 1984; Le Roux, submitted for publication), has velocity nodes at triangle edge midpoints and linear

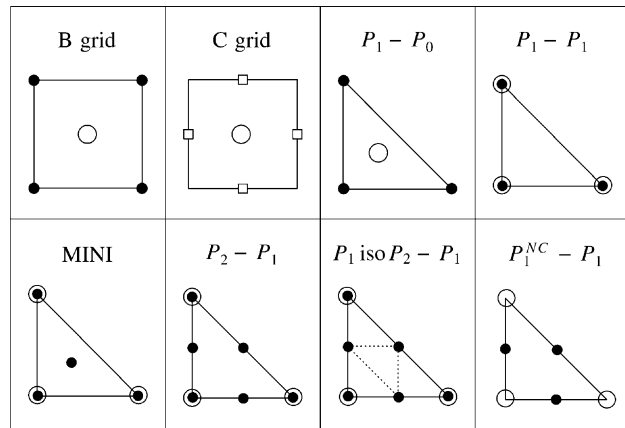


Fig. 1. Two finite-difference grids and six finite-element pairs are presented. The symbols (●) and (○) indicate velocity and surface-elevation nodes, respectively, while the symbol (□) indicates normal velocity nodes.

basis functions are used to approximate the two velocity components on the element's two-triangle support. Since this particular representation of velocity is only continuous across triangle boundaries at midpoint nodes, and discontinuous everywhere else around a triangle boundary, this element is termed non-conforming (NC) in the finite-element literature. The P_1 iso P_2 - P_1 element pair (Bercovier and Pironneau, 1991) has piecewise linear basis functions for velocity on a refined triangulation obtained by dividing each triangle into four subtriangles using the midpoints of triangle sides. There are thus 6 velocity nodes over each unrefined triangle, the same as for a quadratic approximation of velocity, termed P_2 . The designation P_1 in P_1 iso P_2 denotes linear velocity elements on subtriangles, whereas iso P_2 indicates that the nodal placement is that associated with quadratic elements on unrefined triangles. The P_2 - P_1 pair (Hood and Taylor, 1974) has quadratic velocity basis functions while the MINI element has continuous piecewise-linear basis functions at the vertices and bubble functions at the barycenters for velocity (Arnold et al., 1984).

Finally, the last finite-element pair, the P_1 - P_0 pair, has linear basis functions for velocity but discontinuous piecewise-constant basis functions for surface-elevation.

The eight finite-element and finite-difference schemes are now used to compute the dimension of the null space of the following matrices: G, D, C, A-B for $f=0$ and $f \neq 0$, and E. The calculations are carried out using the numerical linear algebra routines of MATLAB and they are performed on a uniform 15×15 Cartesian mesh made up of 196 quadrilaterals or 392 biased right isosceles triangles. The no-normal flow boundary condition (3) is used and the results are summarized in Table 1. It should be noted that the numerical values used for the parameters ($f=10^{-4}\text{s}^{-1}$, $g=9.81\text{ms}^{-2}$, $H=100\text{m}$, $\Delta x = \Delta y = 20\text{km}$), have no impact on the results.

3.2.1. Surface-elevation modes

Spurious surface-elevation modes correspond to the elevation part of the eigensolutions in (10) having zero velocity components. Hence, they are non-constant eigenvectors lying in the null space of the discrete gradient operator. Solution uniqueness is then lost since any multiple of a spurious mode can be added to any solution of the discrete equations and still satisfy them.

Table 1

Dimension of the null space of the matrices: G, D, C, A-B for $f=0$ and $f \neq 0$, and E on a uniform 15×15 Cartesian mesh made up of 196 quadrilaterals. The inviscid case is considered with $\mathbf{u} \cdot \mathbf{n} = 0$ on Γ . The first column refers to the finite-difference grid or the finite-element pair type, while columns 2 and 3 indicate the number of velocity (N) and elevation (M) unknowns, respectively

Mesh 15×15	N	M	G	D	C	A-B $f=0$	A-B $f \neq 0$	E
P_1 - P_0	390	392	15	13	0	28	28	0
P_1 - P_1	390	225	4	169	0	173	127	0
C-grid	364	196	1	169	26	170	170	1
B-grid	390	196	1	195	52	196	146	1
P_1^{NC} - P_1	1176	225	1	952	56	953	171	1
MINI	1174	225	1	950	0	951	125	0
P_2 - P_1	1566	225	1	1342	0	1343	87	0
P_1 iso P_2 - P_1	1566	225	1	1342	0	1343	87	0

Among the schemes examined in Table 1, only the finite-element pairs P_1-P_0 and P_1-P_1 exhibit elevation modes since the null space of their discrete gradient operator is more than one-dimensional. The dimension of the null space increases with increasing grid resolution for the P_1-P_0 pair while this is not observed for the P_1-P_1 pair. This is due to the fact that there are twice as many discrete continuity equations for the P_1-P_0 pair than discrete momentum equations to satisfy them. For the other finite-element pairs and finite-difference grids the null space of the discrete gradient operator is one-dimensional. The corresponding eigenvector is the hydrostatic mode, which can be simply considered as a constant of integration associated with the solution of the governing equations.

3.2.2. Coriolis modes

Coriolis modes may be defined as the velocity part of the eigensolutions in (10) having zero (or constant) surface-elevation components. They are thus non-constant eigenvectors lying in the intersection of the null spaces of the discrete Coriolis and divergence operators, i.e. the null space of E, and they correspond to the inertial limit case.

In Table 1, it is observed that only the finite-difference B- and C-grids and the finite-element pair $P_1^{\text{NC}}-P_1$ may generate spurious Coriolis modes. Indeed, the null space of the discrete Coriolis operator is zero-dimensional for the other pairs. The last column in Table 1 gives the dimension of the null space of E. It thus appears that the B- and C-grids and the $P_1^{\text{NC}}-P_1$ pair only exhibit one Coriolis mode each, and this result is independent of the grid resolution. However, the Coriolis spurious mode associated with the C-grid is quite different from those of the B-grid and the $P_1^{\text{NC}}-P_1$ pair.

Indeed, because the mass matrices for the $P_1^{\text{NC}}-P_1$ pair and the B-grid are diagonal, the strong enforcement of the no-normal flow boundary condition introduces several lines of zero entries in the Coriolis matrix, and those exactly coincide with the number of boundary nodes. Hence, the null space of the discrete Coriolis operator corresponds to the number of boundary nodes for the B-grid and the $P_1^{\text{NC}}-P_1$ pair. As a result, those schemes exhibit a Coriolis mode having non-zero tangential velocities at the boundary nodes of the domain and zero velocities elsewhere. The spurious mode takes the form of a curl vector propagating around the boundary. Some elementary calculations show that this type of Coriolis mode is easy to compute and filter, even for the $P_1^{\text{NC}}-P_1$ pair on unstructured meshes with irregular boundaries.

The Coriolis mode associated with the C-grid is mainly due to the spatial averaging of the Coriolis terms on the grid and it behaves quite differently. Indeed, this mode takes the form of a set of identical cells located around some interior points obtained by joining the horizontal and vertical lines defining the grid. Let (i, j) the position of such a point. The cells are then defined by $v(i + \frac{1}{2}, j) = 1$, $u(i, j + \frac{1}{2}) = -1$, $v(i - \frac{1}{2}, j) = -1$ and $u(i, j - \frac{1}{2}) = 1$. To circumvent the Coriolis modes of the C-grid in the inertial limit, the C-D grid has been introduced (Adcroft et al., 1999). It consists of augmenting the C-grid variables with D-grid velocity variables.

3.2.3. Velocity modes

The last kind of stationary spurious modes that are now examined are termed velocity modes. To date, those modes do not seem to have been thoroughly examined. Velocity modes may be defined as the velocity part of the eigensolutions in (10) having non-constant surface-elevation components.

When $f = 0$, then $C = 0$ in (10), and the dimension of the null space of (A–B) is simply the dimension of the null space of G plus the dimension of the null space of D, which is easily observed in Table 1. In this case the eigensolutions have constant surface-elevation components if the scheme is free of elevation modes and non-constant surface-elevation components otherwise. The velocity part of the eigensolutions lies in the null space of the discrete divergence operator and may thus contain curl vectors (which are highly desirable) and true spurious solutions as well.

When $f \neq 0$, Table 1 shows that the dimension of the null space of (A–B) is considerably reduced, except for the C-grid and the P_1 – P_0 pair. Some long and tedious algebra shows that the dimensions of the discrete divergence and curl operator exactly coincide for the C-grid. Hence, each velocity vector lying in the null space of the divergence operator may be written in the form of a curl vector of some scalar function, at the discrete level. Note this property comes in part from the fact that after applying the no-normal flow boundary condition there are no remaining velocity unknowns on the boundary. The image of the curl vector by the Coriolis operator behaves like a gradient, and because the null space of the gradient operator is one-dimensional this explain why the Coriolis term has no effect upon the null space of (A–B) for the C-grid.

For the B-grid and the other finite-element pairs of Table 1, the null space of (A–B), even reduced by the influence of the Coriolis operator, may still contains spurious modes among the desirable curl vector solutions. In order to estimate the number of spurious modes for the schemes of Table 1, the dimension of the discrete curl operator has to be determined. The main difficulty is to take into account the influence of the boundary at the discrete level. This will be the object of a further study.

3.3. The viscous case

We now consider the viscous linear shallow-water equations in Cartesian coordinates

$$\mathbf{u}_t + f\mathbf{k} \times \mathbf{u} + g\nabla\eta - v\Delta\mathbf{u} = 0, \quad (11)$$

$$\eta_t + H\nabla \cdot \mathbf{u} = 0, \quad (12)$$

subject to the no-slip boundary condition $\mathbf{u} = 0$ on Γ , where v is a positive diffusivity parameter. As for the inviscid case, the system (11) and (12) is then discretized in time and space and rewritten on the matrix form

$$\begin{pmatrix} L_{N,N} + C_{N,N} & G_{N,M} \\ D_{M,N} & 0_{M,M} \end{pmatrix} \begin{pmatrix} \mathbf{u}_i \\ \eta_j \end{pmatrix} = \begin{pmatrix} 0 \\ 0 \end{pmatrix} \quad (13)$$

with $i = 1, \dots, N$ and $j = 1, \dots, M$, and L represents the discrete Laplacian matrix.

We also let $F = (LD)^t$.

The eight finite-element and finite-difference schemes proposed earlier are used to compute the null space of the following matrices: G, D, C, A–B for $f = 0$ and $f \neq 0$, and F. The grid and parameters are the same as those used earlier to compute the results of Table 1, except that the no-slip boundary condition is now imposed with $v = 500 \text{ m}^2 \text{ s}^{-1}$. The results are summarized in Table 2.

As for the inviscid case the finite-element pairs P_1 – P_0 and P_1 – P_1 exhibit elevation modes since the null space of their discrete gradient operator is again more than one-dimensional. But

Table 2

Dimension of the null space of the matrices: G, D, C, A–B for $f=0$ and $f \neq 0$, and F on a uniform 15×15 Cartesian mesh made up of 196 quadrilaterals. The viscous case is considered with $\mathbf{u} = 0$ on Γ . As for Table 1, columns 2 and 3 indicate the number of velocity (N) and elevation (M) unknowns, respectively

Mesh 15×15	N	M	G	D	C	A–B $f=0$	A–B $f \neq 0$	F
B-grid	338	196	2	144	0	2	2	0
P_1 – P_0	338	392	54	0	0	54	54	0
P_1 – P_1	338	225	8	125	0	8	8	0
C-grid	364	196	1	169	26	1	1	0
MINI	1122	225	1	898	0	1	1	0
P_1^{NC} – P_1	1120	225	1	896	0	1	1	0
P_2 – P_1	1458	225	1	1234	0	1	1	0
P_1 iso P_2 – P_1	1458	225	1	1234	0	1	1	0

contrary to the inviscid case the B-grid has now 2 spurious surface-elevation modes since those are no longer linked by the no-normal flow boundary condition. Note that only the null space of P_1 – P_0 increases with increasing grid resolution. For the other finite-element pairs and finite-difference grids the null space of the discrete gradient operator is one-dimensional and it just contains the hydrostatic mode.

In Table 2, it is observed that the B-grid and the P_1^{NC} – P_1 pair do not exhibit Coriolis modes contrary to the inviscid case. This is due to the no-slip boundary condition which prevents the appearance of lines of zero entries in the Coriolis matrix, since there are no longer velocity unknowns lying on the boundary. However, the Coriolis mode associated with the C-grid, and due to the spatial averaging of the Coriolis terms on the grid, is still present and it remains unchanged in the viscous case. Note the dimension of the null space of E is still one for the C-grid.

Finally, the dimension of the null space of (A–B) in Table 2 remains the same in the case $f=0$ and $f \neq 0$, which indicates that the Coriolis terms have no effect upon the results. Further, the null space of (A–B) exactly coincides with the null space of the discrete gradient operator. Consequently, the null space of (A–B) just contains the hydrostatic mode for the MINI, P_1^{NC} – P_1 , P_2 – P_1 and P_1 iso P_2 – P_1 pairs. For each of those pairs, the multiple zero eigenvalue of (A–B) present in the inviscid case has been split into a number of non-zero eigenvalues under the influence of the discrete Laplacian operator. However, the numerical impact of the viscosity on the velocity modes, when they exist, is still unclear and this has not been yet precisely determined. Note the dimension of the null space of F is zero for all the finite-difference grids and finite-element pairs examined here.

4. Conclusion

Most of the numerical methods that are used in ocean modelling poorly approximate the representation of inertia-gravity waves and usually lead to spurious solutions. The spurious modes may take the form of surface-elevation, velocity and/or Coriolis modes, and have dramatic effects upon the existence and the quality of the numerical solution. The occurrence of spurious modes is a manifestation of loss of convergence.

In this paper, a linear algebra approach is proposed to study the behaviour of spurious solutions that may arise from the linearized form of the shallow-water equations. The existence and the behaviour of stationary spurious modes associated with zero frequency are addressed for some popular finite-difference and finite-element grids in both the inviscid and viscous cases.

Spurious velocity modes do not seem to have been thoroughly examined in the past. In order to better identify them and describe their behaviour more accurately, we have suggested to determine the null space of the discrete curl operator for a given numerical scheme. Further, there also exists non-stationary spurious solutions, e.g. inertial modes, that have not been examined in the present paper. All these issues will be the object of a further study.

Acknowledgments

This work is supported by grants to D.Y.L. from the Natural Sciences and Engineering Research Council (NSERC), and to D.Y.L. and V.R. from FQRNT (Fonds Québécois de la Recherche sur la Nature et les Technologies). E.H. is research fellow with the Belgian National Fund for Scientific Research (FNRS).

References

- Adcroft, A.J., Hill, C.N., Marshall, J.C., 1999. A new treatment of the Coriolis terms in C-grid models at both high and low resolutions. *Mon. Weather Rev.* 127, 1928–1936.
- Arnold, D.N., Brezzi, F., Fortin, M., 1984. A stable finite element for the Stokes equations. *Calcolo* 21, 337–344.
- Batteen, M.L., Han, Y.J., 1981. On the computational noise of finite-difference schemes used in ocean models. *Tellus* 33, 387–396.
- Bercovier, M., Pironneau, O., 1979. Error estimates for the finite element method solution of the Stokes Problem in the primitive variables. *Numer. Math.* 33, 211–224.
- Brezzi, F., Fortin, M., 1991. *Mixed and Hybrid Finite Element Methods* Springer Series in Computational Mathematics, vol. 15. Springer-Verlag, Berlin.
- Hood, P., Taylor, C., 1974. Navier–Stokes equations using mixed interpolation. In: Oden, J.T. (Ed.), *Finite Elements in Flow Problems*. The University of Alabama in Huntsville (UAH) Press, Huntsville, AL, USA, pp. 121–132.
- Hua, B.L., Thomasset, F., 1984. A noise-free finite-element scheme for the two-layer shallow-water equations. *Tellus* 36A, 157–165.
- Hughes, T.J.R., Franca, L.P., Balestra, M., 1986. A new finite element formulation for computational fluid dynamics: V. Circumventing the Babuska–Brezzi condition: a stable Petrov–Galerkin formulation of the Stokes problem accommodating equal-order interpolations. *Comput. Meth. Appl. Mech. Eng.* 59, 85–99.
- LeBlond, P.H., Mysak, L.A., 1978. *Waves in the Ocean*. Elsevier, Amsterdam.
- Le Roux, D.Y., 2001. A new triangular finite element with optimum constraint ratio for compressible fluids. *SIAM J. Sci. Comput.* 23, 66–80.
- Le Roux, D.Y., 2003. Dispersion relation analysis of the $P_1^{NC} - P_1$ finite-element pair in shallow-water ocean models. *SIAM J. Sci. Comput.*, submitted for publication.
- Le Roux, D.Y., Staniforth, A., Lin, C.A., 1998. Finite elements for shallow-water equation ocean models. *Mon. Weather Rev.* 126, 1931–1951.
- Lynch, D.R., Gray, W.G., 1979. A wave-equation model for finite-element tidal computations. *Comput. Fluids* 7, 207–228.
- Mesinger, F., Arakawa, A., 1976. *Numerical Methods used in Atmospheric Models*. GARP Publications Series No. 17. WMO-ICSU.

- Staniforth, A., Mitchell, H.L., 1977. A semi-implicit finite-element barotropic model. *Mon. Weather Rev.* 105, 154–169.
- Walters, R.A., 1983. Numerically induced oscillations in finite-element approximations to the shallow-water equations. *Int. J. Numer. Meth. Fluids* 3, 591–604.
- Walters, R.A., Carey, G.F., 1983. Analysis of spurious oscillation modes for the shallow-water and Navier–Stokes equations. *Comput. Fluids* 11, 51–68.
- Walters, R.A., Carey, G.F., 1984. Numerical noise in ocean and estuarine models. *Adv. Water Resour.* 7, 15–20.
- Walters, R.A., Cheng, R.T., 1980. Accuracy of an estuarine hydrodynamic model using smooth elements. *Water Resour. Res.* 16, 187–195.
- Williams, R.T., 1981. On the formulation of the finite-element prediction models. *Mon. Weather Rev.* 109, 463–466.



h , r , and hr adaptivity with applications in numerical ocean modelling

M.D. Piggott *, C.C. Pain, G.J. Gorman, P.W. Power, A.J.H. Goddard

*Applied Modelling and Computation Group, Department of Earth Science and Engineering,
Imperial College, Prince Consort Road, London, SW7 2BP, United Kingdom*

Received 12 April 2003; received in revised form 28 June 2004; accepted 16 July 2004
Available online 2 November 2004

Abstract

The purpose of this article is to introduce techniques for performing h , r , and hr adaptivity in the context of numerical ocean modelling. These supplements to a standard numerical discretization offer the possibility of focusing degrees of freedom, and hence computational resources, in certain important regions. Full flexibility of the definition of these regions may be supplied through a priori and a posteriori error measures, or through consideration of the physics of the underlying problem. One of the most significant advantages present with the use of unstructured meshes in ocean modelling is the possibilities this opens up for the use of adaptive algorithms. Indeed it is hard to envisage unstructured mesh based models becoming a serious viable alternative to models based upon structured meshes until the efficient and robust use of adaptive meshing is employed. Examples of the use of adaptive methods are presented here for free surface flows and circulation in the Mediterranean Sea. Practical issues relating to mesh quality, including anisotropy, element shape, discretization errors, and matrix conditioning are also discussed.

© 2004 Elsevier Ltd. All rights reserved.

* Corresponding author. Tel.: +44 207 5949322; fax: +44 207 5947444.
E-mail address: m.d.piggott@imperial.ac.uk (M.D. Piggott).
URL: <http://www.amcg.es.imperial.ac.uk>

1. Introduction

Modelling of the World's oceans is an extremely complex task and numerical simulation is a necessity. Due to the variety of important physical processes present, as well as the wide range of spatial and temporal scales, this represents a formidable challenge. Numerical models of physical phenomena truncate the infinite degrees of freedom describing the system's exact behaviour to a finite number of unknowns which may be solved for computationally. The particular nature of the truncation is determined by one's choice of method, e.g. finite difference, finite volume, finite element, or spectral. In addition each method has various options that control its quality when applied to a particular problem. The most obvious of these is local accuracy; each method may be made to approximate the underlying equations to higher order in the hope that improved models will result. However this is not necessarily the case, especially in simulations over long time scales where qualitative properties of model may be more important than local truncation errors. Higher order methods will also typically be more expensive, and therefore for acceptable computations the finite number of unknowns must be reduced, although dependent on the problem being solved they may ultimately be more efficient. Whatever the choice of numerical method, physical processes which act on scales smaller than is resolved by the finite number of unknowns will not be present in the model. Therefore important characteristics of the true flow may not be admitted, leading to errors, as well as possibly instabilities which must be controlled numerically, typically at the expense of accuracy. The situation is therefore far from trivial, and often made worse by complex geometries and external forcing.

In general the finite number of unknowns described above may be considered to be located at the nodes of a mesh which covers the problem domain, and upon which the numerical discretization is constructed. The current standard in the majority of ocean models (see [Haidvogel and Beckmann \(1999\)](#) for background material) is for the mesh to be *structured*, so that in the horizontal a curvilinear mesh of quadrilaterals is used to fit the coastlines of the region being modelled as well as possible. It is termed structured since the topology of the mesh is uniform in space, i.e. each quadrilateral (other than those at boundaries) is surrounded by precisely eight neighbours, four of which share an edge, the other four sharing only a corner. Note that it is often the case in practice that meshes are block structured, so that different structured meshes are used and then combined along interfaces. For example this may be used to enable higher resolution in certain regions of interest, to enable a better representation of complex coastlines, and to remove the problem of poles in a structured mesh on the sphere. In the vertical the situation is much the same, the mesh is made up of columns stretching from the ocean surface down to the sea bed. The only available flexibility is in the choice of vertical coordinate. These choices may be viewed as being equivalent to the mesh in the vertical being aligned with surfaces of constant depth (z -coordinate models); to linearly conform to both the bathymetry and the free surface (σ -coordinate models); to be aligned with surfaces of constant density (isopycnal-coordinate models); or some hybrid combination of more than one approach. Research has found that due to the physics governing ocean dynamics the choice of both the discretization in the horizontal and the vertical coordinates is of fundamental importance in the design of numerical models, see [Haidvogel and Beckmann \(1999\)](#); [Griffies et al. \(2000\)](#) and the references therein.

In contrast, *unstructured* meshes (the topic of this volume) allow a virtually arbitrary mesh structure. For example the problem geometry may be partitioned into tetrahedra, the flexibility then comes from the fact that each tetrahedron may, in theory, have an unlimited number of neighbours. This flexibility naturally allows a far better representation of coastlines and bathymetry; increased local resolution with no need for internal mesh boundaries; the spherical pole problem is no longer an issue; and perhaps most importantly, and the topic of this article, this choice is the most natural for developing a model with a dynamically *adaptive* mesh. An unstructured mesh has the advantage that the finite number of unknowns, and hence the resulting computational power, may more simply and generally be placed in particular regions. So that for example in a simulation of the North Atlantic, a higher density aligned mesh may be placed in and around the Gulf Stream, whilst lower resolution may be used in other regions deemed less important. A more optimal use of computational power is thus possible. But what happens when one wishes to model a transient situation where the desired locations of increased resolution are unknown and computed as part of the simulation, or periodically appear and disappear, or vary their position within the domain? Examples may be periodic transient overflows, eddies moving across a basin, wetting and drying in coastal regions, or even a simulation where the Gulf Stream path varies dramatically or shuts down completely. The constant nature of any mesh may even enforce subtle constraints on solution behaviour—an unacceptable situation.

The ability to compute on a mesh which dynamically adapts to vary resolution and follow components of the solution is very attractive. It offers increased efficiency; flexibility in that one model may be used on a variety of scales and problems; the ability to test whether the mesh is unduly affecting results (for example by comparing results from a fixed mesh, and adapting meshes based upon differing criteria); as well as the ability to make quantitative statements regarding the magnitudes of certain error measures. In addition, an adapting unstructured mesh is able to achieve the equivalent of a truly hybrid or general vertical coordinate. An obvious example would be a situation where the bathymetry and free surface are resolved, the mesh is free to follow isopycnals, as well as being able to vary resolution throughout the domain. For example localized non-hydrostatic dynamics may be resolved, with fewer vertical cells being used in shallower regions, or regions where the flow is closer to barotropic.

The purpose of this article is to introduce and review a variety of adaptive methods, to explain how they may be used in an oceanographic context, and to present some simple examples. In Section 2 brief background material on underlying equations and finite element discretizations is presented. In Section 3 motivation for adaptive meshes is given by considering standard interpolation error theory. Consequently the transformation viewpoint of adaptivity is introduced through examples in both one and higher dimensions. Section 4 describes mesh optimization, or *h*-adaptivity. An example of this approach applied to idealized wind driven circulation in a basin is given. Section 5 introduces the concept of mesh movement, or *r*-adaptivity. Several alternate techniques are described and some simple examples given. In Section 6 the possibility of combining different approaches to adaptivity is discussed, and again an example is given to demonstrate the additional power and flexibility of a combined *hr*-adaptive method. In Section 7 the issues of mesh quality, error measures, and their impact on computations are briefly addressed.

2. Background on ocean modelling and the finite element method

The underlying problem considered here is assumed to be described by the non-hydrostatic Boussinesq system of equations

$$\frac{\partial \mathbf{u}}{\partial t} + (\mathbf{u} - \hat{\mathbf{u}}) \cdot \nabla \mathbf{u} + 2\boldsymbol{\Omega} \times \mathbf{u} = -\nabla p - g\nabla\eta - \rho g\mathbf{k} + \nabla \cdot \bar{\bar{\tau}}, \quad (1)$$

$$\nabla \cdot \mathbf{u} = 0. \quad (2)$$

Here, \mathbf{u} represents the three-dimensional (3-D) velocity, p is the perturbation pressure, ρ is the perturbation density, $\boldsymbol{\Omega}$ is the Coriolis rotation vector, and g the acceleration due to gravity. $\hat{\mathbf{u}}$ is a term used to account for a moving reference frame, for example in this work it takes the form of node velocities for numerical discretizations on moving meshes. The stress tensor $\bar{\bar{\tau}}$ is used to represent viscous terms. An equation of state is used to govern the relationship between ρ and quantities such as temperature and salinity which are governed by advection-diffusion equations of the form

$$\frac{\partial T}{\partial t} + (\mathbf{u} - \hat{\mathbf{u}}) \cdot \nabla T = \nabla \cdot (\bar{\bar{\kappa}}\nabla T), \quad (3)$$

where $\bar{\bar{\kappa}}$ is a tensor representing diffusive processes. The free surface height $\eta \equiv \eta(x, y, t)$ measured from the rest state of the ocean may be modelled either via the integrated continuity equation, or for simplicity here by the kinematic boundary condition which simply states that particles on the free surface remain on it, i.e.

$$\frac{\partial \eta}{\partial t} + (\mathbf{u}_H - \hat{\mathbf{u}}_H)|_{z=\eta} \cdot \nabla_H \eta = w|_{z=\eta}, \quad (4)$$

where $\nabla_H \equiv (\partial/\partial x, \partial/\partial y)^T$, and \mathbf{u}_H and $\hat{\mathbf{u}}_H$ are the horizontal components of \mathbf{u} and $\hat{\mathbf{u}}$ respectively.

The system is now closed by imposing suitable initial and boundary conditions. For simplicity here the normal component of velocity is generally taken to be zero on all boundaries except the free surface where stress free normal and tangential conditions are employed. Suitable boundary conditions for pressure are then Neumann conditions on the boundaries where the normal component of velocity is specified, and Dirichlet conditions on the free surface (Gresho and Sani, 1987, 1998).

A standard finite element discretization of (1)–(4) represents solution variables as summations over a finite set of spatial basis functions. Basis functions typically take the form of being unity at a single node of the mesh and then taking the value zero at all other nodes, the variation across elements being polynomial. The resulting representation of solution variables is thus piecewise polynomial. In this work piecewise linear basis functions are used for all variables, in certain notation this is referred to as a $P1 - P1$ element choice. The discrete forms of the solution variables are then substituted into the governing equations and a Galerkin projection is taken by multiplying each equation by a basis function, integrating over the domain, and applying Green's theorem where appropriate to reduce the regularity required of basis functions. Discretization of the temporal derivative yields a large system of coupled nonlinear equations to be solved. Nonlinearity may be dealt with by Newton or Picard iteration for example, and the coupling may be treated

more efficiently by factorization and projection type approaches. Further details of the particular techniques employed here may be found in (Ford et al., 2004).

3. Motivation for adaptive methods

In this section the construction of error measures based upon interpolation theory is reviewed and used as motivation for performing optimisation based anisotropic mesh adaptivity. The resulting a priori estimates can give a simple guide to complex areas of the flow which may warrant increased resolution, and have been used as such in (Löhner et al., 1985; Peraire et al., 1987), importantly they also yield information on the anisotropy required. It is important to note however that the field of error measure design is vast with interpolation theory playing a small, albeit important, role. Discussions on the more complex subjects of a posteriori error estimation may be found in (Strouboulis and Oden, 1990; Ainsworth and Oden, 1997), and goal based error estimation in (Pierce and Giles, 2000; Oden and Prudhomme, 2001). The design of high quality error measures of physical relevance to ocean modelling is a crucially important task, some steps in that direction are given in Power et al. (submitted).

3.1. Interpolation error in 1-D

Suppose that a sufficiently smooth function $u \equiv u(x)$ is approximated by its piecewise linear Lagrange interpolant $\Pi_h u$ on a mesh $x_0 < x_1 < \dots < x_N$. Standard theory states that the interpolation error over the mesh cell $[x_{i-1}, x_i]$ satisfies

$$\varepsilon_i \equiv \|u - \Pi_h u\|_{\infty, i} \leq \hat{\gamma} h_i^2 \|u''\|_{\infty, i}. \quad (5)$$

Here $h_i := x_i - x_{i-1}$ is the local mesh spacing, $\hat{\gamma}$ is an $O(1)$ constant independent of the mesh, and $\|\cdot\|_{\infty, i}$ is the max-norm over the mesh cell $[x_{i-1}, x_i]$. A global interpolation error may be obtained by taking the maximum over all mesh cells. In de Boor (1973) it is established that the optimal choice of mesh is given by making

$$h_i^2 \|u''\|_{\infty, i} = \text{Constant}, \quad \forall i \in \{1, \dots, N\}. \quad (6)$$

3.2. Equidistribution

A computational technique which asymptotically reproduces (6) was also given in de Boor (1973), the continuous version of which, generally termed *equidistribution*, may be written

$$\int_0^{x(\xi)} M(s) ds = \xi \int_0^1 M(s) ds. \quad (7)$$

Here ξ is a new fictive *computational variable* assumed without loss of generality to be defined on $[0, 1]$. M is a so-called *monitor function* which, to correspond with (6), should be taken here to be $|u''|^{1/2}$. Equation (7) now describes a coordinate transformation $x \equiv x(\xi)$ between computational and physical variables. An adapted mesh may then be taken to be the image of a uniform mesh in

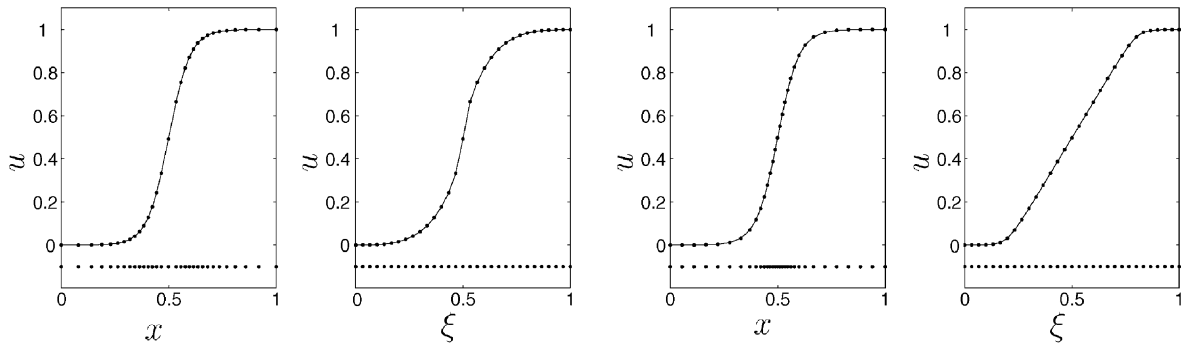


Fig. 1. Plot of a near singular function u and associated meshes in the physical coordinate x and the computational coordinate ξ . First two frames show results using $|u''|^{1/2}$ as monitor function, the third and fourth frames show the same with arc-length as monitor function.

the computational domain, i.e. $x_i := x(i/N)$ for $i = 0, 1, \dots, N$. An example of this is given in Fig. 1, both physical and computational domains are taken to be $[0, 1]$, the mesh is constructed by solving (7) numerically for a coordinate transformation in the case that the function being approximated is the near singular

$$u(x) = \frac{1}{2} + \frac{1}{2} \tanh \left(100 \left(x - \frac{1}{2} \right) \right).$$

The first frame of Fig. 1 shows this function and a resulting adapted mesh of 31 nodes. Due to the choice of monitor function (or error measure), the adapted mesh is clustered in those regions where the function's second derivative is largest. The second frame shows the corresponding structure of this function in the uniform computational domain, as can be seen the function is smoother there. Thus, solving a numerical problem on an appropriate adapted mesh can be seen as being equivalent to solving an easier transformed problem. The particular problem in question here was optimal interpolation, alternate problems such as discretizations of PDEs may require different meshes or coordinate transformations. In this framework this may be achieved simply by varying the monitor function, for example the result of taking the popular choice of arc-length, $M = \sqrt{1 + u_x^2}$, is shown in the third and fourth frames of Fig. 1. In the physical domain the mesh points may be seen to be equally spaced along, or equidistribute, arc-length. Again the function is smoother if viewed in the computational domain. Interpreting and constructing adaptive meshing in terms of continuous coordinate transformations is extremely useful and shall be used more in later material. In (Huang et al., 1994) this approach is generalized to construct various methods which may be used more practically for the adaptive solution of PDEs. Similar ideas are used in Burchard and Beckers (2004) to construct adaptive vertical meshes in an oceanographic context.

3.3. Interpolation error in higher dimensions

In higher dimensions (for background see Schultz (1969); D'Azevedo (1991); D'Azevedo and Simpson (1991)), for example over a mesh of tetrahedra K in 3-D, the analogous result to (5) is given by

$$\varepsilon_K \equiv \|\mathbf{u} - \Pi_h \mathbf{u}\|_{\infty, K} \leq \hat{\gamma} \max_{x \in K} \max_{\mathbf{v} | x + \mathbf{v} \in K} \{\mathbf{v}^T | H(\mathbf{x}) | \mathbf{v}\} \quad (8)$$

for the Hessian $H \equiv \nabla^T \nabla \mathbf{u}$, and another $O(1)$ constant $\hat{\gamma}$. Note that $\mathbf{v}^T H(\mathbf{x}) \mathbf{v}$ is the curvature of the field \mathbf{u} at point \mathbf{x} and in direction \mathbf{v} . The analogue of the mesh spacing squared in (5) comes in here as a result of the fact that \mathbf{v} is chosen such that $\mathbf{x} + \mathbf{v}$ lies within tetrahedra K . Importantly the additional directional information available here may be used to construct optimal *anisotropic* meshes. The Hessian may be diagonalized as $H = Q\Lambda Q^T$, where Λ is the diagonal matrix consisting of the eigenvalues of H (the principal curvatures) and Q is an ortho-normal matrix of eigenvectors. Q may be interpreted geometrically as a rotation and Λ a rescaling. For use as an error indicator with which to construct adapted meshes it is appropriate to take the absolute values of the eigenvalues, *i.e.* in (8) $|H| = Q|\Lambda|Q^T$, and also to limit their values to enable the control over both maximum and minimum element sizes. As in 1-D where a coordinate transformation from a uniform domain was constructed to make the mesh spacing locally proportional to $|u''|^{-1/2}$, in higher dimensions the linear mapping induced by $S = Q\sqrt{|\Lambda|}$ may be used to transform uniform isotropic meshes in a computational space to adapted anisotropic meshes in the physical domain.

3.4. Anisotropic adaptivity

The form of the error estimate (8) in terms of the Hessian means that contours of constant error form families of conics. Since the absolute value of the Hessian appears in (8) these are ellipsoids with a common centre. The conic that passes through the nodes of the element indicates a zero error, the common centre gives the maximum interpolation error if it lies within the element, otherwise the maximum error is given by its value at the midpoint of an element edge or face, for details see (D'Azevedo, 1991). For example in 2-D consider $\Lambda = \text{diag}(4, 1)$ and Q a rotation by an angle $\pi/4$. In Fig. 2 elements and their circumellipses are given, the top and bottom rows give two alternate orientations for the elements, each entry of which show results with different element shapes. The maximum error within each element can easily be found, this must however be divided by the volume of the element to give a useful measure of quality, since ultimately an entire domain must be covered by such elements. Varying the shape, or anisotropy, or the elements gives the two plotted curves to the left in Fig. 2. The three example elements for each orientation correspond respectively to the leftmost, optimal, and rightmost choices indicated by these curves. It can be seen that the ratio of the square roots of the eigenvalues (here 2 or 1/2) gives the optimal scaling ratios for the two element orientations. Additionally, transformation S can be shown to map the family of ellipses to circles, and hence the optimal element, being that which maximizes volume for a given circumcircle, is an equilateral triangle in the transformed computational space. Indeed under transformation S the optimal choices in Fig. 2 do map to equilateral triangles in the isotropic computational space. Hence as in 1-D, an optimal mesh may be found by constructing a homogenous isotropic mesh in a computational space, which may then be mapped back to an adapted mesh. Note that the Hessian considered in this simple illustrative example was constant, and the construction could be performed exactly. In the next section a local optimization approach is introduced that allows spatially varying Hessian matrices.

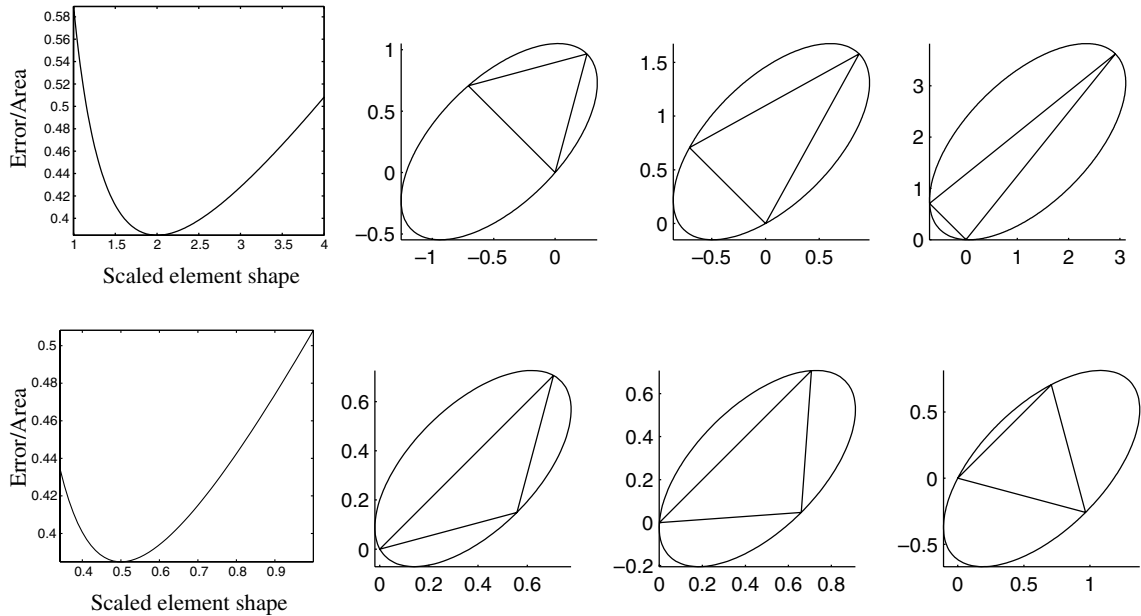


Fig. 2. Interpolation error over area against element shape for the example given in Section 3.4. The two rows gives alternate orientations of elements. For each a single node is moved in a direction normal to its opposite edge. The scaled element shape is then simply this distance divided by the corresponding distance for an equilateral element. Example elements, as well as their circumellipses are also given. These correspond to the leftmost, optimal and rightmost choices in the plotted curves. Both orientations achieve the same optimum, which agrees with theoretical bounds.

4. h -adaptive mesh optimization methods

Although the terms are used as synonyms here, it should be noted that strictly speaking *mesh optimization* represents a generalization of classical *h -adaptivity*. In the previous section a measure of the interpolation error was derived in terms of the Hessian. It was demonstrated that for a constant Hessian and no geometry constraints an optimal adapted mesh is that which is made up of uniformly sized equilateral elements in an appropriate transformed space. A non-constant Hessian, adapting to resolve more than one field on a single mesh, and issues related to covering an arbitrary domain mean that in general this can not be achieved exactly for an entire mesh. In practice an optimization approach may be used to improve the quality of a mesh based upon measurements of the elements as viewed in the transformed space. Equivalently the mesh may be considered as being constructed in a *Riemannian space* with lengths measured in terms of the weighted norm

$$\|\mathbf{v}\|_{\widehat{M}} = (\mathbf{v}^T \widehat{M} \mathbf{v})^{1/2}. \quad (9)$$

Here \widehat{M} is an appropriately chosen *metric tensor* used to control the adapted mesh, just like the monitor function in Section 3.2. In the case corresponding to estimate (8) the metric is chosen such that an element size (or any length) is unity if it has the desired user-defined interpolation error $\hat{\epsilon}$, i.e. $\widehat{M} := \tilde{\gamma} | H | / \hat{\epsilon}$. To arrive at definition (9) the metric is assumed for computational simplicity

to take the value it attains at the midpoint of the vector with magnitude and direction given by \mathbf{v} . For linear basis functions the (second-order) Hessian for each solution field is computed via a reconstruction process, the results may then be combined to yield a single metric which takes into account all solution fields. For many further details see (Pain et al., 2001).

An *objective functional* is now formed which may be used as a gauge of local mesh quality. Here it is given by the max-norm over all elements of the quantity

$$F_e = \frac{1}{2} \sum_{l \in \mathcal{L}_e} (r_l - 1)^2 + \left(\frac{\alpha}{\rho_e} - 1 \right)^2, \quad (10)$$

defined for element e , where \mathcal{L}_e is the set of edges of element e , r_l is the length of edge l , and ρ_e is the radius of the element's inscribed sphere. The first term in this functional gauges the size of element e , and when measured using (9) takes the minimum value zero for an edge with the appropriate length. The second term is used to measure the shape of element e , and again takes the value zero for an element with an aspect ratio of unity (this criterion gives the value of α) as measured using (9).

Mesh optimization may now be performed by seeking to minimize the above functional through a sequence of well defined local topological and geometrical mesh operations. These include edge collapsing and splitting, edge to edge, edge to face, and face to edge swapping (Pain et al., 2001). In addition local node movement (or Laplacian mesh smoothing) may also be employed, this topic will be considered further in a later section.

An example of the use of this approach to mesh adaptivity is given in Fig. 3. Barotropic circulation in a simple flat bottomed Mediterranean Sea is presented. The mesh has adapted to the u and v components of velocity, which here are driven by a wind forcing with a cosine of latitude profile in the u direction. The simulation is purely for demonstration purposes, no attempt has been made to construct a realistic circulation. Initially the mesh had a resolution of approximately $1/4^\circ$ everywhere, the mesh presented has a resolution varying from 1° in the less active regions to $1/30^\circ$ in the more active regions.

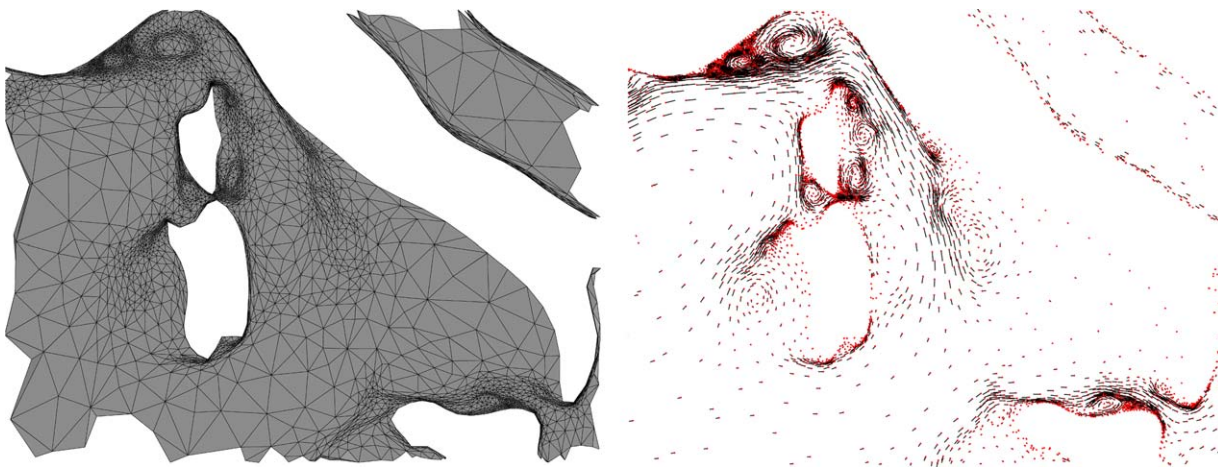


Fig. 3. Simulation of wind driven circulation in a flat bottom barotropic Mediterranean Sea. Blow-up of a portion of the mesh (Left) and flow vectors (Right) are presented. Movies available.

5. r -adaptive moving mesh methods

h -adaptive methods suffer from the drawback that when components of the flow requiring adapted aligned meshes move (e.g. eddies, fronts, gravity currents), nodes must be removed from regions the components have left and new nodes included appropriately in the regions they enter. This is an inefficient process, and also means that interpolation must be employed which may degrade solution quality and overall efficiency. In contrast to making local topological changes to the mesh and its connectivity, r -adaptive methods make local changes to the resolution by moving the locations of a fixed total number of mesh points. This represents an attractive approach, both when the mesh moves in ways dictated by error measures (or solution residuals (Baines, 1994)), but also when it would be beneficial for the mesh to move approximately with the flow. For appropriate error measures it may well turn out that the mesh is quasi-Lagrangian in nature, but is importantly not necessarily restricted to this.

In this way the need for some form of h -adaptivity will be far reduced, although in a totally robust and flexible method it can never be completely removed. Some methods for performing r -adaptivity will now be presented, in a later section the possibility of combining the h and r approaches will be discussed.

5.1. Mesh smoothing based node movement

In Section 4 local node movement was given as one possible operation with which to optimize a mesh. Since there it is included in an algorithm which uses various other operations, it only locally improves the quality of patches of elements rather than allowing true mesh movement. The idea behind Laplacian mesh smoothing is to reposition every node at the centroid of all surrounded connected nodes, see Fig. 4. If this centroid is computed in the Riemannian space given by the error metric (i.e. using (9)) then an approach for performing r -adaptivity results, simply by looping over every node repeatedly in a Gauss–Seidel manner. Viewed in the Euclidean physical space this is equivalent to considering the mesh to be a network of springs of varying stiffness, the stiffness being equal to the error measure evaluated along element edges. Considering each node in isolation the problem of minimizing the local spring energy can be used to obtain a new position of the node, relaxation should be used to ensure a robust algorithm. Further algorithmic details and examples may be found in Ait-Ali-Yahia et al. (1996). In the first frame of Fig. 5 an example of this approach is given, an initially uniform structured (for simplicity) mesh on $\Omega := [-1, 1]^2$ has been adapted via node movement to resolve the top hat function

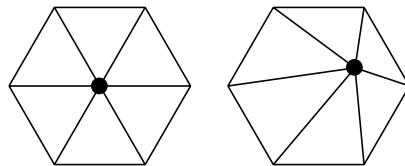


Fig. 4. Node movement via a spring analogy or weighted smoothing. Left frame may be considered an initial node position in relation to its neighbours and the right the result after movement of the centre node. Alternatively, the left frame may be interpreted as the image of the adapted right image under the transformation to the Riemannian space introduced in Section 4.

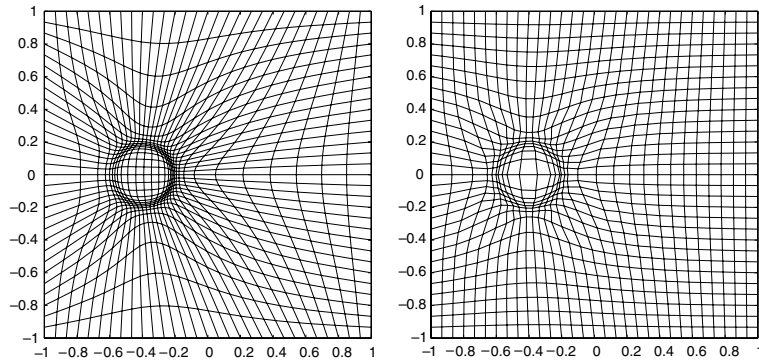


Fig. 5. Mesh adapted to the top hat function (11). (Left) from the spring based technique presented in Section 5.1. (Right) from the variational technique presented in Section 5.2. Movie available.

$$u(x, y, t) = \begin{cases} 1.0 & \text{if } r < 0.18, \\ 0.0 & \text{if } r > 0.22, \\ (0.22 - r)/0.04 & \text{otherwise,} \end{cases} \quad (11)$$

where $r^2 = (x - x_c)^2 + (y - y_c)^2$, $x_c = -0.4 \cos(2\pi t/10)$ and $y_c = 0.4 \sin(2\pi t/10)$. Here the resulting mesh corresponding to $t = 0$ is given, a movie for $0 \leq t \leq 100$ is also available. The metric here is taken to be the analogue of arc-length $\sqrt{1 + |\nabla u|^2 I_2}$ where I_2 is the 2-D identity matrix.

5.2. Variational based mesh movement

The previous approach to mesh movement can be interpreted as the construction of a uniform mesh in a transformed space such that the adapted mesh equidistributes a measure of error, c.f. Sections 3.3 and 3.4. Here an alternate method is presented which seeks to use variational techniques to construct a transformation which minimizes a measure of error or problem complexity. Coordinate transformations ($\xi = \xi(\mathbf{x}, t)$ or equivalently $\mathbf{x} = \mathbf{x}(\xi, t)$) are sought such that the computational variable ξ is the function of the physical variable \mathbf{x} which minimizes a functional involving various adaptation properties (e.g. error, alignment, orthogonality, and smoothness). Again, an adapted mesh in the physical \mathbf{x} coordinate may then be defined as the image under this transformation of a uniform mesh in the computational ξ coordinate. In 3-D consider the adaptation functional

$$I[\xi] = \frac{1}{2} \int_{\Omega} \sum_{i=1}^3 (\nabla \xi_i)^T G_i^{-1} \nabla \xi_i d\mathbf{x}, \quad (12)$$

where ∇ represents the gradient with respect to \mathbf{x} , the $G_i = G_i(\mathbf{x}, \mathbf{u})$ are monitor functions in the language of Section 3.2 or error metrics in the language of Section 4, which take the form here of 3×3 symmetric positive definite matrices. The mesh transformation may then be found by solving the nonlinear elliptic Euler–Lagrange equations (Gelfand and Fomin, 1963) corresponding to (12), these take the form

$$-\frac{\delta I}{\delta \xi_i} = \nabla \cdot (G_i^{-1} \nabla \xi_i) = 0, \quad i = 1, 2, 3. \quad (13)$$

Further details may be found in [Huang and Russell \(1999\)](#), it is also shown there how it is often advantageous to introduce a time derivative and relax the mesh towards that given by the exact solution of (13). In the implementation employed here this *parabolized* system is discretized, for simplicity, with centred finite differences in space and the resulting ODE system for node position solved with the code DASSL ([Brenan et al., 1989](#)). An example of a mesh resulting from this approach is given in the second frame of [Fig. 5](#), here the same top hat function is used and the monitor functions are taken to be equal and given again by arc-length.

5.3. Free surface mesh movement

An even simpler use of mesh movement may be used to account for free surface movement in oceanographic applications. It should be noted that sigma and isopycnal coordinate models may be interpreted as being equivalent to adaptive methods in the sense that they are posed in terms of solution dependent coordinate transformations in the vertical. However, achieving this via numerical rather than analytical coordinate transformations means that generalizations to include the techniques of Sections 5.1 and 5.2 are far more straightforward. Indeed this may be seen as a first step towards the equivalent of a completely general vertical coordinate, controlled by both physical and error measure considerations. It may well turn out that the resulting mesh is close to isopycnal in the ocean interior whilst being closer to a σ or z coordinate as appropriate near the domain surface, bottom, or coastal regions.

When the free surface equation (4) is solved the entire mesh may be stretched in the vertical to account for this. On a structured mesh with nodes stacked one on top of the other this is straightforward. However with a mesh unstructured in the vertical the new value of free surface height η must be passed down through the mesh. This is achieved here either by interpolation or by integrating the differential equation $\partial\eta/\partial z = 0$ down from the free surface with the value of η there being imposed as a boundary condition. The term $g\nabla\eta$ in (1) may then be computed, and the mesh updated. Here nodes at the free surface remain on the free surface and nodes on the sea bed are stationary, with a linear update in between.

An example is given in [Fig. 6](#) for Laitone's approximation of a solitary wave ([Laitone, 1960](#))

$$u = \sqrt{gd} \frac{H}{d} \operatorname{sech}^2(f(x, t)), \quad w = \sqrt{3gd} \left(\frac{H}{d}\right)^{3/2} \frac{z}{d} \operatorname{sech}^2(f(x, t)) \tanh(f(x, t)),$$

$$\eta = H \operatorname{sech}^2(f(x, t)), \quad f(x, t) = \sqrt{\frac{3H}{4d^3}}(x - ct), \quad c = \sqrt{gd(1 + d/H)},$$

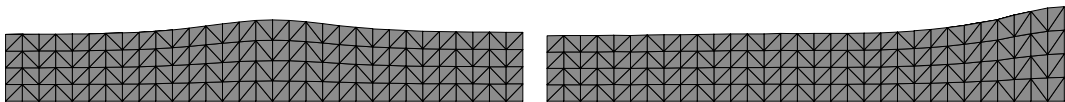


Fig. 6. Simulation of Laitone's approximation to a solitary wave. Mesh movement is employed in the vertical, which here has been stretched by a factor two for visualization. The time step is $\Delta t = 0.2$ and results are shown at $t = 0$ (left) and $t = 7.4$ (right). Movie available.

where d is the still water depth, H is the height of the soliton above this. In Ramaswamy (1990) this problem was considered where a similar arbitrary Lagrangian–Eulerian (ALE) method was employed, and is used here as a guide to parameter choices. The domain is taken to be $16d$ units long with $d = 10$, $H = 2$, and gravity takes the value $g = 9.8$. With these values the speed of the soliton is approximately $c = 10.844$. As can be seen from the position of the bulge, the wave speed is well approximated on a coarse mesh using this approach.

6. hr -adaptive methods

Both h and r methods have advantages and disadvantages (Huerta et al., 1999). For example, with r methods the number of nodes is kept constant; since the level of complex dynamic behaviour may vary throughout a simulation this is very unlikely to always be near-optimal. In addition, it may be difficult to achieve in a straightforward manner large local variations in resolution, it is also possible that constraints in the topology of the mesh mean that inappropriately shaped or tangled meshes result. These problems would largely disappear if a component of h -adaptivity were available when mesh movement alone was found to be insufficient to cope with the solution dynamics. In contrast h methods alone may not be the most efficient manner for performing adaptive simulations in fluid based situations, where regions which require enhanced resolution may well move with the flow. This will result in the excessive use of interpolation, especially when compared to an r method which would typically require none. In addition, since in these regions small elements may well be present along with high velocities and so any CFL based time step restriction present may be severe, an r method which moves the mesh approximately with the flow would have the effect of reducing transport velocities, and hence also time step restrictions for these smaller elements, c.f. the properties of semi-Lagrangian methods. A combined hr method thus seems the ideal.

There are few examples of combined hr -adaptive methods in the literature. In (Lang et al., 2003) a 2-D moving mesh method (based on the ideas presented in Section 5.2) is coupled with an h -adaptive method which locally alters the mesh in order to achieve a desired error tolerance as well as improving poorly shaped elements. An alternate approach is used in (Dompierre et al., 2002) where a 2D mesh optimization method is used which incorporates a moving mesh through repeated weighted mesh smoothing (Sections 4 and 5.1). In (Askes and Rodríguez-Ferran, 2001) the domain is split into appropriate regions where h and r adaptivity are applied separately. These references all demonstrate that the combined use of both the h and r approaches to adaptivity results in improvements over either applied individually.

The use of these ideas, the methods introduced in Sections 4 and 5, and the interpretation of each method in terms of coordinate transformations is being used to develop a robust and efficient hr method in 3-D specifically tailored to oceanographic applications. An example of sloshing free surface motion in a tank is given in Fig. 7. Mesh movement is used to account for the majority of adaptivity required. However as the mesh stretches and becomes inappropriately shaped and sized, as dictated by error measures, the mesh optimization algorithm presented in Section 4 alters the mesh. Movies are available online, including a blow-up of the top right hand corner so that the mesh optimization can be more clearly seen.

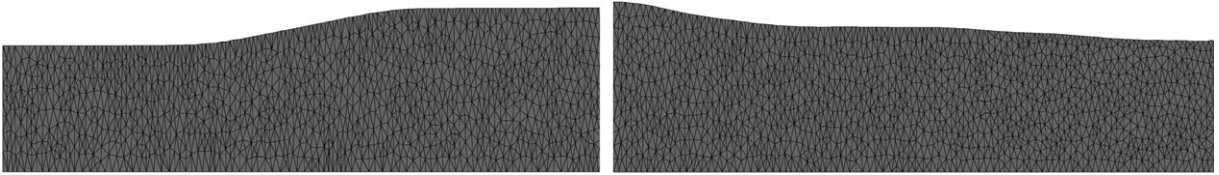


Fig. 7. Free surface dynamics in a sloshing tank with hr -adaptivity (mesh movement and mesh optimization). The vertical has been stretched by a factor two here for visualization. (Movie and blow-up of top right-hand corner available online.)

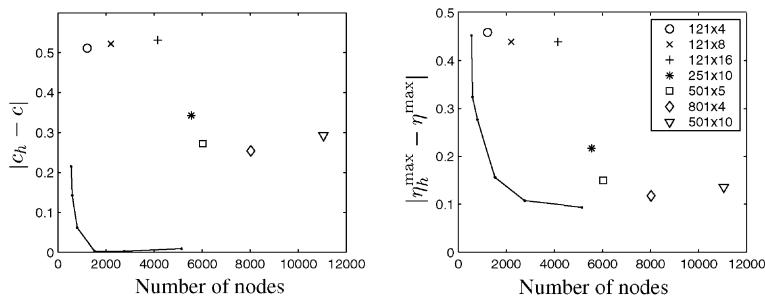


Fig. 8. Results from a simulation of Laitone's solitary wave, c is the speed of the soliton, η^{\max} is the amplitude of the soliton, and the subscript h denotes the numerically computed values. The solid line corresponds to simulations with an hr -adaptive method where the number of nodes is taken as an average over the course of a simulation, each result thus comes from a different computation with decreasing interpolation errors $\hat{\epsilon}$. The individual symbols correspond to various meshes used with r -adaptive mesh movement in the vertical.

The Laitone soliton simulation presented in Section 5.3 has been repeated, this time with the same parameters as before but now the domain is taken to be $160d$ in length, so that the significant dynamical behaviour is restricted to a far smaller proportion of the domain. The simulation is conducted for 50 time units so that the soliton is still far from the domain walls. In Fig. 8 results from both r and hr methods are presented, the legend gives the number of nodes in the horizontal and vertical for the r simulation. No attempt has been made to optimize either these choices, or the interpolation errors for the u , v and η fields used in the mesh optimization, these were reduced in a uniform manner to account for increases in the total number of nodes in each simulation. Both the speed of the soliton (which was computed using a linear least squares fit to the position of the maximum free surface height), and the maximum free surface height at the end of the simulation can be seen to be drastically improved for the hr method over simple mesh movement alone. Note that for this example the vanishing of the 'surface-layer' means that an h -adaptive method needs to modify the mesh more frequently than is necessary from error consideration, thus resulting in a non-competitive method.

7. Error measures and mesh quality

Throughout this work interpolation error has been used as a guide for anisotropic adaptivity. Although this may represent a bound on discretization error in certain situations, and hence be a

valid choice for use as an error indicator, in other situations it may be wise to consider additional or alternate measures. For example the gradient error may also be used, in the language of Section 3.3, by replacing the Hessian with the Hessian squared (D’Azevedo and Simpson, 1991). However these error measures are based upon a priori estimates and do not make use of any information on the underlying differential equation. This may be incorporated by making use of a posteriori measures (Babuška and Rheinboldt, 1978; Ainsworth and Oden, 1997), which involve the solution of local dual problems to account for the accumulation and propagation of errors through the mesh. Similar ideas are exploited in (Power et al., submitted), where an adjoint to the forward model is used to compute the sensitivities of the various fields throughout the domain. Whichever method is used to guide the mesh adaptivity it is important that anisotropic information as described in Section 3.4 be incorporated (Apel, 1999).

When a highly anisotropic mesh is used within a finite element computation, issues related to the quality of the mesh must be considered. For example it is well known that discretization errors, as well as the conditioning of resulting linear systems that must be solved as part of the solution procedure, may be adversely affected by a poor quality mesh (with quality being dependent both on the size and shape of elements in relation to solution fields). For example, early bounds on discretization errors in appropriate norms (e.g. obtained from gradient errors as opposed to the interpolation error (8)) included factors of the form $h/\sqrt{\sin(\theta)}$, where h is a measure of the mesh size and θ the minimum interior element angle (Zlámal, 1968). This factor goes to zero with element size as expected, however the bound approaches infinity for angles close to zero—this is termed the *minimum angle condition* for meshes. As a consequence angles close to π are also forbidden—the *maximum angle condition*. It was later shown by Babuška and Aziz (1976) that although this condition remained, the minimum angle condition was not essential. Therefore long thin elements are permitted provided no angles approach π . These results were extended to tetrahedral elements by Křížek (1992). It is important to note however that these non-sharp *bounds* are derived without taking into account any anisotropic behaviour in solution fields. Rippa (1992) demonstrated that optimal triangulations are those which are long (respectively, thin) in directions where the field being approximated has small (respectively, large) second derivative. This corresponds exactly to the situation of Section 4, i.e. an optimal mesh is one which is made up of (as far as possible) equilateral tetrahedra in an appropriate Riemannian space. Meshes which are made up of elements which appear of good quality in Euclidean space, e.g. from a *Delaunay* mesh generator, but are constructed with no dependence on the underlying fields being approximated, may actually therefore fall foul of maximum angle type conditions, resulting in poorer quality discretizations.

Poorly shaped elements also have an impact on the conditioning of linear systems. For example, following a finite element discretization, the ratio of the maximum and minimum eigenvalues (the *condition number*) of the resulting matrix to be inverted may be directly related to the cost of iterative solvers and the impact of roundoff errors. Again, poorly shaped elements have an adverse impact on the condition number, this time both angles near to zero and π should be avoided. However, coefficients of the underlying PDE as well as the solution fields themselves can have an impact on quality. It is conjectured here that as with interpolation and discretization errors as discussed above, a more accurate gauge of the mesh quality is achieved in an appropriate transformed space where the solution fields appear more uniform and isotropic.

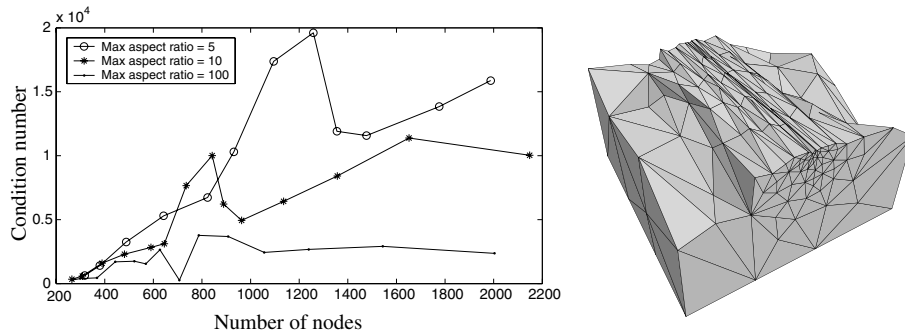


Fig. 9. Condition number of the discretization matrix against number of nodes for varying limits on the maximum aspect ratio in adapted mesh. Also shown is a portion of an example mesh corresponding to a maximum aspect ratio of 100.

As a simple demonstration the Navier–Stokes system has been set up on a unit cube with boundary conditions to impose an exponential profile on the u velocity component only

$$u(x, y, z) = \exp\left(-10\left((y - 1/2)^2 + (z - 1/2)^2\right)\right),$$

the Reynolds number corresponding to the scale of which is 10 here, the time step is 10^{-3} . In Fig. 9 a plot of the condition number of the discretized momentum equation matrix to be inverted, against number of nodes in the adapted mesh is presented. The results were obtained after 10 adapts (20 time steps) by varying a constraint on the maximum aspect ratio (measured in Euclidean physical space) and also by varying the total number of nodes achieved by altering the interpolation errors $\hat{\epsilon}$. Also shown is a sample mesh in the case of a maximum aspect ratio of 100. It can be seen that the use of more anisotropy in the mesh actually improves the conditioning of the resulting system. Note also that for an equivalent number of nodes a more anisotropic mesh should result in smaller errors, thus if plotted against this the result would be even more pronounced. For further details refer to (Fried, 1972; Strang and Fix, 1973; Shewchuk, 2002). It should be noted that these comments, valid for symmetric matrices and conjugate gradient based methods, become less valid for GMRES as the system being inverted becomes more non-normal (is non-commutative with its transpose). For example, as happens when a larger Reynolds number is used and when the advection term is treated implicitly. Although they still may be regarded as a guide provided the Reynolds number is not too large. More suitable bounds on convergence rates may be obtained by considering pseudospectra (Reddy and Trefethen, 1994; Embree, 1999).

8. Concluding remarks

Various alternate approaches for performing mesh adaptivity and their application to numerical ocean modelling have been described. Adaptive unstructured mesh ocean models have many attractive features, and hence their further investigation is crucial. A combination of both mesh optimization and mesh movement (resulting in an hr method) offers increased robustness, flexibility, and optimality. Background theory on each of these methods, possibilities for combining

them and some examples have been presented. It was also discussed how the quality of the mesh as measured in a transformed space may give more useful results with regards the important issues of discretization error and matrix conditioning. It was argued that as well as allowing the more efficient use of finite computational resources, the correct use of adaptive anisotropic meshes may result in an easier to solve and more accurate discrete system than standard fixed isotropic mesh methods. Work is ongoing on further analysis of these issues and the application of the techniques presented to realistic oceanic simulations. A long term additional goal is the inclusion of spectral elements and ultimately a combined *hrp*-adaptive method (Babuška and Suri, 1990).

At the time of writing the current status of this work is that the model introduced in (Ford et al., 2004) is able to simulate flows in extremely complex 3-D domains (Gorman et al., submitted), in the presence of buoyancy and rotation, on adaptive meshes employing the optimization techniques described in Section 4 (see Pain et al., 2004 for further examples). The model also makes use of mesh movement in the vertical, as introduced in Sections 5.3 and 6, to allow the modelling of tides for example. The use of more general *r*-adaptivity in 3-D is currently under development and will be the subject of future publications.

Acknowledgments

This work has been carried out under NERC grant NER/A/S/2000/00375. The authors would like to acknowledge the assistance provided by C.R.E de Oliveira, M.D. Eaton, and A.P. Umpleby. The lead author would also like to thank C.J. Budd and J.F. Williams for many stimulating discussions related to this work.

Appendix A. Supplementary data

Supplementary data associated with this article can be found, in the online version, at [doi:10.1016/j.ocemod.2004.07.007](https://doi.org/10.1016/j.ocemod.2004.07.007).

References

- Ainsworth, M., Oden, J.T., 1997. A posteriori error estimation in finite element analysis. *Comput. Methods Appl. Mech. Eng.* 142, 1–88.
- Ait-Ali-Yahia, D., Habashi, W.G., Tarn, A., Vallet, M.G., Fortin, M., 1996. A directionally adaptive methodology using an edge-based error estimate on quadrilateral grids. *Int. J. Numer. Methods Fluids* 32, 673–690.
- Apel, T., 1999. *Anisotropic finite elements: Local estimates and applications*. Teubner, Stuttgart.
- Askes, H., Rodríguez-Ferran, A., 2001. A combined *hr*-adaptive scheme based on domain subdivision. Formulation and linear examples. *Inter. J. Numer. Methods Eng.* 51, 253–273.
- Babuška, I., Aziz, A.K., 1976. On the angle condition in the finite element method. *SIAM J. Numer. Anal.* 13, 214–226.
- Babuška, I., Rheinboldt, W.C., 1978. Error estimates for adaptive finite element computations. *SIAM J. Numer. Anal.* 15, 736–754.
- Babuška, I., Suri, M., 1990. The *p* and *h-p* version of the finite element method, an overview. *Comput. Methods Appl. Mech. Eng.* 80, 5–26.

- Baines, M.J., 1994. *Moving finite elements*. Oxford University Press.
- Brenan, K.E., Campbell, S.L., Petzold, L.R., 1989. *Numerical solution of initial value problems in differential–algebraic equations*. North-Holland, Amsterdam.
- Burchard, H., Beckers, J.M., 2004. Non-uniform adaptive vertical grids in one-dimensional numerical ocean models. *Ocean Modell.* 6, 51–81.
- D’Azevedo, E.F., 1991. Optimal triangular mesh generation by coordinate transformation. *SIAM J. Sci. Stat. Comput.* 12, 755–786.
- D’Azevedo, E.F., Simpson, R.B., 1991. On optimal triangular meshes for minimizing the gradient error. *Numer. Math.* 59, 321–348.
- de Boor, C., 1973. Good approximation by splines with variable knots. II. In: *Conference on the Numerical Solution of Differential Equations*. Springer Lecture Notes 363, pp. 12–20.
- Dompierre, J., Vallet, M.G., Bourgault, Y., Fortin, M., Habashi, W.G., 2002. Anisotropic mesh adaption: towards user-independent, mesh-independent and solver-independent CFD. Part III. Unstructured meshes. *Int. J. Numer. Methods Fluids* 39, 675–702.
- Embree, M., 1999. *How descriptive are GMRES convergence bounds*. Oxford University Computing Laboratory Numerical Analysis Report 99/08.
- Ford, R., Pain, C.C., Piggott, M.D., Goddard, A.J.H., de Oliveira, C.R.E., Umpleby, A.P., 2004. A non-hydrostatic finite element model for three-dimensional stratified oceanic flows. Part I: Model formulation. *Mon. Weath. Rev.* 132, 12, 2816–2831.
- Fried, L., 1972. Condition of finite element matrices generated from nonuniform meshes. *AIAA J.* 10, 219–221.
- Gelfand, I.M., Fomin, S.V., 1963. *Calculus of variations*. Prentice-Hall, Englewood Cliffs, NJ.
- Gorman, G.J., Piggott, M.D., Pain, C.C., de Oliveira, C., Umpleby, A., Goddard, A.J.H., submitted. Optimal bathymetric representation through constrained unstructured mesh adaptivity. *Ocean Modell.*
- Gresho, P.M., Sani, R., 1987. On pressure boundary conditions for the incompressible Navier–Stokes equations. *Int. J. Numer. Methods Fluids* 7, 1111–1145.
- Gresho, P.M., Sani, R.L., 1998. *Incompressible flow and the finite element method*. John Wiley and Sons, New York.
- Griffies, S.M., Böning, C., Bryan, F.O., Chassignet, E.P., Gerdes, R., Hasumi, H., Hirst, A., Treguier, A.M., Webb, D., 2000. Developments in ocean climate modelling. *Ocean Modell.* 2, 123–192.
- Haidvogel, D.B., Beckmann, A., 1999. *Numerical ocean circulation modeling*. Imperial College Press.
- Huang, W., Ren, Y., Russell, R.D., 1994. Moving mesh partial differential equations (MMPDES) based on the equidistribution principle. *SIAM J. Numer. Anal.* 31, 709–730.
- Huang, W., Russell, R.D., 1999. Moving mesh strategy based on a gradient flow equation for two-dimensional problems. *SIAM J. Sci. Comput.* 20, 998–1015.
- Huerta, A., Rodríguez-Ferran, A., Diez, P., Sarrate, J., 1999. Adaptive finite element strategies based on error assesment. *Int. J. Numer. Methods Eng.* 46, 1803–1818.
- Křížek, M., 1992. On the maximum angle condition for linear tetrahedral elements. *SIAM J. Numer. Anal.* 29, 513–520.
- Laitone, E.V., 1960. The second approximation to choidal and solitary waves. *J. Fluid Mech.* 9, 430–444.
- Lang, J., Cao, W., Huang, W., Russell, R.D., 2003. A two-dimensional moving finite element method with local refinement based on a posteriori error estimates. *Appl. Numer. Math.* 46, 75–94.
- Löhner, R., Morgan, K., Zienkiewicz, K.O., 1985. An adaptive finite element procedure for compressible high speed flows. *Comput. Methods Appl. Mech. Eng.* 51, 441–465.
- Oden, J.T., Prudhomme, S., 2001. Goal-oriented error estimation and adaptivity for the finite element method. *Comput. Math. Applic.* 41, 735–756.
- Pain, C.C., Piggott, M.D., Fang, A.J.H.G.F., Gorman, G.J., Marshall, D.P., Eaton, M.D., Power, P.W., de Oliveira, C.R.E., 2004. Three-dimensional unstructured mesh ocean modelling. *Ocean Modell.* (this volume).
- Pain, C.C., Umpleby, A.P., de Oliveira, C.R.E., Goddard, A.J.H., 2001. Tetrahedral mesh optimisation and adaptivity for steady-state and transient finite element calculations. *Comput. Methods Appl. Mech. Eng.* 190, 3771–3796.
- Peraire, J., Vahdati, M., Morgan, K., Zienkiewicz, O.C., 1987. Adaptive remeshing for compressible flow computations. *J. Comput. Phys.* 72, 449–466.
- Pierce, N.A., Giles, M.B., 2000. Adjoint recovery of superconvergent functionals from pde approximations. *SIAM Rev.* 42, 247–264.

- Power, P., Pain, C.C., Piggott, M.D., Gorman, G., Marshall, D., Goddard, A., submitted. Sensitivity based error norms for adaptive mesh ocean modelling. *Ocean Modell.*
- Ramaswamy, B., 1990. Numerical simulation of unsteady viscous free surface flow. *J. Comput. Phys.* 90, 396–430.
- Reddy, S.C., Trefethen, L.N., 1994. Pseudospectra of the convection-diffusion operator. *SIAM J. Appl. Math.* 54, 1634–1649.
- Rippa, S., 1992. Long and thin elements can be good for linear interpolation. *SIAM J. Numer. Anal.* 29, 257–270.
- Schultz, M.H., 1969. L^∞ -multivariate approximation theory. *SIAM J. Numer. Anal.* 6, 161–183.
- Shewchuk, J.R., 2002. What is a good linear finite element? Interpolation, conditioning, anisotropy, and quality measures, preprint.
- Strang, G., Fix, G.J., 1973. *An analysis of the Finite Element Method*. Prentice-Hall, Englewood Cliffs, NJ.
- Strouboulis, T., Oden, J.T., 1990. A posteriori error estimation of finite element approximations in fluid mechanics. *Comput. Methods Appl. Mech. Eng.* 78, 201–242.
- Zlámal, M., 1968. On the finite element method. *Numer. Math.* 12, 394–409.



An efficient Eulerian finite element method for the shallow water equations

Emmanuel Hanert ^{a,b,*}, Daniel Y. Le Roux ^c,
Vincent Legat ^b, Eric Deleersnijder ^a

^a *Institut d'Astronomie et de Géophysique G. Lemaître, Université Catholique de Louvain, 2 Chemin du Cyclotron, B-1348 Louvain-la-Neuve, Belgium*

^b *Centre for Systems Engineering and Applied Mechanics, Université Catholique de Louvain, 4 Avenue Georges Lemaître, B-1348 Louvain-la-Neuve, Belgium*

^c *Département de Mathématiques et de Statistique, Université Laval, Québec, QC, Canada G1K 7P4*

Received 14 November 2003; received in revised form 2 March 2004; accepted 17 June 2004

Available online 3 November 2004

Abstract

The accuracy and efficiency of an Eulerian method is assessed by solving the non-linear shallow water equations and compared with the performances of an existing semi-Lagrangian method. Both methods use a linear non-conforming finite element discretization for velocity and a linear conforming finite element discretization for surface elevation. This finite element pair is known to be computationally efficient and free of pressure modes. The model equations are carefully derived and a comparison is performed by simulating the propagation of slow Rossby waves in the Gulf of Mexico. Simulations show that the Eulerian model performs well and gives results comparable to high order semi-Lagrangian schemes using kriging interpolators.

© 2004 Elsevier Ltd. All rights reserved.

Keywords: Finite elements; Eulerian; Semi-Lagrangian; Shallow water equations; Rossby waves; Non-conforming linear interpolation; Kriging

* Corresponding author. Address: Institut d'Astronomie et de Géophysique G. Lemaître, Université Catholique de Louvain, 2 Chemin du Cyclotron, B-1348 Louvain-la-Neuve, Belgium. Tel.: +32 10 472354.

E-mail address: hanert@astr.ucl.ac.be (E. Hanert).

1. Introduction

The ocean circulation may be represented as the interaction of many different physical processes in a domain of complex shape. Those interactions are often non-linear and spatially localized. As a consequence, a numerical model of the world ocean should be able to deal with non-linearities, irregular geometries and localized phenomena.

Unstructured grids permit to accurately represent complex domains. Their flexibility also allows to achieve high resolution in regions of interest thanks to suitable grid refinements. In the last years an increased interest has been paid toward ocean or coastal models using unstructured meshes. For those models, the spatial discretization is based either on finite elements (e.g. LeProvost et al., 1994; Myers and Weaver, 1995; Lynch et al., 1996; LeRoux et al., 2000; Legrand et al., 2001; Hanert et al., 2003; Nechaev et al., 2003; Danilov et al., 2004), spectral elements (e.g. Iskandarani et al., 1995; Iskandarani et al., 2003) or finite volumes (Casulli and Walters, 2000; Chen et al., 2003).

The numerical treatment of non-linear advection terms in the mass and momentum equations can be done either with an Eulerian, a Lagrangian or a semi-Lagrangian scheme. In Eulerian schemes, the evolution of the system is monitored from fixed positions in space. As a consequence, those methods are easy to implement as all the variables are computed at fixed grid points in the domain. However, their accuracy is often not so high as Lagrangian methods where the information is integrated along characteristics. Eulerian methods are used in most ocean circulation models. In Lagrangian schemes, the evolution of the system is monitored from fluid parcels that move with the flow. Such schemes often allow much larger time steps than Eulerian schemes. Their main disadvantage is that the distribution of fluid parcels can quickly become highly non-uniform which can render the scheme inaccurate. Such a problem can be circumvented by using semi-Lagrangian schemes. The idea behind those schemes is to choose a completely new set of parcels at every time step. This set of parcels is chosen such that they arrive exactly on the nodes of a regularly spaced mesh at the end of each time step. This method has proved to work particularly well in atmosphere modelling, especially when combined with a semi-implicit scheme (Robert, 1981; Robert, 1982; Robert et al., 1985). An extensive review of the applications of semi-Lagrangian methods to atmospheric problems is provided by Staniforth and Côté (1990). In ocean modelling, Behrens (1998) and LeRoux et al. (2000) showed that the combination of semi-Lagrangian schemes and finite elements could be an interesting approach.

In the present study, we compare an Eulerian and a semi-Lagrangian finite-element shallow water model to assess both approaches in the context of ocean modelling. Both models use a linear non-conforming approximation for velocity and a linear conforming approximation for elevation. Such a finite element pair is denoted $P_1^{\text{NC}} - P_1$. Non-conforming finite elements have been introduced by Crouzeix and Raviart (1973) to solve Stokes equations. They have proved to be well suited to represent transport processes thanks to an important flexibility and the ability to allow upwind weighed formulations (Hanert et al., 2004). The combination of linear conforming and non-conforming finite elements has first been studied by Hua and Thomasset (1984) to solve the shallow water equations. They showed that this finite element pair is computationally efficient and properly models the dispersion of the inertia-gravity waves. LeRoux (submitted for publication) performed a dispersion analysis and showed that the discrete frequency was monotonic for all resolutions.

The paper is organized as follows. We first present the model equations and the finite element discretization in Sections 2 and 3 respectively. The $P_1^{\text{NC}} - P_1$ finite element pair is described in Section 4. The Eulerian and semi-Lagrangian schemes are derived in Sections 5 and 6 respectively. Section 7 presents the numerical experiments and a discussion of the methods performances. Conclusions are given in Section 8.

2. Governing equations

We consider the following formulation of the shallow water problem: Let Ω be the two-dimensional model domain, we seek the velocity $u(\mathbf{x}, t)$ and the surface elevation $\eta(\mathbf{x}, t)$ which are solutions of the following equations:

$$\frac{\partial \eta}{\partial t} + \nabla \cdot [(h + \eta)\mathbf{u}] = 0, \quad (1)$$

$$\frac{\partial \mathbf{u}}{\partial t} + \mathbf{u} \cdot \nabla \mathbf{u} + f\mathbf{k} \times \mathbf{u} = -g\nabla \eta, \quad (2)$$

where h is the reference depth of the fluid, f is the Coriolis parameter, \mathbf{k} is a unit vector in the vertical direction, g is the gravitational acceleration, ∇ is the two-dimensional gradient operator.

Another form of Eqs. (1) and (2) can be obtained by introducing total derivatives and writing the mass equation in terms of the logarithm of $h + \eta$:

$$\frac{D \ln(h + \eta)}{Dt} + \nabla \cdot \mathbf{u} = 0, \quad (3)$$

$$\frac{D\mathbf{u}}{Dt} + f\mathbf{k} \times \mathbf{u} = -g\nabla \eta, \quad (4)$$

where $D/Dt = \partial/\partial t + \mathbf{u} \cdot \nabla$ denotes the total or Lagrangian derivative. Eqs. (3) and (4) will be used to derive the semi-Lagrangian scheme. Obviously, the two sets of equations are strictly equivalent in the continuous limit, while in the numerical or discrete limit, they are no longer equivalents.

The selection of the logarithmic form of the mass equation follows the approach of LeRoux et al. (2000). Such a formulation of the continuity equation may not appear obvious. First of all, the logarithmic term may be problematic as it cannot be computed exactly in a numerical scheme. The resulting semi-Lagrangian scheme is then likely to be non-conservative. The same conservation issue arises from the interpolation procedures that are also generally non-conservative. Therefore, the conservation has to be explicitly enforced at each time step by adding a constant elevation correction to the computed elevation field. This is a classical way to proceed even if other strategies exist to deliver conservative semi-Lagrangian schemes. The interest of the logarithmic form of the mass equation is to get a linear divergence term at the prize of a linearization of the logarithm. Other forms could also be selected (e.g. Behrens, 1998) but will not be analyzed here.

For both sets of equations, the solution is specified by imposing no normal flow boundary conditions ($\mathbf{u} \cdot \mathbf{n} = 0$ on $\partial\Omega$) and initial conditions.

3. Finite element spatial discretization

Let \mathcal{P} be a partition of the domain Ω into N_E disjoint open elements Ω_e :

$$\bar{\Omega} = \bigcup_{e=1}^{N_E} \bar{\Omega}_e \quad \text{and} \quad \Omega_e \cap \Omega_f = \emptyset \quad \text{for } e \neq f,$$

where $\bar{\Omega}$ is the closure of Ω . Each element Ω_e has a boundary $\partial\Omega_e$ and the outward unit normal to $\partial\Omega_e$ is \mathbf{n}_e . Let Γ be the ensemble of interelement boundaries $\Gamma_l = \partial\Omega_e \cap \partial\Omega_f$ with $e > f$ inside the domain, with all possible combinations:

$$\bar{\Gamma} = \bigcup_{l=1}^{N_\Gamma} \bar{\Gamma}_l \quad \text{and} \quad \Gamma_l \cap \Gamma_m = \emptyset \quad \text{for } l \neq m,$$

where N_Γ is the number of elements in Γ . Each $\Gamma_l \in \Gamma$ is associated with a unique unit normal vector \mathbf{n} which points from Ω_e to Ω_f . In this paper, \mathcal{P} will be a triangulation of non-overlapping triangles. The total number of vertices and segments in the triangulation are denoted N_V and N_S .

The variational or weak formulation of Eqs. (1) and (2) is built in such a way that the solution for elevation is continuous everywhere whereas the solution for velocity can be discontinuous between the elements Ω_e . It requires continuity constraints on the solution values and reads:

Find $\eta(\mathbf{x}, t) \in \mathcal{E}$ and $\mathbf{u}(\mathbf{x}, t) \in \mathcal{U}$ such that

$$\sum_{e=1}^{N_E} \int_{\Omega_e} \left(\frac{\partial \eta}{\partial t} \hat{\eta} - (h + \eta) \mathbf{u} \cdot \nabla \hat{\eta} \right) d\Omega + \sum_{e=1}^{N_E} \int_{\partial\Omega_e} (h + \eta) \hat{\eta} \mathbf{u} \cdot \mathbf{n}_e d\Gamma = 0 \quad \forall \hat{\eta} \in \mathcal{E}, \quad (5)$$

$$\begin{aligned} \sum_{e=1}^{N_E} \int_{\Omega_e} \left(\frac{\partial \mathbf{u}}{\partial t} \cdot \hat{\mathbf{u}} - (\nabla \cdot (\mathbf{u}\hat{\mathbf{u}})) \cdot \mathbf{u} + f(\mathbf{k} \times \mathbf{u}) \cdot \hat{\mathbf{u}} + g \nabla \eta \cdot \hat{\mathbf{u}} \right) d\Omega + \sum_{e=1}^{N_E} \int_{\partial\Omega_e} (\mathbf{u}\mathbf{u} \cdot \mathbf{n}_e) \cdot \hat{\mathbf{u}} d\Gamma \\ + \sum_{l=1}^{N_\Gamma} \int_{\Gamma_l} [\mathbf{u}] \cdot [\mathbf{a}(\hat{\mathbf{u}})] d\Gamma = 0 \quad \forall \hat{\mathbf{u}} \in \mathcal{U}, \end{aligned} \quad (6)$$

where $[\mathbf{s}] = \mathbf{s}|_{\Omega_e} - \mathbf{s}|_{\Omega_f}$ is the jump of \mathbf{s} on an interior edge Γ_l , $\mathbf{s}|_{\Omega_e}$ denotes the restriction of \mathbf{s} on Ω_e , and \mathcal{E} and \mathcal{U} are suitable functional spaces. The test functions $\hat{\eta}$ and $\hat{\mathbf{u}}$ belong to \mathcal{E} and \mathcal{U} respectively. The last integral in (6) is a continuity constraint that weakly imposes the continuity of the velocity between elements. The function \mathbf{a} has to be selected to balance the continuity requirement versus the fulfilment of the differential equations in the weak formulation. It reads:

$$\mathbf{a}(\hat{\mathbf{u}}) = \begin{cases} \mathbf{u} \cdot \mathbf{n}(\lambda - 1/2) \hat{\mathbf{u}} & \text{on } \Omega_e, \\ \mathbf{u} \cdot \mathbf{n}(\lambda + 1/2) \hat{\mathbf{u}} & \text{on } \Omega_f, \end{cases}$$

where $\lambda \in [-1/2, 1/2]$. Centered and upwind momentum advection schemes are obtained by choosing $\lambda = 0$ and $\lambda = \frac{1}{2} \text{sign}(\mathbf{u}(\mathbf{x}) \cdot \mathbf{n}(\mathbf{x}))$ respectively. In the following, we will use the upwind parametrization that is usually selected (Houston et al., 2000; Hanert et al., 2004).

With this choice for the weight function and some standard algebra (Houston et al., 2000; Hanert et al., 2004), the variational formulation may be rewritten as:

Find $\eta(\mathbf{x}, t) \in \mathcal{E}$ and $\mathbf{u}(\mathbf{x}, t) \in \mathcal{U}$ such that

$$\begin{aligned} \sum_{e=1}^{N_E} \int_{\Omega_e} \left(\frac{\partial \eta}{\partial t} \hat{\eta} - (h + \eta) \mathbf{u} \cdot \nabla \hat{\eta} \right) d\Omega + \sum_{l=1}^{N_\Gamma} \int_{\Gamma_l} \left(\langle (h + \eta) \mathbf{u} \cdot \mathbf{n} \rangle [\hat{\eta}] + [(h + \eta) \mathbf{u} \cdot \mathbf{n}] \langle \hat{\eta} \rangle \right) d\Gamma \\ = 0 \quad \forall \hat{\eta} \in \mathcal{E}, \end{aligned} \quad (7)$$

$$\begin{aligned} \sum_{e=1}^{N_E} \int_{\Omega_e} \left(\frac{\partial \mathbf{u}}{\partial t} \cdot \hat{\mathbf{u}} - (\nabla \cdot (\mathbf{u} \hat{\mathbf{u}})) \cdot \mathbf{u} + f(\mathbf{k} \times \mathbf{u}) \cdot \hat{\mathbf{u}} + g \nabla \eta \cdot \hat{\mathbf{u}} \right) d\Omega + \sum_{l=1}^{N_\Gamma} \int_{\Gamma_l} \langle \mathbf{u} \mathbf{u} \cdot \mathbf{n} \rangle_\lambda \cdot [\hat{\mathbf{u}}] d\Gamma \\ = 0 \quad \forall \hat{\mathbf{u}} \in \mathcal{U}, \end{aligned} \quad (8)$$

where $\langle \mathbf{s} \rangle$ and $\langle \mathbf{s} \rangle_\lambda$ denote the average and weighed average of \mathbf{s} on the segment Γ_l respectively, with:

$$\begin{aligned} \langle \mathbf{s} \rangle &= \frac{1}{2} (\mathbf{s}_{|\Omega_e} + \mathbf{s}_{|\Omega_f}), \\ \langle \mathbf{s} \rangle_\lambda &= (1/2 + \lambda) \mathbf{s}_{|\Omega_e} + (1/2 - \lambda) \mathbf{s}_{|\Omega_f}. \end{aligned}$$

A finite element approximation to the exact solution of Eqs. (1) and (2) is found by replacing η and \mathbf{u} with finite element approximations η^h and \mathbf{u}^h in (7) and (8). Those approximations respectively belong to finite dimensional spaces $\mathcal{E}^h \subset \mathcal{E}$ and $\mathcal{U}^h \subset \mathcal{U}$. They read:

$$\begin{aligned} \eta &\approx \eta^h = \sum_{i=1}^{N_V} \eta_i \phi_i, \\ \mathbf{u} &\approx \mathbf{u}^h = \sum_{j=1}^{N_S} \mathbf{u}_j \psi_j, \end{aligned}$$

where η_i and \mathbf{u}_j represent elevation and velocity nodal values, and ϕ_i and ψ_j represent the elevation and velocity shape functions associated with a particular node. The nodal values are then computed by using the Galerkin procedure which amounts to replacing $\hat{\eta}$ by ϕ_i and $\hat{\mathbf{u}}$ by $(\psi_j, 0)$ and $(0, \psi_j)$ in Eqs. (7) and (8) respectively, for $1 \leq i \leq N_V$ and $1 \leq j \leq N_S$.

4. The non-conforming mixed $P_1^{\text{NC}} - P_1$ discretization

In this study, the elevation and velocity variables are approximated by linear conforming (P_1) and linear non-conforming (P_1^{NC}) shape functions respectively (Fig. 1). Elevation nodes are thus lying on the vertices of the triangulation and velocity nodes are located at mid-segments. With this choice of shape functions, the discrete elevation field is continuous everywhere whereas the discrete velocity field is only continuous across triangle boundaries at mid-side nodes and discontinuous everywhere else around a triangle boundary. A major advantage of non-conforming shape functions is their orthogonality property:

$$\int_{\Omega} \psi_p \psi_q d\Omega = \frac{A_q}{3} \delta_{pq},$$

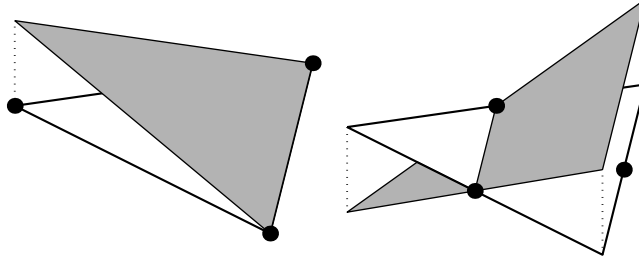


Fig. 1. Linear conforming (left) and non-conforming (right) shape functions.

where A_q is the area of the support of ψ_q , and δ_{pq} is the Kronecker delta. Such an unusual property increases the computational efficiency of the numerical model. Like the elevation, the depth h is discretized with linear conforming shape functions.

To improve the efficiency of the scheme, it may appear natural to perform the following approximation in the variational formulation (7) and (8):

$$\underbrace{\int_{\Gamma_l} \langle (h + \eta) \mathbf{u} \cdot \mathbf{n} \rangle [\phi_i] d\Gamma}_{=0} + \int_{\Gamma_l} [(h + \eta^h) \mathbf{u}^h \cdot \mathbf{n}] \langle \phi_i \rangle d\Gamma \simeq 0. \quad (9)$$

As P_1 shape functions are continuous, the jump of the elevation shape function vanishes and the first term in (9) is exactly equal to zero. The second term is neglected in order to enforce mass conservation. Indeed, the thickness flux is discontinuous between triangles and neglecting the second integral amounts to weakly impose its continuity. As a result, mass conservation is guaranteed at the cost of a small loss of accuracy.

A second approximation in the formulation (7) and (8) amounts to use a global linear approximation for the product of \mathbf{u}^h with f :

$$\int_{\Omega_e} f(\mathbf{k} \times \mathbf{u}^h) \psi_j d\Omega = \int_{\Omega_e} f \sum_{i=1}^{N_S} (\mathbf{k} \times \mathbf{u}_i) \psi_i \psi_j d\Omega \simeq \int_{\Omega_e} \underbrace{\sum_{i=1}^{N_S} f_i(\mathbf{k} \times \mathbf{u}_i) \psi_i}_{(f\mathbf{k} \times \mathbf{u})^h} \psi_j d\Omega, \quad (10)$$

where f_j represent the value of the Coriolis parameter at a velocity node. Eq. (10) greatly simplifies the algebra and has a small impact on the accuracy of the solution since f varies very smoothly.

To summarize, the space discretized equations for the Eulerian formulation simply read:

$$\sum_{e=1}^{N_E} \int_{\Omega_e} \left(\frac{\partial \eta^h}{\partial t} \phi_i - (h + \eta^h) \mathbf{u}^h \cdot \nabla \phi_i \right) d\Omega = 0 \quad \text{for } 1 \leq i \leq N_V, \quad (11)$$

$$\begin{aligned} & \sum_{e=1}^{N_E} \int_{\Omega_e} \left(\frac{\partial \mathbf{u}^h}{\partial t} \psi_j - \mathbf{u}^h \nabla \cdot (\mathbf{u}^h \psi_j) + (f\mathbf{k} \times \mathbf{u})^h \psi_j + g \nabla \eta^h \psi_j \right) d\Omega \\ & + \sum_{l=1}^{N_\Gamma} \int_{\Gamma_l} \langle \mathbf{u}^h \mathbf{u}^h \cdot \mathbf{n} \rangle_z [\psi_j] d\Gamma = 0 \quad \text{for } 1 \leq j \leq N_S. \end{aligned} \quad (12)$$

The last boundary term can be interpreted as follows. Weak continuity of the normal flow through the segment Γ_l between adjacent elements Ω_e and Ω_f is imposed in the usual way of the Discontinuous Galerkin formulation. For a so-called fully upwind scheme ($\lambda = \frac{1}{2} \text{sign}(\mathbf{u} \cdot \mathbf{n})$), the continuity is enforced as a weak inlet boundary condition for Ω_e if the characteristics that go through Γ_l are going in Ω_e . This is fully in line with the mathematical theory of hyperbolic partial differential equations and the presentation of the Discontinuous Galerkin formulation in the pioneering paper of LeSaint and Raviart (1974).

The proposed Eulerian formulation strictly conserves mass but does not exactly conserve the total energy of the flow. The formulation appropriate for semi-Lagrangian time stepping can be obtained by applying the same spatial discretization procedure to Eqs. (3) and (4).

5. Eulerian scheme

To obtain an Eulerian discretization of the nonlinear shallow water equations, (11) and (12) still need to be discretized in time. In order to simplify the notations, we present the temporal discretization of (1) and (2). So, for a given time step $\Delta t = t^{n+1} - t^n$, we obtain:

$$\frac{\mathbf{u}^{n+1} - \mathbf{u}^n}{\Delta t} + \mathbf{u}^n \cdot \nabla \mathbf{u}^n + f \mathbf{k} \times (\beta \mathbf{u}^{n+1} + (1 - \beta) \mathbf{u}^n) + g(\alpha \nabla \eta^{n+1} + (1 - \alpha) \nabla \eta^n) = 0, \quad (13)$$

$$\frac{\eta^{n+1} - \eta^{n-1}}{2 \Delta t} + \nabla \cdot (\gamma h \mathbf{u}^{n+1} + (1 - \gamma) h \mathbf{u}^{n-1}) + \nabla \cdot (\eta^n \mathbf{u}^n) = 0, \quad (14)$$

where α , β and γ are implicity coefficients in $[0, 1]$ used to vary the time centering of the gradient, Coriolis and divergence terms respectively.

In Eqs. (13) and (14), all linear terms are discretized with a so-called θ -scheme and the non-linear terms are treated explicitly. In such an approach, the most constraining terms (i.e. those responsible for the propagation of inertia-gravity waves) can be treated implicitly. In particular, the Coriolis term is always discretized semi-implicitly. The value of the other parameters is problem dependent and is given below where numerical experiments are described. A leap frog time scheme is used in Eq. (14) to discretize the term $\nabla \cdot (\eta^n \mathbf{u}^n)$. Indeed, the scheme would be unconditionally unstable if an Euler scheme was used instead. However, when the surface-elevation is small compared to the depth of the fluid, i.e. $\eta \ll h$, the term $\nabla \cdot (\eta^n \mathbf{u}^n)$ may be neglected in (14) and an Euler scheme can then be used in the mass equation. The divergence term $\nabla \cdot (h \mathbf{u})$ is then discretized at time steps $n + 1$ and n instead of $n + 1$ and $n - 1$. It should be noted that treating the non-linear terms explicitly, does not lead to very constraining stability conditions for large scale applications. However, for applications that require high resolution, it may be penalizing.

After replacing η^h and \mathbf{u}^h by their expression in terms of the nodal values in Eqs. (11) and (12) and applying the temporal discretization described above, the following set of linear equations is obtained:

$$\begin{pmatrix} \mathbf{B}_{UU} & \mathbf{G}_{UH} \\ -\mathbf{D}_{HU} & \mathbf{M}_{HH} \end{pmatrix} \begin{pmatrix} \mathbf{U}^{n+1} \\ \mathbf{H}^{n+1} \end{pmatrix} = \begin{pmatrix} \mathbf{R}_U \\ \mathbf{R}_H \end{pmatrix}, \quad (15)$$

where U^{n+1} and H^{n+1} are the nodal values vectors, defined as:

$$U^{n+1} = \begin{pmatrix} u_i \\ v_i \end{pmatrix} \quad \text{and} \quad H^{n+1} = (\eta_j),$$

with $1 \leq i \leq N_S$ and $1 \leq j \leq N_V$. The matrix in the left hand side (lhs) of (15) and the vector in the right hand side (rhs) of (15) are explicitly written in [Appendix A](#).

Thanks to the orthogonality of linear non-conforming shape functions, the matrix B_{UU} is composed of four diagonal sub-matrices. Its inverse can thus be easily computed. The solution vector for the velocity is expressed from (15) as:

$$U^{n+1} = -B_{UU}^{-1}G_{UH}H^{n+1} + B_{UU}^{-1}R_U, \tag{16}$$

and then substituted in the mass balance equation, to give:

$$\underbrace{(M_{HH} + D_{HU}B_{UU}^{-1}G_{UH})}_{\equiv A_{HH}} H^{n+1} = R_H + D_{HU}B_{UU}^{-1}R_U, \tag{17}$$

where the matrix A_{HH} is a sparse matrix (as shown in [Fig. 2](#)) having an average of 13 non-zero entries per line.

A linear solver is only required to solve [Eq. \(17\)](#). Once the elevation nodal values are obtained, the velocity nodal values are computed explicitly from [\(16\)](#). The substitution greatly reduces the computational cost as we solve a system of only N_V equations instead of $2N_S + N_V$, i.e. approximately $7N_V$ equations. [Fig. 2](#) shows the sparsity patterns of the initial and final system of equations. Both matrices are represented on the same scale. A generalized minimal residual iterative solver ([Saad and Schultz, 1986](#)) has been selected as A_{HH} is a nonsymmetric matrix in view of the Coriolis term.

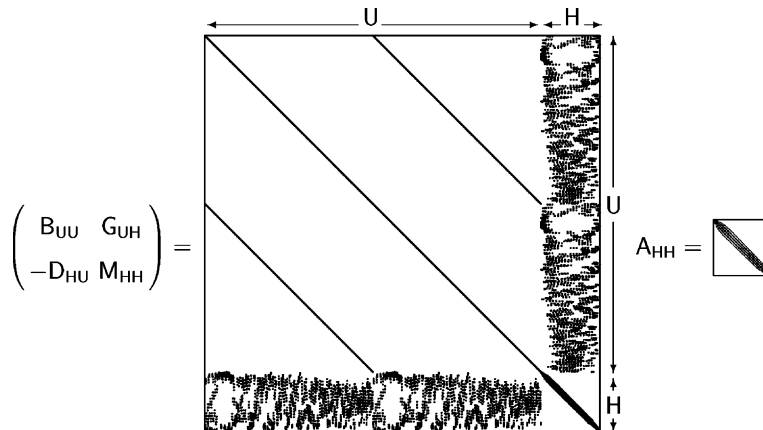


Fig. 2. Sparsity patterns of the system matrix before (left) and after (right) the substitution procedure. Both matrices are represented on the same scale.

6. Semi-Lagrangian scheme

In the semi-Lagrangian method, total derivatives are treated as time differences along particles trajectories while preserving the gridpoint nature of Eulerian schemes. This is achieved by selecting a specific set of fluid parcels at each time step and requiring that they arrive at mesh nodes at the end of the time step. Therefore, the total derivative of a function f is simply the value of f at the arrival point (a mesh node) minus the value of f at the departure point (usually not a mesh node), divided by Δt . By tracking back fluid parcels in time, it is possible to locate their upstream positions at previous time steps. An interpolation formula is then needed to determine the upstream value of the advected quantity at the departure points.

The temporal discretization used for the semi-Lagrangian scheme reads:

$$\frac{\mathbf{u}^{n+1} - \mathbf{u}_d^n}{\Delta t} + f\mathbf{k} \times (\beta\mathbf{u}^{n+1} + (1 - \beta)\mathbf{u}_d^n) + g(\alpha\nabla\eta^{n+1} + (1 - \alpha)\nabla\eta_d^n) = 0, \quad (18)$$

$$\frac{(\ln(h + \eta))^{n+1} - (\ln(h + \eta))_d^n}{\Delta t} + \nabla \cdot (\gamma\mathbf{u}^{n+1} + (1 - \gamma)\mathbf{u}_d^n) = 0, \quad (19)$$

where the subscript d denotes the evaluation at the departure point and the absence of subscript denotes evaluation at the arrival point. The coefficients α , β and γ are defined as in the Eulerian case. It should be noted that semi-Lagrangian discretizations generally allow the use of larger time steps than Eulerian discretizations.

As for the Eulerian scheme, we substitute \mathbf{u} in terms of η in the continuity equation at the discrete level. Since Eq. (19) is weakly nonlinear due to the logarithm, a Newton's procedure has to be used to linearized it. An Helmholtz equation for the elevation is then produced.

6.1. Calculation of total derivatives

The semi-Lagrangian procedure requires to evaluate the departure points of the fluid parcels. If $(\mathbf{x}_m, t + \Delta t)$ denotes the arrival point of a fluid parcel, its departure point is then $(\mathbf{x}_m - \mathbf{d}_m, t)$. The displacement of the parcel, \mathbf{d}_m , is obtained from a number of iterations (usually two) of a second-order mid-point Runge–Kutta corrector:

$$\mathbf{d}_m^{(k+1)} = \Delta t \mathbf{u}(\mathbf{x} - \mathbf{d}_m^{(k)}/2, t + \Delta t/2), \quad (20)$$

with a first order estimate $\mathbf{d}_m^{(0)} = \Delta t\mathbf{u}(\mathbf{x}, t)$. This amounts to approximate the exact trajectory of the fluid parcel by a straight line (Fig. 3). The velocity at time $t + \frac{\Delta t}{2}$ in (20) is found by extrapolating the velocity field at time t and $t - \Delta t$, using a two time level scheme (Temperton and Staniforth, 1987; McDonald and Bates, 1987) and yielding an $O(\Delta t^2)$ -accurate estimate. When iteratively solving (20), interpolation is required to compute the velocity between mesh points. As observed by Staniforth and Côté (1990), negligibly small differences in the solution result from using linear rather than cubic interpolation while solving equation (20). Hence linear interpolation is adopted here.

Once the departure points are computed, the advected variables have to be evaluated at those points. As they usually do not lie on mesh nodes, some form of interpolation is needed. The choice

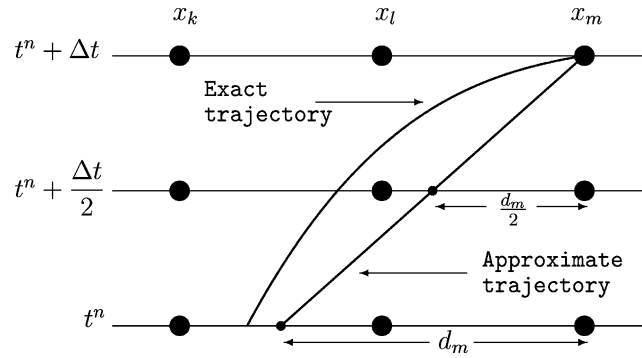


Fig. 3. A two-time-level semi-Lagrangian advection scheme. Approximate and exact trajectories arrive at node x_m at time $t^n + \Delta t$. Here, d_m is the displacement of the particle in the x -direction in time Δt .

of the interpolator has a crucial impact on the accuracy of the method. In regular domains with structured meshes, various polynomial interpolation schemes have been tried, including linear, quadratic, cubic and quintic Lagrange polynomials, and bicubic splines. McCalpin (1988) showed that low order interpolations can have a very diffusive effect. As a result, semi-Lagrangian models of the atmosphere are usually build with high order interpolations. Among those, bicubic spline interpolations are found to be a good compromise between accuracy and computational cost (Purnell, 1976; Pudykiewicz and Staniforth, 1984).

However, most of atmospheric models are based on orthogonal grids, made up of quadrilaterals. It is found that when the mesh loses its orthogonality, the bicubic spline interpolation is much less accurate. Since we intend to interpolate on an unstructured ocean mesh, another method is needed and interpolation schemes that do not depend on the geometry should be preferred. LeRoux et al. (1997) suggested to use a kriging scheme.

6.2. Kriging interpolation

The term “kriging” has been introduced by Matheron (1973) to honor the pioneering work of Krige (1951). A kriging interpolator can be defined as the best linear unbiased estimator of a random function. It yields equally favourable results for structured and unstructured meshes. Given a serie of N measurements f_i of a function f at different locations \mathbf{x}_i ($1 \leq i \leq N$), kriging constructs an approximate function f^h expressed as the sum of a drift $a(\mathbf{x})$ and a fluctuation $b(\mathbf{x})$:

$$f(\mathbf{x}) \approx f^h(\mathbf{x}) = a(\mathbf{x}) + b(\mathbf{x}).$$

The drift is generally a polynomial which follows the physical phenomenon and the fluctuation is adjusted so that the interpolation fits the data points exactly.

For the sake of simplicity, we illustrate kriging by constructing the approximate function in the one dimensional case, using a linear drift:

$$f^h(x) = a(x) + b(x) = a_1 + a_2x + \sum_{j=1}^N b_j K(|x - x_j|),$$

where the function K , known as the generalized covariance, fixes the degree of the fluctuation. The coefficients $a_1, a_2, b_1, \dots, b_N$ are calculated by requiring that: (1) the interpolation has no bias, (2) the squared variance of the fluctuation is minimal and (3) the interpolation fits the data points exactly (Trochu, 1993). Those constraints read:

$$\sum_{j=1}^N b_j = 0, \quad \sum_{j=1}^N b_j x_j = 0 \quad \text{and} \quad f^h(x_i) = f(x_i) \quad \text{for } 1 \leq i \leq N.$$

Hence, the following linear system, known as the dual linear kriging system, is obtained:

$$\left(\begin{array}{cc|cc} & & 1 & x_1 \\ & K_{ij} & \vdots & \vdots \\ & & 1 & x_N \\ \hline 1 & \dots & 1 & 0 & 0 \\ x_1 & \dots & x_N & 0 & 0 \end{array} \right) \begin{pmatrix} b_1 \\ \vdots \\ b_N \\ a_1 \\ a_2 \end{pmatrix} = \begin{pmatrix} f(x_1) \\ \vdots \\ f(x_N) \\ 0 \\ 0 \end{pmatrix}, \quad (21)$$

where $K_{ij} = K(|x_i - x_j|)$. The matrix of the linear system is a full matrix with zeros on the diagonal. As it only depends on mesh node positions, a LU decomposition needs only to be performed once. Nevertheless, each interpolation requires the resolution of a linear system. The computational cost can thus be significant, especially for problems with large data sets. The final system of discrete shallow water equations is still solved with a GMRES iterative solver.

The accuracy of the kriging interpolation method is determined by a suitable choice of the drift and the fluctuation. The drift is usually a low order polynomial. The choice of an admissible generalized covariance has been discussed by Matheron (1980) and Christakos (1984) and the most employed are $K(h) = -h$, $K(h) = h^2 \ln h$ and $K(h) = h^3$, with $h = |x_i - x_j|$, for $1 \leq i, j \leq N$.

7. Numerical simulations and discussions

In this section, we perform some experiments to assess the different numerical models introduced previously. As a test problem, we consider the propagation of slow Rossby waves. Despite the fact that they are very slow, Rossby waves have a major effect on the large scale circulation, and thus on weather and climate. For instance, Rossby waves can intensify western boundary currents, as well as push them off their usual course. As those currents transport huge quantities of heat, it is readily understood that even a minor shift in the position of the current can dramatically affect weather over large areas of the globe. Those waves can be represented with the shallow water equations.

The two numerical tests used in LeRoux et al. (2000) are reproduced here with the $P_1^{\text{NC}} - P_1$ pair in the Eulerian and semi-Lagrangian approaches. For both tests, the model is run as a reduced gravity model with parameters set to correspond to the first internal vertical mode of a baroclinic model. A second passive layer is implicitly assumed infinitely deep and at rest. The depth of the fluid h is set constant.

7.1. Equatorial Rossby soliton

We first reproduce the propagation of the equatorial Rossby soliton of [Boyd \(1980\)](#). This experiment has also been performed by [Iskandarani et al. \(1995\)](#) with their spectral element shallow water model. The model equations are rewritten in their dimensionless form on an equatorial β plane. Dimensionless variables read: $\mathbf{x}' = \mathbf{x}/L$, $t' = t/T$, $\mathbf{u}' = \mathbf{u}/U$ and $\eta' = \eta/h$. The characteristic length (L), time (T) and velocity (U) scales are expressed in terms of the Lamb parameter E :

$$L = \frac{a}{E^{1/4}}, \quad T = \frac{E^{1/4}}{2\Omega}, \quad U = \sqrt{g'h}, \quad E = \frac{4\Omega^2 a^2}{g'h},$$

where a is the radius of the Earth and Ω denotes here the angular frequency of the Earth rotation. The reduced gravity and mean depth are taken as $g' = 4 \times 10^{-2} \text{ m s}^{-2}$ and $h = 100 \text{ m}$ respectively. The mean gravity wave speed is then $U = 2 \text{ m s}^{-1}$ and it corresponds to the wave speed of the first baroclinic mode. Those values yield a time scale of 41 h and a length scale of 296 km.

The rectangular domain non-dimensional extent is 32×8 . The mesh is unstructured and its resolution goes from 0.5 to 1 non-dimensional unit ([Fig. 4a](#)). There are 1768 elements and 946 nodes. The temporal discretization is semi-implicit ($\alpha = \beta = \gamma = 1/2$) and the non-dimensional time step is set to 0.25. As initial conditions, we use the zeroth-order solution introduced by [Boyd \(1980\)](#) at time $t' = 0$. This solution reads:

$$\begin{aligned} u'(x', y', t') &= AB^2 \frac{(6y'^2 - 9)}{4} \text{sech}^2(B(x' - ct')) \exp(-y'^2/2), \\ v'(x', y', t') &= -4AB^3 y' \tanh(B(x' - ct')) \text{sech}^2(B(x' - ct')) \exp(-y'^2/2), \\ \eta'(x', y', t') &= AB^2 \frac{(6y'^2 + 3)}{4} \text{sech}^2(B(x' - ct')) \exp(-y'^2/2), \end{aligned}$$

where $A = 0.771$ and $B = 0.395$. The non-dimensional, linear, non-dispersive velocity phase speed is $c = -\frac{1}{3} - 0.395B^2$. The initial elevation field is shown in [Fig. 4b](#). It should be noted that

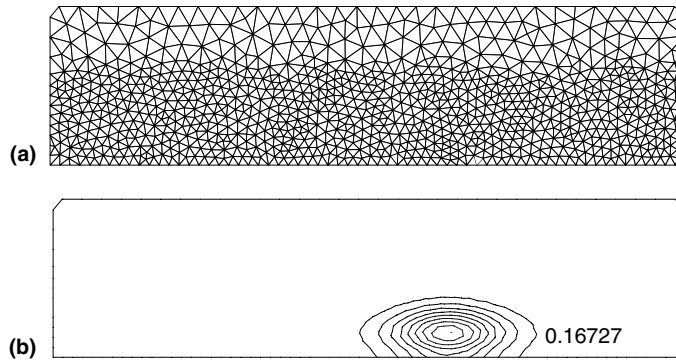


Fig. 4. (a) Mesh used in the equatorial Rossby soliton experiment. (b) Isolines of the elevation field at initial time, the non-dimensional maximum value is specified in the bottom-right corner. There are 10 isolines at equidistributed values ranging from zero to the maximum value specified.

Boyd (1985) gives a first order solution to the Rossby soliton problem. This solution is however not considered in this work.

At the beginning of the integration, the soliton loses approximately 5% of its amplitude which propagates eastward as equatorial Kelvin waves. This is due to the initial condition that is not exactly a solitary wave. Meanwhile, the soliton propagates westward with little change in shape and amplitude, in agreement with the theory. The elevation field after 32 non-dimensional time units is shown in Fig. 5 for the Eulerian scheme and the semi-Lagrangian method. The asymptotic solution of Boyd (1980) is also given. The semi-Lagrangian approach is based on linear and kriging interpolation schemes. The latter use the following generalized covariance functions: $-h$,

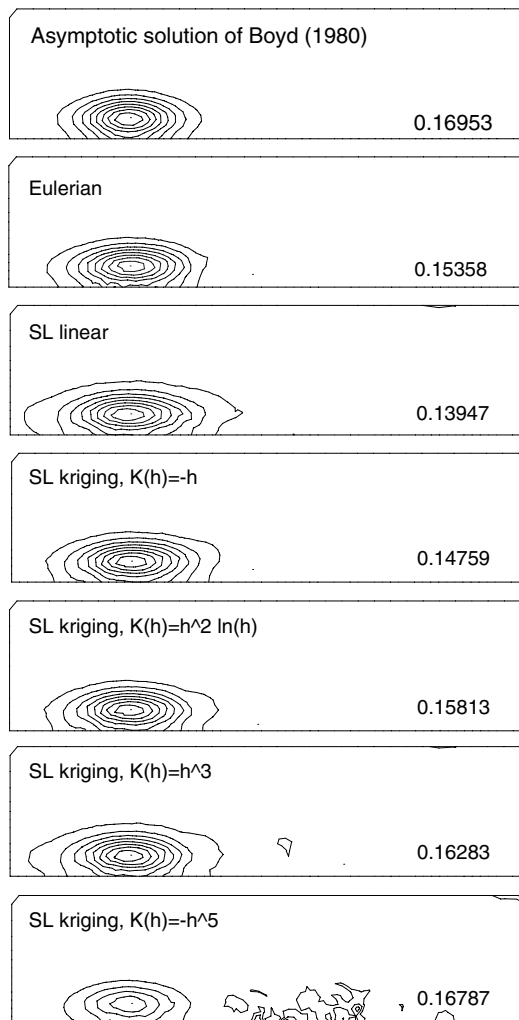


Fig. 5. Elevation fields after 55 days ($t = 32T$) obtained from the asymptotic relation, the Eulerian scheme and various the semi-Lagrangian schemes. The non-dimensional maximum value is specified at the bottom-right corner of each panel. The number of isolines is the same as in Fig. 4.

$h^2 \ln(h)$, h^3 and $-h^5$. The Eulerian scheme preserves the shape of the soliton quite well with moderate damping. It gives a phase speed of 0.783 ms^{-1} which is in good agreement with the asymptotic solution of Boyd (1980) that predicts a value of 0.79 ms^{-1} . The semi-Lagrangian models provide a phase speed ranging from 0.78 to 0.83 ms^{-1} for Lagrangian linear and the various kriging interpolations. It is observed that the phase speed increases with the order of the interpolation used. As expected, the semi-Lagrangian method using low order interpolating schemes shows more damping. As the order of the interpolation increases, the solution gets better. However, for high order interpolations, there is very little numerical diffusion and instabilities may arise. This is observable in Fig. 5 for the kriging scheme with $K(h) = -h^5$.

7.2. Eddy propagation in the Gulf of Mexico

In the second experiment, the slowly propagating Rossby modes are simulated in the case of the evolution of a typical anticyclonic eddy at midlatitudes. The Gulf of Mexico is chosen as the domain to test the model in a realistic geometry. In the present simulation, we ignore the inflow and outflow through the Yucatan Channel and Florida Straits and the basin is assumed closed. Although this experiment is highly idealized, it is expected to represent some of the features of the life cycle of anticyclonic eddies in the Western part of the Gulf. The experiment focuses mainly on the westward propagation of the eddies and their interaction with the boundary. This is why the unstructured mesh, shown in Fig. 6, has a higher resolution in the western part of the domain. There are 8001 elements and 4092 nodes. The domain extent is approximately $1800 \text{ km} \times 1350 \text{ km}$ and the resolution of the mesh goes from 20 to 60 km.

A Gaussian distribution of η , centered at the origin of the domain, is prescribed at initial time:

$$\eta(x, y, 0) = C \exp[-D(x^2 + y^2)],$$

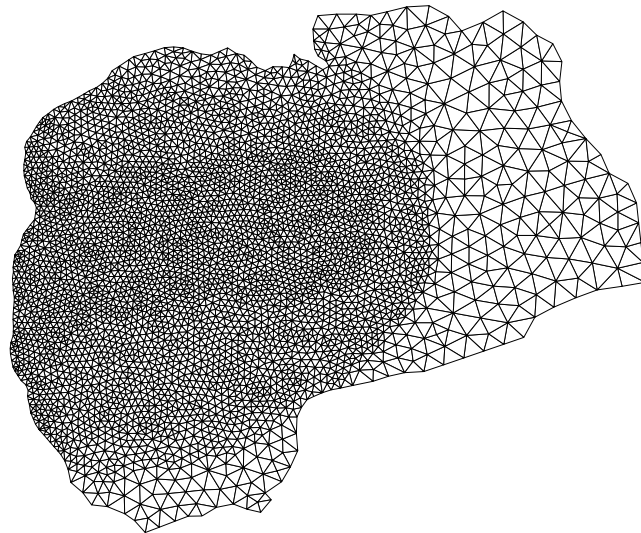


Fig. 6. A triangular unstructured mesh of the Gulf of Mexico. The resolution goes from 20 km in the western part to 60 km in the eastern part.

where $C = 68.2\text{ m}$ and $D = 5.92 \times 10^{-11}\text{ m}^{-2}$. The β -plane assumption is made (i.e. $f = f_0 + \beta y$) and f_0 and β are evaluated at 25° N . The reduced gravity and mean depth are taken as $g' = 1.37 \times 10^{-1}\text{ m s}^{-2}$ and $h = 100\text{ m}$, respectively, so that the mean gravity wave speed is $c \equiv \sqrt{g'h} \approx 3.7\text{ m s}^{-1}$. The radius of deformation at midbasin is thus $R_d \equiv cf_0 \approx 6 \times 10^4\text{ m}$. The initial velocity field is taken to be in geostrophic balance and so

$$u(x, y, 0) = 2\frac{g'}{f}CDy \exp[-D(x^2 + y^2)],$$

$$v(x, y, 0) = -2\frac{g'}{f}CDx \exp[-D(x^2 + y^2)].$$

By setting $C = 68.2\text{ m}$, the maximum flow speed is 1 m s^{-1} . The parameters values are chosen to match the observations of the eddies made by Lewis and Kirwan (1987). In (13) and (14), the temporal discretization is now explicit for the divergence term, and semi-implicit for Coriolis and the gradient terms ($\alpha = \beta = 1/2$, $\gamma = 0$). The time step is set to 300 s , hence the gravitational Courant number is close to 0.1 .

In this experiment, we consider the Eulerian scheme and the semi-Lagrangian method using Lagrangian linear and kriging (with $K(h) = h^3$) interpolation schemes. The Lagrangian linear interpolation is chosen to illustrate the poor results obtained with low order interpolations. The kriging scheme with $K(h) = h^3$ is selected as it appeared to give good results for the soliton experiment, with very small damping. This interpolation scheme is equivalent to cubic spline interpolation (LeRoux et al., 1997).

The semi-Lagrangian method using the kriging scheme develop some small-amplitude noise in the velocity field, which progressively amplified as the integration progressed and ultimately led to unacceptable results. As most high order schemes, such an approach exhibiting better accuracy is more sensitive to errors accumulation. Some harmonic diffusion was therefore introduced for velocity. At the end of each time step, a diffusive correction is applied to the provisional velocity field computed from the semi-Lagrangian scheme, denoted \mathbf{u}^* . The corrected velocity field, \mathbf{u} , is then obtained by solving:

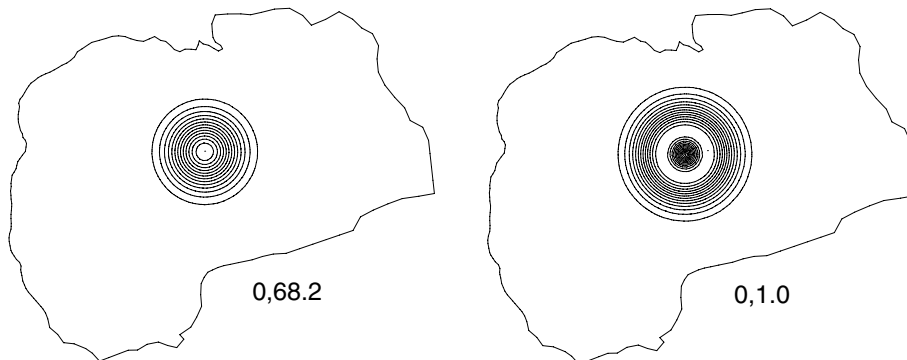


Fig. 7. Isolines of the elevation field (bottom-left) and flow-speed field (bottom-right) at initial time. The minimum and maximum values are specified under each figure. For both variables, there are 15 isolines at equidistributed values ranging from the minimum to the maximum values specified (in m and m s^{-1} respectively).

$$\frac{\mathbf{u} - \mathbf{u}^*}{\Delta t} = \nu \nabla^2 \mathbf{u}^*,$$

subject to zero-flux boundary conditions, where ν is the diffusion coefficient. A value of $\nu = 175 \text{ m}^2 \text{ s}^{-1}$ was found sufficient to suppress the noise in the velocity field.

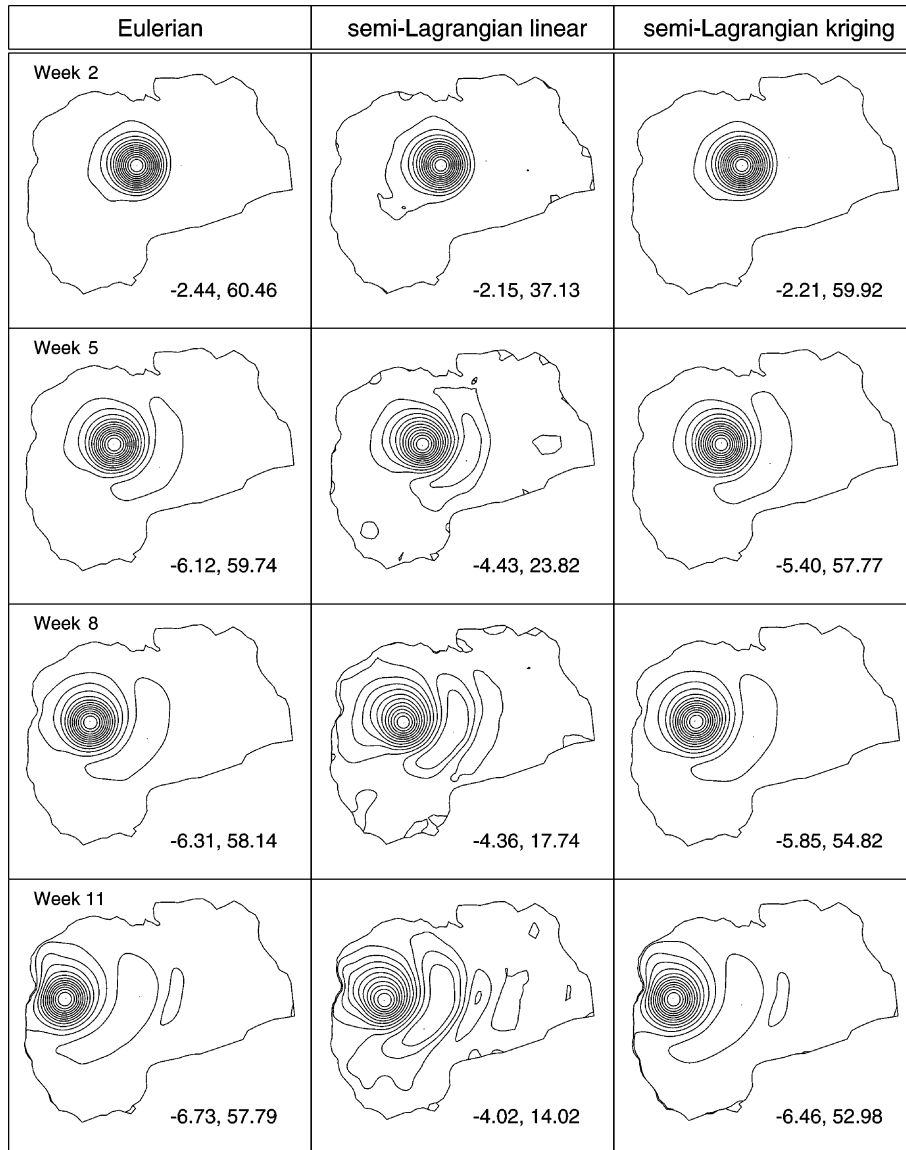


Fig. 8. Isolines of the elevation field at different times of the propagation for the Eulerian, semi-Lagrangian with linear interpolator and semi-Lagrangian with kriging interpolator ($K(h) = h^3$) schemes. The minimum and maximum values (in m) are specified at the bottom right corner of each panel. The number of isolines is the same as in Fig. 7.

At initial time, the eddy is located in the middle of the Gulf of Mexico (Fig. 7) and different stages of its propagation are shown in Figs. 8 and 9 for the Eulerian and the semi-Lagrangian models. Shortly after initialization, there is a readjustment of the flow and η loses approximately 10% of its amplitude. Afterward, the Rossby wave propagates westward with a slight southwesterly drift that is due to non-linear effects. The reduction in amplitude that follows the readjustment is due to the explicit and/or implicit diffusion in the numerical schemes. The implicit

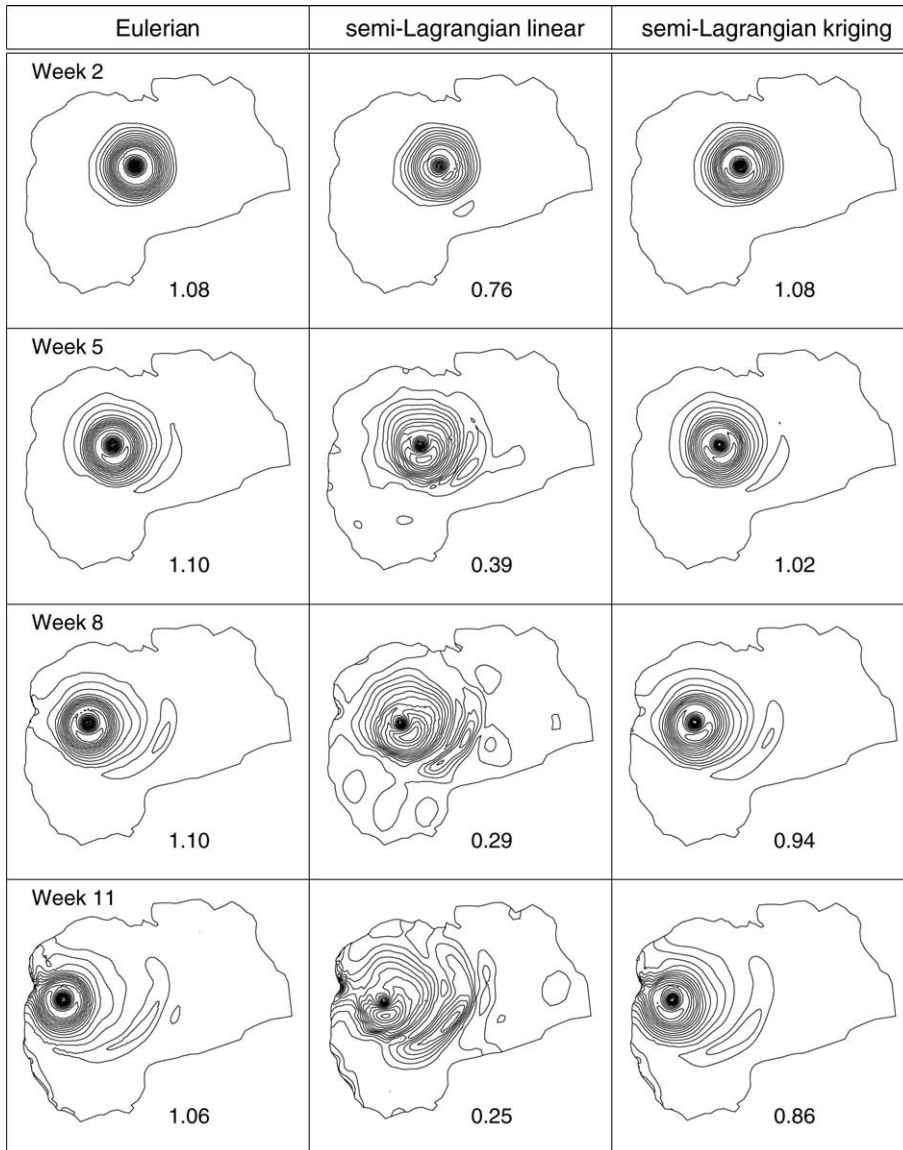


Fig. 9. Isolines of the flow-speed field at different times of the propagation for the Eulerian, semi-Lagrangian with linear interpolator and semi-Lagrangian with kriging interpolator ($K(h) = h^3$) schemes. The minimum and maximum values (in ms^{-1}) are specified at the bottom right corner of each panel. The number of isolines is the same as in Fig. 7.

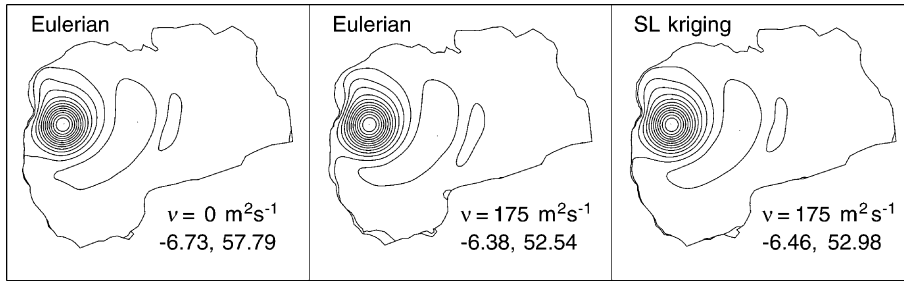


Fig. 10. Isolines of the elevation field after 11 weeks for the inviscid Eulerian scheme, and for the Eulerian and kriging semi-Lagrangian schemes with an explicit diffusion $\nu = 175 \text{ m}^2 \text{ s}^{-1}$. The minimum and maximum values are specified at the bottom right corner of each panel. The number of isolines is the same as in Fig. 7.

diffusion is due to the upwind treatment of momentum advection for the Eulerian scheme, and to the interpolation procedure for the semi-Lagrangian schemes. The Eulerian and the high order semi-Lagrangian schemes qualitatively give comparable results. For both schemes, the translation speed is approximately 6.8 km day^{-1} which is in good agreement with that predicted by the theory ($\beta R_d^2 = 6.5 \text{ km day}^{-1}$). The linear semi-Lagrangian schemes shows more dispersion and gives a slower propagation speed. The maximum values of the elevation and flow-speed fields show that the semi-Lagrangian scheme using a linear interpolation is very diffusive as the eddy loses approximately 70% of its amplitude compared to the Eulerian scheme during the simulation. This is due to the low order interpolation procedure. The high order semi-Lagrangian scheme performs better but the viscosity required to avoid instabilities leads to a 8% reduction in η compared to the Eulerian scheme, after 11 weeks of simulation.

The Eulerian scheme is stable enough to run without explicit diffusion whereas the high order semi-Lagrangian scheme requires some explicit diffusion to run properly. The stability of the Eulerian scheme is partly due to the upwind treatment of momentum advection which has a diffusive effect. We estimate the amount of artificial diffusion in the Eulerian scheme by running that model with an explicit diffusion $\nu = 175 \text{ m}^2 \text{ s}^{-2}$. By comparing the results of the Eulerian and high order semi-Lagrangian model when both use the same explicit diffusion, it is possible to estimate the effect of the artificial diffusion “hidden” in the Eulerian model. The high order semi-Lagrangian model is assumed to have a very small implicit diffusion. The final elevation fields obtained with the inviscid Eulerian, the viscous Eulerian and the viscous kriging semi-Lagrangian schemes are shown in Fig. 10. It can be seen that the results obtained with the viscous Eulerian scheme are very close to those obtained with the viscous kriging semi-Lagrangian scheme. This suggests that the amount of artificial diffusion introduced in the Eulerian scheme by the upwind treatment of momentum advection is very small and has less impact than the explicit diffusion needed to run the high-order semi-Lagrangian scheme.

8. Conclusions

The non-linear shallow water equations have been discretized on an unstructured triangular grid by using the $P_1^{\text{NC}} - P_1$ finite element pair. Eulerian and semi-Lagrangian advection schemes

have been compared and assessed in the context of ocean modelling. It has been shown that the Eulerian method gives an accurate representation of the Rossby waves as the amplitude and phase speed of those modes are well preserved during propagation. The method works well without explicit diffusion and the implicit numerical diffusion, mainly due to an upwind momentum advection discretization, seems to have a small impact on the accuracy of the results.

Semi-Lagrangian schemes well reproduce Rossby waves when a high order kriging interpolation is used. Indeed, a high order accuracy is then reached even on unstructured grids. However, we were forced to add a small Laplacian diffusion to the model to be able to get an acceptable solution. In other words, numerical diffusion has to be incorporated explicitly when using the high order semi-Lagrangian model. In the Eulerian approach, it is observed that the amount of numerical diffusion introduced by upwinding is quite small in comparison.

The comparison of the computational cost between Eulerian and semi-Lagrangian methods is not straightforward as it depends strongly on the implementation, on some numerical strategies and on the linear solver. In one hand, the main advantage of the semi-Lagrangian method compared to the Eulerian scheme, is the possibility of using larger time steps. However, the use of larger time steps leads to a poorer conditioning of the linear system and the benefit in terms of computational cost is not always as good as expected. Moreover, the interpolation procedure and the tracking calculation requires cumbersome implementation and a high computational cost. In the other hand, the Eulerian approach is quite more easy to implement and seems to be considerably much cheaper in terms of CPU requirements. As implemented in our codes, the semi-Lagrangian calculations are at least ten times more expensive than the Eulerian ones.

The Eulerian $P_1^{\text{NC}} - P_1$ model seems to be a promising initial step toward the construction of an ocean general circulation model using unstructured triangular meshes. The $P_1^{\text{NC}} - P_1$ finite element pair combines several advantages such as the absence of pressure modes, a reasonable computational cost even compared to traditional finite-difference schemes and the possibility to efficiently perform upwinding while computing momentum advection.

Acknowledgments

Emmanuel Hanert and Eric Deleersnijder are Research fellow and Research associate, respectively, with the Belgian National Fund for Scientific Research (FNRS). The support of the Convention d'Actions de Recherche Concertées ARC 97/02-208 with the Communauté Française de Belgique is gratefully acknowledged. Daniel Y. Le Roux is supported by grants from the Natural Sciences and Engineering Research Council (NSERC) and the Fonds Québécois de la Recherche sur la Nature et les Technologies (FQRNT).

Appendix A. Details on the matricial form of the discrete equations

The matrix figuring in (15) is written as:

$$\left(\begin{array}{c|c} \underline{\underline{B_{UU}}} & \underline{\underline{G_{UH}}} \\ \hline -\underline{\underline{D_{HU}}} & \underline{\underline{M_{HH}}} \end{array} \right) = \left(\begin{array}{c|c|c} \sum_e \int_{\Omega_e} \psi_i \psi_j & -\beta \Delta t \sum_e \int_{\Omega_e} \psi_i f_j \psi_j & \alpha g \Delta t \sum_e \int_{\Omega_e} \psi_i \phi_{j,x} \\ \hline \beta \Delta t \sum_e \int_{\Omega_e} \psi_i f_j \psi_j & \sum_e \int_{\Omega_e} \psi_i \psi_j & \alpha g \Delta t \sum_e \int_{\Omega_e} \psi_i \phi_{j,y} \\ \hline -\gamma \Delta t \sum_e \int_{\Omega_e} h \phi_{i,x} \psi_j & -\gamma \Delta t \sum_e \int_{\Omega_e} h \phi_{i,y} \psi_j & \sum_e \int_{\Omega_e} \phi_i \phi_j \end{array} \right).$$

The matrix B_{UU} is composed of the velocity mass matrix and the Coriolis matrix. As non-conforming shape functions are orthogonal, the four sub-matrices in B_{UU} are diagonal and the inverse of B_{UU} may thus be easily computed. The matrices G_{UH} and D_{HU} respectively correspond to the gradient and divergence matrices. If h is constant, the divergence matrix is proportional to the transpose of the gradient matrix. Finally, the matrix M_{HH} is the elevation mass matrix.

The rhs of Eq. (15) reads:

$$\left(\begin{array}{c} \underline{\underline{R_U}} \\ \underline{\underline{R_H}} \end{array} \right) = \left(\begin{array}{c} \sum_e \int_{\Omega_e} \psi_i u_n^h + \Delta t \sum_e \int_{\Omega_e} \nabla \cdot (\mathbf{u}_n^h \psi_i) u_n^h + \beta \Delta t \sum_e \int_{\Omega_e} \psi_i f v_n^h \\ \quad - \alpha g \Delta t \sum_e \int_{\Omega_e} \psi_i \eta_{n,x}^h - \Delta t \sum_l \int_{\Gamma_l} \langle u_n^h \mathbf{u}_n^h \cdot \mathbf{n} \rangle_\lambda [\psi_i] \\ \hline \sum_e \int_{\Omega_e} \psi_i v_n^h + \Delta t \sum_e \int_{\Omega_e} \nabla \cdot (\mathbf{u}_n^h \psi_i) v_n^h - \beta \Delta t \sum_e \int_{\Omega_e} \psi_i f u_n^h \\ \quad - \alpha g \Delta t \sum_e \int_{\Omega_e} \psi_i \eta_{n,y}^h - \Delta t \sum_l \int_{\Gamma_l} \langle v_n^h \mathbf{u}_n^h \cdot \mathbf{n} \rangle_\lambda [\psi_i] \\ \hline \sum_e \int_{\Omega_e} \phi_i \eta_n^h + \gamma \Delta t \sum_e \int_{\Omega_e} h \mathbf{u}_n^h \cdot \nabla \phi_i + \Delta t \sum_e \int_{\Omega_e} \eta_n^h \mathbf{u}_n^h \cdot \nabla \phi_i \end{array} \right),$$

where \mathbf{u}_n^h denotes the value of \mathbf{u}^h at time step n .

References

- Behrens, J., 1998. Atmospheric and ocean modeling with an adaptive finite element solver for the shallow-water equations. *Applied Numerical Mathematics* 26, 217–226.
- Boyd, J.P., 1980. Equatorial solitary waves. Part I. Rossby solitons. *Journal of Physical Oceanography* 10, 1699–1717.
- Boyd, J.P., 1985. Equatorial solitary waves. Part 3. Westward-traveling modons. *Journal of Physical Oceanography* 15, 46–54.
- Casulli, V., Walters, R.A., 2000. An unstructured grid, three-dimensional model based on the shallow water equations. *International Journal for Numerical Methods in Fluids* 32, 331–348.
- Chen, C., Liu, H., Beardsley, R.C., 2003. An unstructured grid, finite-volume, three-dimensional, primitive equations ocean model: Applications to coastal ocean and estuaries. *Journal of Atmospheric and Oceanic Technology* 20, 159–186.
- Christakos, G., 1984. On the problem of permissible covariance and variogram models. *Water Resources Research* 20, 251–265.
- Crouzeix, M., Raviart, P., 1973. Conforming and nonconforming finite-element methods for solving the stationary Stokes equations. *R.A.I.R.O. Analyse Numérique* 7, 33–76.
- Danilov, S., Kivman, G., Schröter, J., 2004. A finite element ocean model: principles and evaluation. *Ocean Modelling* 6, 125–150.
- Hanert, E., LeRoux, D.Y., Legat, V., Deleersnijder, E., 2004. Advection schemes for unstructured grid ocean modelling. *Ocean Modelling* 7, 39–58.

- Hanert, E., Legat, V., Deleersnijder, E., 2003. A comparison of three finite elements to solve the linear shallow water equations. *Ocean Modelling* 5, 17–35.
- Houston, P., Schwab, C., Suli, E., 2000. Discontinuous *hp*-finite element methods for advection diffusion problems. Tech. Rep. NA-00/15, Oxford University.
- Hua, B.L., Thomasset, F., 1984. A noise-free finite element scheme for the two-layer shallow water equations. *Tellus* 36A, 157–165.
- Iskandarani, M., Haidvogel, D.B., Boyd, J.B., 1995. A staggered spectral element model with application to the oceanic shallow water equations. *International Journal for Numerical Methods in Fluids* 20, 393–414.
- Iskandarani, M., Haidvogel, D.B., Levin, J.C., 2003. A three-dimensional spectral element model for the solution of the hydrostatic primitive equations. *Journal of Computational Physics* 186, 397–425.
- Krige, S.R., 1951. A statistical approach to some basic mine valuation problems on the Witwatersrand. *Journal Chemical and Metallurgical Mineral Society of South Africa* 52, 119–139.
- LeProvost, C., Bernier, C., Blayo, E., 1994. A comparison of two numerical methods for integrating a quasi-geostrophic multilayer model of ocean circulations: Finite element and finite difference methods. *Journal of Computational Physics* 110, 341–359.
- LeRoux, D.Y., submitted for publication. Analysis of the $P_1^{\text{NC}} - P_1$ finite-element pair in shallow-water ocean models. *SIAM Journal of Scientific Computing*.
- LeRoux, D.Y., Lin, C.A., Staniforth, A., 1997. An accurate interpolating scheme for semi-Lagrangian advection on an unstructured mesh for ocean modelling. *Tellus* 49 (A2), 119–138.
- LeRoux, D.Y., Staniforth, A., Lin, C.A., 2000. A semi-implicit semi-Lagrangian finite-element shallow-water ocean model. *Monthly Weather Review* 128, 1384–1401.
- LeSaint, P., Raviart, P., 1974. On the finite element method for solving the neutron transport equations. In: deBoor, C. (Ed.), *Mathematical Aspects of Finite Elements in Partial Differential Equations*. Academic Press, pp. 89–145.
- Legrand, S., Legat, V., Deleersnijder, E., 2001. Delaunay mesh generation for an unstructured-grid ocean general circulation model. *Ocean Modelling* 2, 17–28.
- Lewis, J.K., Kirwan, A.D., 1987. Genesis of a Gulf of Mexico ring as determined from kinematic analyses. *Journal of Geophysical Research* 92, 11727–11740.
- Lynch, D.R., Ip, J.T.C., Naimie, C.E., Werner, F.E., 1996. Comprehensive coastal circulation model with application to the Gulf of Maine. *Continental Shelf Research* 16, 875–906.
- Matheron, G., 1973. The intrinsic random functions and their applications. *Advances in Applied Probability* 5, 439–468.
- Matheron, G., 1980. Splines et krigeage: leur équivalence formelle. Tech. Rep. N-667, Centre de Géostatistique, Ecole des Mines de Paris, Fontainebleau, France.
- McCalpin, J.D., 1988. A quantitative analysis of the dissipation inherent in semi-Lagrangian advection. *Monthly Weather Review* 116, 2330–2336.
- McDonald, A., Bates, J.R., 1987. Improving the estimate of the departure point position in a two-level semi-Lagrangian and semi-implicit scheme. *Monthly Weather review* 115, 737–739.
- Myers, P.G., Weaver, A.J., 1995. A diagnostic barotropic finite-element ocean circulation model. *Journal of Atmospheric and Oceanic Technology* 12, 511–526.
- Nechaev, D., Schröter, J., Yaremchuk, M., 2003. A diagnostic stabilized finite-element ocean circulation model. *Ocean Modelling* 5, 37–63.
- Pudykiewicz, J., Staniforth, A., 1984. Some properties and comparative performances of the semi-Lagrangian method of Robert in the solution of the advection-diffusion equation. *Atmosphere-Ocean*, 283–308.
- Purnell, D.K., 1976. Solution of the advective equation by upstream interpolation with a cubic spline. *Monthly Weather Review* 104, 42–48.
- Robert, A., 1981. A stable numerical integration scheme for the primitive meteorological equations. *Atmosphere-Ocean* 19, 35–46.
- Robert, A., 1982. A semi-Lagrangian and semi-implicit numerical integration scheme for the primitive meteorological equations. *Japan Meteorological Society* 60, 319–325.
- Robert, A., Yee, T.L., Ritchie, H., 1985. A semi-Lagrangian and semi-implicit numerical integration scheme for multilevel atmospheric models. *Monthly Weather Review* 113, 388–394.

- Saad, Y., Schultz, M.H., 1986. GMRES: a generalized minimal residual algorithm for solving nonsymmetric linear systems. *SIAM Journal on Scientific Computing* 7, 856–869.
- Staniforth, A.N., Côté, J., 1990. Semi-Lagrangian schemes for atmospheric models—a review. *Monthly Weather Review* 119, 2206–2223.
- Temperton, C., Staniforth, A.N., 1987. An efficient two-time level semi-Lagrangian semi-implicit integration scheme. *Quarterly Journal of the Royal Meteorological Society* 113, 1025–1039.
- Trochu, F., 1993. A contouring program based on dual kriging interpolation. *Engineering with Computers* 9, 160–177.



High resolution methods for multidimensional advection–diffusion problems in free-surface hydrodynamics

Vincenzo Casulli *, Paola Zanolli

Civil and Environmental Engineering, University of Trento, via Mesiano 77, 38050 Povo (Trento), Italy

Received 14 November 2003; received in revised form 12 April 2004; accepted 21 June 2004

Available online 2 November 2004

Abstract

In this paper the numerical solution of advection–diffusion problems in free-surface hydrodynamic is analyzed. A new finite volume scheme for unstructured grid is derived. It is shown how both, mass conservation and maximum principle can be assured by the present method. The issue of numerical accuracy is also addressed in two and three-dimensional problems. Suggestions for grid generation are also implied. © 2004 Elsevier Ltd. All rights reserved.

Keywords: Advection schemes; Unstructured grids; Free-surface

1. Introduction

Numerical modelling of free-surface hydrodynamic is by itself a challenging task (see, e.g., [Stelling, 1984](#); [Casulli and Zanolli, 2002](#)). Once the velocity field and free-surface elevation have been computed, one is often interested in the transport of a scalar variable such as salinity, temperature or any passive constituent that may represent sediment or a biological specie. This latter problem may not be trivial especially if high resolution together with specific qualitative behavior of the numerical solution is expected.

* Corresponding author. Tel.: +39 461 882676.

E-mail address: vincenzo.casulli@unitn.it (V. Casulli).

From an analytical point of view the differential equation governing the advection and diffusion of a scalar variable can be written equivalently in a conservative or in a non-conservative form each expressing two important properties, namely the conservation of the scalar quantity and the satisfying of a general maximum principle. Whereas analytically one can easily switch from one formulation to the other under rather general assumptions that the fluid is incompressible and that the scalar quantity is a differentiable variable, from a numerical point of view this may not be the case. Specifically, when the conservative equation is discretized, one may be able to show that the resulting numerical solution is conservative but the discrete maximum principle may not be guaranteed. Similarly, when the non-conservative equation is discretized, one may be able to show that the resulting numerical solution satisfies the discrete maximum principle but conservation may not be guaranteed.

Assuming that the discrete volume conservation is assured by the hydrodynamic variables (fluid velocity and free surface elevation), in this paper the advection–diffusion equation of a scalar quantity will be discretized in such a fashion that the resulting numerical solution is mass conservative and, at the same time, satisfies the maximum principle.

Furthermore, the issue of numerical accuracy will also be addressed by use of appropriate flux limiting functions. Accurate transport computations require two aspects: (a) a high resolution algorithm and (b) an accurate flow field. Additionally, it will be shown that a properly devised grid may also play an important role to obtain a higher numerical accuracy.

Although the concepts presented in this paper can apply to several free-surface hydrodynamic model as long as conservation of fluid volume is guaranteed, particular attention will be devoted to a class of highly efficient semi-implicit algorithms that allows for high-resolution and long time range simulations at low computational cost. These are a semi-implicit method for two- and three-dimensional hydrostatic free-surface flow on unstructured grids (Casulli and Walters, 2000) and a more recent semi-implicit algorithm for non-hydrostatic multidimensional flows (Casulli and Zanolli, 2002).

2. A two-dimensional transport model

The two-dimensional equations describing free-surface flows are the well known vertically averaged, shallow water equations. Such equations, expressing the physical principle of conservation of momentum and fluid volume, are given by

$$u_t + uu_x + vv_y - fv = -g\eta_x + v^h(u_{xx} + u_{yy}) - \gamma u, \quad (1)$$

$$v_t + uv_x + vv_y + fu = -g\eta_y + v^h(v_{xx} + v_{yy}) - \gamma v, \quad (2)$$

$$\eta_t + (Hu)_x + (Hv)_y = 0, \quad (3)$$

where $u(x, y, t)$ and $v(x, y, t)$ are the vertically averaged velocity components in the horizontal x and y directions, respectively; $\eta(x, y, t)$ is the free-surface elevation; f is the Coriolis parameter; v^h is a prescribed non-negative coefficient of horizontal eddy viscosity; γ is a non-negative bottom friction coefficient and $H(x, y, t) = h(x, y) + \eta(x, y, t)$ is the total water depth with $h(x, y)$ being bathymetry measured from the undisturbed water surface.

The mass conservation of a scalar variable is expressed by the following differential equation:

$$(HC)_t + (HuC)_x + (HvC)_y = (K^h HC_x)_x + (K^h HC_y)_y, \tag{4}$$

where $C(x, y, t)$ denotes the vertically averaged concentration of any scalar transported specie and K^h is a prescribed non-negative horizontal diffusivity coefficient.

2.1. Orthogonal unstructured grid

Before discretizing Eqs. (1)–(4), the horizontal (x, y) domain is covered by a set of non-overlapping convex polygons. Each side of a polygon is either a boundary line or a side of an adjacent polygon. Moreover, it is assumed that within each polygon there exist a point (hereafter called *center*) such that the segment joining the centers of two adjacent polygons and the side shared by the two polygons have a non-empty intersection and are *orthogonal* to each other (see Fig. 1). One such a grid is called *unstructured orthogonal grid* (see Casulli and Walters, 2000).

Once the (x, y) domain has been covered with an unstructured orthogonal grid, one has N_p polygons, each having an arbitrary number of sides $S_i \geq 3, i = 1, 2, \dots, N_p$. Let N_s be the total number of sides in the grid and let $\lambda_j, j = 1, 2, \dots, N_s$ be the length of each side. The sides of the i th polygon are identified by an index $j(i, \ell), \ell = 1, 2, \dots, S_i$, so that $1 \leq j(i, \ell) \leq N_s$. Similarly, the two polygons which share the j th side of the grid are identified by the indices $i(j, 1)$ and $i(j, 2)$ so that $1 \leq i(j, 1) \leq N_p$ and $1 \leq i(j, 2) \leq N_p$. Let P_i be the area of the i th polygon. Moreover, $m(i, j)$ denotes the neighbor of polygon i that shares the side j with the i th polygon. The non-zero distance between the centers of two adjacent polygons which share the j th side is denoted with δ_j (see Fig. 1).

The discrete velocities and water surface elevation are defined at staggered locations as follows. The water surface elevation η_i^n , assumed to be constant within each polygon, is located at the center of the i th polygon; the velocity component u_j^n normal to each side of a polygon, oriented from $i(j, 1)$ to $i(j, 2)$ and assumed to be constant over the side, is defined at the point of intersection between the side and the segment joining the centers of the two polygons which share the side; the concentrations C_i^n are located at the center of the i th polygon. Finally, the water depth h_j is specified and assumed constant on each side of a polygon.

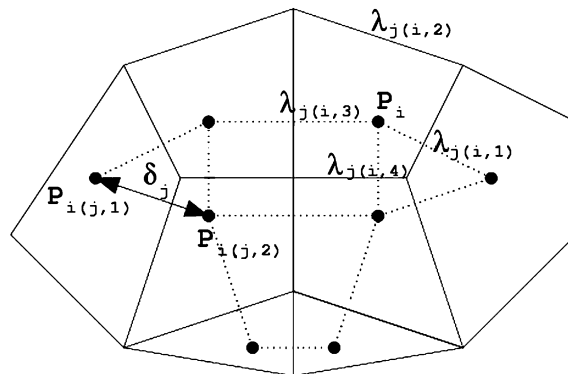


Fig. 1. Orthogonal unstructured grid.

2.2. Numerical approximation

The semi-implicit scheme used to discretize Eqs. (1)–(3) on an orthogonal unstructured grid is a particular case of the three-dimensional algorithm presented in Casulli and Walters (2000) for a one layer calculation. In this scheme the gradient of surface elevation in the horizontal momentum Eqs. (1) and (2) and the velocity in the free-surface Eq. (3) are discretized by the θ -method. Moreover, for stability, the bottom friction is discretized implicitly.

Since Eqs. (1) and (2) are invariant under solid rotation of the x and y axis on the horizontal plane, a consistent semi-implicit finite difference discretization for the horizontal velocity component perpendicular to each side of a polygon is taken to be

$$u_j^{n+1} = Fu_j^n - g \frac{\Delta t}{\delta_j} [\eta_{i(j,2)}^{n+\theta} - \eta_{i(j,1)}^{n+\theta}] - \Delta t \gamma_j^n u_j^{n+1}, \quad (5)$$

where θ is an implicitness factor and F is an explicit finite difference operator which accounts for the contributions from the discretization of the Coriolis, advection and horizontal viscosity terms.

A semi-implicit finite volume discretization for the free-surface Eq. (3) at the center of each polygon is taken to be

$$P_i \eta_i^{n+1} = P_i \eta_i^n - \Delta t \sum_{\ell=1}^{S_i} s_{i,\ell} \lambda_{j(i,\ell)} H_{j(i,\ell)}^n u_{j(i,\ell)}^{n+\theta}, \quad (6)$$

where $s_{i,\ell}$ is a sign function which accounts for the orientation of the normal velocity defined on the ℓ th side of the polygon i .

By denoting with S_i^+ the set of sides belonging to the i th polygon through which the water is leaving the i th polygon and with S_i^- the set of sides through which the water is entering the i th polygon, Eq. (6) can also be written as follows:

$$P_i H_i^{n+1} = P_i H_i^n - \Delta t \left(\sum_{j \in S_i^+} |Q_j^{n+\theta}| - \sum_{j \in S_i^-} |Q_j^{n+\theta}| \right), \quad (7)$$

where $Q_j^{n+\theta} = \lambda_j H_j^n u_j^{n+\theta}$ is the flow rate across the j th side of the grid.

When the implicitness factor θ is chosen in the range $\frac{1}{2} \leq \theta \leq 1$ the stability of the resulting scheme (5), (6) is independent from the free-surface wave speed and bottom friction (Casulli and Cattani, 1994).

Eqs. (5) and (6) constitute a linear system of $N_s + N_p$ equations. A robust and efficient algorithm for solving this system has been described in Casulli and Walters (2000).

2.3. Scalar transport

Regarding the transport Eq. (4), it is immediate to recognize that it is written in a conservative form. This equation, in fact, expresses the principle of conservation of mass. Assuming that the functions involved in Eq. (4) are differentiable, by expanding the derivatives and by using the continuity Eq. (3), one obtains the following non-conservative form of the advection–diffusion Eq. (4)

$$C_t + uC_x + vC_y = \frac{1}{H} [(K^h HC_x)_x + (K^h HC_y)_y]. \quad (8)$$

Eq. (8) is equivalent to its conservative form (4) and expresses another important property, namely, the maximum principle. Thus, its analytical solution $C(x, y, t)$ is always bounded, above and below, by the maximum and by the minimum, respectively, of its initial and boundary values.

From the analytical point of view, one can switch between Eqs. (4) and (8) thus to say that the solution $C(x, y, t)$ is conservative and satisfies the max–min property. Once these equations are discretized, however, the corresponding numerical solution will, in general, either be conservative or satisfy a discrete max–min property. As an example, the explicit upwind discretization of Eq. (4) is given by

$$P_i H_i^{n+1} C_i^{n+1} = P_i H_i^n C_i^n - \Delta t \left[\sum_{j \in S_i^+} |Q_j^n| C_i^n - \sum_{j \in S_i^-} |Q_j^n| C_{m(i,j)}^n \right] + \Delta t \sum_{j \in S_i^- \cup S_i^+} D_j^n [C_{m(i,j)}^n - C_i^n], \quad (9)$$

where $Q_j^n = \lambda_j H_j^n u_j^n$ and $D_j^n = \lambda_j H_j^n \frac{K_j^h}{\delta_j}$ are the advective and the diffusive flux coefficients, respectively.

The new mass $P_i H_i^{n+1} C_i^{n+1}$ resulting from the finite volume Eq. (9) is conserved because it is expressed in flux form. In general, however, the resulting numerical solution C_i^{n+1} will not satisfy a discrete max–min property. Hence, unrealistic new maximum or new minimum may be generated.

A conservative discretization of Eq. (4) will yield a solution that also possesses the discrete max–min property, only if it is consistent with the discretized continuity Eq. (7). An explicit finite volume approximation for the advection–diffusion Eq. (4), that yields a numerical solution which is conservative and satisfies the discrete max–min property, is given by

$$P_i H_i^{n+1} C_i^{n+1} = P_i H_i^n C_i^n - \Delta t \left[\sum_{j \in S_i^+} |Q_j^{n+\theta}| C_i^n - \sum_{j \in S_i^-} |Q_j^{n+\theta}| C_{m(i,j)}^n \right] + \Delta t \sum_{j \in S_i^- \cup S_i^+} D_j^n [C_{m(i,j)}^n - C_i^n], \quad (10)$$

where the advective coefficient is now defined as $Q_j^{n+\theta} = \lambda_j H_j^n u_j^{n+\theta}$. Clearly, since a finite volume approach is being used, this scheme is mass conservative. In order to show that the numerical solution obtained from (10) also possesses the discrete min–max property both sides of this equation are divided by $P_i H_i^{n+1}$. Then, by using the discretized continuity Eq. (7) and by grouping together all the terms with C_i^n and $C_{m(i,j)}^n$, one has

$$C_i^{n+1} = \frac{P_i H_i^n - \Delta t \left(\sum_{j \in S_i^+} |Q_j^{n+\theta}| + \sum_{j \in S_i^- \cup S_i^+} D_j^n \right)}{P_i H_i^n - \Delta t \left(\sum_{j \in S_i^+} |Q_j^{n+\theta}| - \sum_{j \in S_i^-} |Q_j^{n+\theta}| \right)} C_i^n + \Delta t \frac{\sum_{j \in S_i^-} |Q_j^{n+\theta}| C_{m(i,j)}^n + \sum_{j \in S_i^- \cup S_i^+} D_j^n C_{m(i,j)}^n}{P_i H_i^n - \Delta t \left(\sum_{j \in S_i^+} |Q_j^{n+\theta}| - \sum_{j \in S_i^-} |Q_j^{n+\theta}| \right)}. \quad (11)$$

One can now verify that, if the time step size Δt is chosen sufficiently small so that $P_i H_i^n - \Delta t (\sum_{j \in S_i^+} |Q_j^{n+\theta}| + \sum_{j \in S_i^- \cup S_i^+} D_j^n) \geq 0$, then the right hand side of (11) is a weighted average of C_i^n and $C_{m(i,j)}^n$, $j \in S_i^+ \cup S_i^-$. Since the weights are non-negative and their sum is exactly 1, the discrete max–min property follows readily (Greenspan and Casulli, 1988).

Note that the only and crucial improvement of Eq. (10) over (9) consists in the use of the advective coefficient $Q_j^{n+\theta}$ at the semi-implicit time $n + \theta$. It is this choice, in fact, that being consistent with the discrete continuity Eq. (7) leads to the discrete max–min property.

2.4. High resolution schemes

One known disadvantage of a first order upwind method such as given by (10) is poor accuracy due to high artificial (or numerical) diffusion (see, e.g., LeVeque, 1990). In order to recover some accuracy, Eq. (4) is discretized in a more general formulation as

$$P_i H_i^{n+1} C_i^{n+1} = P_i H_i^n C_i^n - \Delta t \left[\sum_{j \in S_i^+} |Q_j^{n+\theta}| C_i^n - \sum_{j \in S_i^-} |Q_j^{n+\theta}| C_{m(i,j)}^n \right] - \frac{\Delta t}{2} \sum_{j \in S_i^- \cup S_i^+} \Phi_j^n |Q_j^{n+\theta}| [C_{m(i,j)}^n - C_i^n] + \Delta t \sum_{j \in S_i^- \cup S_i^+} D_j^n [C_{m(i,j)}^n - C_i^n], \quad (12)$$

where Φ_j^n is the so-called flux limiter function. Thus, for example, if $\Phi_j^n = 0$ then Eq. (12) reduces to the upwind scheme (10). The second order central difference scheme is obtained for $\Phi_j^n = 1$. The first order but less diffusive downwind formula is obtained for $\Phi_j^n = 2$.

For a linear finite volume scheme of the form (12) the max–min property can only be assured with a sufficiently fine grids so that the distances δ_j are so small to satisfy the following inequality:

$$\Phi_j^n |Q_j^{n+\theta}| \leq 2D_j^n. \quad (13)$$

Clearly, inequality (13) may be too restrictive for advection dominated diffusion problems. This inequality also indicates that Eq. (12) cannot apply to pure advection ($K^n = D = 0$) unless the upwind method ($\Phi_j^n = 0$) is used.

Since, in general, a restriction on the grid size δ_j is not desirable, one can choose the limiter function Φ_j^n in such a way that inequality (13) is always satisfied although the desired scheme (and the corresponding accuracy) may not be obtained. Thus, for example, if a second order accuracy is sought, one may choose $\Phi_j^n = \phi_j^n$, where ϕ_j^n is given by

$$\phi_j^n = \min \left(1, \frac{2D_j^n}{|Q_j^{n+\theta}|} \right). \quad (14)$$

Although the choice of the flux limiter function as given by Eq. (14) provides the closest possible solution to obtain a second order method, the values of Φ_j^n so obtained may be far from being 1. Thus, the flux limiter function is allowed to depend on the solution C_i^n . In so doing the resulting scheme will become nonlinear but, with a properly chosen limiter function, the conservative property and the maximum principle will remain valid while higher resolution is obtained. To this purpose one sets

$$\Phi_j^n = \phi_j^n + \psi(r_j^n), \quad (15)$$

where ψ is an additional contribution to the flux limiter function that depends on the ratio of consecutive gradients r_j^n . For $j \in S_i^+$, r_j^n can be defined as

$$r_j^n = \frac{1}{C_{m(i,j)}^n - C_i^n} \frac{\sum_{\ell \in S_i^-} |Q_\ell^{n+\theta}| [C_i^n - C_{m(i,\ell)}^n]}{\sum_{\ell \in S_i^-} |Q_\ell^{n+\theta}|}. \quad (16)$$

There are many ways to determine a form for Φ . A few possible choices that have been widely studied and applied (see, e.g., van Leer, 1979; Sweby, 1984; Roe, 1985) are

$$\text{Minmod: } \Phi(r) = \max[\phi, \min(1, r)], \quad (17)$$

$$\text{van Leer: } \Phi(r) = \max \left[\phi, \frac{r + |r|}{1 + |r|} \right], \quad (18)$$

$$\text{Superbee: } \Phi(r) = \max[\phi, \min(1, 2r), \min(2, r)], \quad (19)$$

so that $\Phi(r) \leq 2$, $\psi(r) = \Phi(r) - \phi \geq 0$ and $\psi(r) = 0$ for $r \leq 0$. Thus, by substituting Eq. (15) into (12) one gets

$$\begin{aligned} P_i H_i^{n+1} C_i^{n+1} &= P_i H_i^n C_i^n - \Delta t \left[\sum_{j \in S_i^+} |Q_j^{n+\theta}| C_i^n - \sum_{j \in S_i^-} |Q_j^{n+\theta}| C_{m(i,j)}^n \right] \\ &\quad - \frac{\Delta t}{2} \sum_{j \in S_i^- \cup S_i^+} \psi_j^n |Q_j^{n+\theta}| [C_{m(i,j)}^n - C_i^n] + \Delta t \sum_{j \in S_i^- \cup S_i^+} d_j^{n+\theta} [C_{m(i,j)}^n - C_i^n], \end{aligned} \quad (20)$$

or, equivalently,

$$\begin{aligned} P_i H_i^{n+1} C_i^{n+1} &= P_i H_i^n C_i^n - \Delta t \left[\sum_{j \in S_i^+} |Q_j^{n+\theta}| C_i^n - \sum_{j \in S_i^-} |Q_j^{n+\theta}| C_{m(i,j)}^n \right] - \frac{\Delta t}{2} \sum_{j \in S_i^-} \psi_j^n |Q_j^{n+\theta}| [C_{m(i,j)}^n - C_i^n] \\ &\quad - \frac{\Delta t}{2} \sum_{j \in S_i^+} \frac{\psi_j^n}{r_j^n} |Q_j^{n+\theta}| \frac{\sum_{\ell \in S_i^-} |Q_\ell^{n+\theta}| [C_i^n - C_{m(i,\ell)}^n]}{\sum_{\ell \in S_i^-} |Q_\ell^{n+\theta}|} + \Delta t \sum_{j \in S_i^- \cup S_i^+} d_j^{n+\theta} [C_{m(i,j)}^n - C_i^n], \end{aligned} \quad (21)$$

where $d_j^{n+\theta} = D_j^n - \frac{1}{2} \psi_j^n |Q_j^{n+\theta}| = \max(0, D_j^n - \frac{1}{2} |Q_j^{n+\theta}|)$. By grouping together the terms with C_i^n and $C_{m(i,j)}^n$, Eq. (21) can also be written as

$$\begin{aligned} P_i H_i^{n+1} C_i^{n+1} &= \left\{ P_i H_i^n - \Delta t \left[\sum_{j \in S_i^+} \left(1 + \frac{\psi_j^n}{2r_j^n} \right) |Q_j^{n+\theta}| - \sum_{j \in S_i^-} \frac{\psi_j^n}{2} |Q_j^{n+\theta}| + \sum_{j \in S_i^+ \cup S_i^-} d_j^{n+\theta} \right] \right\} C_i^n \\ &\quad + \Delta t \sum_{j \in S_i^-} \left[\left(1 - \frac{\psi_j^n}{2} \right) |Q_j^{n+\theta}| + \left(\sum_{\ell \in S_i^+} \frac{\psi_\ell^n}{2r_\ell^n} |Q_\ell^{n+\theta}| \right) \frac{|Q_j^{n+\theta}|}{\sum_{\ell \in S_i^-} |Q_\ell^{n+\theta}|} + d_j^{n+\theta} \right] C_{m(i,j)}^n \\ &\quad + \Delta t \sum_{j \in S_i^+} d_j^{n+\theta} C_{m(i,j)}^n. \end{aligned} \quad (22)$$

Since $0 \leq \psi \leq 2$ and $0 \leq \psi/r \leq 2$, all the coefficients of $C_{m(i,j)}^n$ on the right hand side of Equation (22) are always non-negative. Additionally, with a sufficiently small time step size, the coefficient of C_i^n will be non-negative as well. Moreover, since the sum of all these coefficients is exactly equal to the right hand side of Eq. (7), the new concentration C_i^{n+1} given by Eq. (22) is a weighted average of C_i^n and $C_{m(i,j)}^n$. Accordingly, the max–min property, and hence stability, is implied. The above limitation on the time step size is assured by the following inequality:

$$\Delta t \leq \frac{P_i H_i^n}{2 \sum_{j \in S_i^+} |Q_j^{n+\theta}| + \sum_{j \in S_i^+ \cup S_i^-} d_j^{n+\theta}}. \quad (23)$$

Should this restriction be too severe for the hydrodynamic model, a sub-cycling approach can be used. To this purpose it is sufficient to observe that the discrete continuity Eq. (7) is still satisfied at any substep level provided that the total water depths at substep level are linearly interpolated between H_i^n and H_i^{n+1} .

2.5. Advection in a curved channel

As an example, consider a U-shaped channel of length $L = 8570$ m, width $W = 120$ m and constant depth $h = 10$ m. The channel is open at both ends where a different water surface elevation $\eta_1 = 9$ cm and $\eta_2 = -9$ cm is specified in order to drive a constant flow. The channel is then covered with a uniform grid of square polygons with side $\lambda = 20$ m (see Fig. 2a).

A steady flow is assumed after 1 h of hydrodynamic simulation using a time step $\Delta t = 30$ s. Then a tracer of constant concentration $C = 1$ is specified at the inflow open boundary for 12 min and the horizontal diffusion coefficient is set to zero so that pure transport is being considered.

Fig. 3 shows the computed concentrations at times $t = 2$ h 15 min, $t = 3$ h 30 min and $t = 4$ h 45 min by using the upwind method obtained from Eq. (12) without flux limiter ($\Phi = 0$). Fig. 4 shows the computed concentrations at same times obtained with the same method where the *superbee* flux limiter (19) was activated. In both cases precise mass conservation and maximum principle was obtained and, as expected, use of the flux limiter leads to a less diffusive solution as shown in Fig. 4.

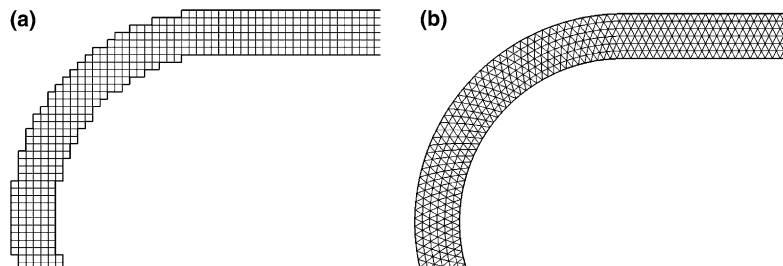


Fig. 2. U-shaped channel discretized with a uniform square grid (a) and a with flow-aligned grid (b).

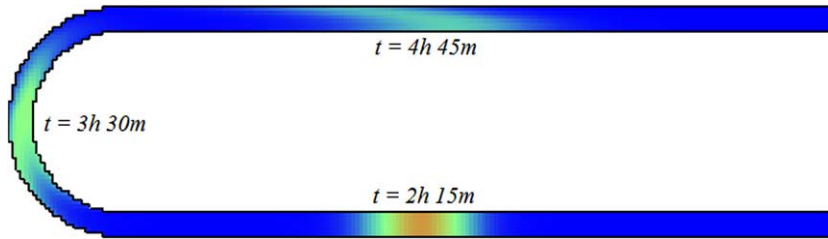


Fig. 3. Tracer concentration obtained with the upwind method.

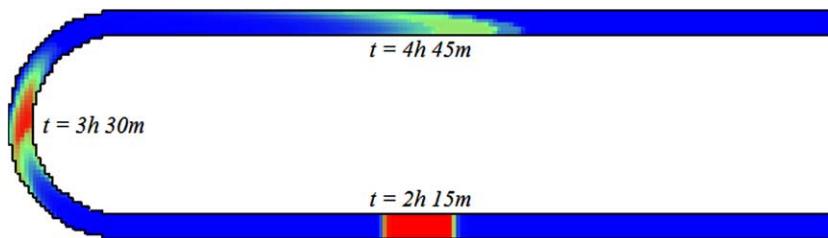


Fig. 4. High resolution obtained with a flux limiter.

2.6. Role of grid alignment

In the previous example of pure advection in a two-dimensional steady flow, the expected solution for the tracer concentration is a step function with values $C = 0$ and 1 .

The known diffusive character of the upwind method, with no surprise, is shown in Fig. 3. The second run that uses the flux limiter shows a rather sharp solution in the first straight section of the channel. This, however, deteriorates in the curved section and maintains its modified shape again in the second straight section of the channel. This loss of accuracy can be attributed to both, the use of inaccurate flow field (as obtained in the curved section of the channel) and the inability of the present flux limiter approach to prevent numerical diffusion in this region.

These results suggest that the grid alignment may play an important role in the accuracy of the computed results. Indeed, whenever possible, the grid lines should be aligned with the flow or with the expected net flow.

As a second example, in fact, the above curved channel is covered with a boundary fitted triangular grid and with grid lines aligned to the expected flow (see Fig. 2b).

Fig. 5 shows the computed concentrations by using the *superbee* flux limiter. Again, precise mass conservation and maximum principle was obtained. Moreover, a comparison between Figs. 4 and 5 shows the importance of grid alignment with the flow: in this latter example one can clearly observe a much more realistic profile and sharper fronts.

This example shows that, in addition to a high resolution method, a properly devised grid plays an important role for the accuracy of the numerical result. After all, a flow that is perfectly aligned

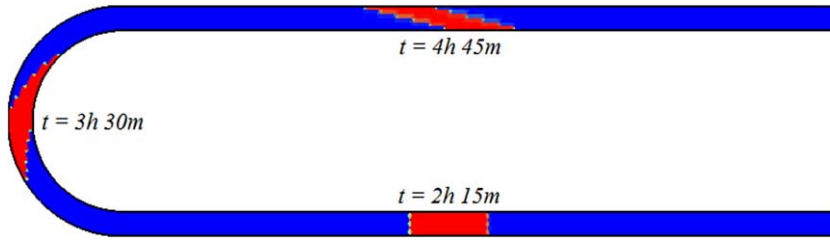


Fig. 5. Higher resolution on a flow aligned grid.

to the grid is equivalent to a set of one-dimensional transport problems for which these methods are proven to be extremely accurate (LeVeque, 1990). Consequently, for practical two-dimensional problems the grid generation issue should also address the possibility of producing grids that are flow aligned, or, at least with grid lines oriented with the net flow field.

3. Three-dimensional extensions

The concepts described above also extend to three-dimensional advection–diffusion problems. The governing hydrodynamic equations are the Reynolds averaged Navier–Stokes equations that express the physical principle of conservation of momentum and water volume:

$$u_t + uu_x + vu_y + wu_z - fv = -p_x + v^h(u_{xx} + u_{yy}) + (v^v u_z)_z, \quad (24)$$

$$v_t + uv_x + vv_y + wv_z + fu = -p_y + v^h(v_{xx} + v_{yy}) + (v^v v_z)_z, \quad (25)$$

$$w_t + uw_x + vw_y + ww_z = -p_z + v^h(w_{xx} + w_{yy}) + (v^v w_z)_z - \frac{\rho}{\rho_0} g, \quad (26)$$

$$u_x + v_y + w_z = 0, \quad (27)$$

where $u(x, y, z, t)$, $v(x, y, z, t)$ and $w(x, y, z, t)$ are the velocity components in the horizontal x -, y - and vertical z -directions, respectively; $p(x, y, z, t)$ is the normalized pressure and v^h and v^v are non-negative coefficients of horizontal and vertical eddy viscosity, respectively. Finally, ρ denotes the water density and ρ_0 is a constant reference density.

Integrating the continuity Eq. (27) over depth and using a kinematic condition at the free-surface leads to the following free-surface equation (see, e.g., Casulli and Zanolli, 2002)

$$\eta_t + \left[\int_{-h}^{\eta} u dz \right]_x + \left[\int_{-h}^{\eta} v dz \right]_y = 0. \quad (28)$$

The mass conservation of a scalar variable is expressed by the following differential equation:

$$C_t + (uC)_x + (vC)_y + (wC)_z = (K^h C_x)_x + (K^h C_y)_y + (K^v C_z)_z, \quad (29)$$

where K^h and K^v are prescribed non-negative horizontal and the vertical diffusivity coefficients, respectively.

The system is finally closed by an equation of state that relates the water density to the concentration of each scalar variable. This equation takes the form

$$\rho = \rho(C). \tag{30}$$

3.1. Numerical approximation

Once the (x, y) domain has been covered with an unstructured orthogonal grid, along the vertical direction a simple finite difference discretization, not necessarily uniform, is adopted. By denoting with $z_{k+\frac{1}{2}}$ a given level surface, the vertical discretization step is defined by $\Delta z_k = z_{k+\frac{1}{2}} - z_{k-\frac{1}{2}}$, $k = 1, 2, \dots, N_z$.

The three-dimensional space discretization consists of prisms whose horizontal faces are the polygons of a given orthogonal grid and whose height is Δz_k .

The discrete velocities and water surface elevation are defined at staggered locations as follows. The water surface elevation η_i^n , assumed to be constant within each polygon, is located at the center of the i th polygon; the velocity component normal to each face of a prism, assumed to be constant over the face, is defined at the point of intersection between the face and the segment joining the centers of the two prisms which share the face; the pressure $p_{i,k}^n$ and the concentrations $C_{i,k}^n$ are located at the center of the i th polygon and half way between $z_{k+\frac{1}{2}}$ and $z_{k-\frac{1}{2}}$. Finally, the water depth h_j is specified and assumed constant on each side of a polygon.

Since Eqs. (24) and (25) are invariant under solid rotation of the x and y axis on the horizontal plane, with a properly chosen reference frame, a consistent semi-implicit finite difference discretization for the horizontal velocity component on each vertical face of a prism takes the following form:

$$u_{j,k}^{n+1} = Fu_{j,k}^n - \frac{\Delta t}{\delta_j} [p_{i(j,2),k}^{n+\theta} - p_{i(j,1),k}^{n+\theta}] + \frac{\Delta t}{\Delta z_{j,k}^n} \left(v_{j,k+\frac{1}{2}}^v \frac{u_{j,k+1}^{n+1} - u_{j,k}^{n+1}}{\Delta z_{j,k+\frac{1}{2}}^n} - v_{j,k-\frac{1}{2}}^v \frac{u_{j,k}^{n+1} - u_{j,k-1}^{n+1}}{\Delta z_{j,k-\frac{1}{2}}^n} \right), \tag{31}$$

$$k = m_j, m_j + 1, \dots, M_j^n,$$

where $u_{j,k}^n$ denotes the horizontal velocity component normal to the j th side of the grid, at vertical level k and time step n . The positive direction for $u_{j,k}^n$ has been chosen to be from $i(j, 1)$ to $i(j, 2)$. F is an explicit finite difference operator which accounts for the contributions from the discretization of the Coriolis, atmospheric pressure, baroclinic pressure, advection and horizontal viscosity terms.

The vertical space increment $\Delta z_{j,k}^n$ is defined as the distance between two consecutive level surfaces, except near the bottom and near the free surface where $\Delta z_{j,k}^n$ is the distance between a level surface and the bottom or free-surface, respectively. Thus, in general, $\Delta z_{j,k}^n$ depends on the spatial location and near the free-surface it also depends on the time step. The vertical space increment $\Delta z_{j,k}^n$ is also allowed to vanish in order to account for wetting and drying. Of course, the discrete momentum equation (31) are not defined at the grid points characterized by $\Delta z_{j,k}^n = 0$. Finally, m_j and M_j^n , $1 \leq m_j \leq M_j^n \leq N_z$, denote the lower and upper limit for the k -index representing the bottom and the top finite difference stencil, respectively. As indicated, m and M depend on their

spatial location and M may also change with the time level to account for the free-surface dynamics. For notational simplicity, the subscript and the superscript to m_j and M_j^n will be omitted in the following development.

In analogy with Eq. (31) a consistent semi-implicit discretization for the vertical component of the velocity at the top face of each computational prism is derived from Eq. (26) and takes the following form:

$$w_{i,k+\frac{1}{2}}^{n+1} = Fw_{i,k+\frac{1}{2}}^n - \frac{\Delta t}{\Delta z_{i,k+\frac{1}{2}}^n} [p_{i,k+1}^{n+\theta} - p_{i,k}^{n+\theta}] + \frac{\Delta t}{\Delta z_{i,k+\frac{1}{2}}^n} \left(v_{i,k+1}^v \frac{w_{i,k+\frac{3}{2}}^{n+1} - w_{i,k+\frac{1}{2}}^{n+1}}{\Delta z_{i,k+1}^n} - v_{i,k}^v \frac{w_{i,k+\frac{1}{2}}^{n+1} w_{i,k-\frac{1}{2}}^{n+1}}{\Delta z_{i,k}^n} \right),$$

$$k = m_i, m_i + 1, \dots, M_i^n - 1, \quad (32)$$

where the explicit finite difference operator F accounts only for the contributions from the discretization of the advection and horizontal viscosity terms.

In each computational cell below the free-surface, the finite volume form of the incompressibility condition (27) is taken to be

$$\sum_{\ell=1}^{S_i} S_{i,\ell} \lambda_{j(i,\ell)} \Delta z_{j(i,\ell),k}^n u_{j(i,\ell),k}^{n+\theta} + P_i \left(w_{i,k+\frac{1}{2}}^{n+\theta} - w_{i,k-\frac{1}{2}}^{n+\theta} \right) = 0, \quad k = m_i, m_i + 1, \dots, M_i^n - 1. \quad (33)$$

At the free-surface, the finite difference approximation of Eq. (28) is taken to be

$$P_i \eta_i^{n+1} = P_i \eta_i^n - \Delta t \sum_{\ell=1}^{S_i} [S_{i,\ell} \lambda_{j(i,\ell)} \Delta z_{j(i,\ell),M}^n u_{j(i,\ell),M}^{n+\theta}] + \Delta t P_i w_{i,M-\frac{1}{2}}^{n+\theta}, \quad (34)$$

Finally, by assuming that the pressure in the surface cells is hydrostatic, the system is closed by the following hydrostatic relation:

$$p_{i,M}^{n+1} = g(\eta_i^{n+1} - z_M). \quad (35)$$

The set of Eqs. (31)–(34) forms a linear system of $N_z(N_s + 2N_p)$ with unknowns $u_{j,k}^{n+1}$, $w_{i,k+\frac{1}{2}}^{n+1}$, $p_{i,k}^{n+1}$ and η_i^{n+1} to be solved at each time step. An efficient numerical algorithm to solve this system can be found in Casulli and Zanolli (2002).

When the space and time scale of the hydrodynamic problem allows the hydrostatic approximation to be valid, the governing Eqs. (24)–(26) and the corresponding discretizations (31), (32) are simplified. The discrete incompressibility condition (33) and the discrete free surface Eq. (34), however, remain valid as given above (for details see Casulli and Zanolli, 2002).

3.2. Scalar transport

By using the incompressibility condition (27), the mass conservation Eq. (29) can also be written in a non-conservative form which implies the maximum principle.

In order to derive a conservative scheme for Eq. (29) that also yield the max–min property, it must be consistent with both, the discretized continuity Eq. (33) and the discretized free surface Eq. (34). Assuming that the vertical component of the velocity is positive, a general semi-implicit form of such a scheme is derived in a similar way to its two-dimensional equivalent (20) and is taken to be

$$\begin{aligned}
 P_i \Delta z_{i,k}^{n+1} C_{i,k}^{n+1} &= P_i \Delta z_{i,k}^n C_{i,k}^n - \Delta t \left[\sum_{j \in S_i^+} |Q_{j,k}^{n+\theta}| C_{i,k}^n - \sum_{j \in S_i^-} |Q_{j,k}^{n+\theta}| C_{m(i,j),k}^n \right] \\
 &\quad - \Delta t \left[|Q_{i,k+\frac{1}{2}}^{n+\theta}| C_{i,k}^n - |Q_{i,k-\frac{1}{2}}^{n+\theta}| C_{i,k-1}^n \right] + \Delta t \sum_{j \in S_i^- \cup S_i^+} d_{j,k}^{n+\theta} [C_{m(i,j),k}^n - C_{i,k}^n] \\
 &\quad + \Delta t \left[d_{i,k+\frac{1}{2}}^{n+\theta} (C_{i,k+1}^{n+1} - C_{i,k}^{n+1}) - d_{i,k-\frac{1}{2}}^{n+\theta} (C_{i,k}^{n+1} - C_{i,k-1}^{n+1}) \right] \\
 &\quad - \frac{\Delta t}{2} \left[\psi_{i,k+\frac{1}{2}}^n |Q_{i,k+\frac{1}{2}}^{n+\theta}| (C_{i,k+1}^n - C_{i,k}^n) - \psi_{i,k-\frac{1}{2}}^n |Q_{i,k-\frac{1}{2}}^{n+\theta}| (C_{i,k}^n - C_{i,k-1}^n) \right] \\
 &\quad - \frac{\Delta t}{2} \sum_{j \in S_i^- \cup S_i^+} \psi_{j,k}^n |Q_{j,k}^{n+\theta}| [C_{m(i,j),k}^n - C_{i,k}^n], \tag{36}
 \end{aligned}$$

where $Q_{j,k}^{n+\theta} = \lambda_j \Delta z_{j,k}^n u_{j,k}^{n+\theta}$, $Q_{i,k\pm\frac{1}{2}}^{n+\theta} = P_i w_{i,k\pm\frac{1}{2}}^{n+\theta}$ and $D_{j,k} = \lambda_j \Delta z_{j,k}^n \frac{K_{j,k}^h}{\delta_j}$, $D_{i,k\pm\frac{1}{2}}^n = P_i \frac{K_{i,k\pm\frac{1}{2}}^v}{\Delta z^n}$ are the advective and the diffusive flux coefficients, respectively; $d = \max(0, D - \frac{1}{2}|Q|)$ and $\psi(r)$ is the additional contribution to the flux limiter function that depends on the ratio of consecutive gradients.

Note that an implicit discretization is used for the vertical diffusion terms in order to prevent that the use of relatively small vertical space increment leads to a severe stability restriction.

One interesting property of the present discretization is in the fact that when only one layer is considered ($M = 1$) then $\Delta z = H$ and the finite volume scheme (36) reduces to the corresponding two-dimensional Formula (20).

When the flux limiter function is taken to be one of (17), (18) or (19), by using the discrete continuity Eqs. (33) and (34) and with similar arguments as given for the two-dimensional model, a sufficient condition that yields the max–min property, and hence stability of Eq. (36), can be shown to be

$$\Delta t \leq \frac{P_i \Delta z_{i,k}^n}{2 \sum_{j \in S_i^+} |Q_{j,k}^{n+\theta}| + 2 |Q_{i,k+\frac{1}{2}}^{n+\theta}| + \sum_{j \in S_i^+ \cup S_i^-} d_{j,k}^{n+\theta}}. \tag{37}$$

With properly specified boundary conditions, Eq. (36) form a set of N_p linear, tridiagonal systems with unknowns $C_{i,k}^{n+1}$ on the same water column. The coefficient matrix of these systems is strongly diagonally dominant, symmetric and positive definite. Thus, the scalar concentration $C_{i,k}^{n+1}$ can be readily determined by solving these systems with a direct method.

Once the new concentrations $C_{i,k}^{n+1}$ have been computed for each scalar variable, the equation of state (30) is used to update the water density $\rho_{i,k}^{n+1}$ in every computational prism.

3.3. Lock exchange

The third example is concerned with the so-called "lock exchange" problem. This is a severe test case that requires both, an accurate non-hydrostatic flow algorithm, as well as an accurate advection scheme.

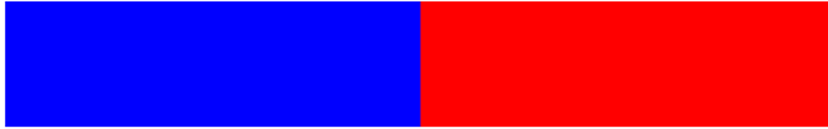


Fig. 6. Initial configuration for the lock exchange problem.

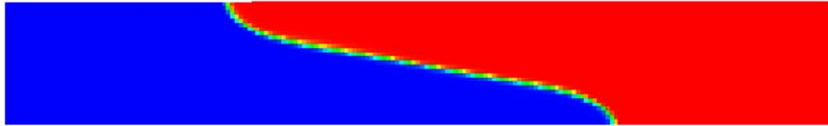


Fig. 7. Lock exchange solution at $t = 10$ s.

A rectangular basin of length $L = 2$ m, and depth $h = 0.3$ m is initially filled with two fluids with different densities $\rho_1 = 1.03$ and $\rho_2 = 1.0$, separated by a vertical dam located centrally in the basin (see Fig. 6).

No physical diffusion was considered but a positive horizontal and vertical viscosity has been specified in order to prevent the development of Kelvin–Helmholtz interfacial instability. The initial velocity is zero and the initial free surface is flat, horizontal.

The computational domain is discretized using an horizontal grid of $N_p = 200$ equilateral triangles of side $\ell = 2$ cm and a uniform vertical increment of $\Delta z_k = 1$ cm.

The calculation is carried out with a time step $\Delta t = 0.01$ s. Once the dam is removed the resulting solution shows the evolution of the fluid interface. The numerical solution obtained at time $t = 10$ s with the *superbee* flux limiter is shown in Fig. 7. As expected, the mass is rigorously conserved and the maximum principle is never violated.

The present results are in agreement with early calculations obtained with traditional finite difference method and with experimental results (see Casulli and Stelling, 1998)). It is also to be noted that the chosen grid is uniform and flow independent. Nevertheless, also in this example use of flux limiters leads to a high resolution of the density profile.

4. Conclusions

A finite volume algorithm for solving the scalar transport equation in free surface hydrodynamic has been derived, discussed and applied. The discrete velocity field and free surface elevation are assumed to strictly satisfy the volume conservation. Although most concepts presented here also extend to general unstructured grid models, a detailed analysis has been presented on *orthogonal* unstructured grids for which a recent, robust, efficient and conservative hydrodynamic model is available.

The resulting algorithm for advection–diffusion equation is locally and globally mass conservative. Moreover it satisfies a discrete maximum principle. Accordingly, the computed results are stable and are guaranteed to have oscillation free profiles. Higher resolution can be obtained by using appropriate flux limiters and, whenever possible, by using a grid that is oriented with the expected net flow.

Further studies concerning the applications of the present algorithm to estuaries and coastal seas are in progress and the preliminary results obtained so far are definitely encouraging.

References

- Casulli, V., Cattani, E., 1994. Stability, accuracy and efficiency of a semi-implicit method for three-dimensional shallow water flow. *Computers and Mathematics with Applications* 27, 99–112.
- Casulli, V., Stelling, G.S., 1998. Numerical simulation of three-dimensional quasi-hydrostatic, free-surface flows. *ASCE Journal of Hydraulic Engineering* 124, 678–686.
- Casulli, V., Walters, R.A., 2000. An unstructured grid, three-dimensional model based on the shallow water equations. *International Journal for Numerical Methods in Fluids* 32, 331–348.
- Casulli, V., Zanolli, P., 2002. Semi-implicit numerical modeling of non-hydrostatic free-surface flows for environmental problems. *Mathematical and Computer Modelling* 36, 1131–1149.
- Greenspan, D., Casulli, V., 1988. *Numerical Analysis for Applied Mathematics, Science and Engineering*. Addison Wesley, 341 pp.
- LeVeque, R.J., 1990. *Numerical Methods for Conservation Laws. Lectures in Mathematics*, Birkhauser Verlag, 214 pp.
- Roe, P.L., 1985. Some contributions to the modeling of discontinuous flows. *Lectures Notes in Applied Mathematics* 22, 163–193.
- Stelling, G.S., 1984. On the construction of computational methods for shallow water flow problems. *Rijkswaterstaat Communications* 35, 226.
- Sweby, P.K., 1984. High resolution schemes using flux limiters for hyperbolic conservation laws. *SIAM Journal of Numerical Analysis* 21, 995–1011.
- van Leer, B., 1979. Towards the ultimate conservative difference scheme. V. A second order sequel to Godunov's method. *Journal of Computational Physics* 32, 101–136.



A scalable unstructured grid 3-dimensional finite volume model for the shallow water equations

David A. Ham ^{*}, Julie Pietrzak, Guus S. Stelling

*Faculty of Civil Engineering and Geosciences, Environmental fluid Mechanics Section,
Delft University of Technology, Stevinweg 1, 2628CN Delft, The Netherlands*

Received 5 December 2003; received in revised form 21 June 2004; accepted 24 August 2004

Available online 2 November 2004

Abstract

We present an unstructured grid finite volume three-dimensional hydrostatic model. An important aspect in 3D models is the choice of horizontal discretisation. For problems that are governed by complex coastal boundaries an unstructured grid approach seems attractive. This paper focuses on the development of a new unstructured grid three-dimensional hydrostatic model. An efficient and highly scalable implicit solution technique is adopted for the solution of the free surface elevation and an semi-Lagrangian approach is adopted for the advection of momentum and scalars. A number of tests are presented which show that the model is capable of simulating Kelvin waves in a circular basin and the North Sea.

© 2004 Elsevier Ltd. All rights reserved.

1. Introduction

Numerical models of coastal and ocean flows have generally employed finite differences on Cartesian grids. However, standard Cartesian meshes are restricted in their ability to fit arbitrary geometries. [Adcroft and Marshall \(1998\)](#) demonstrated that the staircase representation of coastlines, which is typical of structured grids, exerts a spurious form stress on model boundary

^{*} Corresponding author. Tel.: +31 152784069; fax: +31 152785975.

E-mail address: d.a.ham@citg.tudelft.nl (D.A. Ham).

URL: <http://fluidmechanics.tudelft.nl>

currents. A number of methods exist to overcome this problem and of these, finite volume and finite element unstructured grid approaches have many attractive features. Both methods have been demonstrated to work well in both ocean modelling and climate studies, for example Danilov et al. (2004) and Iskandarani et al. (2003) as well as in coastal studies (Pietrzak and Labeur, 2004, Casulli and Walters, 2000, Zhang and Baptista, in press). In this paper we present a new coastal ocean circulation model.

Walters and Casulli (1998) introduced a finite element method based on the Raviart–Thomas element. Their objective was to develop a robust method suitable for extreme hydraulics events with extensive flooding and drying. They therefore selected low order elements free of computational modes, such that continuity could be satisfied and in which wetting and drying was greatly simplified. Miglio et al. (1999) adopted a similar method. However, they used a different pressure gradient formulation, which effectively used the circumcentres of the elements instead of the centroids.

Here we adopt as a starting point the unstructured grid finite volume approach of Casulli and Walters (2000). This approach employs a semi-implicit time integration scheme in place of the commonly used technique of mode splitting. This scheme avoids the difficulties in maintaining consistency between internal and external modes which are a potential drawback of the latter approach. The technique of Casulli and Walters (2000) also allows for the inclusion of flooding and drying in a straightforward manner. They adopted an unstructured orthogonal grid, see Nicolaides (1993) and developed a method that allows any polygonal shape to be used. The simplicity of this approach, the grid flexibility and good scaling properties are attractive features of this method. However it, like the other previous work cited above, also suffers from one serious drawback: the grid is orthogonal. This places severe restrictions on the grid. On a triangular grid the circumcentres must be used in place of the centroid as the cell centre. Unless all of the angles of a given triangle are acute, the circumcentre will lie outside the triangle. In order to overcome this problem we use a pressure gradient discretisation which removes the orthogonality constraint. In addition we have developed a different semi-Lagrangian advection scheme.

In the following a new model is presented that is based upon an unstructured grid finite volume approach for the solution of the three-dimensional shallow water equations. With one layer the model reduces to a semi-implicit method for the two-dimensional vertically integrated equations. The paper is organised as follows: the shallow water equations are described in Section 2, the unstructured grid is described in Section 3, the discretisation of the equations is described in Sections 4 and 5, the scalability in Section 6, some test cases are described in Section 7 and conclusions are presented in Section 8.

2. Equations of motion

Large scale coastal flows may be modelled by the shallow water equations, a well known simplification of the Navier–Stokes equations based on the hydrostatic pressure assumption.

Let \mathbf{d} be any unit vector in the horizontal plane and let e be the projection of the fluid velocity, \mathbf{u} , onto \mathbf{d} . Then the shallow water equations are given by

$$\nabla \cdot \mathbf{u} = 0 \quad (1)$$

$$\frac{De}{Dt} = g\nabla\eta \cdot \mathbf{d} + v^h \left(\frac{\partial^2 e}{\partial x^2} + \frac{\partial^2 e}{\partial y^2} \right) + \frac{\partial}{\partial z} v^v \frac{\partial e}{\partial z} + (2(\boldsymbol{\Omega} \cdot \mathbf{k})\mathbf{k} \times \mathbf{u}) \cdot \mathbf{d} \quad (2)$$

Here, η is the free surface height, v^h and v^v are the horizontal and vertical turbulence viscosities, $\boldsymbol{\Omega}$ is the Earth's rotation vector, \mathbf{k} is the upward unit normal vector and g is acceleration due to gravity.

We choose to present Eq. (2), the momentum equation, in this form to demonstrate its rotational invariance: it is not necessary to solve for horizontal momentum components in the directions of the conventional basis vectors, and we do not propose to do so.

By integrating Eq. (1) from the bed ($z = h$) to the surface ($z = \eta$) and applying kinematic boundary conditions at the surface and bed we obtain an expression for the free surface. Once again, we choose to present this equation in basis independent form

$$\frac{\partial \eta}{\partial t} + \nabla_{xy} \cdot \int_h^\eta \mathbf{u}_{xy} dx = 0 \quad (3)$$

The vertical velocity follows from Eq. (1), the continuity equation.

3. The unstructured grid

3.1. Variable resolution

In order to achieve accurate results in particular regions of interest, in this case the coastal region, it is necessary to employ a grid with a small mesh size. However, using a very fine grid in regions whose detailed structure is of less interest is a highly inefficient use of computational resources. To be able to resolve the coast accurately while modelling the sea at acceptable cost, it is therefore necessary to vary the grid resolution in space. In addition, since coastal flows are strongly influenced by the shape of the coastline, it is important that flow artifacts introduced by the presence of grid corners on the coast be avoided. While some grid variation is possible using curvilinear structured grids, to achieve highly variable resolution in complex geometries, it is necessary to employ unstructured grids.

In previous work similar to this, a requirement was made that the grid used be orthogonal (Casulli and Walters, 2000). That is, the line joining two adjacent column centres must be orthogonal to the column face between them. On a triangular grid, this can be achieved by using the circumcentres as the centres of the triangles. However, unless all of the angles in a triangle are acute, its circumcentre will lie outside the triangle. Generating triangular grids in complex geometries which contain no obtuse angles is a formidable challenge. We therefore choose not to impose an orthogonality requirement. This choice allows the use of a much wider range of grids but has implications for the treatment of the pressure gradient term.

3.2. Element shape

The generation of unstructured grids based on simplices is a well developed field. This is in large part due to the long history of unstructured finite element codes. In the shallow water case, the

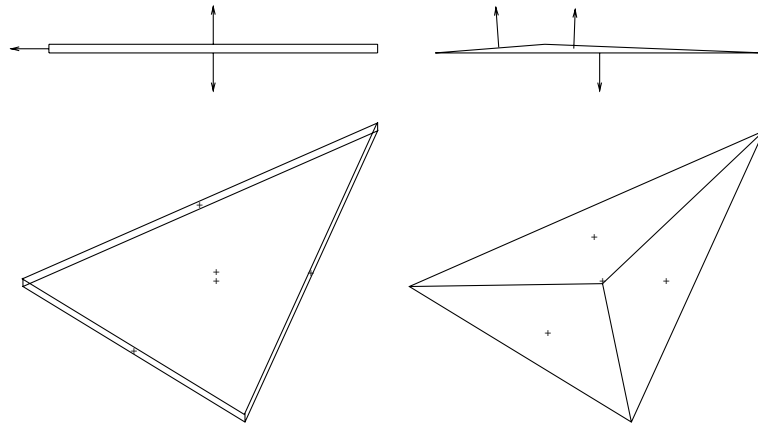


Fig. 1. Elevation and perspective views of prismatic and tetrahedral elements showing face centres and a representative selection of face normal vectors. It is evident in the case of the tetrahedron that the horizontal components of those vectors are small.

geometry of the problem presents particular challenges to the use of 3-dimensional simplices (tetrahedra) in staggered grid finite volume calculations. Since the horizontal cell dimensions may be orders of magnitude larger than the vertical dimension, the cell face normal vectors of a tetrahedron will be approximately vertical making accurate resolution of horizontal velocities difficult. By instead using prisms as cells we can ensure vertical cell faces thereby obtaining horizontal normal vectors and hence accurate horizontal velocity resolution (Fig. 1).

The use of prismatic elements also simplifies the task of grid generation. First a two-dimensional grid is generated for the domain. This grid defines a set of water columns stretching from the free surface down to the bed. Each water column is then divided into a series of cells. This is currently implemented as a z -level scheme, although other vertical discretisations are in principle possible (Pietrzak et al., 2002). A further important benefit of this grid structure is that the scalar and momentum evaluation points are aligned vertically. This both facilitates the efficient evaluation of the pressure gradient term and enables a partial decoupling of the momentum and continuity equations which has advantageous scaling properties. We will return to this matter in Section 6.

3.3. Grid notation

To facilitate discussion of the discretised problem, we adopt the following conventions based loosely on those found in Casulli and Walters (2000). Let G be an unstructured grid and (G, E) its graph. We adopt the convention that i will always indicate an index in G while j will always indicate an index in E . For example \mathbf{x}_i refers to the position of the i th column centre while \mathbf{x}_j refers to the position of the j th column face. Let S_i be the set of the indices of the column faces adjacent to column i . Then define the function j such that $j(i, l)$, $1 \leq l \leq |S_i|$ is the index of the l th column face adjacent to column i . Similarly, we define $i(j, l)$, $l \in \{1, 2\}$ to be the column(s) adjacent to face j . Fig. 2 illustrates this naming scheme. Finally, we will reserve the index k to refer to the layer of a given cell and define L and a function k in an analogous manner to S and the function j . The layer

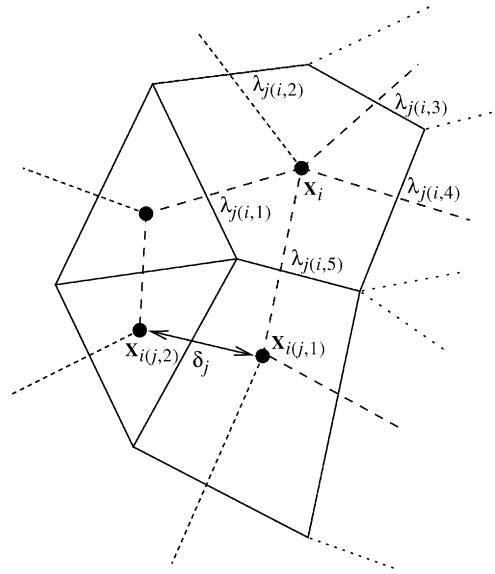


Fig. 2. Grid fragment showing indexing conventions for water columns and column faces.

of a horizontal face above level k is $k + \frac{1}{2}$ and the layer below is naturally $k - \frac{1}{2}$. Observe that this numbering is physically consistent in that $(k + 1) - \frac{1}{2} = k + \frac{1}{2}$.

In addition to the index numbers for water columns and column sides, some notation will be used to consistently refer to the data associated with those objects. These are displayed in Table 1. The notation \mathbf{n} and \mathbf{N} require a little explanation. \mathbf{N}_j is the fixed normal vector associated with column side j . $\mathbf{n}_{i,j}$ on the other hand is the normal vector at side j which points outwards relative to the adjacent column cell i . This is most often used in the case of the quantity $(\mathbf{n} \cdot \mathbf{N})_{i,j}$ which has value 1 if \mathbf{N}_j is outward pointing and -1 if it is inward pointing relative to column i . Then,

$$(\mathbf{n} \cdot \mathbf{N})_{i(j,1),j} = -(\mathbf{n} \cdot \mathbf{N})_{i(j,2),j} \tag{4}$$

In the case of horizontal cell faces, we remove some notational clutter by specifying, without loss of generality, that all normal vectors point upwards. That is, we require

$$\forall g_i \in G \forall k \in L_i \mathbf{N}_{i,k \pm \frac{1}{2}} = (0, 0, 1)$$

4. Discretisation of the equations

Generalising the approach in Casulli and Walters (2000), we adopt a semi-implicit finite difference discretisation of the momentum equation and semi-implicit finite volume discretisations of the continuity equation. For the remainder of this section, let G be an unstructured grid and (G, E) its graph.

Table 1
Notation for data associated with water columns and column sides

A_i	Cross section area
$A_{*,k}$	Cell face area
h_*	Bed depth
L_*	Set of layer indices of a water column or column side
$\mathbf{n}_{i,*,[k]}$	Cell or column face outward normal vector
$\mathbf{N}_{*,[k]}$	Cell or column face normal vector
S_i	Set of column side indices of water column i
$u_{*,k}$	Cell face normal velocity component
$\mathbf{u}_{*,k}$	Velocity vector
$\mathbf{x}_{*,[k]}$	Position
$\Delta z_{*,k}$	$\ \mathbf{x}_{*,k+\frac{1}{2}} - \mathbf{x}_{*,k-\frac{1}{2}}\ $
δ_j	Distance between $\mathbf{x}_{i(j,1)}$ and $\mathbf{x}_{i(j,2)}$
η_*	Free surface height
λ_j	Length of polygon edge
$g_{i,[k]}$	Cell or water column per se
$e_{*,[k]}$	Cell or water face per se

An asterisk is a wildcard for a member of $\{i,j\}$ while square brackets ([]) indicate an optional argument. For temporally variable data, time step will be indicated with a superscript.

4.1. The free surface equation

As one way of ensuring conservation of mass, we adopt a finite volume discretisation of the Eq. (3)

$$A_i \frac{\partial \eta_i}{\partial t} + \sum_{j \in S_i} \left((\mathbf{n} \cdot \mathbf{N})_{i,j} \sum_{k \in L_j} A_{j,k} u_{j,k} \right) = 0 \quad (5)$$

Adopting a semi-implicit θ scheme in time and rewriting in vector notation, we have

$$A_i \eta_i^{n+1} = A_i \eta_i^n - \theta \Delta t \sum_{j \in S_i} ((\mathbf{n} \cdot \mathbf{N})_{i,j} A_j \cdot U_j^{n+1}) - (1 - \theta) \Delta t \sum_{j \in S_i} ((\mathbf{n} \cdot \mathbf{N})_{i,j} A_i \cdot U_j^n) \quad (6)$$

where

$$A_j = \begin{bmatrix} A_{j,k(j,1)} \\ \vdots \\ A_{j,k(j,|L_j|)} \end{bmatrix}, \quad U_j = \begin{bmatrix} u_{j,k(j,1)} \\ \vdots \\ u_{j,k(j,|L_j|)} \end{bmatrix}$$

The continuity equation integrated over a single cell rather than the whole water column is used to solve for $u_{i,k+\frac{1}{2}}$. In this case Eq. (1) becomes

$$A_i \left(u_{i,k+\frac{1}{2}} - u_{i,k-\frac{1}{2}} \right) + \sum_{j \in S_i} (\mathbf{n} \cdot \mathbf{N})_{i,j} A_{j,k} u_{j,k} = 0 \quad (7)$$

4.3. The pressure gradient term

On an orthogonal staggered grid, the pressure gradient can be discretised in a straightforward manner with a central difference scheme

$$H_j = (\mathbf{n} \cdot \mathbf{N})_{i(j,1),j} \frac{\eta_{i(j,2)} - \eta_{i(j,1)}}{\delta_j} \quad (11)$$

In the non-orthogonal case, the interval joining two adjacent column centres is not parallel to the normal of the face between those water columns. It is therefore necessary to use more information, and hence a larger stencil, to calculate the projection of the discretised pressure gradient onto the column face normal. We adopt here the path integral method introduced for curvilinear structured grids in van Beek et al. (1995) and generalised to unstructured grids in Wenneker et al. (2002). The essence of this approach is that the positions of nearby column centres are used to construct a basis for \mathbb{R}^2 and the gradient of the pressure field is evaluated with respect to that basis by applying a central difference approximation on the surface elevations at those column centres. The gradient vector so constructed is then projected onto the water column face normal.

For some arbitrary $e_j \in E$ we will construct $\{\mathbf{t}_{j,1}, \mathbf{t}_{j,2}\}$, a unit (although not necessarily orthogonal) basis for \mathbb{R}^2 . We choose

$$\mathbf{t}_{j,1} = (\mathbf{n} \cdot \mathbf{N})_{i(j,1),j} \frac{\mathbf{x}_{i(j,2)} - \mathbf{x}_{i(j,1)}}{\delta_j}$$

so that

$$\nabla P \cdot \mathbf{t}_{j,1} \approx \frac{\eta_{i(j,2)} - \eta_{i(j,1)}}{\delta_j}$$

For numerical reasons, it is important that $|\mathbf{t}_{j,1} \cdot \mathbf{t}_{j,2}| \ll 1$. That is, the basis vectors should be far from collinear. This can be achieved by using the four water column centres $\{\alpha, \beta, \gamma, \delta\}$ indicated in Fig. 3 to interpolate the surface elevations at ϵ and ζ . We then choose

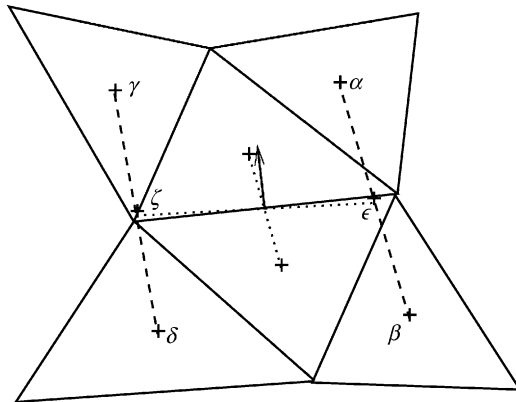


Fig. 3. The grid stencil of the path integral discretisation for the pressure gradient term.

$$\mathbf{t}_{j,2} = \frac{\mathbf{x}_\epsilon - \mathbf{x}_\zeta}{\|\mathbf{x}_\epsilon - \mathbf{x}_\zeta\|} = \frac{\mathbf{x}_\alpha + \mathbf{x}_\beta - \mathbf{x}_\gamma - \mathbf{x}_\delta}{\|\mathbf{x}_\alpha + \mathbf{x}_\beta - \mathbf{x}_\gamma - \mathbf{x}_\delta\|}$$

The corresponding component of the pressure gradient vector is then given by

$$\nabla P \cdot \mathbf{t}_{j,2} \approx \frac{\eta_\alpha + \eta_\beta - \eta_\gamma - \eta_\delta}{\|\mathbf{x}_\alpha + \mathbf{x}_\beta - \mathbf{x}_\gamma - \mathbf{x}_\delta\|}$$

After some rearrangement, this yields an expression for the water column face normal component of the pressure

$$H_j = \left(\begin{pmatrix} \left[\begin{matrix} \mathbf{t}_{j,1}^T \\ \mathbf{t}_{j,2}^T \end{matrix} \right]^{-1} \\ \mathbf{N}_j \end{pmatrix} \cdot \left[\begin{matrix} (\mathbf{n} \cdot \mathbf{N})_{i(j,1),j} \frac{\eta_{i(j,2)} - \eta_{i(j,1)}}{\delta_j} \\ \frac{\eta_\alpha + \eta_\beta - \eta_\gamma - \eta_\delta}{\|\mathbf{x}_\alpha + \mathbf{x}_\beta - \mathbf{x}_\gamma - \mathbf{x}_\delta\|} \end{matrix} \right] \right) \quad (12)$$

By construction of $\mathbf{t}_{j,1}$, in the special case, where $\mathbf{t}_{j,1} = \mathbf{N}_j$, H_j reduces to (11). It should be noted that, for each j , H_j is a linear operator on $\{\eta_i\}$ with coefficients constant in time. It is therefore only necessary to calculate these coefficients once for each water column face.

An advantage of pressure gradient discretisation on orthogonal grids is that Eq. (11) represents a symmetric operator and the resulting free surface matrix is symmetric positive definite (Casulli and Walters, 2000). This enables the use of the conjugent gradient method which is efficient and guaranteed to converge. The path integral formulation does not share this property and the resulting matrix must therefore be solved using a more general technique such as GMRES or BiCG-Stab. It should be noted, however, that on a high quality grid, that is one in which the cells are close to regular in shape, the path integral formulation is dominated by $\mathbf{t}_{j,1}$ so that the resulting matrix may be considered a perturbed symmetric matrix. It is therefore to be expected that the additional cost of the matrix solution will not be excessive. Similarly, no significant convergence problems have been encountered.

It is also necessary to derive an expression for I_j , the column side tangential pressure gradient component in (10). In the orthogonal case, (11) provides no information concerning the tangential component of the pressure gradient so Zhang and Baptista (in press) resort to interpolating the surface heights at the corners of the water columns. The path integral formulation adopted here, however, yields a direct expression for the full pressure gradient vector so that an expression for the tangential component follows immediately

$$I_j = \left(\begin{pmatrix} \left[\begin{matrix} \mathbf{t}_{j,1}^T \\ \mathbf{t}_{j,2}^T \end{matrix} \right]^{-1} \\ \mathbf{T}_j \end{pmatrix} \cdot \left[\begin{matrix} (\mathbf{n} \cdot \mathbf{N})_{i(j,1),j} \frac{\eta_{i(j,2)} - \eta_{i(j,1)}}{\delta_j} \\ \frac{\eta_\alpha + \eta_\beta - \eta_\gamma - \eta_\delta}{\|\mathbf{x}_\alpha + \mathbf{x}_\beta - \mathbf{x}_\gamma - \mathbf{x}_\delta\|} \end{matrix} \right] \right) \quad (13)$$

where \mathbf{T}_j is the horizontal column face tangent vector. It should be noted that (13) is not required for the solution of the surface elevation field so that (10) is, in fact, explicit in η .

4.4. The advection and Coriolis terms

Advection of momentum is simulated using an semi-Lagrangian approach based on the reverse tracking of streamlines while the Coriolis term is calculated on the basis of an extrapolated velocity. At this stage we disregard horizontal viscosity. Under this approach, the operator F in (8) becomes

$$Fu_{j,k}^n = \mathbf{u}_{j,k}^* \cdot \mathbf{n}_j + f(v_{j,k}^n + \gamma(v_{j,k}^{n-1} - v_{j,k}^n)) \quad (14)$$

where $\mathbf{u}_{j,k}^*$ is the velocity interpolated at the end of a streamline followed back through the interval Δt from the point $\mathbf{x}_{j,k}$, $f = 2\boldsymbol{\Omega} \cdot \mathbf{k}$ is the Coriolis parameter and $\gamma \in [0, 1]$ is an extrapolation parameter which is most often set to 0.5. Whereas the derivations in the previous sections apply on unstructured grids composed of prisms of arbitrary cross-section, we shall assume for the derivations of the semi-Lagrangian scheme that the grid is composed purely of triangular prisms.

4.5. Interpolating the velocity

Since the water column sides are known to be vertical, it is only necessary to interpolate the horizontal components of the velocity field. Should the vertical component be required, for example as a diagnostic tool, this can be interpolated from the vertical velocities at cell top and bottom faces independently of the horizontal components.

The horizontal velocity components are interpolated in a linear two stage process. First, consider $P_{i,k}$, the intersection of the plane containing the points $\{\mathbf{x}_j | j \in S_{i,k}\}$ with the water column g_i . Then, for any $\mathbf{x} \in P_{i,k}$, the horizontal velocity may be interpolated using linear Raviart–Thomas basis functions.

Finally, the horizontal velocity vector at any point $\mathbf{x} \in g_i$ may be constructed by interpolating between adjacent planes $P_{i,k}$, $P_{i,k+1}$ along the vertical line through \mathbf{x} .

5. Streamline tracking

The quality of the streamline algorithm has been recognised as an important factor in the suitability of an semi-Lagrangian advection model (Oliveira and Baptista, 1998). Care must be had that the calculated streamlines do not exhibit unphysical behaviour, such as crossing each other or a closed boundary. If momentum, and ultimately other scalar quantities, are to be conserved it is also imperative that the conservation of mass which is ensured by the finite volume discretisation of the continuity equation is translated to closed streamlines.

The approach we adopt is a generalisation of that originally developed for structured grids in two dimensions in Dunsbergen (1994). First, a velocity field, $\hat{\mathbf{u}}$, is constructed throughout the grid. This velocity field is then integrated analytically to produce an expression for the evolution of the position of a point under the flow in time. This function can then be evaluated to find appropriate Lagrangian trajectories for (14). There are a number of properties which are desirable in such a field

- (1) It must agree with known data.
- (2) It must be easy to integrate analytically.
- (3) The streamlines produced by integrating the field must not cross each other or closed boundaries.
- (4) It should satisfy the continuity equation everywhere.

If we choose a cell-wise linear velocity field then condition 2 is satisfied automatically since the position function may be recovered by solving a system of at most three first order linear ODEs for each cell. It is an immediate consequence of Gauss' Theorem that a cell-wise linear velocity field which satisfies the continuity equation integrated over a cell in fact satisfies continuity at every point in that cell. Since a finite volume discretisation was adopted for the continuity equation, any cell-wise linear interpolation $\hat{\mathbf{u}}$ which satisfies

$$\int_{e_{*,k}} \hat{\mathbf{u}} \cdot \mathbf{N}_{*,k} \, dA = A_{*,k} u_{*,k} \quad (15)$$

will ensure that condition 4 is satisfied. Due to the linearity of $\hat{\mathbf{u}}$, an equivalent condition to (15) is that, at any cell face centroid, $\hat{\mathbf{u}} \cdot \mathbf{N}_{*,k} = u_{*,k}$. So, on a grid whose face centres are defined to be the centroids of those faces, and for cell-wise linear $\hat{\mathbf{u}}$, condition 4 is equivalent to condition 2.

One possible solution is to use the same Raviart–Thomas basis functions used to interpolate velocity in Section 4.5. Such a field, however, is not in general continuous. In particular this means that the face normal velocity component may change sign discontinuously at the cell face in violation of condition 3. This is a fatal problem. Not only does it adversely affect the conservation properties of advected quantities, it prevents the unambiguous following of streamlines which is essential for the semi-Lagrangian scheme.

An alternative approach is to require that the normal velocity to each cell face be constant over that cell face. This constraint ensures that the velocity field is continuous along cell faces. It also significantly reduces the complexity, and hence the cost, of calculating the field in each cell. For each cell $g_{i,k}$, the velocity field may be written

$$\hat{\mathbf{u}}_{i,k}(\mathbf{x}) = \mathbf{A}_{i,k} \mathbf{x} + b_{i,k} \quad (16)$$

Since the cell sides are known to be vertical

$$\frac{\partial \hat{u}}{\partial z} = \frac{\partial \hat{v}}{\partial z} = 0 \quad (17)$$

Similarly, since the top and bottom faces of a cell are horizontal

$$\frac{\partial \hat{w}}{\partial x} = \frac{\partial \hat{w}}{\partial y} = 0 \quad (18)$$

A consequence of (17) and (18) is that $\mathbf{A}_{i,k}$ is block diagonal. In other words, the equations for \hat{u} and \hat{v} are decoupled from the equation for \hat{w} . This reduces the problem of integrating the velocity field to the solution of a two-dimensional linear first order ODE and a single first order linear ODE.

5.1. Accuracy

An semi-Lagrangian linear interpolation as proposed in the preceding sections is equivalent to a linear upwind scheme. Such schemes are first order in space. The constant face normal velocity component requirement of the streamline algorithm is also a first order discretisation. A mechanism for making the streamline tracking component second order was proposed in Dunsbergen (1994) while flux-corrected transport algorithms were proposed in Oliveira and Fortunato

(2002) as a better alternative to simple linear interpolation. The improvement of the semi-Lagrangian scheme will form an important part of the future development of the model.

6. Scalability

The scale of the problems under consideration dictates that the code must be implemented for parallel computers. For this to be successful, both the operation count per step and the communication load must scale appropriately. A feature of the shallow water equations is that it is possible to solve for free surface height and vertical velocity profile separately so that the size of the largest semi-implicit linear system which needs to be solved at each time step depends on the horizontal but not the vertical resolution. The same technique means that the communication load for the solution of that system is only dependent on the horizontal resolution. If we assume that a sparse system of m equations may be solved by Krylov subspace methods in $\mathcal{O}(m^2)$ operations (Trefethen and Bau, 1997) then the following scaling relationships in Table 2 will hold.

It is important to note that the computational requirements increase with resolution faster than the communication requirements. This guarantees that for sufficiently large problems, computational resources rather than communication bandwidth will be the limiting factor. Since communication is the weak link in many current cluster computing facilities, this result is important in establishing that this is a problem which can be solved effectively on those machines.

7. Examples

7.1. Closed circular streamlines

A key feature of the streamline tracking algorithm is that streamlines of a steady two-dimensional flow which remain in the domain should be closed (Batchelor, 1967, pp. 75–77). To test this, a simple rotating flow in a circular basin was specified and a streamline traced backwards through several rotations (Fig. 4). The basin diameter is 150 km and the streamline is at a radius of 75 km. The velocity at the streamline is 0.5 m/s. The error in the closure of the streamline is approximately 1 m in 470 km, a relative error of 2×10^{-6} . Since some of the input data was calculated to single precision, this error may be attributable to machine noise.

Table 2

Scaling properties of the Navier–Stokes and shallow water equations. N_x and N_z are characteristic horizontal and vertical cell counts respectively

	3D Navier–Stokes	Decomposed 3D Shallow water
Operations per time step	$\mathcal{O}((N_x^2 N_z)^2)$	$\mathcal{O}(N_x^2)$
Communications per time step	$\mathcal{O}((N_x^2 N_z)(N_x N_z))$	$\mathcal{O}(N_x(N_x^2))$

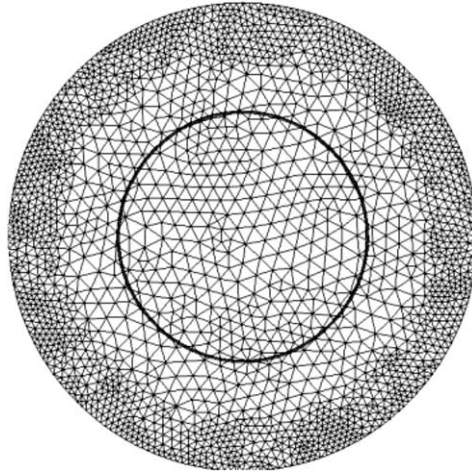


Fig. 4. Streamline tracking in a rotating flow. The basin width is 150 km and the streamline is tracked at a range of 75 km. The error in the tracking is not visible at this scale.

7.2. Standing wave in a basin

The accuracy of the pressure discretisation and the degree of artificial diffusion present in the scheme are tested by constructing a standing wave in a channel. This test case is based on that found in Pietrzak et al. (2002). As in that case, we specify a long, shallow basin 1000 m in length and 200 m in width. The depth is set at 10.197 m resulting in a theoretical long wave phase speed of 10 m/s. The basin was meshed with an unstructured grid of triangles with a requested typical side length of 10 m. Vertical layers were established at intervals of 1.02 m. Since an objective of this test is the observation of artificial diffusion, the dissipative terms (the vertical viscosity and the bed friction) were set to zero. The system is driven only by an initial surface elevation of cosine form with wavelength twice the basin length and amplitude 5 mm. The low amplitude is designed to ensure that the wave response of the system is linear. The implicitness (θ) of the time integration is set to 0.51 and the simulation was run for 2000 s (10 periods of the standing wave). The test was repeated for time steps of 1, 2, 5 and 10 s. On an unstructured grid, the Courant number is not a precisely defined quantity, however using the specified typical side length, we can obtain approximate Courant numbers of 1, 2, 5 and 10 respectively. The evolution of the surface height at one end of the channel is shown in Fig. 5. Very good agreement with the predicted period and minimal loss of amplitude are observed in the low Courant number cases while phase lag and loss of amplitude are somewhat more visible as the Courant number increases.

7.3. Kelvin wave in a basin

To test the efficacy of the pressure gradient and Coriolis discretisations, simulations were conducted of the propagation in a closed basin of a wave. The first simulation was conducted in a circular basin of radius 250 km with a water depth (h) of 5 m. The latitude was set at 45, θ was

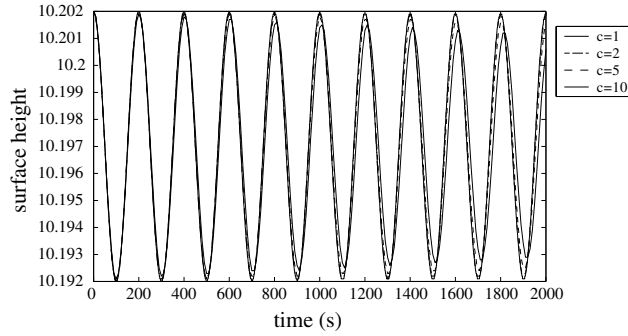


Fig. 5. Surface height evolution at the centre of one end of the channel.

set to 0.51 and the time step was 20 min. The viscosity and bed friction terms were set to zero. The system was driven by an initial free surface displacement and velocity

$$\eta(r, \theta) = 0.05e^{(r-r_0)/L_D} \cos \theta \quad (19)$$

$$u_\theta(r, \theta) = 0.05\sqrt{g/h}e^{(r-r_0)/L_D} \cos \theta \quad (20)$$

$$u_r(r, \theta) = 0 \quad (21)$$

where L_D is the Rossby radius, in this case approximately 68 km. In the limiting case of an infinitely large basin, this is the expression for a Kelvin wave of amplitude 5 cm (Csanady (1982)).

Some results of this simulation are presented in Fig. 6. The Kelvin wave is not the only free mode exhibited by a circular basin (Lamb, 1932; Csanady, 1982). In this simulation we also observed a mode crossing the basin. Due to the generation of higher frequency basin modes the amplitude of the Kelvin wave decreased almost immediately to 0.3 m. The continued evolution of the Kelvin wave is illustrated in Fig. 7.

This simulation has been run for up to three months simulation time with good results. After 3 months the solution becomes noisy. With bottom friction was imposed the model was stable over a year of simulated time, but the Kelvin wave was damped. The noise generated appears to be related to the Coriolis term and further work on its discretisation is underway.

To demonstrate the capacity of the model to accurately resolve coastlines, we created a basin with the coastline and bathymetry of the North Sea. Typical mesh length scales range from 20 km in the open sea down to 300 m on the coast (Fig. 8(a)). A mesh of this quality with this range of scales would be impossible to construct using conventional Cartesian methods. To simplify boundary conditions, the open boundaries were closed. The complex geometry of the basin makes the calculation of an initial Kelvin wave solution impractical. Instead, we simply applied an initial set-up so that the surface height in the North-Eastern corner of the simulation was 40 cm higher than that in the English channel. The bottom friction coefficient was set to 0.0025. Horizontal viscosity was, as in the derivation of the model, neglected. The time step was set to 20 min. The Kelvin wave was observed to propagate around the edge of the basin with a phase velocity consistent with theoretical expectations.

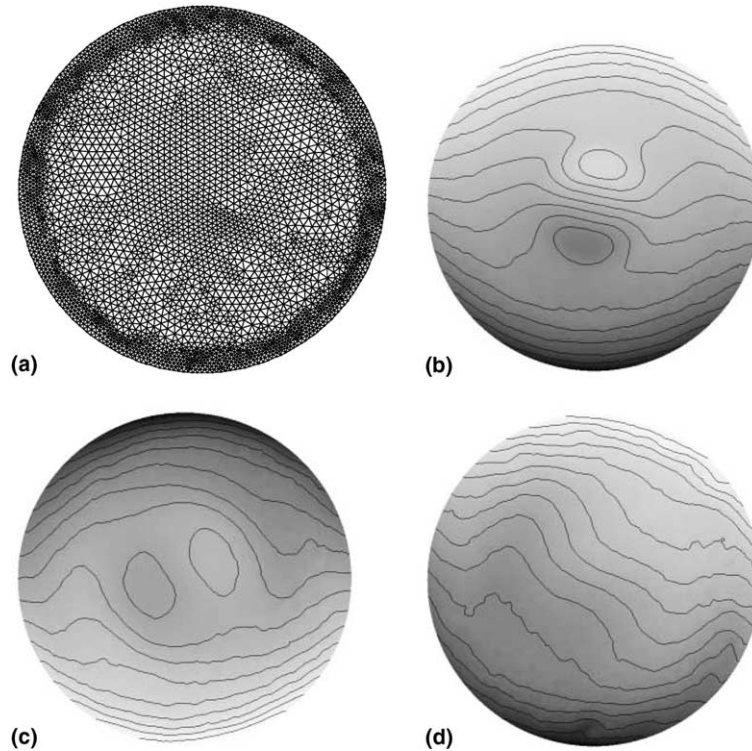


Fig. 6. A Kelvin wave in a round basin. (a) The grid used for the Kelvin wave test case. (b) The Kelvin wave after 53 h. The wave has travelled just over one rotation. The surface height in this figure ranges from -0.029 m to 0.030 m. (c) The Kelvin wave after 242 h (just over 10 days). The surface height range is now -0.026 m to 0.030 m. (d) The Kelvin wave after 480 h (20 days). The surface height range is -0.022 m to 0.026 m.

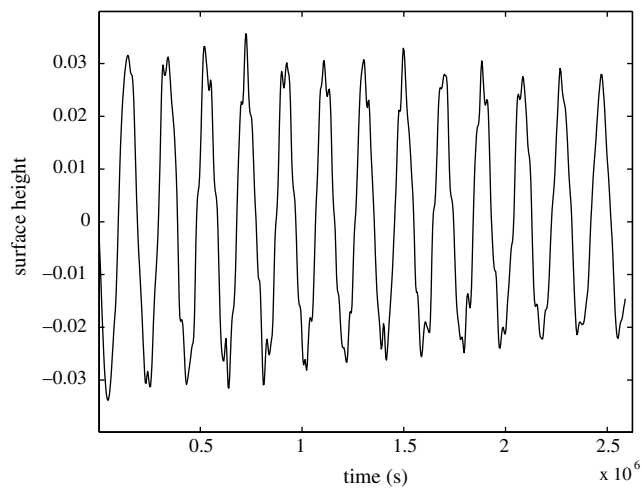


Fig. 7. The surface elevation at the point $(0, 250000)$. The irregular peaks in the signal are caused by the higher frequency cross basin modes and are expected.

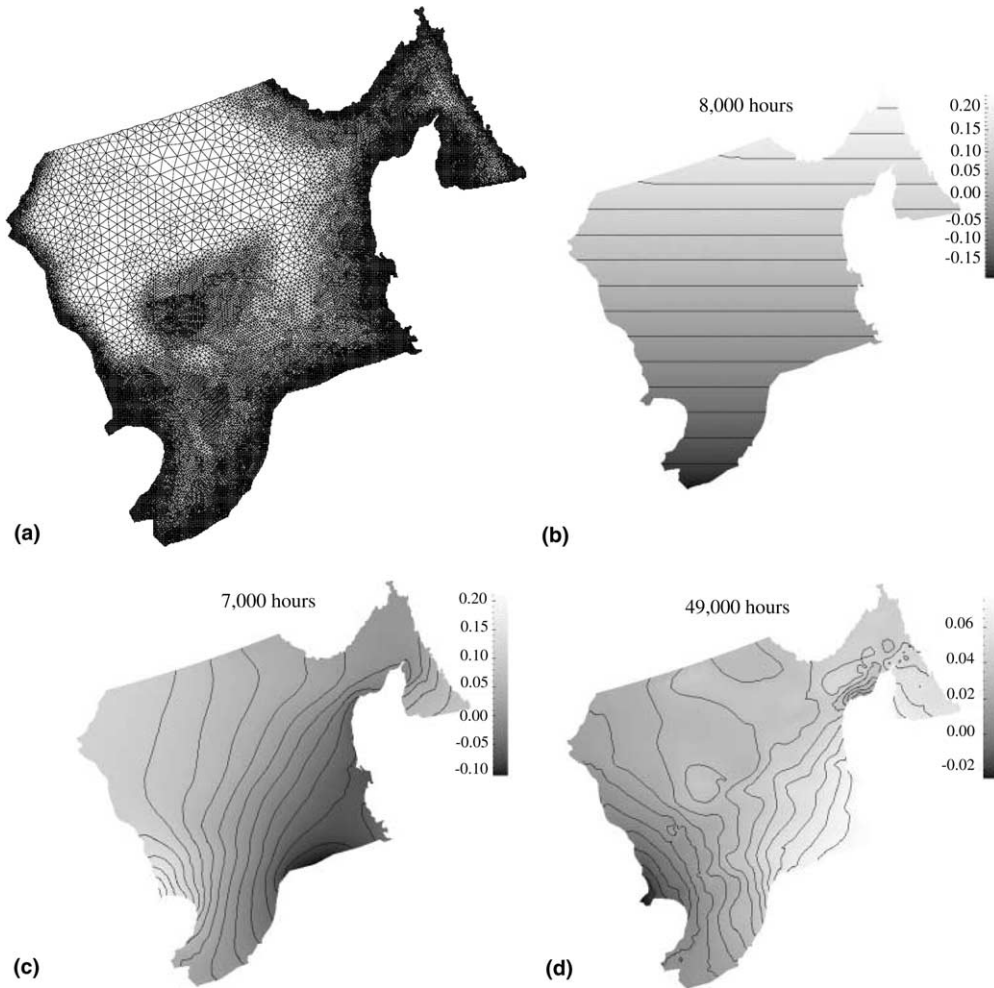


Fig. 8. Propagation of a Kelvin wave in a closed basin. The shading indicates surface elevation displacement from a reference value. Fifteen equally spaced contours are added in each case. (a) The grid used for the North Sea simulation. (b) The initial state. (c) After 7 h the trapped coastal wave is clearly visible. (d) At 49 h the trapped wave has travelled around the basin almost twice.

8. Conclusion

A new unstructured mesh three-dimensional finite volume model for the shallow water equations has been presented. The model builds on existing work in this field (Casulli and Walters, 2000; Miglio et al., 1999; Walters and Casulli, 1998) by applying a different and more flexible pressure gradient discretisation and a novel streamline tracking algorithm based on analytical integration of the velocity field. The examples shown demonstrate the advantage of an unstructured grid approach and illustrate a key advantage of the streamline tracking algorithm presented here. The authors believe that this model forms a basis for the simulation of shallow water in complex

geometries, and in particular coastal seas, with significant advantages over more traditional techniques.

References

- Adcroft, A., Marshall, J., 1998. How slippery are piecewise constant coastlines in numerical models? *Tellus A* 50, 95–108.
- Batchelor, G.K., 1967. *An Introduction to Fluid Dynamics*. University Press, Cambridge.
- Casulli, V., Walters, R.A., 2000. An unstructured grid, three-dimensional model based on the shallow water equations. *International Journal for Numerical Methods in Fluids* 32, 331–348.
- Csanady, G., 1982. *Circulation in the coastal ocean*. Reidel, Dordrecht.
- Danilov, S., Kivman, G., Schroter, J., 2004. A finite element ocean model: principles and evaluation. *Ocean Modelling* 6, 125–150.
- Dunnsbergen, D.W., 1994. Particle models for transport in three-dimensional flow. Ph.D. thesis, Delft University of Technology.
- Iskandarani, M., Haidvogel, D., Levin, J., 2003. A three dimensional spectral model for the solution of the hydrostatic primitive equations. *Journal of Computational Physics* 186, 397–425.
- Lamb, H., 1932. *Hydrodynamics*. Cambridge University Press, Cambridge, UK.
- Miglio, E., Quarteroni, A., Saleri, F., 1999. Finite element approximation of quasi-3d shallow water equations. *Computer Methods in Applied Science and Engineering* 174, 255–369.
- Nicolaides, R., 1993. The covolume approach to computing incompressible flows. In: Gunzberger, M., Nicolaides, R. (Eds.), *Incompressible Computational Fluid Dynamics*. Cambridge University Press, Cambridge, pp. 295–333.
- Oliveira, A., Baptista, A.M., 1998. On the role of tracking on Eulerian–Lagrangian solutions of the transport equation. *Advances in Water Resources* 21, 539–554.
- Oliveira, A., Fortunato, A.B., 2002. Toward an oscillation-free, mass conservative, Eulerian–Lagrangian transport model. *Journal of Computational Physics* 183, 142–164.
- Pietrzak, J., Jakobson, J.B., Buchard, H., Vested, H.J., Petersen, O., 2002. A three-dimensional hydrostatic model for coastal and ocean modelling using a generalised topography following co-ordinate system. *Ocean Modelling* 4, 173–205.
- Pietrzak, J.D., Labeur, R.J., 2004. Trapped internal waves over undular topography and mixing in a partially mixed estuary. *Ocean Dynamics* 54, 315–323.
- Trefethen, L.N., Bau, D., 1997. *Numerical Linear Algebra*. Society for Industrial and Applied Mathematics, Philadelphia.
- van Beek, P., van Nooyen, R., Wesseling, P., 1995. Accurate discretisation of gradients on non-uniform curvilinear staggered grids. *Journal of Computational Physics* 117, 364–367.
- Walters, R., Casulli, V., 1998. A robust finite element model for hydrostatic surface water flows. *Communications in Numerical Methods in Engineering* 14, 931–940.
- Wenneker, I., Segal, A., Wesseling, P., 2002. A mach-uniform unstructured staggered grid method. *International Journal for Numerical Methods in Fluids* 40, 1209–1235.
- Zhang, Y., Baptista, A., in press. A cross-scale model for 3d baroclinic circulation in estuary-plume-shelf systems: I. formulation and skill assessment. *Continental Shelf Research*.



amatos: Parallel adaptive mesh generator for atmospheric and oceanic simulation

Jörn Behrens^{a,*}, Natalja Rakowsky^b, Wolfgang Hiller^c, Dörthe Handorf^d,
Matthias Läuter^d, Jürgen Pöpke^d, Klaus Dethloff^d

^a Technische Universität München, Center for Mathematical Sciences (M3), 85747 Garching, Germany

^b Technische Universität Hamburg–Harburg, Computing Center, 21071 Hamburg-Harburg, Germany

^c Alfred Wegener Institute for Polar and Marine Research, Computing Center, 27515 Bremerhaven, Germany

^d Alfred Wegener Institute for Polar and Marine Research, 14401 Potsdam, Germany

Received 1 December 2003; received in revised form 1 June 2004; accepted 14 June 2004

Available online 2 November 2004

Abstract

The grid generator *amatos* has been developed for adaptive modeling of ocean and atmosphere circulation. It features adaptive control of planar, spherical, and volume grids with triangular or tetrahedral elements refined by bisection. The user interface (GRID API), a Fortran 90 module, shields the application programmer from the technical aspects of mesh adaptation like *amatos*' hierarchical data structure, the OpenMP parallelization, and the effective calculation of a domain decomposition by a space filling curve (SFC) approach.

This article presents the basic structure and features of *amatos*, the powerful SFC ordering and decomposition of data, and two example applications, namely the modeling of tracer advection in the polar vortex and the development of the adaptive finite element atmosphere model PLASMA (parallel large scale model of the atmosphere).

© 2004 Elsevier Ltd. All rights reserved.

Keywords: Grid generation; Finite elements; Parallelization; Ocean and atmosphere modeling

* Corresponding author.

E-mail address: behrens@ma.tum.de (J. Behrens).

1. Introduction

The grid generator `amatos` (Behrens, 1996, 2003) has been developed to make adaptive mesh generation available for dynamic time dependent flow problems as arising in climate simulations. The philosophy of `amatos` is to hide away all nontrivial tasks concerning mesh generation and adaptation from the application programmer. The complete mesh generation process can be controlled by approx. 25 Fortran 90 subroutines provided by a programming interface (GRID API). This Fortran 90 module also defines additional variables, data structures and constants.

The generic field of application for `amatos` is atmosphere and ocean circulation modeling with semi-Lagrangian advection schemes. The time stepping scheme, however, is not part of `amatos`. The semi-Lagrangian background is merely reflected by the choice of service routines (e.g., interpolation) implemented in the user interface, which may be extended for further needs. A complete description of the functionality in `amatos` cannot be the focus of this article, however, there are several techniques included in the library that are new to the atmospheric and oceanic modeling communities and are worth mentioning. This is the intention of Section 2.

Recently, several authors showed different approaches to adaptive ocean or atmosphere modeling (e.g. Blayo and Debreu, 1999; Bacon et al., 2000; Giraldo, 2000; Barros and Garcia, 2004). Most of the approaches differ from the one taken here, by the way the grid is refined. While most adaptive models to date use locally structured quadrilateral grids, `amatos` generates triangular grids. In order to manage unstructured and hierarchical triangular grids efficiently, we utilize space-filling curves (SFC). A description of the benefits of SFC can be found in Section 3.

Finally with the machinery of `amatos` at hand, we show some examples of successful adaptive experiments. Starting from simple linear advection, we show results of the development of an adaptive dynamical kernel in Section 4.

2. Features of `amatos`

In essence, `amatos` is a grid generation library that supports the development of adaptive ocean and atmosphere models. The refinement strategy used in the 2D version as well as in the 3D version of `amatos` is bisection of triangle's resp. tetrahedra's marked edge (Bänsch, 1991). The user has to provide an initial coarse mesh and a topographic outline of the domain. The initial mesh should be as coarse as possible in order to take maximum advantage of the underlying tree structure. `amatos` then refines the mesh uniformly up to a given basic level and refines further locally, based on marked grid cells. Two sequences of meshes, starting from the user-given initial mesh, are depicted in Figs. 1 and 2. Note that for spherical grids and also for irregular boundaries, the refined cells are not necessarily nested into the original coarse cells.

`amatos` supports arbitrary finite element methods (among them spectral elements) by providing a signature data structure that defines the basic properties of a finite element. That is

- the order of approximation,
- the number of degrees of freedom (DOF) per element,
- the degrees of freedom per element's node/edge/interior,
- the DOF's position in barycentric coordinates.

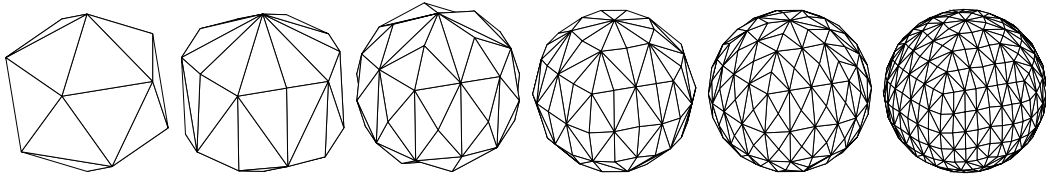


Fig. 1. Initial triangulation (icosahedron) and uniform refinement of a spherical grid.

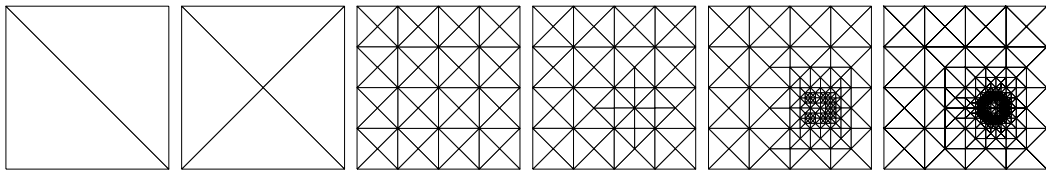


Fig. 2. Initial triangulation and subsequent uniform and adaptive refinement of a square grid.

Once element types are defined as an abstract item (before compiling the library), a registration mechanism allows users to allocate as many variables as required on each pre-defined element type at run time. Examples of element types and their signatures are given in Table 1.

Since finite element methods (FEM) use basis functions that are defined every where in the computational domain, interpolation within the FEM framework is easy to achieve. One only has to evaluate the basis function with the right coefficients at the given coordinate. Additionally, `amatos` provides cubic spline interpolation and radial basis function (RBF) interpolation. A RBF interpolation function is given by

$$I_f(x) = \sum_{l=1}^K [\lambda_l \cdot \varphi(\|\xi_l - x\|)] + P(x),$$

Table 1
Components of the data structure `fem_signatur` and examples for commonly used finite element types

Element type		Linear Lagrange	Lin. non-conform.	Quadr. Lagr.	Cubic Lagrange
					
<code>i_order:</code>	order	1	1	2	3
<code>i_unknows:</code>	total #variables	3	3	6	10
<code>i_npoints:</code>	#var. per vertex	1	0	1	1
<code>i_gpoints:</code>	#var. per edge	0	1	1	2
<code>i_epoints:</code>	#var. per element	0	0	0	1
<code>r_gweights:</code>	var. pos. on edge	–	$(\frac{1}{2}, \frac{1}{2})$	$(\frac{1}{2}, \frac{1}{2})$	$(\frac{1}{3}, \frac{2}{3}), (\frac{2}{3}, \frac{1}{3})$
<code>r_eweights:</code>	var. pos. on elem.	–	–	–	$(\frac{1}{3}, \frac{1}{3}, \frac{1}{3})$

where $I_l(\xi_i) = f(\xi_i)$ for $l = 1:K$ fulfills the interpolation condition, K is a given number of neighboring sample points ξ_i , $\|\cdot\|$ is the Euclidean norm, and $P(x)$ is a polynomial that is required to close the arising problem of calculating coefficients λ_l from the given interpolation conditions. For a more detailed description of RBF the reader is referred to [Buhmann \(2003\)](#).

In particular the RBF interpolation is suitable for adaptive refinement, since it is constructed for arbitrarily scattered data points. Additionally, RBF interpolation can be easily used to estimate gradients at arbitrary points, even if the particular FEM representation does not allow for derivation. This is true, because the basis functions φ can be chosen such that an analytic derivative is easy to calculate. `amatos` defines a unified user interface to all the available interpolation and gradient estimation routines.

The interpolation is provided for semi-Lagrangian time discretization schemes. Since the semi-Lagrangian discretization of advection dominated partial differential equations is based on interpolation of the above mentioned type, there are no stability issues with the refinement scheme used by `amatos`. [Neta and Williams \(1986\)](#) found instabilities for so called criss-cross grids with a special finite element discretization of the advection equation. `amatos`'s refinement scheme can produce those grids as can be seen in [Fig. 2](#). Users therefore should avoid discretization schemes that are vulnerable to criss-cross instabilities.

In order to gain maximum performance in both, the grid generation phase and the numerical calculation phase, these two phases of a typical adaptive program are well separated in the philosophy underlying the design of `amatos`. [Fig. 3](#) demonstrates this splitting. The grid is viewed

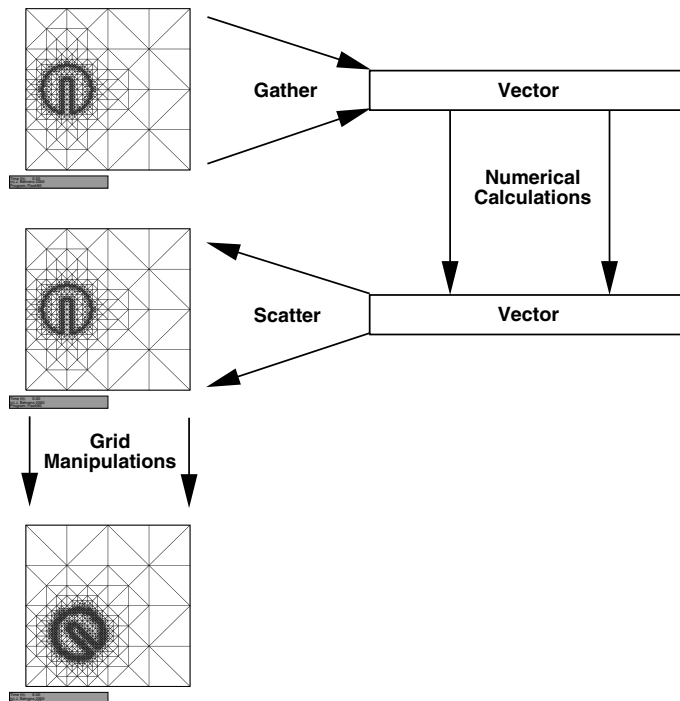


Fig. 3. `amatos` uses a gather and scatter step to switch between numerical calculation phase and grid manipulation phase within the adaptive program.

as a container of data that can be accessed by a user program by gather or scatter operations. Once a gather operation has been conducted data is available in a consecutive (vector-like) data structure. Code optimization for such data structures is easily performed. In order to efficiently perform grid manipulations and parallel data communication, the grid is in an object oriented tree structured data format. Note that for typical programs the gather and scatter steps incur an overhead of less than 1%.

Before compiling the library, the user has to choose between the planar, spherical, or volume version of `amatos`. OpenMP parallelization is toggled by the corresponding compiler directives. `amatos` has been successfully executed on different hardware and operating systems, including *SGI Origin*, *SUN Fire*, *IBM Regatta*, *Linux* with Intel's Fortran90 compiler *ifc*. Corresponding *Make-files* are included in the package.

3. Grid partitioning with a space-filling curve approach

Grid partitioning is a crucial part of adaptive mesh generation, because the computational load of realistic simulations demands for efficient parallelization, and for an adaptive mesh the partitioning has to be recalculated frequently. In `amatos`, Behrens and Zimmermann (2000) employ a space filling curve approach (SFC). This partitioning is very fast, guarantees optimal load balancing and good data locality by construction and results in rather short (though not optimal) interface length. For the quality of SFC induced partitions see Zumbusch (2001). Moreover, due to the fractal nature of the SFC the resulting ordering retains data locality on any level of memory hierarchy from cache levels to main memory. Last but not least, the SFC induces a very efficient ordering of stiffness matrices for solvers with ILU-type pre-conditioners. Thus, a further local renumbering on sub-domains becomes obsolete.

The global SFC index is calculated at the time of an element's construction. As depicted in Fig. 4(a) and (b), the algorithm is straight forward on the hierarchical mesh when regarding the indices as binary numbers. Stepping down all levels of refinement and adding the corresponding bits according to the relative position in the bisected parent triangle yields the SFC index. The

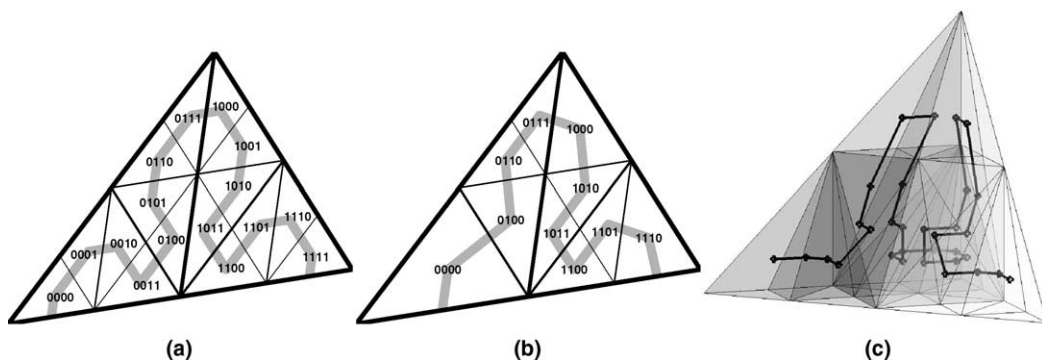


Fig. 4. Construction of the space filling curve (SFC) through the elements for (a) uniform planar, (b) irregularly refined, and (c) uniform tetrahedral grids.

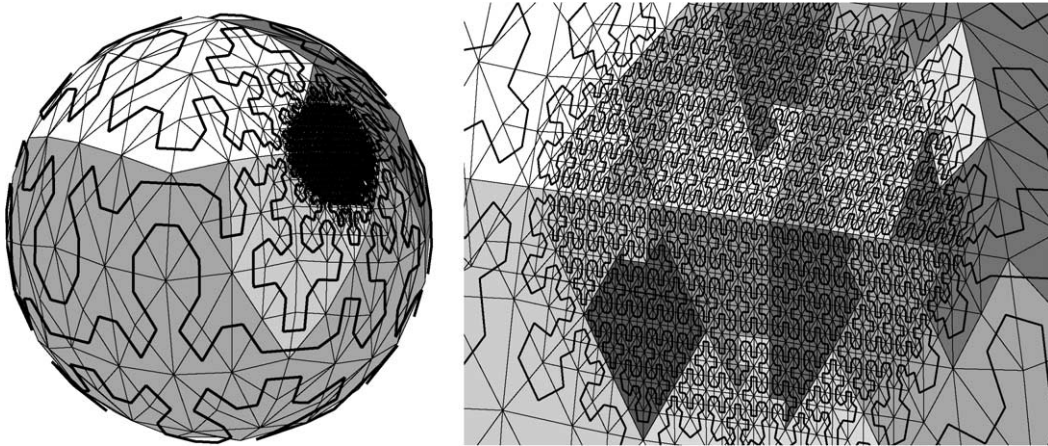


Fig. 5. SFC through the elements and a mesh partitioning into 14 sub-domains.

algorithm can easily be extended to tetrahedral grids, again relying on bisection refinement Fig. 4(c). Fig. 5 shows an adaptive grid on the sphere with a SFC through the elements and a zoom into the refined region. The partitioning is obtained by simply dividing the SFC index space into equal sets.

In most applications, one is ultimately interested in ordering the unknowns (degrees of freedom, DOF). Taking this into account, `amatos` sets up an ordering of all DOF located at vertices, edges, and/or elements (depending on the FE basis function) by collecting and counting them on the way along the elements' SFC. For matrix ordering, the reverse of this numbering should be taken to obtain a local arrow head down shape in the sparsity pattern. When the user retrieves data arrays from the GRID API, all arrays are sorted along this reverse SFC (rSFC).

Often, numerical schemes require the solution of a sparse linear system. A powerful class of methods, widely used for such problems, are Krylov subspace solvers with preconditioning based on incomplete matrix factorization. The efficiency of these pre-conditioners strongly depends on matrix ordering. In the following, we present an example showing that the rSFC can compete with other matrix reordering strategies.

The sparsity pattern of a typical stiffness matrix for linear FE with rSFC numbering of DOFs can be studied in Fig. 6. Most entries are clustered very close to the diagonal. More complex matrices for coupled linear equations with several variables and mixed FE (e.g., in the atmosphere model PLASMA, see section 4.2) can be set up according to the SFC numbering, too, with a similar sparsity pattern.

For incomplete LU-factorization (ILU) preconditioning, the rSFC ordering proves to be a powerful candidate among well known fill-in reducing orderings like reverse Cuthill-McKee (RCM) and quotient minimum degree (QMD). An example for a coupled linear equation in PLASMA with approx. 200,000 unknowns is given in Table 2. We employ the FoSSI solver interface (Frickenhaus et al., 2004) and choose the PETSc solver library (Balay et al., 2003) with BiCGstab and level ILU(l) as pre-conditioner to reduce the residual by a factor of 10^{-13} . Original and rSFC ordering are provided by the calling routine, while RCM and QMD ordering are calculated by the PETSc solver.

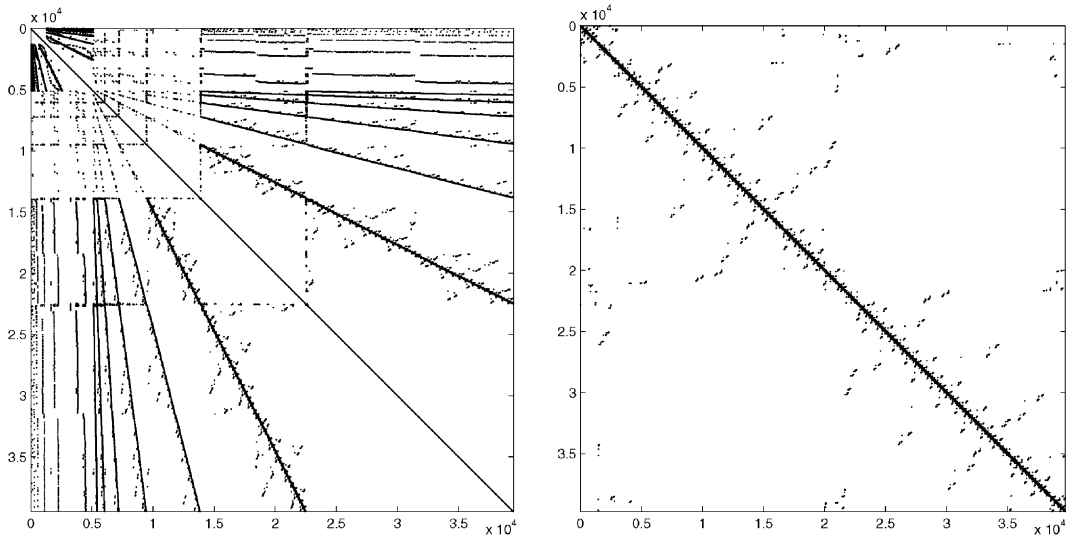


Fig. 6. Sparsity pattern of the stiffness matrix for an adaptively refined grid with original numbering (nodes in the order of creation) and rSFC numbering of nodes.

Table 2

Influence of matrix orderings on the iteration count and computation time for ILU(1)-preconditioned BiCGstab on one processor of a SunFire 15k: natural *amatos* numbering (original), reverse Cuthill-McKee (RCM), quotient minimum degree (QMD), reverse space filling curve (rSFC)

Ordering	Original	RCM	QMD	rSFC
# iterations	66	22	20	12
Solution time (s)	355.0	94.5	92.7	77.9

4. Examples

4.1. Advection model for tracer transport

First experiments with adaptivity in atmospheric modeling allowed to model tracer advection in the polar vortex with high resolution on a workstation computer (Behrens et al., 2000). Snapshots of the adaptive grid are depicted in Fig. 7. In the mentioned study it could be shown that increasing resolution locally decreases numerical dissipation such that fine filaments, caused by shear stress in the wind field, can be represented. For a more detailed discussion see the cited publication.

4.2. Barotropic shallow water model of the atmosphere: PLASMA

In order to achieve reliable assessments of future climate development and the impact of anthropogenic influence an improved understanding of natural climate variability on time-scales from seasons to decades is required. For this, nonlinear interactions between atmospheric

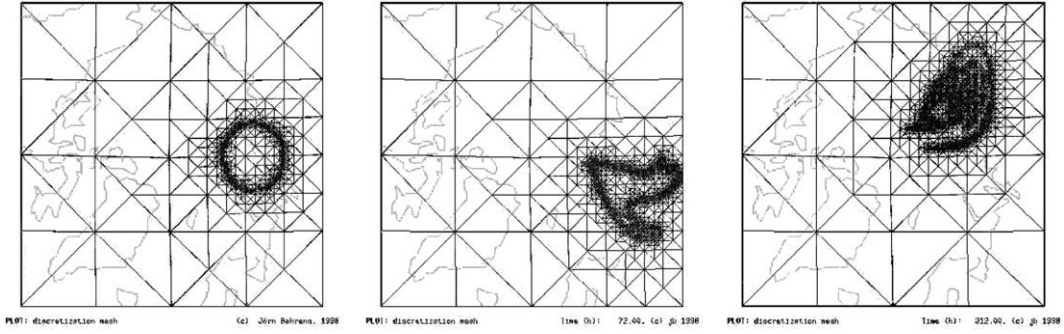


Fig. 7. Snapshots from an adaptive model (5 km minimal resolution) for tracer transport in a simulated wind field of the polar vortex.

processes at different spatial and temporal scales play a fundamental role. A realistic representation of such multi-scale interaction is important not only for climate modeling but also for numerical weather prediction. The application of adaptive techniques for atmospheric flows, therefore, seems to be natural. For the development of the atmospheric model PLASMA (Parallel Large-scale Self-adaptive Model of the Atmosphere) we utilized the mesh generator `amatos` and controlled the refinement strategy by atmospheric flow processes.

To date, a barotropic version of the model has been implemented based on the nonlinear shallow-water equations (SWE). SWE describe the horizontal flow of an hydrostatic gas with constant density within a shallow atmospheric layer. The current implementation of PLASMA uses a scalar formulation of the SWE on the unit sphere S , derived from the constrained vector formulation in (Côté, 1988) by applying rot_s and div_s to the momentum equation. By defining vorticity $\zeta := \text{rot}_s \mathbf{u}$ and divergence $\delta := \text{div}_s \mathbf{u}$ we obtain our model equations on S for the simulation time T and the static underlying orography $\Phi_{\text{oro}}: S \rightarrow \mathbf{R}$

$$\begin{aligned}
 \partial_t \zeta + \mathbf{u} \cdot \nabla_s \zeta + \zeta \delta + f \delta &= -\mathbf{u} \cdot \nabla_s f, \\
 \partial_t \delta + \mathbf{u} \cdot \nabla_s \delta + \Delta_s \Phi - f \zeta &= -(\mathbf{n} \times \mathbf{u}) \cdot \nabla_s f - \sum_{i,j=1}^3 (\nabla_s u_i)_j (\nabla_s u_j)_i - \mathbf{u} \cdot \mathbf{u}, \\
 \partial_t \Phi + \mathbf{u} \cdot \nabla_s \Phi + \Phi \delta - \Phi_{\text{oro}} \delta &= \mathbf{u} \cdot \nabla_s \Phi_{\text{oro}}, \\
 -\Delta_s \psi &= \zeta, \\
 \Delta_s \chi &= \delta, \\
 \mathbf{rot}_s \psi + \nabla_s \chi &= \mathbf{u}.
 \end{aligned} \tag{1}$$

This set of equations represents the scalar formulation of the SWE applying a Helmholtz decomposition. f is the Coriolis parameter and \mathbf{n} the unit vector in the vertical direction, $\mathbf{u}: S \times (0, T) \rightarrow \mathbf{R}^3$ with $\mathbf{u} \cdot \mathbf{n} = 0$ denotes the horizontal velocity field and $\Phi: S \times (0, T) \rightarrow \mathbf{R}$ the geopotential height field. The spherical differential operators ∇_s , Δ_s , rot_s , div_s , \mathbf{rot}_s on S have been defined according to ideas by (Dziuk, 1988). Functions $\psi, \chi: S \times (0, T) \rightarrow \mathbf{R}$ denote the stream function and the velocity potential respectively.

For the numerical implementation of these spherical SWE the Lagrange-Galerkin method has been applied (Morton et al., 1988; Süli, 1988). This method combines the semi-Lagrangian

method (SLM) with the finite element method (FEM) on the sphere. The SLM discretizes the material derivative along trajectories and has good stability properties (Pironneau, 1989; Quartarone and Valli, 1997). The FEM on the sphere (Dziuk, 1988) is constructed on an approximating polyhedron consisting of a triangular grid with nodes on the sphere. A detailed description of the numerical methods can be found in Lauter (2003).

For developing appropriate numerical schemes the mesh generator `amatos` plays a crucial role. `amatos` provides complex adaptive data structures for spherical triangular grids. Furthermore the solver package FoSSI (Frickenhaus et al., 2004) solves large linear systems generated by the elaborate treatment of nonlinearities in the model equations.

To evaluate the implemented numerical schemes, different test cases have been regarded. In order to compute the numerical error exactly, we have chosen cases for which an analytical solution is known. Test cases include simulations of solid body rotation with different rotation axes. The angle α denotes the inclination of the flow’s rotation axis to the earth’s axis, see Fig. 8. For $\alpha = 0$, the test case is a steady state solution of the SWE consisting of a zonal flow corresponding to test case 2 of Williamson et al. (1992). For $\alpha = \frac{\pi}{4}$ a non-stationary periodic solution is obtained. Initial conditions are given by

$$\begin{aligned} \mathbf{u}_0(\mathbf{x}) &= c_0 \mathbf{a}(\alpha) \times \mathbf{x} \iff \zeta_0(\mathbf{x}) = c_0 2\mathbf{a}(\alpha) \cdot \mathbf{x}, \quad \delta_0(\mathbf{x}) = 0, \quad \forall \mathbf{x} \in S \\ \Phi_0(\mathbf{x}) &= -\frac{1}{2} [(c_0 \mathbf{a}(\alpha) \cdot \mathbf{x})^2 + c_0 2\mathbf{a}(\alpha) \cdot \mathbf{x} \Omega \cdot \mathbf{x}] + H, \quad \forall \mathbf{x} \in S \end{aligned}$$

where $c_0 := u_0/R$, $\mathbf{a}(\alpha) := (-\sin(\alpha), 0, \cos(\alpha))^T \cdot u_0 = 30 \text{ m/s}$ is the maximum velocity, R the earth’s radius and Ω the angular velocity vector of the earth. The constant H is determined in such a way that the mean value of Φ_0 corresponds to an atmospheric scale height of 8 km. With the underlying orography $\Phi_{\text{oro}}(\mathbf{x}) = \frac{(\Omega \cdot \mathbf{x})^2}{2}$ we obtain the solutions for solid body rotation.

Fig. 9 displays the temporal evolution of the relative L^2 discretization error of the numerical solution for different time steps and grid widths. For $\alpha = 0$, the discretization error decreases considerably for increased spatial resolution. Because this test case is in steady-state, the SLM provides a good approximation of the upwind points independently of the time step length. Thus, the dependence of discretization error on the time step is rather small. For the non-steady solid-body rotation with $\alpha = \frac{\pi}{4}$ the discretization error decreases significantly with decreasing time step, because the calculation of the trajectories with the SLM strongly depends on the time step.

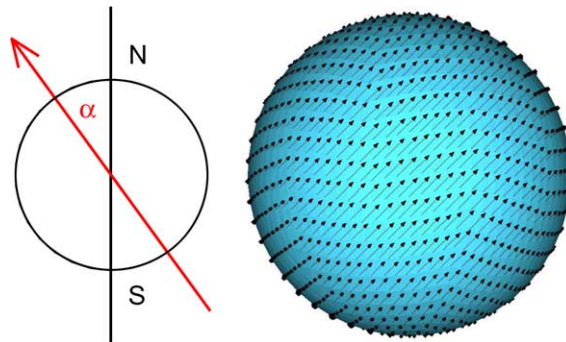


Fig. 8. Validation of PLASMA. Inclination angle α and initial condition of the velocity field \mathbf{u} for the solid body rotation with $\alpha = 45^\circ$ (non-stationary analytical solution).

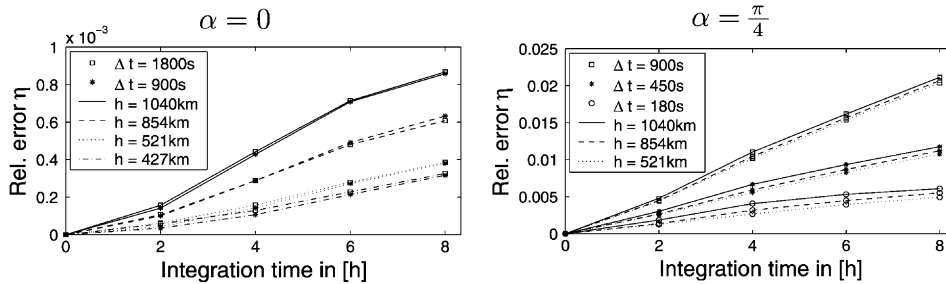


Fig. 9. Simulation of analytical test cases with PLASMA. Temporal evolution of the relative discretization error L^2 for the geopotential height field Φ .

The influence of increased spatial resolution is rather small. For these simulations of analytical test cases we have demonstrated, that the discretization error decreases for increasing spatial and temporal resolution and thus the experimental convergence of the numerical method has been proven.

We have obtained first insights into the capability of the model to cope with more realistic atmospheric flow situations by studying the development of quasi-stationary planetary Rossby waves, forced by orography. Here, we intended to reproduce Rossby waves by forcing a tropospheric westerly current with one localized mountain. The scale height of the atmospheric layer is 8 km. A mountain of 2 km height with a zonal extension of ≈ 6700 km and a meridional extension of ≈ 3900 km is situated at 30° N, 0° W. The westerly flow has its maximum of 30 m/s at 30° N and a meridional extension of 20° (cf. the orography and the initial geopotential height field together with the initial wind field in the upper row of Fig. 10).

For this test case, two simulations over 20 days have been performed, one with a static, uniform grid with grid width of 522 km (middle row, right plot of Fig. 10), the other one with a time-dependent, adaptive grid, generated every time step by *amatos* according to the development of the flow. The grid refinement criteria is determined for every time step by the absolute values of vorticity and divergence. The initial grid has a uniform grid width of 428 km, the grid after 20 days simulation time is displayed in the lower row, right plot of Fig. 10. One can notice fine resolution in the region of the westerly flow and coarse resolution outside the jet region.

Both simulations reveal the development of quasi-stationary, orographically forced Rossby waves with wavelengths of ≈ 5000 km which is in good agreement with typical wave lengths of observed Rossby waves and results from Rossby wave theory. After 20 days, both simulations show a similar large scale structure of these waves (see Fig. 10, left plots in middle and lower row). Non-negligible differences can be found in the structure of the smaller scale areas of high and low geopotential values northward and southward of the jet. The feedback of these structures into large scale waves and therefore into the adaptive grid control of *amatos* can only be studied by performing longer simulations. This will be a matter of future research.

The demonstrated successful application of adaptive mesh control with *amatos* in the global atmospheric model PLASMA represents a feasible approach to an adequate representation of two-way feedback between global and regional scales. Numerical convergence could be proved as well as the model's capability to simulate the most important feature of the extra-tropical large scale circulation, namely the planetary Rossby-wave formation. Future studies will put special emphasis on two-way feedback and the influence on the variability of Rossby-waves.

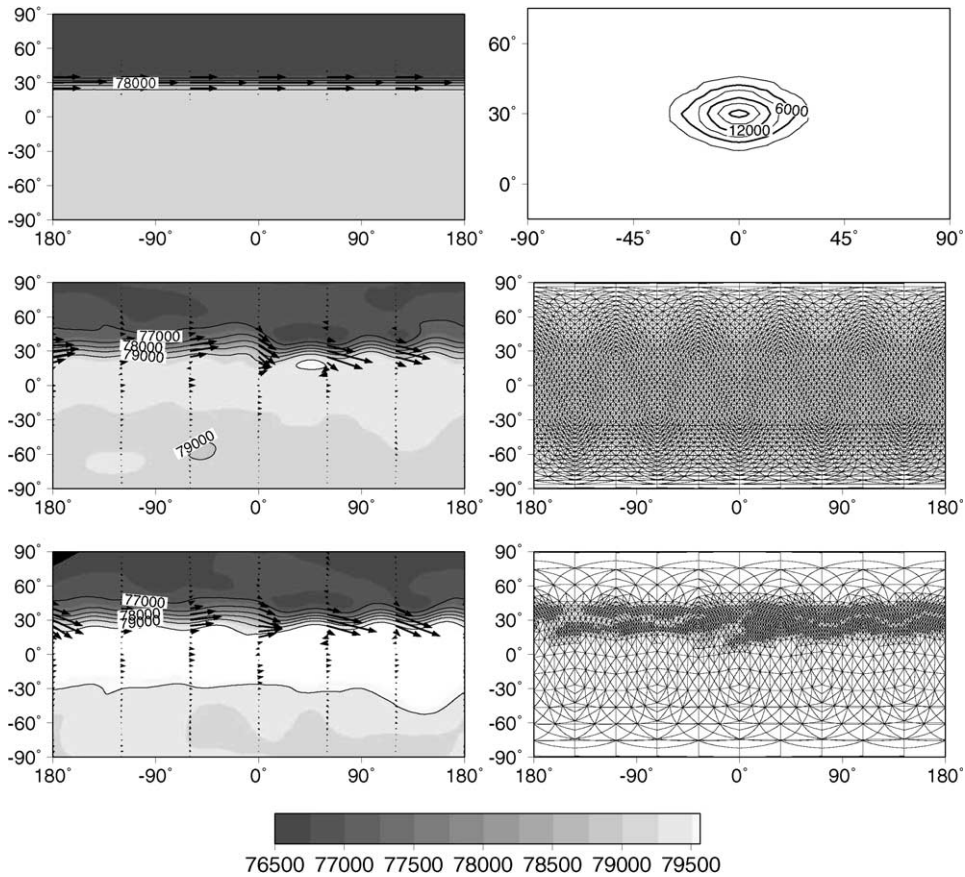


Fig. 10. Simulation of Rossby waves with PLASMA. Upper row: initial geopotential height field (left, in m^2/s^2) and orography (right, in m^2/s^2). Middle row: geopotential height fields after 20 days for static uniform grid (left, in m^2/s^2) and corresponding grid with 522 km grid width (right). Lower row: Geopotential height fields after 20 days for process-controlled adaptive grid (left, in m^2/s^2) and corresponding grid with grid widths between 428 and 1041 km (right).

4.3. *amatos* in oceanography

From the grid generation point of view, the difference between atmospheric and oceanographic modeling is the highly irregular geometry of ocean basins. *amatos* is capable of handling complex boundaries given by polygonal lines or land-ocean bitmaps. While still an initial mesh has to be given by the user, this initial grid is required to only approximately resemble the given domain. In a first step, this initial mesh is corrected such that all boundary nodes exactly match an actual boundary position. In the refinement, inserted new boundary nodes are moved such that the grid resembles the domain outline.

Some adjustments are necessary to correct numerical schemes in *amatos* that depend on the tree structure and nesting of refined grids, since at the boundary exact nesting can no longer be satisfied. Special care regarding the initial grid has to be taken near corners and bays in order to guarantee a good mesh quality and coverage of the domain. An example mesh of a complex geometry is depicted in Fig. 11.

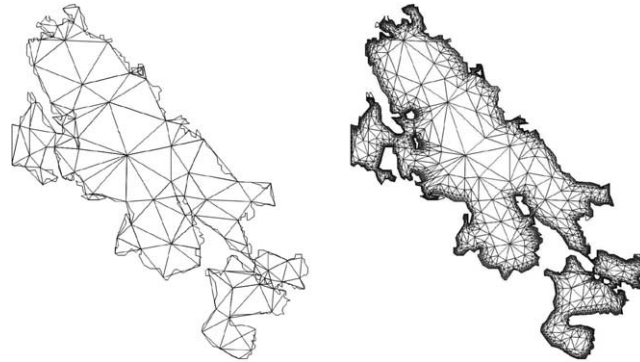


Fig. 11. Example of a grid that resolves a highly irregular coast line, that is Lago Titicaca in the Andes of South America. Left: initial grid, right: after refining 12 levels.

5. Outlook

An ongoing project is the concise validation and code optimization of `amatos` version 2.0. The support of arbitrary finite element types introduced more data nodes which in turn made considerable extensions of the SFC support and the routines for data retrieval necessary.

Further plans reflect the needs of applications carried out with `amatos`. In the range of the PLASMA project, error estimators based on mathematical and physical criteria are developed.

A major concern are sparse linear solvers. As `amatos` is parallelized with OpenMP while state of the art parallel sparse solver packages are based on MPI, we had to find a way to establish efficient communication between OpenMP-threads and MPI-task (Rakowsky et al., 2003). However, a pure OpenMP library of sparse solvers remains desirable and we have started to implement the most promising domain decomposition solvers in OpenMP (Frickenhaus et al., 2004). Another promising approach is to make use of `amatos`' hierarchical data structure in a multi-grid solver, e.g., a cascading multi-grid solver (Bornemann and Krause, 1998).

Acknowledgments

The authors gratefully acknowledge the support by the *Bundesministerium für Bildung und Forschung* in the DEKLIM framework under number 01LD0037. Furthermore, we would like to thank the anonymous reviewers for their valuable input that greatly improved the manuscript. Finally, we are grateful to Florian Klaschka for providing Fig. 11.

References

- Bacon, D.P. et al., 2000. A dynamically adapting weather and dispersion model: The Operational Multiscale Environment Model with Grid Adaptivity (OMEGA). *Mon. Weather Rev.* 128, 2044–2076.
- Bänsch, E., 1991. Local mesh refinement in 2 and 3 dimensions. *Impact Comput. Sci. Eng.* 3, 181–191.

- Balay, S., Buschelman, K., Eijkhout, V., Gropp, W.D., Kaushik, D., Knepley, M., McInnes, L.C., Smith, B.F., Zhang, H., 2003. PETSc users manual. Tech. Rep. ANL-95/11 - Revision 2.1.6, Argonne National Laboratory, Available from <http://www.mcs.anl.gov/petsc>.
- Barros, S.R.M., Garcia, C.I., 2004. A global semi-implicit semi-Lagrangian shallow water-model on locally refined grids. *Mon. Weather Rev.* 132, 53–65.
- Behrens, J., 1996. Adaptive Semi-Lagrange-Finite—Elemente-Methode zur Lösung der Flachwassergleichungen: Implementierung und Parallelisierung. Berichte zur Polarforschung 217, Alfred-Wegener-Institut, Bremerhaven, PhD thesis, Universität Bremen.
- Behrens, J., July 2003. amatos Documentation. Technische Universität München, second Edition, Available from <http://www-m3.ma.tum.de/m3/software/amatos/index.html>.
- Behrens, J., Dethloff, K., Hiller, W., Rinke, A., 2000. Evolution of small scale filaments in an adaptive advection model for idealized tracer transport. *Mon. Weather Rev.* 128, 2976–2982.
- Behrens, J., Zimmermann, J., 2000. Parallelizing an unstructured grid generator with a space-filling curve approach. In: Bode, A., Ludwig, T., Karl, W., Wismüller, R. (Eds.), Euro-Par 2000 Parallel Processing, sixth International Euro-Par Conference, Munich, Germany, August/September 2000, Proceedings. Vol. 1900 of Lecture Notes in Computer Science. Springer-Verlag, 815–823.
- Blayo, E., Debreu, L., 1999. Adaptive mesh refinement for finite difference ocean models: first experiments. *J. Phys. Oceanogr.* 29, 1239–1250.
- Bornemann, F.A., Krause, R., 1998. Classical and cascadic multigrid—a methodological comparison. In: Bjørstadt, P., Espedal, M., Keyes, D. (Eds.), Proceedings of the ninth International Conference on Domain Decomposition Methods 1996, Ullensvang, Norway. Domain Decomposition Press, Bergen, 64–71.
- Buhmann, M.D., 2003. Radial Basis Functions: Theory and Implementations. Cambridge University Press, Cambridge.
- Côté, J., 1988. A Lagrange multiplier approach for the metric terms of semi-Lagrangian models on the sphere. *Q. J. Roy. Meteor. Soc.* 114, 1347–1352.
- Dziuk, G., 1988. Finite elements for the Beltrami operator on arbitrary surfaces. In: Hildebrandt, S., Leis, R. (Eds.), Partial Differential Equations and Calculus of Variations. Springer, 142–155.
- Frickenhaus, S., Hiller, W., Best, M., 2004. FoSSI: family of simplified solver interfaces for parallel sparse solvers in numerical atmosphere and ocean modeling. *Ocean Modelling*, accepted for publication.
- Giraldo, F.X., 2000. The Lagrange-Galerkin Method for the Two-Dimensional Shallow Water Equations on Adaptive Grids. *Int. J. Numer. Meth. Fluids* 33, 789–832.
- Läuter, M., 2003. An adaptive Lagrange-Galerkin method for the shallow-water equations on the sphere. In: PAMM—Proceedings in Applied Mathematics and Mechanics. Vol. 3, 48–51.
- Morton, K.W., Priestley, A., Süli, E., 1988. Stability of the Lagrange-Galerkin method with non-exact integration. *Math. Mod. Num. Anal.* 22, 625–653.
- Neta, B., Williams, R.T., 1986. Stability and phase speed for various finite element formulations of the advection equation. *Comput. Fluids* 14, 393–410.
- Pironneau, O., 1989. Finite element methods for fluids. Masson, Paris.
- Quarteroni, A., Valli, A., 1997. Numerical Approximation of Partial Differential Equations. Springer, Berlin.
- Rakowsky, N., Frickenhaus, S., Hiller, W., Läuter, M., Handorf, D., Dethloff, K., 2003. A self-adaptive finite element model of the atmosphere. In: Zwiefelhofer, W., Kreitz, N. (Eds.), ECMWF Workshop on the Use of High Performance Computing in Meteorology: Realizing TeraComputing, 4–8 November 2002, Reading UK. ECMWF, World Scientific, Singapore, 279–293.
- Süli, E., 1988. Convergence and nonlinear stability of the Lagrange-Galerkin method for the Navier-Stokes equations. *Numer. Math.* 53, 459–483.
- Williamson, D.L., Drake, J.B., Hack, J.J., Jakob, R., Swarztrauber, P.N., 1992. A standard test set for numerical approximations to the shallow water equations in spherical geometry. *J. Comp. Physics* 102, 211–224.
- Zumbusch, G.W., 2001. On the quality of space-filling curve induced partitions. *Z. Angew. Math. Mech.* 81 (Suppl. 1), 25–28, also as report SFB 256, Universität Bonn, no. 674.



FoSSI: the family of simplified solver interfaces for the rapid development of parallel numerical atmosphere and ocean models

Stephan Frickenhaus^{a,b,*}, Wolfgang Hiller^b, Meike Best^{b,1}

^a *Competence Center of High Performance Computing, BremHLR, Bremen, Germany*

^b *Alfred-Wegener-Institute for Polar and Marine Research, Computing Center, Columbusstrasse 27568, Bremerhaven, Germany*

Received 28 November 2003; received in revised form 1 June 2004; accepted 14 June 2004

Available online 2 November 2004

Abstract

The portable software FoSSI is introduced that—in combination with additional free solver software packages—allows for an efficient and scalable parallel solution of large sparse linear equations systems arising in finite element model codes. FoSSI is intended to support rapid model code development, completely hiding the complexity of the underlying solver packages. In particular, the model developer need not be an expert in parallelization and is yet free to switch between different solver packages by simple modifications of the interface call.

FoSSI offers an efficient and easy, yet flexible interface to several parallel solvers, most of them available on the web, such as PETSC, AZTEC, MUMPS, PILUT and HYPRE. FoSSI makes use of the concept of handles for vectors, matrices, preconditioners and solvers, that is frequently used in solver libraries. Hence, FoSSI allows for a flexible treatment of several linear equations systems and associated preconditioners at the same time, even in parallel on separate MPI-communicators. The second special feature in FoSSI is the task specifier, being a combination of keywords, each configuring a certain phase in the solver setup. This enables the user to control a solver over one unique subroutine. Furthermore, FoSSI has rather similar features for all solvers, making a fast solver intercomparison or exchange an easy task. FoSSI is a community

* Corresponding author. Address: Alfred-Wegener-Institute for Polar and Marine Research, Computing Center, Columbusstrasse 27568, Bremerhaven, Germany. Tel.: +49 471 4831 1179; fax: +49 471 4831 1590.

E-mail address: sfrickenhaus@awi-bremerhaven.de (S. Frickenhaus).

¹ Funded by the German Ministry for Education and Research (DEKLIM-PLASMA).

software, proven in an adaptive 2D-atmosphere model and a 3D-primitive equation ocean model, both formulated in finite elements.

The present paper discusses perspectives of an OpenMP-implementation of parallel iterative solvers based on domain decomposition methods. This approach to OpenMP solvers is rather attractive, as the code for domain-local operations of factorization, preconditioning and matrix–vector product can be readily taken from a sequential implementation that is also suitable to be used in an MPI-variant. Code development in this direction is in an advanced state under the name ScOPES: the Scalable Open Parallel sparse linear Equations Solver.

© 2004 Elsevier Ltd. All rights reserved.

Keywords: Sparse parallel solvers; Iterative solvers; Finite element; User interface

1. Introduction

Modularized software is the basis for efficient and portable code development and is a prerequisite for rapid software development of co-operating working-groups for example in the field of earth system modeling. The resulting inter-operability of software components nowadays plays an important role also in scientific computing. This is due to the fact that inter-disciplinary research has become a major paradigm. However, software infrastructure for efficient co-operation are frequently missing. Furthermore, creation of long-term re-usable and thus portable software requires knowledge about the life-time and capabilities of the used software components. In the field of scientific research another serious problem may arise. During research successful algorithms turn to be no longer applicable with growing problem complexity. As an example one may consider the development of a finite-element-model that in the initial phase uses linear elements and later needs higher-order elements, e.g., for stability reasons. In such a case it may turn out that the initially used solver libraries cannot be used in the final code version. It may then be not feasible to switch to another solver within the remaining project time. The solution to this problem is to use an almost omnipotent solver that integrates almost all solvers present on the web. Such a solver package can be found for example within the SLES module of PETSC (Balay et al., 2002), the Portable Extensible Toolkit for Scientific Computing. However, it still remains an open problem how developers of the model code may test various combinations of solvers and preconditioners offered by the underlying solver library within a reasonable time and without deep knowledge of the spectrum of applicable methods. Thus there is a strong demand for a simple-to-use programming-interface for the end user that is programmed and maintained by an expert, who is able to rapidly extend the interface on user-demands. FoSSI, the Family of Simplified Solver Interfaces, is such a collection of user-interfaces to different parallel sparse linear solvers, grown up on user demands. The interfacing is greatly simplified for linear systems with matrix-representations in compressed sparse row (CSR) format. The supported MPI-parallel (Gropp et al., 1994) sparse iterative solvers (Saad, 1996; van der Vorst, 2003) are PETSC, PILUT (Karypis and Kumar, 1997), AZTEC (Tuminaro et al., 1999), HYPRE (Falgout and Yang, 2002), and the parallel direct solver MUMPS (Amestoy et al., 2000). The interfaces are able to keep several matrices and preconditioners within each solver library, allowing to reuse distributed matrix values and factorizations for consecutive solves. Each solver is equipped with a single subroutine for solver

configuration and invocation. Different tasks within the interface, e.g., distribution of matrix values, incomplete factorization, solution and cleanup, can be combined within a single task-identifier. The parallelism is completely hidden behind the specification of an MPI-communicator, allowing to use various solvers at the same runtime, or, alternatively, allowing parallel solution of many different linear equation systems synchronously. FoSSI can be downloaded from the web under

<http://www.awi-bremerhaven.de/InfoCenter/IT/WorkingGroups/SciComp/FoSSI.html>. Version 1.2 is tested on the following list of platforms (Type/OS/MPI/Compilers):

SGI/Irix6.5/MPT/MIPS, IBM-Power4/AIX5.1L/POE/XLF,XLC, IA32-PC/RedHat 9/LAM-MPI/Intel, SUNFire/Solaris9/ClusterTools/Forte-7.

2. FoSSI—overview

FoSSI emerged from a user interface developed for the PILUT-solver (Karypis and Kumar, 1997) within the FENA project, which is the precursor of the Finite Element Ocean Model FEOM (Danilov et al., 2004). It has been found that the usage of such a powerful user interface makes code development very efficient. Nevertheless, PILUT in its MPI-2 variant turned out not to be a good choice on some compute platforms, e.g., the IBM-Regatta. Therefore, and for convenience (user acceptance), the interface principles have been overtaken for other solver libraries, such as PETSC, AZTEC and HYPRE. All three of these offer the user a wide area of accessible data structures and configuration options. Especially the library internal storage of distributed matrices, vectors and preconditioners and their reference by handles can be exploited within the user interfaces by attributing to each parallel linear equations system a FoSSI-handle, which is simply a user selected number out of a limited range. The second principle of the mentioned libraries is to separate the setup of matrices, vectors, preconditioners, the configuration of the solver, the invocation of the solver and the deallocation of solver internal data structures. This feature has been made transparent to the user within the FoSSI-interfaces by means of the task specifier concept. A task specifier is a sum of elementary task specifiers, each being a configuration or action option for the parallel solver. For example, in the PETSC-interface a parallel matrix structure is generated, filled with symmetrically scaled values by specifying the task `PET_STRUCT + PET_MVALS + PET_SYM_SCAL`. A more detailed preconditioner configuration is given by the task specifier `PET_PCASM + PET_ASMB + PET_ICC + PET_OVL_2`, which sets up an additive Schwarz-preconditioner with overlap 2 in a symmetric implementation (known in PETSC as `PETSC_ASM_BASIC`), and an incomplete Cholesky factorization on the subdomains. This setup is specified together with the solve specifier, e.g., `PET_SOLVE + PET_CG` for a conjugate gradient iterative solver.

For a good solver selection and tuning, the user needs detailed performance (timing) information. At least, the number of applied iterations and the times for factorization and solution should be given back to the user or be printed on output. FoSSI gives some more information back to the user, such as the elapsed time for setup of a parallel matrix, for gathering the solution, for the full call, or even the cumulated time for all calls. The specifier `PET_REPORT` orders performance information in text form before the code returns from the FoSSI-interface routine. The main limitation of the current state of FoSSI is its required input format of matrices and vectors. FoSSI

uses global matrix and vector data. However, the interface needs only values on rows that are actually used by the MPI-task the row is attributed to (according to the user-given partitioning). In this way, the user does not have to take care about distributed data formats. This limitation will be overcome in the implementation of a self-contained solver library equipped with a FoSSI similar user interface. This solver will be independent of other solver packages (see last section).

3. FoSSI used in atmosphere and ocean modeling

FoSSI is currently used in two projects: first, within the Finite Element Ocean Model FEOM (Danilov et al., 2004), which is a 3D primitive equation ocean model on a static mesh of columns of tetraheders, and second, within the PLASMA model (Läuter et al., 2003), which is a 2D-adaptive atmosphere model based on the shallow water equations on the sphere, formulated in finite elements with a semi-Lagrangian discretization of time. Both codes currently work with up to approximately 0.5 million degrees of freedom. The setup times for the matrix and vector distribution through FoSSI is negligible within both models (below 0.5s for four CPUs, perfectly scaling; data not shown). It has been found within the adaptive code, that the overhead to redistribute data based on new global matrix structures due to re-meshing is also negligible. Detailed performance data is not given in the present paper as the underlying numerical cores of the model codes are described in other papers. Accordingly, we do not report on performance measurements of the employed solver packages. However, it is worth mentioning that the PETSC-solver has demonstrated a superior scalability and flexibility with respect to the spectrum of preconditioners. The HYPRE algebraic multigrid preconditioners used for the solution of 3D tracer advection equation in the FEOM code showed comparable performance.

4. An OpenMP implementation performance outlook

For some model codes, based on OpenMP-parallelization (see Chandra et al., 2000), a solver based on the same parallelization technique is needed, as the coupling of a multi-threaded (OpenMP) code to an MPI-solver, waiting in the background, may become rather costly. Although it is possible to communicate data between threads and MPI-tasks in a safe way (Rakowsky et al., 2002), an optimal scheduling of the threads and/or MPI-tasks may require each of them to run on a separate processor. In particular, a “spinning” MPI-Task is awakening faster, but does not allow for a fast context switch to a corresponding OpenMP-thread running on the same processor. The consequence is, that on some compute platforms, for a scalable code the number of required processors is the number of MPI-tasks in the solver plus the number of threads in the rest of the code. Such a processor setup obviously is not easily load-balanced, as the processors running the multi-threaded code have to wait for the solution of the linear equations system, thus wasting compute time.

Generally, an OpenMP (multi-threaded) parallel iterative solver can be programmed on the basis of a sequential (single CPU) code by distributing parallel work within OpenMP parallel do-loops. Here, the problem of memory affinity arises: for larger SMP computers memory is distributed over several CPU-boards of the system, being remotely accessible at an increased latency

time, typically an extra 200–300 ns per cache line. Thus, requests for data from a remote board generate overhead in terms of idle CPU time. On some systems this can be overcome by a so called “first touch memory allocation policy”, meaning, that physical memory addresses are generated at the first time memory is accessed (e.g., initialized), rather than when it is allocated. This allows the operating system to place pages of memory near the accessing CPU, e.g., on the same system board. As memory access on cache-based systems is organized in the cache hierarchy by reference to pages, the memory of a data array may be stored physically on more than one system board. Obviously, to reach performance, the programmer must organize memory accesses in his code in such a way that memory affinity is preserved throughout the runtime of the program code. This means, that parallel memory access patterns must be repeated, i.e., access to an array of data must be parallelized in the same way throughout the code, such that each thread deals most of the time with processor near, i.e., affine memory.

Iterative sparse solvers are based on three time intensive operations: preparation of a preconditioner (in most cases a variant of incomplete factorization), the matrix–vector product and the preconditioning step (application of a preconditioner to approximately solve a sub-problem within the iterative algorithm). The matrix–vector product can be easily OpenMP-parallelized through a parallel outer (row-) loop. If the matrix is ordered with near diagonal structure, it makes sense to store vectors and matrix values in a processor affine memory, such that only a minor fraction of matrix–vector values is accessed from remote memory. In contrast, the more robust preconditioners based on incomplete factorizations of higher level, have an immanent sequential part in their preparation as well as in their application. One standard way to overcome this problem is to treat the problem with a domain decomposition technique (see Chan and Mathew, 1994), separating work into independent subdomains, each treated by its own processor. Within OpenMP, regarding the memory affinity, this is naturally done by introducing a thread-index into shared (global) data structures. Technically spoken, a static global data array is always shared between the threads, and its pages physical locations may be governed by memory affinity. To preserve memory affinity in a transparent way, each subdomain may be given a leading index to the global arrays used for communication, e.g., a buffer vector `Buff[i]` becomes `Buff[t][i]`, where `t` is the logical thread number (obtained from `omp_get_thread_num()`). Within this approach, it is straight forward to code the basis of OpenMP-parallel solvers from MPI-parallel solvers. The MPI-send and receive operations can simply be replaced by memory copy operations between buffers. Furthermore, the code for factorization and preconditioner application can be taken over from an MPI-implementation without changes. In the next version of FoSSI, an efficient and robust parallel solver will be provided to the community that is independent of the parallelization paradigm, namely, the user may choose the MPI- or the OpenMP-version with the same set of features and rather similar performance characteristics.

To demonstrate the efficiency of the approach discussed above, performance measurements are presented in Table 1, allowing to compare the overhead of communication of the MPI- and the OpenMP version of code. It is seen that the vector update (also known as vector gather) in the domain decomposition method is more efficient in OpenMP than in MPI (columns 2 vs. 3). This is due to the overhead of the MPI-implementation over the direct memory-to-memory-copy in the OpenMP-code, although the MPI communication is forced to work over shared memory. In the matrix–vector product, the MPI version of code shows more overhead than expected from the pure update timings. Obviously, the matrix–vector product of the domain-decomposed code

Table 1

Communication times in seconds for 1000 vector updates/matrix–vector products on IBM-p690 (1.3 GHz); the matrix is from the 2D-Poisson problem

#CPUs	MPI-update	OMP-update	MPI-mvu	OMP-mvu	mv omp-for
2	0.06	0.06	23.9	20.5	20.6
4	0.09	0.05	12.47	10.4	10.4
8	0.11	0.03	6.26	6.1	5.7
16	0.13	0.06	3.51	3.5	3.3
30	0.15	0.2	2.32	3.1	4.1

mvu means domain decomposed matrix–vector product with vector update. mv omp-for is the row-loop-parallel OpenMP version of the global sparse matrix–vector product.

performs similarly fast as the parallel loop code. On a p690, four 8-CPU subsystems (Multi-Chip-Modules) are coupled by a communication bus, thus the communication overhead is expected to increase when more than eight CPUs are used. It is noteworthy that we did not analyse how processes and threads were distributed over the 32 CPUs. To achieve a reliable memory affinity it is necessary to bind processes/threads to CPUs.

5. Conclusion

We introduced a convenient way to access various parallel solvers for finite element modeling codes of geophysical flow, even for the unexperienced user. The Family of Simplified Solver Interfaces provides a flexible and highly performing parallel tool. Further development in the field of robust iterative solvers parallelized in OpenMP and MPI are in progress and necessary, in particular, for real domain decomposed model codes, i.e., where global matrices and vectors are not available. The emerging solvers will also take into consideration system specific optimization options such as processor binding for memory affinity and higher optimization techniques for vector architectures. In contrast to the existing solvers with FoSSI-interfaces, these new solvers will allow for a matrix and vector distribution in such a way that the user may program the code around the solver in a completely domain decomposed way with only processor local data structures. This is achieved by handing over the communication routine for vector updates to the user. It is planned to make these solvers accessible to the scientific community for non-commercial use in source form as a portable maintained stand-alone software package under the acronym ScOPES.

As presented in this paper, FoSSI may serve as a starting point to rapid parallelization of model codes strongly preserving the performance characteristics of the underlying solver packages. Furthermore, FoSSI can be read as an exemplary code for modularization techniques that make code development much easier. The reader is strongly encouraged to make free use of the concepts and the know-how gathered within the freely available source code of FoSSI.

Acknowledgement

The development of FoSSI in the context of PLASMA is funded by the German Ministry for Education and Research within the German climate research programme DEKLIM. The devel-

opment of ScOPES is partly funded within the Competence Center for High Performance Computing Bremen (BremHLR) by the Ministry for Education and Science Bremen. The authors are very grateful for the contribution of test problems by the FEOM-developers Genady Kivman and Sergej Danilov as well as by the PLASMA co-developers Natalja Rakowsky and Matthias Läuter.

References

- Amestoy, P.R., Duff, I.S., L'Excellent, J.-Y., 2000. Multifrontal parallel distributed symmetric and unsymmetric solvers. *Comput. Methods Appl. Mech. Eng.* 184, 501–520, Available from <<http://www.enseiht.fr/apo/MUMPS/>>.
- Balay, S., Gropp, W., Curfman-McInnes, L., Smith, B., 2002. *Petsc users manual*. Technical Report ANL-95/11. Revision 2.1.3. Available from <<http://www-fp.mcs.anl.gov/petsc/>>.
- Chandra, R., Dagum, L., Kohr, D., 2000. *Parallel Programming in OpenMP*. Morgan Kaufmann Publishers.
- Chan, T.F., Mathew, T.P., 1994. Domain decomposition algorithms. *Acta Numer.*, 61–143.
- Danilov, S., Kivman, G., Schröter, J., 2004. A finite element ocean model: principles and evaluation. *Ocean Modell.* 6, 125–150.
- Falgout, R.D., Yang, U.M., 2002. HYPRE: a library of high performance pre-conditioners, Part III. *Comput. Sci.* 2002.
- Gropp, W., Lusk, E., Skjellum, A., 1994. *Using MPI*. MIT Press, Cambridge.
- Karypis, G., Kumar, V., 1997. Parallel threshold-based ILU Factorization. In: *Proceedings of 9th Supercomputing Conference*, San Diego. ACM SIGARCH, pp. 1–24. Available from <<http://www.supercomp.org/sc97/proceedings/>>.
- Läuter, M., Handorf, D., Dethloff, K., Frickenhaus, S., Rakowsky, N., Hiller, W., 2003. An adaptive Lagrange–Galerkin shallow-water model on the sphere. In: Heinze, T., Lanser, D., Layton, A.T. (Eds.), *Proceedings of the Workshop on Current Development in Shallow Water Models on the Sphere*, 10–14 March 2003. Munich University of Technology, Munich, Germany.
- Rakowsky, N., Frickenhaus, S., Hiller, W., Läuter, M., Handorf, D., Dethloff, K., 2002. A self-adaptive finite element model of the atmosphere. In: Zwielfhofer, W., Kreitz, N. (Eds.), *Proceedings of the 10th ECMWF Workshop on the Use of High Performance Computing in Meteorology: Realizing Ter-aComputing*. World Scientific.
- Saad, Y., 1996. *Iterative Methods for Sparse Linear Systems*. PWS Publishing Company.
- Tuminaro, R.S., Heroux, M., Hutchinson, S.A., Shadid, J.N., 1999. *Official aztec users guide: version 2.1*. Available from <http://www.cs.sandia.gov/CRF/pspapers/Aztec_ug_2.1.ps>.
- van der Vorst, H., 2003. *Iterative Methods for Large Linear Systems*. Cambridge University Press.



The influence of an irregular grid upon internal wave propagation

Philip Hall *, Alan M. Davies

Proudman Oceanographic Laboratory, 6 Brownlow Street, Liverpool L3 5DA, UK

Received 28 November 2003; received in revised form 26 May 2004; accepted 14 June 2004

Available online 2 December 2004

Abstract

A cross-sectional non-linear model of wind induced circulation in a stratified basin of constant depth, neglecting rotational effects, is used to examine the influence of grid resolution upon the accuracy of internal wave propagation. In addition the effect upon the accuracy and stability of the solution on an irregular grid of using a scale selective formulation of horizontal diffusion is considered.

The initial response to an along-basin wind impulse is coastal downwelling at the downwind end, with upwelling of heavy water and convective mixing at the upwind end. Subsequently a horizontal density front and associated internal waves propagate away from the coast. Calculations show that the intensity of the horizontal and vertical currents associated with the front depends upon vertical and horizontal eddy viscosity, with intensity and hence horizontal gradient increasing as viscosity decreases.

Calculations using a range of uniform and variable horizontal grids show the importance of a fine near-coastal grid on the short time scale when the front is formed. With an irregular grid and constant horizontal viscosity physically unrealistic short waves appear as the frontal region propagates onto the coarser grid. However when horizontal viscosity is computed using a Smagorinsky formulation, this acts as a grid size dependent filter and removes the physically unrealistic short internal waves, thereby stabilizing the solution. If the empirical coefficient in the Smagorinsky formulation is too large, excessive smoothing can occur, spoiling the advantages of using an irregular grid. A reduced value of the coefficient reflecting the grid refinement on an irregular grid gave a stable solution without excessive smoothing.

© 2004 Elsevier Ltd. All rights reserved.

* Corresponding author. Tel.: +44 151 795 4858; fax: +44 151 795 4801.

E-mail addresses: pjh@pol.ac.uk (P. Hall), amd@pol.ac.uk (A.M. Davies).

1. Introduction

Historically the application of irregular (in the sense that the grid resolution in physical space varies with position, usually by the use of a transformation of the equations i.e. a mapping technique) or unstructured grid schemes either in the form of finite differences and boundary fitted coordinates (e.g. Johns et al., 1981) or the more common finite element method (e.g. Luetich and Westerink, 1995) in three-dimensional oceanographic models has primarily focussed upon homogeneous sea regions. In such cases enhanced spatial variability and hence the need for a finer grid increases as the water shallows and the coastline is approached. This has led to grid refinements in near coastal regions with a coarser grid offshore. As we will show the situation is more complex in the case of internal wave propagation.

Although unstructured grids have been used for some time in large scale baroclinic (stratified) oceanographic models (Naimie et al., 2001 and references therein), in recent years there has been an increasing interest in the problem of developing unstructured grid models for internal wave propagation and determining an optimal arrangement of the grid in these models. In particular the role of internal waves in shelf edge regions has become increasingly important. Recently processes involving the generation and propagation of internal waves and the mixing associated with them upon the large scale circulation (e.g. Spall, 2001), with application to climate studies has been recognized as an important problem. In the case of internal waves generated in shelf edge regions there is a clear case for enhanced resolution in the generation region to follow complex variations in bottom topography. However, as we will show, even in the case of flat bottom topography, the physical aspects of internal wave generation and propagation may restrict the degree to which a grid can be refined, and the need to use some form of scale selective horizontal diffusion parameterization.

To illustrate the importance of these effects in a problem involving internal wave generation and propagation we examine the case of the wind response of a stratified region to a sudden wind impulse. In order to separate on the short time scale, and hence study in isolation the initial upwind and downwind response to an imposed wind stress, a closed cross-sectional model of 400 km extent rather than a short lake type situation was used. A constant water depth $h = 250$ m was assumed. This geographical extent and water depth corresponds to a cross-sectional model of the northern North Sea which is stratified in summer (Davies, 1980). This problem is an ideal test case in that in the absence of rotation and for a constant water depth there is an analytical solution for a linear two-layer system (Heaps, 1966).

For the non-linear problem there is no analytical solution, however an accurate solution (namely a “benchmark”) can be obtained using a fine horizontal uniform grid. The degree to which the solution from the irregular grid calculations differs from this “benchmark” as the grid varies can be used to assess the influence of grid variation upon the accuracy of the solution. The analytical solution together with the numerical solutions presented here yields significant insight into the parameters that control the success or failure of irregular grids in modelling internal wave propagation.

The objective of the paper is to use this problem to determine the key parameters that control the accuracy and stability of an irregular grid three-dimensional model when applied to internal wave propagation. The importance of using a scale selective horizontal diffusion is examined. A three-dimensional non-linear model (Xing and Davies, 2001) which has been applied previously

with a regular grid in realistic sea regions, is used here with an irregular grid to examine the importance of grid resolution upon internal wave production and propagation.

An overview of the three-dimensional model with brief details of the numerical methods used is given in the next section. In subsequent sections the numerical results with a range of uniform and non-uniform grids are presented, with conclusions given in a final section.

2. Hydrodynamic numerical model

As the three-dimensional non-linear hydrodynamic equations and transport equation for temperature using Cartesian coordinates in the horizontal and σ coordinates in the vertical have been given previously (Xing and Davies, 2001) only brief details will be presented here.

Since the model solves the fully non-linear baroclinic equations it contains the Baroclinic Pressure Force terms, the full three-dimensional momentum advection terms, and the vertical and horizontal diffusion terms. In initial calculations horizontal viscosity (A_m) and diffusivity (A_h) are given by $A_m = 100 \text{ m}^2 \text{ s}^{-1}$ and $A_h = 100 \text{ m}^2 \text{ s}^{-1}$. Subsequently a shear and grid size dependent formulation for A_m using a Smagorinsky (1963) formulation, given by

$$A_m = C \Delta x \Delta y \left[\left(\frac{\partial u}{\partial x} \right)^2 + \frac{1}{2} \left(\frac{\partial v}{\partial x} + \frac{\partial u}{\partial y} \right)^2 + \left(\frac{\partial v}{\partial y} \right)^2 \right]^{1/2}$$

with C an arbitrary scaling coefficient and Δx , Δy horizontal grid spacing is applied. In the model, u , v , w denote velocity in the x , y , z coordinates. At the land boundary the normal component of flow is set to zero. The surface stress is set equal to the wind stress. At the seabed a linear friction law is applied with a coefficient $K = 0.0005 \text{ m s}^{-1}$, an appropriate value in a shallow region. The numerical solution proceeds by discretizing the equations on an Arakawa C grid, with a single time-stepping method. By this means uncoupling of solutions that can occur in the two time step ‘‘leap frog’’ method is avoided. The irregular nature of the grid in physical space was produced by introducing a mapping factor into the hydrodynamic equations (e.g. Johns et al., 1981). By this means a central and hence second order accurate finite difference scheme could be applied to discretize the transformed (mapped equations). The model equations are transformed by a mapping factor from a variable grid to a unit length Cartesian grid by letting variables, f , be functions of variables (X , Y) which are in turn functions of x and y , thus

$$f(X, Y) = f(X(x), Y(y)), \quad x = [0, 1], \quad y = [0, 1]$$

and the horizontal derivatives are then

$$\frac{\partial f}{\partial X} = \frac{1}{X_x} \frac{\partial f}{\partial x}, \quad \frac{\partial f}{\partial Y} = \frac{1}{Y_y} \frac{\partial f}{\partial y}$$

with subscript denoting partial differential.

As we will show, in some calculations, there is a sharp horizontal density gradient associated with internal wave propagation. To be able to retain this effect, temperature advection is solved using a Total Variation Diminishing (TVD) scheme described by James (1996). This method has

been very successful in advecting sharp density gradients associated with internal tides over steep topography (Xing and Davies, 1998).

3. Calculations

3.1. Analytical and bench-mark solution

In all calculations described subsequently a cross-sectional region of lateral extent 400 km, bounded by two coastlines, with a constant depth $h = 250$ m was examined. Rotational effects were ignored. A uniform initial temperature distribution with corresponding density given by the profile in Fig. 1 was assumed. The eddy viscosity profile (Fig. 1) is identical to that used by Davies (1980) with diffusivity having the same profile and values. Motion was started from a state of rest by the sudden imposition of a wind pulse of 0.5 Pa and duration 12 h. This is identical to that used by Davies (1980), and is designed to produce internal waves without excessive mixing. By this means results can be understood in terms of the analytical model of Heaps (1966).

By approximating the density distribution used in the numerical model, by two homogeneous layers of thickness h_1 and h_2 with density ρ_1 and ρ_2 in each layer, it is possible to derive an analytical solution (Heaps, 1966) for the internal motion. One important difference between layered and continuous models is that in a two-layered model only the surface mode (seiche) and the first

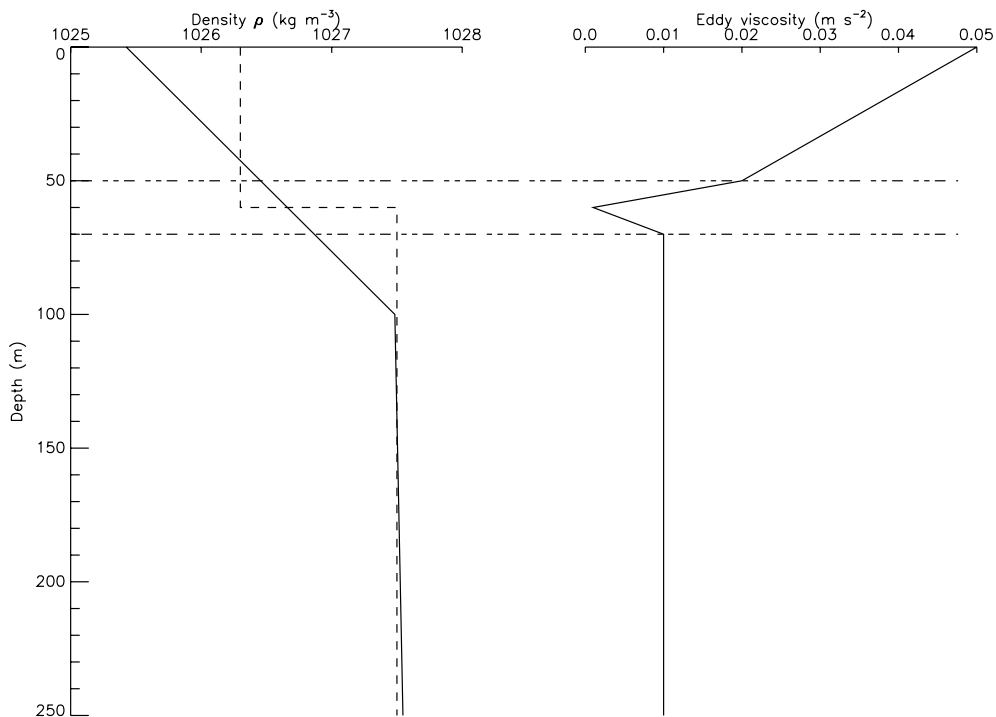


Fig. 1. Profiles of (a) initial density, (b) assumed (specified) eddy viscosity profile.

internal seiche, together with their higher harmonics can be generated, whereas in a continuously stratified basin, an infinite number of internal modes with higher harmonics are possible.

Neglecting the effect of bottom friction on the periods of the seiches, and approximating the density distribution by two layers $h_1 = 55$ m, $h_2 = 195$ m, with $\rho_1 = 1026.3 \text{ kgm}^{-3}$ and $\rho_2 = 1027.5 \text{ kgm}^{-3}$ (see Fig. 1) gives a first internal mode seiche period of $T_1 = 317$ h. The extent to which the numerical model reproduces this will indicate how well it can advect the density field.

Heaps (1966) showed that for a suddenly applied wind stress of the form used here, a narrow coastal region of downwelling at the downwind end of the basin, with a corresponding upwelling at the opposite end occurred. As time progressed the higher modes were damped. Physically this corresponds to the lateral propagation and broadening of the boundary layers. Internal seiche motion then takes place. During this period further damping of the higher modes occurs due to bottom and internal friction, leaving eventually the first mode, which has a single node in the centre of the basin.

This problem is ideal for testing an irregular grid in that the initial response occurs in the lateral boundary layers with a subsequent propagation away from these into the interior. Consequently the grid must be able to resolve the initial response, and the subsequent propagation, without excessive damping or smoothing of the propagating internal wave field. The analytical solution therefore suggests that the crucial test of accuracy is the near coastal response on the short time scale.

However, the solution with the non-linear numerical model will be more complex than the analytical. One source of additional complexity arises from the non-linear terms, which allow energy to move to shorter wavelengths with the possibility of non-linear instability. The other is that at the upwelling favourable end of the basin, heavy (cold) water is moved above lighter (warm) and convective mixing occurs. By using a wide basin the two different responses can initially be studied in isolation, enabling the irregular grid to be studied under different conditions.

Before applying the irregular grid it is essential to obtain an accurate solution on a fine regular grid which can be used as a “benchmark” solution against which the accuracy of other solutions can be determined. A benchmark grid size was chosen based on the convergence of the solutions and had 6250 grid boxes each of 64 m and used to determine the accuracy of the coarser grid solutions. In order to examine the influence of reducing grid resolution, and hence understand its impact in the irregular grid calculations, a range of uniform grids of decreasing resolution namely UG1 (0.2 km), UG2 (2.0 km) and UG3 (20 km) was also used (Table 1). For the variable grid resolution meshes (Table 1) the placement of the boxes was either by means of a piecewise linear

Table 1
Details of the various grid resolutions

Grid	Resolution (km)
UG1	0.2 (uniform)
UG2	2.0 (uniform)
UG3	20.0 (uniform)
VG1	2.0–20.0 (variable)
VG2	0.2–12.3 (variable)
VG3	0.2–3.25 (variable)

“curve” (VG1, VG2) or by means of a quadratic curve (VG3), see Fig. 2. In all calculations following Xing and Davies (2001), 27 sigma levels were used in the vertical, with enhanced resolution in the surface wind driven high shear layer.

Results from the benchmark solution show that during the first 10 h a surface wind driven current (Fig. 3) occurs with downwelling at the down wind end of the basin, and a corresponding upwelling at the opposite end. This leads to a displacement of the temperature surfaces in a near coastal layer, of the order of a couple of grid boxes wide. The circulation in the basin is shown by the streamlines (Fig. 3, $t = 10$ h), with closely spaced streamlines indicating stronger currents.

At the downwind end of the basin a horizontal temperature gradient is produced which gradually propagates to the left (Fig. 3, $t = 20$ h). Associated with the wind forced surface current upwelling occurs at the other end of the basin, leading to some convective mixing, which reduces the horizontal temperature gradient which propagates away from the coastal boundary.

The rate of propagation of the temperature front can be understood in terms of the first internal mode period of the basin, which has a period $T_1 = 317$ h. Associated with this, in a two-layer model there is a speed of propagation of the internal wave ($C_i = 2.53 \text{ km h}^{-1}$). Consequently based on the two-layer analytical model after 40 h the temperature disturbance generated at the lateral boundaries has propagated 101 km. From Fig. 3, $t = 40$ h it is evident that the temperature front has propagated 100 km. This suggests that the TVD method used to advect temperature in the numerical model, besides retaining the sharp temperature gradient can also propagate the disturbance at the correct speed on a uniform grid.

As time progresses, internal seiche motion in the basin produces downwelling at the left end, with corresponding upwelling at the right end, giving rise to nearly horizontal temperature surfaces at $t = 160$ h. Since both ends of the basin have experienced upwelling and downwelling periods by this time, the solution exhibits symmetrical features about the centre (Fig. 3). By $t = 160$ h the higher modes are substantially damped by bottom and internal friction, and the first internal mode corresponding to a linear anti-symmetric vertical displacement of temperature surfaces, about a zero displacement in the centre of the basin remains. This solution on the 64 m grid is

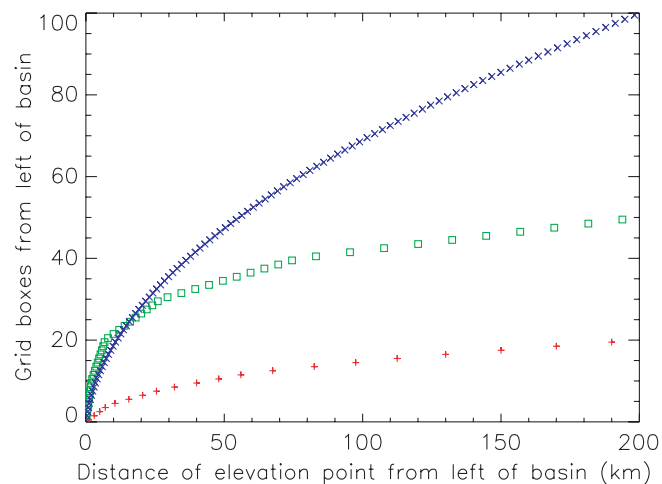


Fig. 2. Spatial distribution of grid boxes in the near coastal region, with (+) grid VG1, (□) grid VG2 and (×) grid VG3.

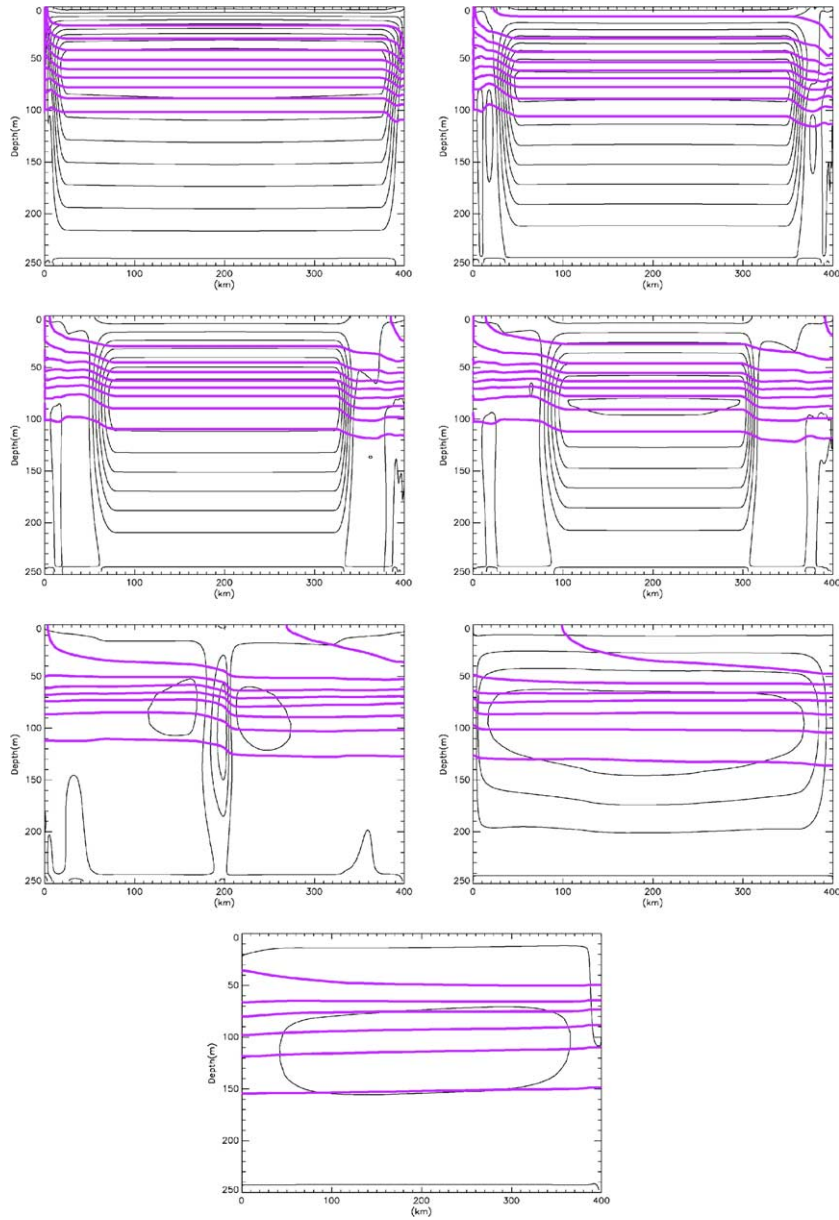


Fig. 3. Temperature contours (in pink) and stream functions over the whole basin at $t = 10, 20, 30, 40$ h and $t = 80, 160$ and 320 h, computed with the high resolution (64 m) grid. (For interpretation of colour in this figure legend, the reader is referred to the web version of the article.)

in excellent agreement, in terms of the time decay of the modes with the analytical solution, although non-linear and convective mixing give rise to some physical differences.

The progressive time damping of the higher modes which contribute to the initial up/downwelling in the coastal boundaries can be seen in the across basin variation with time of

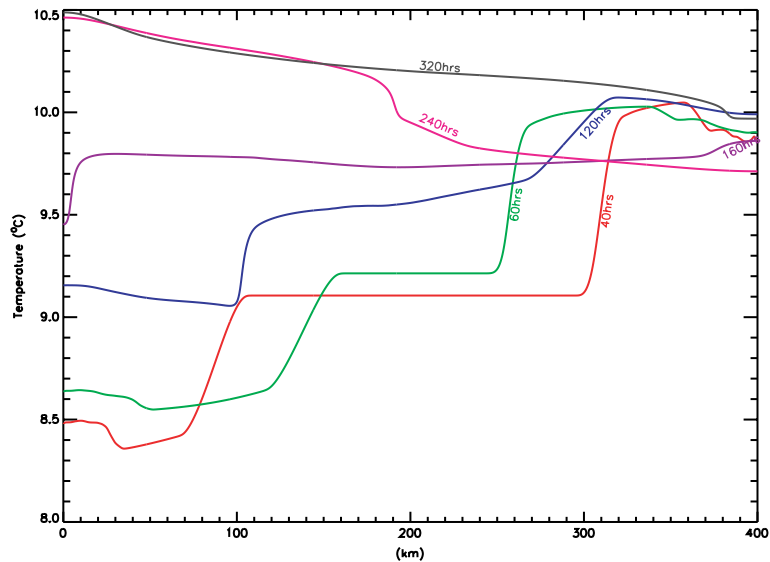


Fig. 4. Contours of temperature at 90 m below the surface at $t = 40, 60, 120, 160, 240$ and 320 h computed with the high resolution (64 m) grid.

the temperature at about 90 m below the surface (Fig. 4). At $t = 40$ h, it is evident that outside the boundary layers, which by this time, have extended 100 km from the basin sides (see earlier discussion) the temperature is unchanged. However at the basin edges there is significant spatial variability due to contributions from the higher modes. By $t = 160$ h a more linear across basin temperature variation occurs which then oscillates at about the period of the first internal seiche. The gradual increase in mean across basin temperature is due to diffusion from the warm surface layer down to depth.

This initial calculation with a high-resolution regular grid clearly shows that horizontal resolution will be particularly important in the coastal regions on the short time scale when higher horizontal modes are present. The processes that affect the sharpness and intensity of the temperature front that propagates away from the lateral boundary will also affect the resolution required to accurately resolve this feature, and the success or failure of an irregular grid.

3.2. Calculations using a range of grid resolutions

In this series of calculations initially the effect of changes in horizontal grid resolution is examined. In particular their influence upon the small-scale features generated in the lateral boundary layer during the initial stage of the calculation is considered. Calculations are performed with a range of uniform grids UG1, 2, 3 (Table 1) in order to gain some insight into how the numerical solution responds to a decrease in grid resolution. These calculations with the uniform grid give significant insight as to the behaviour of the solution on irregular grids, namely grids VG1–VG3 (Table 1). These grids are designed (Fig. 2) to yield grid refinements in the boundary layer going gradually from 2 km (nearshore) to 20 km (offshore), variable grid (VG1), from 0.2 km (nearshore) to 12.3 km (offshore) (VG2), and finally 0.2 km (nearshore) to 3.25 km (offshore) (VG3).

In addition to the influence of grid resolution, in subsequent calculations the effect of changes in vertical and horizontal viscosity is briefly considered.

As shown earlier the initial response is at the coast, with the coastal boundary layer gradually propagating towards the centre of the basin. Associated with this is a region of significant vertical velocity and strong horizontal gradient in the u component of current. To gain some insight into the influence of grid resolution and viscosity upon the solution a detailed series of calculations using a range of A_v and A_m values were performed with both the uniform and variable grids. These calculations showed that as A_v was reduced below that used by Davies (1980), the surface wind driven current in the centre of the basin increased. This gave an enhanced horizontal gradient in u , and increased downwelling in the frontal region at $t = 40$ h. Decreasing the horizontal viscosity on the high-resolution grid produced no significant difference in the large-scale circulation. However on the coarser grid horizontal diffusion influenced the solution.

To consider the effects of grid resolution (both uniform and irregular) in detail we will consider the case where vertical viscosity is a tenth of that used by Davies (1980) and horizontal viscosity is low at $A_m = 10 \text{ m}^2 \text{ s}^{-1}$. A cross-basin plot of horizontal and vertical velocity magnitude at $t = 40$ h at a depth of about 90 m below the surface, the region of the thermocline where the vertical velocity is a maximum was produced (Fig. 5). This plot shows the gradient in horizontal velocity and the rapid increase in vertical velocity for a range of grids. As the horizontal grid size is increased, the coastal boundary layer widens, and shows less spatial variability as the model does not have sufficient resolution to adequately resolve the region of rapid change.

In particular the cross-basin variation of the u component of current determined with the uniform 2 km (grid UG2) or variable (grid VG2) shows an artificial (compared with the higher resolution (grid UG1 or VG3)) variation close to the left coastal boundary. This appears to be associated with the formation of two vertical gyres. In the case of the coarse grid (20 km) the

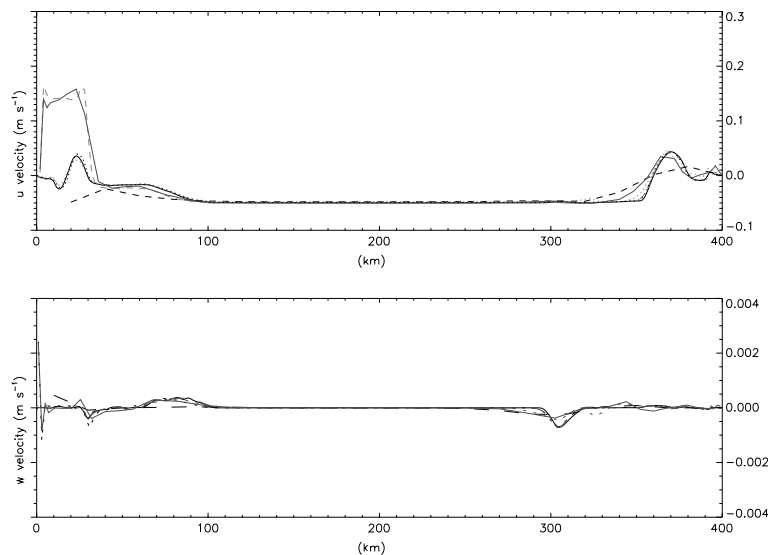


Fig. 5. Across basin plot of (i) u current, and (ii) w current. For grid UG1 (black solid line), UG2 (black dotted), UG3 (black dashed), VG1 (grey solid), VG2 (grey dotted) and VG3 (grey dashed).

model cannot resolve the spatial variability of u current that occurs in the lateral boundary layer. The vertical velocity w computed with the fine grid (UG1) has a region of rapid change (particularly on the right side of the basin), which is well resolved on the 0.2 km grid (UG1). The region is also well resolved on the variable resolution grids (VG2 and VG3). However there are some problems with the VG1 and UG3 grids where the resolution is too coarse. To quantify the accuracy of the solution root mean square errors (RMS) and maximum errors (E) of the difference between u and w velocities at $t = 40$ h computed with the grids, and the benchmark solution were determined. RMS errors for u and w for the right-hand side of the basin (the left-hand side had a comparable distribution) show a maximum on the coarse grid (Fig. 6) in the region of maximum u and w velocity. As the centre of the basin is approached errors decrease to zero, as the disturbance is confined to the coastal region at $t = 40$ h. Refining the grid leads to a significant reduction in the error with the variable grid model giving an RMS error below $8.4 \times 10^{-3} \text{ ms}^{-1}$ (u), $2.3 \times 10^{-4} \text{ ms}^{-1}$ (w), and $2.1 \times 10^{-1} \text{ }^\circ\text{C}(T)$. Although the maximum error (E) not plotted is larger

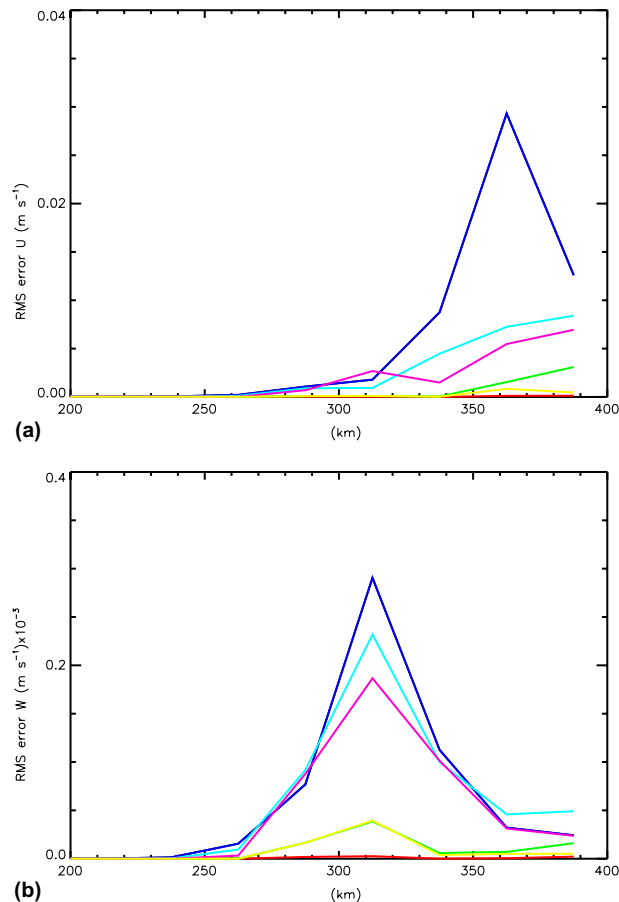


Fig. 6. RMS errors (ms^{-1}) in (a) u velocity, (b) w velocity over the right-hand side of the basin for a range of grid resolutions given by UG1 (red), UG2 (green), UG3 (blue), VG1 (cyan), VG2 (pink) and VG3 (yellow). (For interpretation of colour in this figure legend, the reader is referred to the web version of the article.)

than the RMS error (namely $2.3 \times 10^{-2} \text{ ms}^{-1}$ (u), $4.2 \times 10^{-4} \text{ ms}^{-1}$ (w) and $2.9 \times 10^{-1} \text{ }^\circ\text{C}$ (T)) it can be used to determine the maximum error in a particular parameter for a given grid (e.g. $2.9 \times 10^{-1} \text{ }^\circ\text{C}$ for T on grid VG1).

As discussed previously, as time progresses the disturbance propagates into the interior of the basin, leading to non-zero errors in this region (not presented). However the nature of the problem is that the higher modes are damped with time. Hence, maximum errors for a given grid distribution are reduced (not shown).

An extended series of calculations (not presented) showed that the spatial variability of both u and w was sensitive to the value of horizontal eddy viscosity, with higher values of A_m as expected reducing the horizontal gradients in u and w . Just how A_m influences the solution will be discussed later. In addition to this for a fixed A_m , as the value of vertical eddy viscosity is reduced, then for a given grid resolution there is a more intense surface current, leading to an enhanced up/downwelling in the lateral boundary layers, and a sharper horizontal gradient in u and w , that must be resolved. Consequently the horizontal gradients in u and w are not influenced simply by the value of A_m but are affected by A_v values.

3.3. Influence of horizontal viscosity

In this section we consider in more detail how horizontal viscosity influences the solution, and the effect of using a Smagorinsky formulation. As horizontal viscosity is reduced the resolution within the lateral boundary layers becomes more important on the short time scale (of order 10 h for the problem considered here). As discussed previously the time scale for disturbances to propagate out of the boundary layer is determined by the internal wave speed which depends in a two-layer system upon density and thickness of each layer and water depth. On the longer time scale with an irregular grid small scale features associated with the initial excitation of higher modes (seiches) propagate away from these boundary layers into regions where the grid is coarser. As shown in the analytical solution (Heaps, 1966) the damping of these higher modes is larger than for the lower modes and consequently any disturbance that propagates from the lateral boundaries will be damped with time. However this could be a problem on an irregular grid where propagation into a coarse grid region could lead to a spurious solution if the propagation to the coarse grid region was rapid compared with the damping. Since the analytical two-layer solution shows that the speed of propagation and damping of higher modes depends upon density and layer thickness then as water depth and density differences between layers increases, and bottom friction (which influences mode damping) decreases, then the boundary layer generated at the coast will be more intense and propagate more rapidly into the interior. Consequently in order to maintain stability a larger value of A_m must be applied, or this should be determined in terms of the local horizontal shear and grid size. This problem is examined in this section.

In an initial calculation (Calc. 1) variable grid VG3 was used with a low value of A_m and vertical viscosity. Cross-basin contours of T , u , w at 90 m below the surface at 10 h intervals up to 80 h (Fig. 7a) show a disturbance propagating away from each coastal boundary with some indication of a Gibbs type oscillation in the T field following the frontal region, as it propagates into the coarser grid, suggesting a lack of resolution in this region. On the longer time scale (Fig. 7b) it is evident that the intensity of the ripples particularly on the T contours increases. As the model is fully non-linear any short waves that are produced can, on the longer time scale, transfer energy

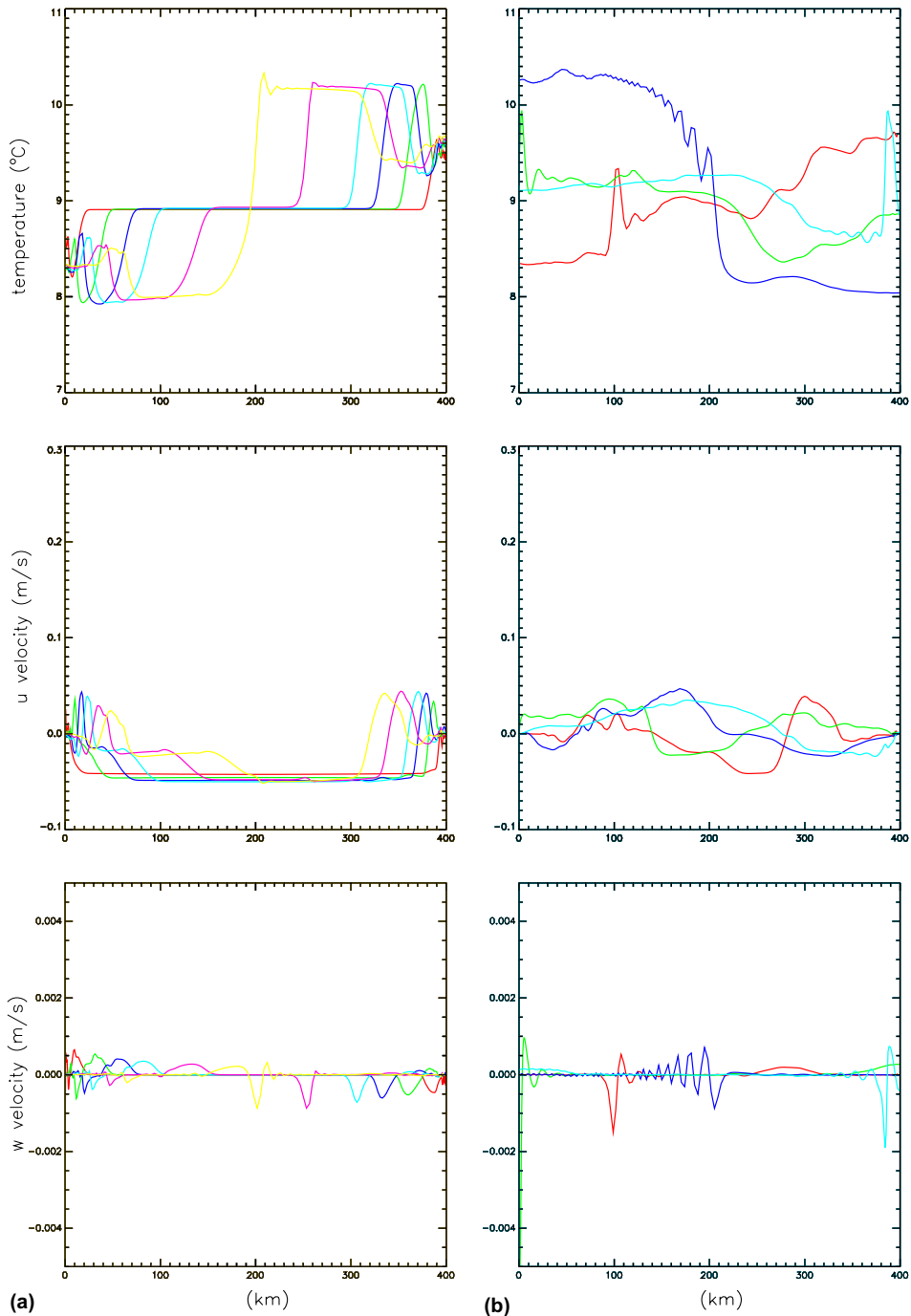


Fig. 7. Across basin contours of (i) temperature ($^{\circ}\text{C}$), (ii) u velocity (m s^{-1}), (iii) w velocity $\times 10^{-3}$ (m s^{-1}) at (a) $t = 10$ (red line), 20 (green), 30 (blue), 40 (cyan), 60 (magenta), 80 (yellow) h and (b) $t = 120$ (red), 160 (green), 240 (blue), 320 h. (cyan) computed with variable grid resolution VG3. (For interpretation of colour in this figure legend, the reader is referred to the web version of the article.)

down to grid scale waves giving rise to an unstable solution due to non-linear instability. This together with the irregular nature of the grid will be the reason for the oscillations found on this

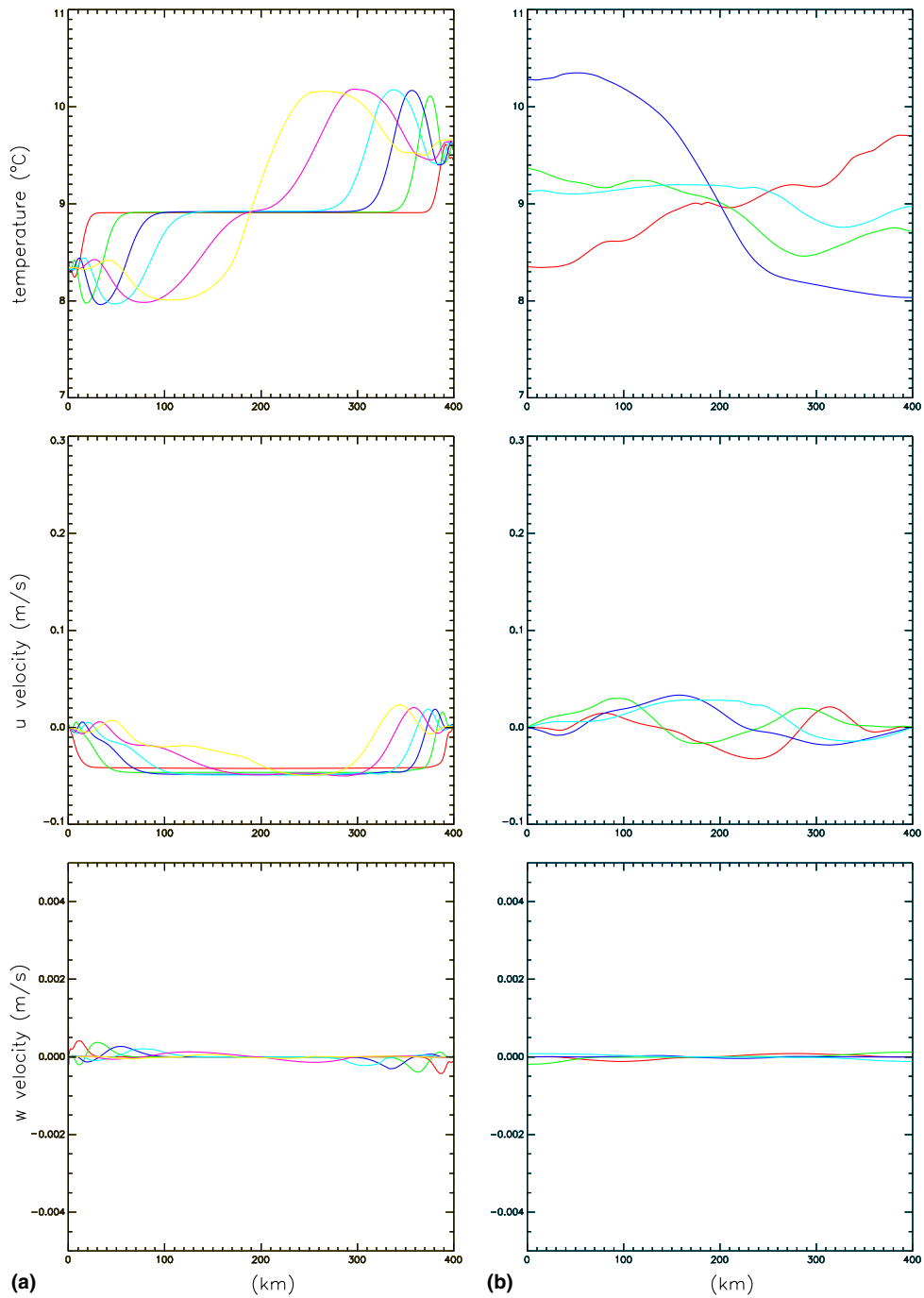


Fig. 8. As Fig. 7 but for A_m computed with the Smagorinsky formulation ($C = 0.2$).

longer time scale. Root mean square and maximum errors between this solution and a benchmark using the 64 m grid at times $t = 40, 80$ and 160 h show (results not presented) that initially the error is a maximum in the near coastal region. As time evolves, and the solution propagates into the interior the error in the coastal region decreases, with an increase away from the coast.

Calculations (not presented) showed that as the value of A_m was increased, then more horizontal smoothing was introduced and a stable solution could be obtained. However this excessive smoothing negated the effects of having an enhanced resolution in the lateral boundary layers. To try and avoid this, the Smagorinsky form of horizontal diffusion with $C = 0.2$ was applied (Calc. 2) using the irregular grid.

From Fig. 8a it is evident that although on the very short time scale ($t < 20$ h) the model can reproduce the disturbance coming from the coastal boundary, on the slightly longer time scale $t = 80$ h, as the disturbance reaches the coarser grid excessive horizontal smoothing takes place. Differences in accuracy between this and the benchmark solution are reflected in the RMS errors in the temperature field (Fig. 9). This figure shows that even with grid VG3 there is an unacceptably large RMS error in the temperature field in the centre of the basin associated with excessive smoothing in the temperature field. Similarly on the long time scale ($t = 240$ h, Fig. 8b) the temperature field shows none of the small-scale structure found previously. In addition there are no spikes in the vertical velocity field. This excessive smoothing on the irregular grid using the Smagorinsky formulation with $C = 0.2$ can be attributed to the fact that A_m determined with this formulation depends not only on horizontal shear but grid scale Δx which increases in the coarse grid region of the model. This calculation suggests that to retain the scale selective filtering qualities of the Smagorinsky form of A_m without excessive damping and the introduction of unacceptable errors the value of C needs to be reduced.

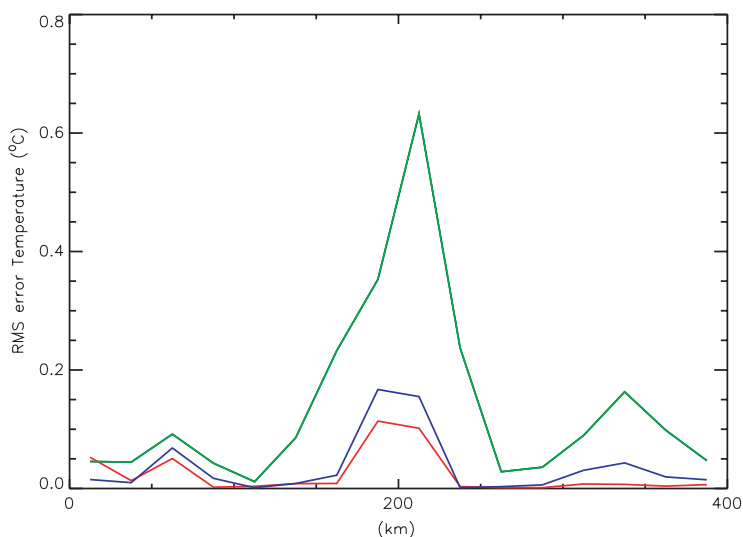


Fig. 9. RMS errors ($^{\circ}\text{C}$) in the temperature for various values of C , namely $C = 0.2$ (green), $C = 0.002$ (blue) used in the Smagorinsky formulation of A_m . Also given (red) are RMS values using the same value of A_m as in the benchmark calculation. All calculations were performed using grid VG3. (For interpretation of colour in this figure legend, the reader is referred to the web version of the article.)

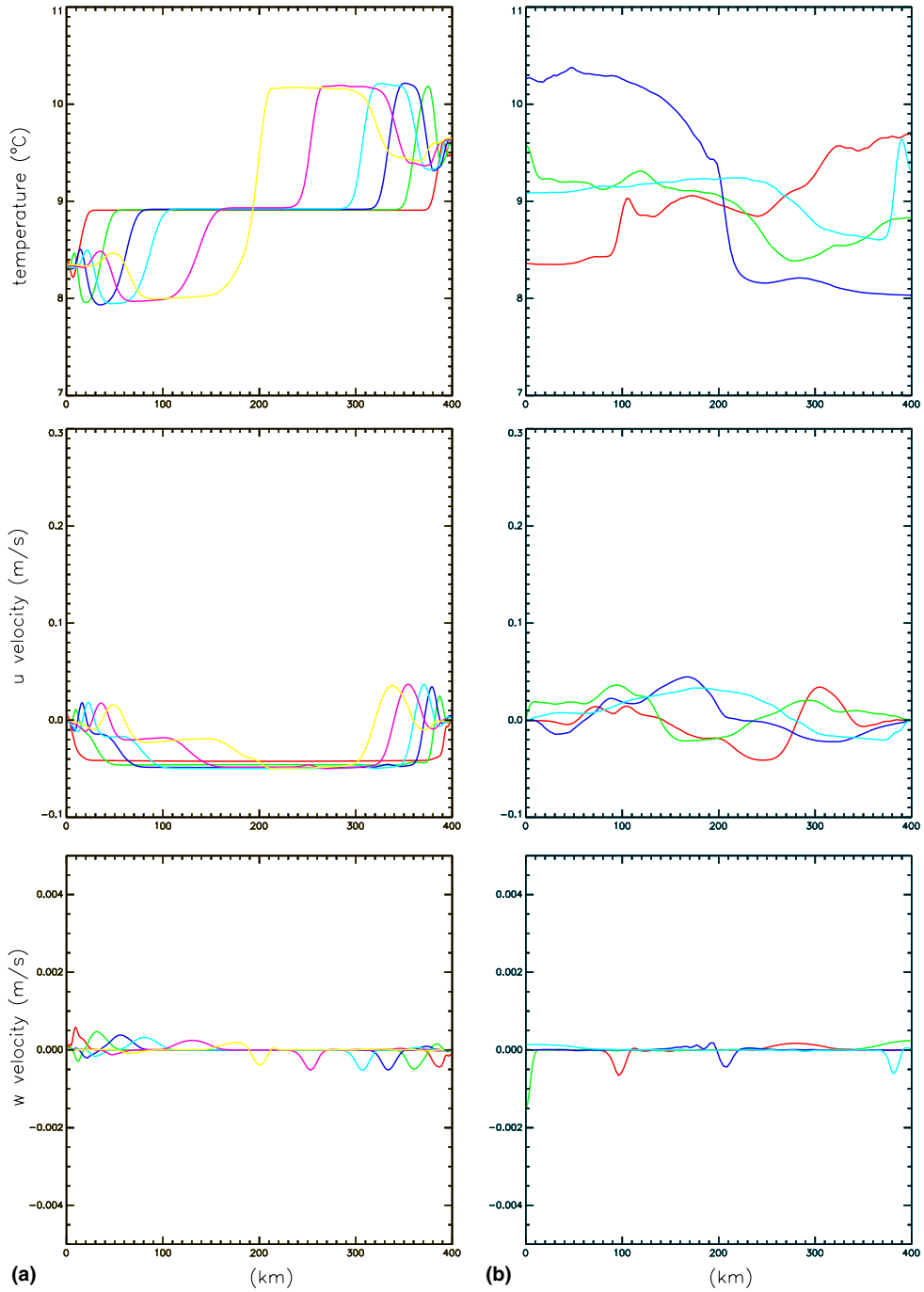


Fig. 10. As Fig. 7 but for A_m computed with the Smagorinsky formulation ($C = 0.002$).

A detailed error analysis (not shown, but illustrated with respect to temperature, Fig. 9) of cross-basin, T , u , w fields computed using the variable grid (VG3) but with C reduced to 0.002

on the short time scale (up to $t = 80$ h) (Fig. 10a) showed an excellent agreement with the benchmark solution (Fig. 9). However, even on this short time scale it is apparent (Fig. 10a) that the maximum value of w associated with the disturbance which propagates from the coastal boundary has been reduced. On the longer time scale, the T and u distributions (Fig. 10b) were found to be in good agreement (errors not presented) with those computed with the benchmark although the magnitude of the vertical velocity spikes has been significantly reduced. A detailed investigation showed that the use of a Smagorinsky formulation with $C = 0.002$, with an irregular grid, does not introduce excessive smoothing (hence negating the advantages of an irregular grid) or allow for a build up of grid scale energy on the coarse grid leading to a physically unrealistic solution. It is apparent from Fig. 9, and a detailed error analysis (not presented) that the solution computed with $C = 0.002$ and the Smagorinsky form of viscosity was not significantly different to that computed in the benchmark calculation (compare errors in Fig. 9 with those derived using the same fixed A_m value as in the benchmark calculation, and grid VG3). This series of calculations clearly demonstrates that when the Smagorinsky formulation for A_m is used on an irregular grid the choice of an optimum value of C will depend upon the degree of mesh refinement in the grid.

4. Concluding remarks

Calculations of internal wave seiching in a wide basin using fixed vertical eddy viscosity have shown that this is an ideal problem for examining the influence of grid resolution upon the accuracy of the solution. Results show that reducing vertical eddy viscosity leads to a rapid horizontal change in both the u and w components of velocity associated with density fronts that propagate away from the coastal boundaries. If horizontal viscosity is large the accuracy of the solution is degraded due to excessive horizontal smoothing. Calculations presented here using an irregular grid with low A_m and A_v values showed that as the temperature front propagated away from the coastal boundary into the coarse grid region, a Gibbs type effect occurred behind the propagating front. This suggested a lack of local grid resolution. Since the model was non-linear, on the longer time scale this led to short wave ripples in the large-scale solution.

Solutions computed using a Smagorinsky formulation for A_m with $C = 0.2$ showed that significant smoothing occurred as A_m was increased in the coarse grid region. This had the effect of negating the benefits of using a finer grid in the boundary layers. A solution with $C = 0.002$ and the irregular grid was however in good agreement with a highly accurate solution. This suggested that in an irregular grid model where a fine grid was used to accurately resolve the internal wave generation region then the use of a Smagorinsky formulation of A_m with C value substantially less (reduced by the order of the grid refinement of the irregular grid in this case 100) than that used on a uniform grid was required. This avoided excessive damping (which negated the effect of the fine grid) whilst maintaining a stable solution.

In essence these calculations showed the importance of maintaining a high resolution in internal wave generation regions, e.g. frontal (Xing and Davies, 2004) and shelf edge (Xing and Davies, 1998). In order to represent their subsequent propagation away from those areas it is essential to maintain adequate grid resolution to represent these small scale waves. If resolution is inadequate then energy can build up at the grid scale, leading in a non-linear model to numerical instability unless a scale selective filter is applied. On a non-uniform grid the computation of A_m using

the Smagorinsky formulation with C below the classical value used on a uniform grid is an effective way of maintaining stability without excessive smoothing.

Acknowledgement

The authors are indebted to Mrs. L. Parry for typing the paper and Mr. R.A. Smith for help in figure preparation.

References

- Davies, A.M., 1980. Three dimensional hydrodynamic numerical models. Part 1. A homogeneous ocean-shelf model. Part 2. A stratified model of the Northern North Sea. In: Saetre, R., Mork, M. (Eds.), *The Norwegian Coastal Current*. Bergen University, pp. 370–426.
- Heaps, N.S., 1966. Wind effects on the water in a narrow two-layered lake. *Philosophical Transactions of the Royal Society of London* 259, 391–430.
- James, I.D., 1996. Advection schemes for shelf sea models. *Journal Marine Systems* 8, 237–254.
- Johns, B., Dube, S.K., Mohanty, U.C., Sinha, P.C., 1981. Numerical simulation of the surge generated by the 1977 Andhra cyclone. *Quarterly Journal Royal Meteorological Society* 107, 919–934.
- Luettich, R.A., Westerink, J.J., 1995. Continental shelf scale convergence studies with a barotropic tidal model. In: Lynch, D.R., Davies, A.M. (Eds.), *Quantitative Skill Assessment for Coastal Ocean Models*. American Geophysical Union, pp. 349–372.
- Naimie, C.E., Blain, C.A., Lynch, D.R., 2001. Seasonal mean circulation in the Yellow Sea—a model-generated climatology. *Continental Shelf Research* 21, 667–695.
- Smagorinsky, J., 1963. General circulation experiments with the primitive equations I. The basic experiment. *Monthly Weather Review* 91, 99–164.
- Spall, M.A., 2001. Large-scale circulations forced by localized mixing over a sloping bottom. *Journal of Physical Oceanography* 31, 2369–2384.
- Xing, J., Davies, A.M., 1998. A three-dimensional model of internal tides on the Malin–Hebrides shelf and shelf edge. *Journal of Geophysical Research* 103, 27821–27847.
- Xing, J., Davies, A.M., 2001. A three-dimensional baroclinic model of the Irish Sea: formation of thermal fronts and associated circulation. *Journal of Physical Oceanography* 31, 94–114.
- Xing, J., Davies, A.M., 2004. On the influence of a surface coastal front on near-inertial wind-induced internal wave generation. *Journal of Geophysical Research* 109, C01023, doi:10.1029/2003JC001794.



A finite element circulation model for embayments with drying intertidal areas and its application to the Quoddy region of the Bay of Fundy

David A. Greenberg ^{a,*}, Jennifer A. Shore ^{b,1}, Fred H. Page ^c, Michael Dowd ^d

^a Fisheries and Oceans Canada, Bedford Institute of Oceanography, P.O. Box 1006, Dartmouth, Nova Scotia, Canada B2Y-4A2

^b Oceanography, Byrd Polar Research Center, Ohio State University, Columbus, OH, USA

^c Fisheries and Oceans Canada, St. Andrews Biological Station, St. Andrews, New Brunswick, Canada E5B-2L9

^d Department of Mathematics and Statistics, Dalhousie University, Halifax, Nova Scotia, Canada B3H-3J5

Received 6 February 2004; received in revised form 24 May 2004; accepted 22 June 2004

Available online 2 November 2004

Abstract

A three-dimensional, triangular-mesh, finite element model has been adapted to allow for the flooding and drying of intertidal areas. The new algorithm sets velocities in dry areas to zero and removes elements from the computation when they are completely *dry*. Model tests simulating an idealized sloping beach that includes a tidal pool and a narrow deep channel laterally bounded by shallow drying sides, give qualitatively reasonable results. A simulation of the Quoddy region of the Bay of Fundy also gave good results when calibrated against available observations. This region includes extensive intertidal flats, tidal pools and channels that are blocked at low water by emerging shallows. The model is a clear improvement over a three-dimensional linear model and a fully nonlinear model without the drying routines using the same model grid. The drying model reproduces the tidal elevations with higher accuracy and has more realistic tidal currents.

Crown Copyright © 2004 Published by Elsevier Ltd. All rights reserved.

* Corresponding author. Tel.: +1 902 426 2431; fax: +1 902 426 6927.

E-mail addresses: davidgreenberg@alumni.uwaterloo.ca, greenbergd@mar.dfo-mpo.gc.ca (D.A. Greenberg), jennifer.shore@rmc.ca (J.A. Shore), pagef@mar.dfo-mpo.gc.ca (F.H. Page), mdowd@mathstat.dal.ca (M. Dowd).

¹ Present address: Department of Physics, Royal Military College of Canada, P.O. Box 17000, Station Forces Kingston, Ont., Canada K7K 7B4.

Keywords: Finite elements; Tides; Coastal zone; Intertidal; Canada; USA; Maine; New Brunswick; Fundy; Passamaquoddy

1. Introduction

The nearshore ocean environment is subject to many stresses resulting from increasing human activity including aquaculture, fisheries, recreation, sewage inputs and marine transportation. An understanding of the physical oceanography of nearshore areas provides a foundation for the study of processes such as sediment transport and biogeochemistry, as well as a basis for effective management of the coastal zone. One potentially important physical attribute of many embayments which is often neglected in coastal circulation models, is the presence of significant drying intertidal areas. Models without the capability of simulating the dry areas may have errors in the area of the wet domain and/or in the volume of water within the domain. It is the purpose of this study to provide a means to effectively model the nearshore hydrodynamics of intertidal drying areas through the inclusion of a new algorithm in a comprehensive, finite element numerical circulation model. With this addition, we will be able to take advantage of the finite element variable resolution to include detailed nearshore topography and coastlines without sacrificing a realistic representation of the physical processes.

The presence of intertidal areas influences the hydrodynamics of coastal embayments through a variety of physical mechanisms. Long waves, such as tides, entering an embayment are distorted due to the nonlinear interaction of hydrodynamics and basin geometry, transferring energy from the primary harmonic to higher harmonics. A number of physical mechanisms are responsible for this feature. The tidally-varying water depth affects the phase speed, and hence the shape of long waves (e.g. Lamb (1932)). Asymmetric distortions of sea level and velocity also occur in channels with tidally varying geometry, where the dominant terms in the momentum equation reflect the balance between advection and the pressure gradient (e.g. Stigebrandt (1980), van de Kreeke (1988)). Bottom friction also affects long wave propagation, leading to tidal phasing differences which enhance dispersion through tidal trapping (Okubo, 1973). In many small, well mixed embayments the primary force balance is between bottom friction and the pressure gradient (Friedrichs et al., 1992). For these cases, Friedrichs and Aubrey (1988) shows that the flood or ebb dominance of tidal velocity can be understood in terms of simple geometrical parameters such as the ratio of the tidal amplitude relative to the channel depth, and the intertidal storage volume relative to the mean tide volume. A variety of localized effects result from circulation directly over the tidal flats; these strongly influence the turbidity and sediment properties of the intertidal zone (LeHir et al., 2000; Uncles and Stephens, 2000).

For realistic cases, the hydrodynamic effects that result from intertidal changes in embayment geometry must be simulated using a numerical model. The inclusion of intertidal areas in a three-dimensional circulation model presents many challenges, such as having to account for a time varying coastline and simulating flows in extremely shallow areas. In a model without drying, shallow water would be considered either always *wet* with a specified minimum depth necessarily below the minimum simulated sea level at that point, or always *dry* and forming part of the model's coastal boundary (e.g. Brooks et al. (1999)). Finite difference models such as those of Flather

and Heaps (1975) and Leendertse and Gritton (1971) include drying areas with fairly simple grid point based algorithms that set velocities to zero when the sea surface falls to the ocean bottom, or some minimum depth of water. Although we use an analogous treatment of velocities here, the integration over each element to obtain elevation presents an additional complexity. Solutions presented in finite element studies of solids with phase changes or sintering of metals and ceramics address similar problems (see Dorri et al. (1987) and Sullivan et al. (1987) for an entry into this literature). In hydrodynamics, finite element techniques have been developed for deforming the mesh to accommodate the changing spatial domain (e.g. see Sidén and Lynch (1988)). These techniques have been of limited use because either: (1) the boundary nodes would move or (2) a larger part of the mesh would be deformed. Such continually changing grid geometry leads to complex, expensive computations necessary for tracking spatially varying topography with moving nodal points. A more useful two-dimensional technique has been developed by McLaughlin et al. (2003) for shallow water in which the physics is reduced to a basic balance between friction and the pressure gradient. In that case, a fixed mesh is maintained and when the surface elevation falls to the bottom, the flow can continue at a reduced rate through a simulated porous bottom layer with different groundwater characteristics.

In contrast to the above, the work presented in this paper describes the adaptation of a three-dimensional finite element model with full dynamics to include areas that wet and dry at different levels of the tide. It needs to be emphasized that the purpose of this work is not to accurately model the intertidal and near intertidal areas, but to have them approximated with enough detail and accuracy to permit good simulations of the adjacent waters. We first test the properties of this formulation using a geometrically idealized case in order to examine how well the model simulates the hydrodynamics associated with water level changes in intertidal areas. This case includes the pooling of water in an isolated reservoir, as well as the draining and flooding of an intertidal shore bisected by a deep channel. The model is then applied to M_2 tidal motion in the Quoddy region, a geometrically complex and tidally dominated area in the Bay of Fundy, on the east coast of Canada (Trites and Garrett, 1983). Here, we emphasize the non-local effects of drying intertidal areas by comparing the performance of the new model formulated to include intertidal drying, with a linear-harmonic model and the original nonlinear model without drying. We examine the model in terms of its ability to explain the observed M_2 amplitude and phase, for both sea level and velocity.

2. Model

2.1. The underlying nonlinear model

The present numerical model, developed for use in areas with drying intertidal elements, is an adaptation of the model *QUODDY* which has been applied in several continental shelf studies (Lynch and Werner, 1991; Lynch et al., 1996, 1997; Werner et al., 1993). [Note that the naming of the model preceded this application to the Quoddy region by several years.] The model has the following properties: implicit or explicit time stepping, fully nonlinear, three-dimensional, prognostic in temperature and salinity, advanced turbulence closure scheme (Mellor and Yamada, 1982), free surface and several possible surface or lateral ocean boundaries. *QUODDY* is

described in Lynch et al. (1996) so only a cursory description will be given here, bringing out those parts that will differ in the modified version, *QUODDY_dry*.

In Cartesian coordinates, the wave equation, from which we determine elevation, ζ , is

$$\begin{aligned} \frac{\partial^2 \zeta}{\partial t^2} + \tau_0 \frac{\partial \zeta}{\partial t} - \nabla_{xy} \cdot \left[-\mathbf{v}|_{z=\zeta} \frac{\partial \zeta}{\partial t} + \int_{-h}^{\zeta} \left[\mathbf{v} \cdot \nabla \mathbf{v} + \frac{g}{\rho_0} \int_z^{\zeta} \nabla_{xy} \rho dz' - \mathbf{F} \right] dz \right. \\ \left. + gH \nabla_{xy} \zeta + \mathbf{f} \times H \bar{\mathbf{v}} - \tau_0 H \bar{\mathbf{v}} - H \Psi + C_d |\mathbf{v}_b| \mathbf{v}_b \right] = 0 \end{aligned} \quad (1)$$

The horizontal components of \mathbf{v} are determined from the momentum equation

$$\frac{\partial \mathbf{v}}{\partial t} + \mathbf{v} \cdot \nabla \mathbf{v} + \mathbf{f} \times \mathbf{v} + g \nabla_{xy} \zeta - \frac{\partial}{\partial z} \left(N \frac{\partial \mathbf{v}}{\partial z} \right) = -\frac{g}{\rho_0} \int_z^{\zeta} \nabla_{xy} \rho dz + \mathbf{F} \quad (2)$$

where we have

$\zeta(x, y, t)$ height of the water surface above the undisturbed level

$h(x, y)$ depth of the undisturbed water (positive down)

$H(x, y, t)$ total depth = $\zeta(x, y, t) + h(x, y)$

$\mathbf{v}(x, y, z, t)$ three-dimensional velocity

$\bar{\mathbf{v}}(x, y, t)$ depth-averaged velocity

$\mathbf{V}_b(x, y, t)$ bottom velocity

$\mathbf{F}(x, y, t)$ non-advective horizontal exchange of momentum

$N(x, y, z, t)$ vertical eddy viscosity

$\rho(x, y, z, t)$ water density

ρ_0 reference value for water density

$\Psi(x, y, t)$ wind stress

τ_0 numerical constant for mass conservation (see Kinmark (1986) and Section 2.2)

\mathbf{f} Coriolis

g gravitational constant

C_d bottom stress drag coefficient

$\nabla(\nabla_{xy})$ the (horizontal) gradient operator

As in Lynch et al. (1996), $\mathbf{F}(x, y, t)$ is expressed in Laplacian form, $\mathbf{F}(x, y, t) = \nabla_{xy} \cdot (A_h \nabla_{xy} \mathbf{v})$, with A_h , the horizontal eddy viscosity, having a Smagorinsky (1963) type grid resolution dependence.

At each time step, there is a two-dimensional computation of the surface elevation using Eq. (1) followed by a node by node determination of the horizontal velocity at vertical levels using equation (2). The implicit treatment of the gravity term (Lynch and Gray, 1979) in the wave equation gives rise to a large time-invariant matrix which can have significant bandwidth. Solving such a system requires large memory for direct matrix solutions or extra computation time if iterative solvers are used. If solved explicitly, the integration collapses to a tri-diagonal matrix. This has the advantage of reducing the computational requirements of the large system of simultaneous equations. A disadvantage is the shorter time step which is now limited by the more restrictive Courant–Friedrichs–Lewy (CFL) limit ($\Delta t < \Delta x / \sqrt{2gh}$) instead of Courant condition ($\Delta t < \Delta x / |\mathbf{v}|$). This can increase the number of iterations for a given simulation, lengthening the computation time. For our variable resolution computations we estimate this maximum time step

by computing $\min(\sqrt{A_i/2gh})$ where A_i is the area of element i and the inequality is satisfied for all elements in the model domain.

The three-dimensional velocities are computed on user-specified, arbitrarily-spaced, terrain-following levels between $z = -h$ and $z = \zeta$. At coastal boundary nodes, $\mathbf{v} \cdot \mathbf{n} = 0$. A minimum depth, $h > h_{\min}$ is set so that $H > 0$ at all times. In this paper we do not consider baroclinic motions.

2.2. Adaptation for drying areas

In this section we describe briefly how *QUODDY_{dry}* differs from the *QUODDY* scheme presented above. More detail is given in [Appendix A](#).

Implicit computation of the wave equation (1) in *QUODDY* requires simultaneous computations for ζ . Because the drying model requires tests on individual nodes, it can be run only in explicit mode where the computation of each elevation does not depend on elevations at unconnected nodes as would be the case in the implicit algorithm. Also in these computations, the bottom depth h is not restricted to be greater than a minimum h_{\min} . The elevation at a node can fall to or below the model bottom depth, i.e. we can have $\zeta < -h$, (see [Fig. 1](#)) and ζ can continue to vary in time if connected to at least one node which is wet ($\zeta \geq -h$). At coastal boundaries where $\zeta \geq -h$ there is no normal flow ($\mathbf{v} \cdot \mathbf{n} = 0$). It was found empirically in testing that setting the velocity $\mathbf{v} = 0$ at interior *and* coastal nodes, when $\zeta < -h + 0.05$ m, improved stability and permitted a better calibration.

The terrain-following levels are still prescribed down to h_{\min} , as in *QUODDY*, which means that they can be below the actual bottom. On levels where $-h_{\min} < z_j < -h$, we set $\mathbf{v}(z_j) = 0$, thus the number of levels active in resolving the three-dimensional motions is reduced in shallow areas

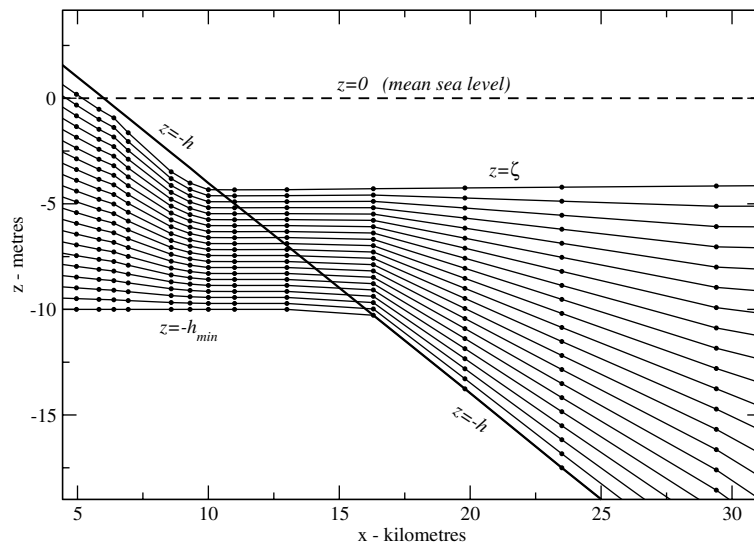


Fig. 1. Representative section from the eastward part of the central transect in [Fig. 2](#) showing vertical level locations used in the drying algorithm.

and dependent on the tidal height (see Appendix A). The bottom velocity for the friction computation, v_b , is taken to be at the deepest vertical node that is wet ($z \geq -h$). For the depth averaged current and for conservation of mass, \bar{v} is computed by integrating from the bottom wet node to ζ . As mentioned in the previous paragraph, if all vertical nodes at a horizontal position are below 0.05 m above the bottom ($\zeta < -h + 0.05$), then $v(z_j) = 0 \Rightarrow \bar{v} = 0$.

The constant τ_0 has important numerical properties in Eq. (1) (Kinnmark, 1986). It ensures that solutions satisfy the conservation of mass equation. A value of $\tau_0 = 2 \times 10^{-4} \text{ s}^{-1}$ has been typical in *QUODDY* (Lynch and Werner, 1991), giving it a magnitude similar to other terms in the equation such as the Coriolis term. Clearly if the value is taken to be large it can make Eq. (1) behave like the continuity equation, giving undesirable solutions (Lynch and Gray, 1979) as the model functions more like a primitive equation model. This undesirable characteristic is seen in finite difference and finite element models that have coincident elevation and velocity computation points. If too small, local and global mass conservation properties are poor. In some of the testing of the drying routines (Section 3) it was found that using a value an order of magnitude or more larger than $2 \times 10^{-4} \text{ s}^{-1}$ gave better local mass conservation properties without detracting from the smoothness or stability of the solution. More sophisticated methods of determining τ_0 such as those described in Kolar et al. (1994) and Atkinson et al. (2004) are not employed here.

3. Numerical experiments on an idealized mesh

We initially test this model on an idealized mesh (Fig. 2) depicting a square bay, $51 \text{ km} \times 51 \text{ km}$, with an open eastern boundary and closed (land) boundaries on the north, south and west sides. There are 1651 nodes, 3155 elements with approximate minimum and maximum element sides of 0.5 and 4.1 km, respectively, and mean 1.25 km. The bottom rises linearly from 45 m below sea level at the eastern boundary to 6 m above mean sea level in the west. In addition to the intertidal area with a constant slope, there are two extreme topographic features specified to test model capabilities: a “tidal pool” 6 m deep in the northwest corner, which is isolated at low water; and in the south-west corner, a narrow, deep (6 m) channel with shallow sides narrowing to minimal resolution—central nodes at 6 m below sea level that will always be wet are connected to nodes on the channel sides that wet and dry with the tide.

We use 21 vertical levels with the spacing between the levels following a sinusoidal distribution, (higher resolution, $\Delta z = 1 \text{ m}$, near the surface and the bottom) but equally spaced when $h \leq 20 \text{ m}$. The h_{\min} used here in defining these is 10 m. When the bottom depth is shallower than h_{\min} , the number of active levels will be reduced, although clearly the vertical resolution will remain high in these areas. The Coriolis parameter is appropriate for a latitude of 45° N . We set the quadratic bottom stress parameter $C_d = 5.0 \times 10^{-3}$ and use a minimum value of $C_d |v_b| > 5.0 \times 10^{-4} \text{ m} \cdot \text{s}^{-1}$, implying a minimum damping due to unmodelled background currents of $0.1 \text{ m} \cdot \text{s}^{-1}$. Horizontal eddy viscosity changes with resolution as in Lynch et al. (1996), appropriate for damping unresolved motions in the varying mesh size. Although mass is globally conserved in these finite element models (Lynch, 1985; Lynch and Holboke, 1997), there can be a local imbalance. In early tests of this drying scheme, this was clearly seen in the surface of the tidal pool which continued to drop ($\sim 1\text{--}2 \text{ m}$) when it was isolated from the rest of the bay. By increasing τ_0 to $1 \times 10^{-2} \text{ s}^{-1}$ the level of the tide pool varied by less than 0.06 m when isolated.

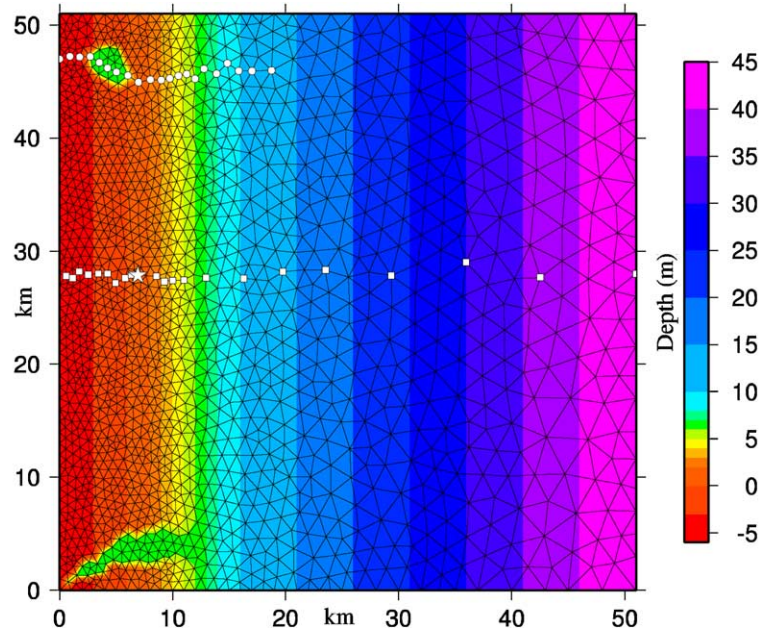


Fig. 2. The finite element mesh used in testing the drying routines. The squares identify the locations of the nodes used in Figs. 1,3 and 4(a). The tidal pool transect in Fig. 4b are circled. The node illustrated in Fig. A.1 is indicated by the star. The bathymetry is shaded (metres). With the exception of the narrow channel and the tidal pool, the bathymetry varies linearly, east to west from 45m below sea level at the open boundary to 6m above sea level. Tidal forcing is along the eastern open boundary. The other three boundaries are closed. (For discussion purposes, we consider north to be towards the top of the grid.)

Along the open boundary there is a sinusoidal tide with amplitude 4m, uniform phase and 12.0h period. The motion is gradually spun up from rest ($v = 0$). To avoid numerical problems with initial wetting of dry model levels that are above $\zeta = 0$, the surface elevation is initially set to the shallowest depth of the model, (in this case $h = -6$ m, so $\zeta = 6$ m) so they are all wet at start-up. Over the first tidal cycle the boundary tidal amplitude is ramped up from 0 to 4m and the mean boundary elevation is ramped down from 6m to 0. In this simulation, the tidal motions are steady after only 3 or 4 cycles.

The surface elevation from successive nodes in the direction across the sloping bottom is shown in Fig. 3. The length of time a node is *active*, i.e. changing in time, varies from zero at the shallowest node (it is never wet) to the full tidal cycle when seaward of the intertidal area. There is also typical shallow water tidal asymmetry in evidence, seen in the steeper rise and the more gradual fall of sea level. The surface currents at the same nodes are zero when the surface elevation falls below the bottom. From the two figures it can be deduced that the second shallowest node is always dry because the velocity is always zero, even though it does change elevation, being connected to a node that is wet for part of the tidal cycle. The apparent small scale noise seen in the currents of the shallow nodes is due to wetting and drying of connected nodes and the activating and deactivating of vertical levels as the tide rises and falls (see Appendix A).

Surface elevation sequences over a tidal cycle for transects crossing the sloping beach (Fig. 4a) and the tide pool (Fig. 4b) show the amplification and phase lag of the sea level signal in the

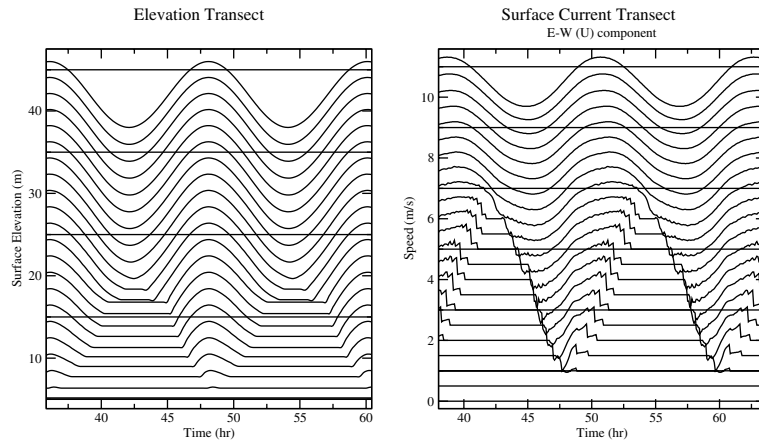


Fig. 3. The surface elevations and surface currents at 22 progressively deeper nodes (the line of squares in Fig. 2). The shallowest node is at the bottom and the deepest (offshore) node at the top. The x -axis indicates the time since the start of the model from rest. The successive elevation curves are offset by 2m. When the elevation falls to a level at or below the bottom and the connected nodes are also *dry*, the elevation remains frozen until the tide rises. Negative velocities are onshore, positive velocities are offshore. The successive current curves are offset by $0.5\text{ m}\cdot\text{s}^{-1}$ in y .

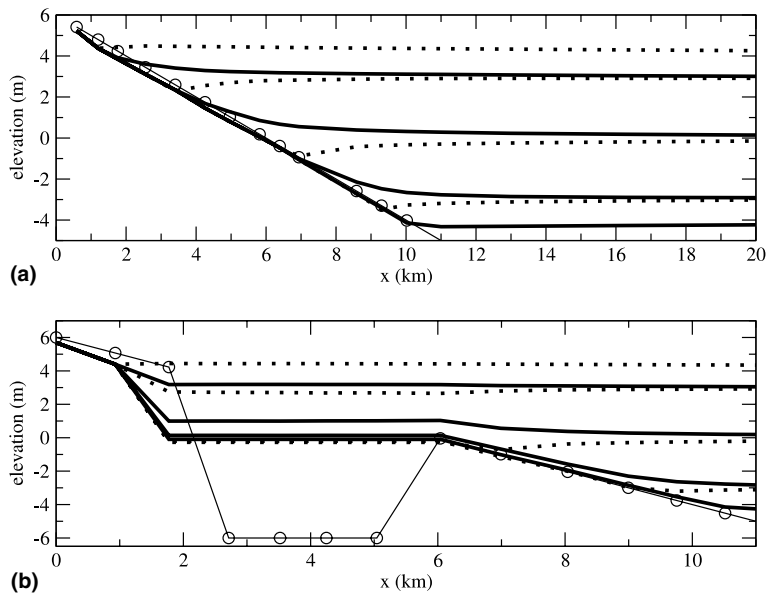


Fig. 4. The progression of the tide falling (thick solid lines) and rising (dotted lines) (a) over the beach slope (along the left end of the line of squares in Fig. 2) and (b) over the tidal pool (circles in upper left of Fig. 2). The circles show the x locations of the nodes on the bottom (h), the thin solid line. The surface elevation can fall below the bottom (see Section 3 and the appendix).

shallower water. The water level in the tidal pool remains constant when disconnected from the bay at low water if we use the higher value of τ_0 given above.

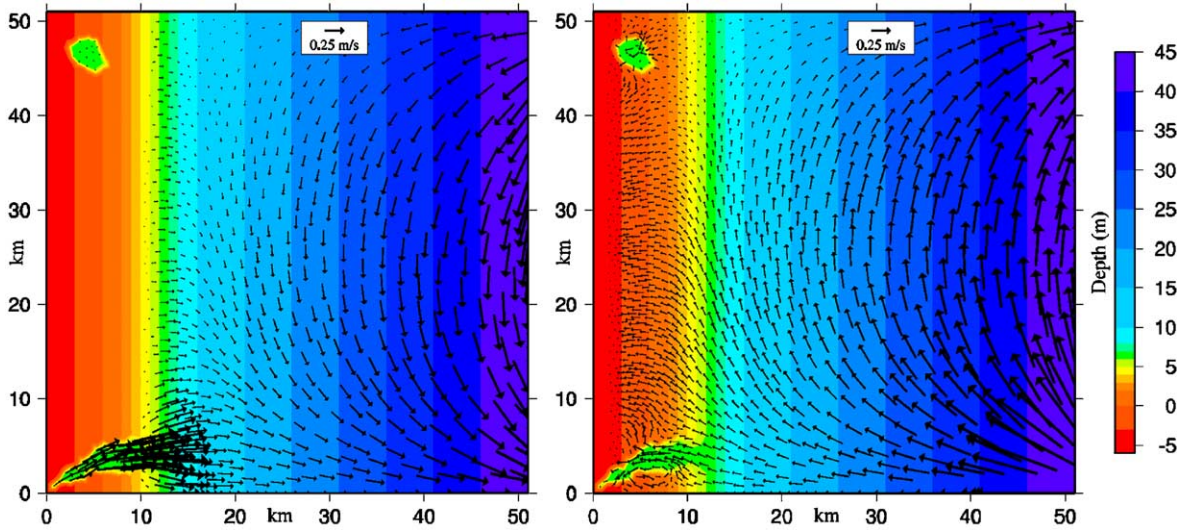


Fig. 5. The surface currents (left) near the time of low water, and (right) near the time of high water.

It can be seen that the elevation stops changing at a level near the depth of connected nodes as explained in [Appendix A](#). This artificial movement of the sea surface past the bottom (only in wetting/drying areas) is smallest in regions with small bottom slope and can be minimized in areas with large bottom slopes by increasing the resolution. Over a tidal cycle there is no net gain/loss of water from the sea level passing below the bottom since anything lost on ebb tide is gained on the flood tide and vice versa. It will be a function of the shallow bathymetry variation in the area modelled as to how significant this characteristic is to the solutions sought. In most cases good grid resolution in any critical steeply sloping drying areas can mitigate any undesired effects.

Snapshots of the current regime show the phase lag between the eastern (open) and the western ends of the bay. The water in the east is still falling/rising near the time of low/high water while the currents are reversing in the west ([Fig. 5](#)). At low water, the tidal pool is isolated from the rest of the bay, the motion on the beach has stopped and the flow out of the narrow channel is confined to the deep areas. At high water, the upper beach is still flooding and the tidal pool is still filling as is the narrow channel. The shallow areas beside the tidal pool and the channel are being flooded from these deeper areas since they offer a less obstructed path for the water to flow.

4. The Quoddy region

The United States/Canada border between Maine and New Brunswick cuts through the St. Croix river at the head of Passamaquoddy Bay, through the Quoddy region and out into the Bay of Fundy. The model domain ([Fig. 6](#)) encompasses the Quoddy region on both sides of the border, the eastern coast of Maine, the western coast of New Brunswick, three large islands and over 30 smaller islands (some of which have land bridges form between them as the tide recedes). The open boundary extends from the southeastern coast of Maine to New Brunswick and encompasses the entrances around Campobello Island.

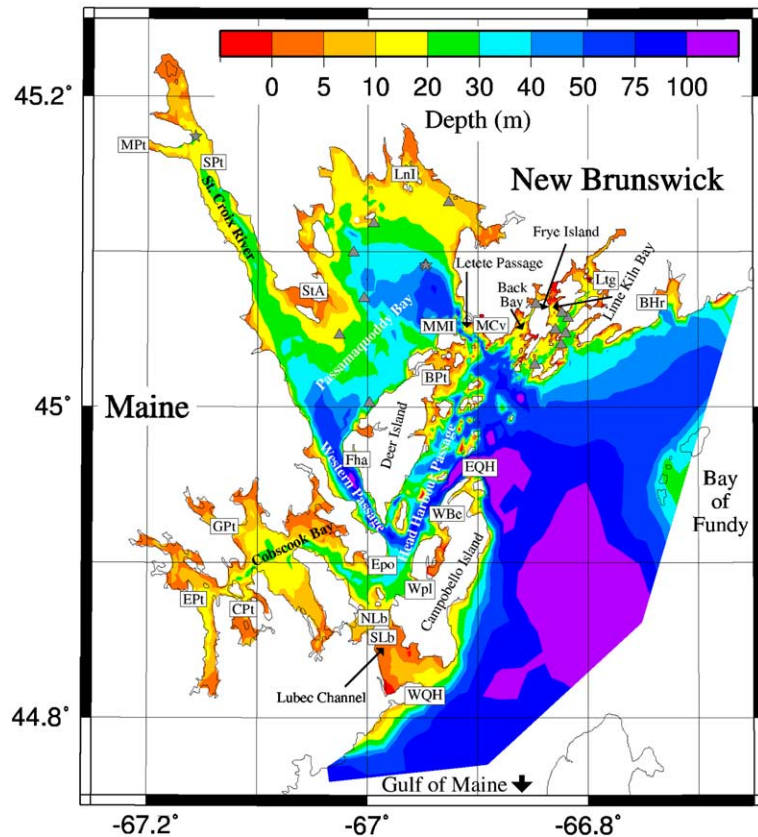


Fig. 6. The Quoddy region and model bathymetry. The boxed three letter symbols refer to the tidal comparison stations. The triangles show the positions of current metre observations. The islands along the northeastern Bay of Fundy boundary are not included in the model. There was no noticeable influence on solutions in the areas of interest from setting the depths in this area to those of the surrounding water.

The Gulf of Maine and the Bay of Fundy are in near resonance with semidiurnal tidal forcing of the open ocean (Garrett, 1972; Greenberg, 1979) with a tidal range of 16m at the head of the Bay of Fundy. Comparatively, it is approximately 2–4m in the Gulf. Observations in Passamaquoddy Bay have found the tidal ranges of M_2 (the dominant tidal component) from 2.2 to 2.7m and phases from 95 to 105 degrees. Deer Island blocks off most of the northern embayment from the southern portion and all of the tidal exchange occurs through Western and Letete Passages around Deer Island (Brooks, 1992; Trites and MacGregor, 1959). The tidal flow is highly sheared in these narrow passages (Thompson et al., 2002). A comparison of time series of tidal elevation and velocity shows Western Passage lags behind Letete Passage in both peak sea elevation and peak current flood (Brooks, 1992).

The model grid for this area (Fig. 7) has 8084 nodes and 13,778 elements. The length of the element sides varies from 35m to 3.88km. Depths range from 148m below the undisturbed surface to 5m above mean sea level. The area around Frye Island illustrates the necessity for high resolution and the significance of intertidal areas to the flow. This area, with complex topography,

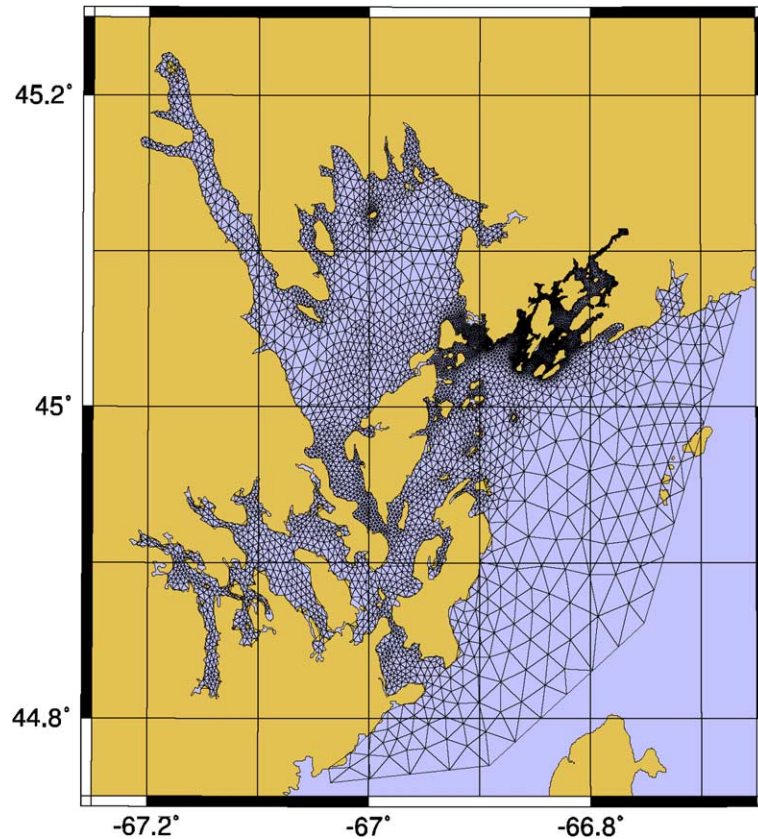


Fig. 7. The finite element model grid of the Quoddy region.

provides a particular focus for aquaculture related studies. At low water, Lime Kiln Bay and Back Bay will be separated by a tidal flat and tidal pools will form in small bays with shallow sills.

With this model resolution the CFL stability condition dictates a time step of near 2 s (see Section 2.1). We have found that in these models with very high resolution and extensive drying areas, experimentation with different damping parameters is necessary to achieve stability and the best calibration. The results presented below were obtained using the values of: the drag coefficient, $C_d = 0.025$; the minimum horizontal eddy viscosity, $A_h = 50 \text{ m}^2 \text{ s}^{-1}$; and the minimum vertical eddy viscosity, $N = 1 \times 10^{-4} \text{ m}^2 \text{ s}^{-1}$. For better calibration and stability, we set τ_0 to be $5 \times 10^{-3} \text{ s}^{-1}$. Other parameters were as in Section 3.

4.1. Tidal elevation

The M_2 tide on the open boundary was taken from a roughly calibrated model of the outer Bay of Fundy (Greenberg, unpublished). These boundary amplitudes and the phases from the outer Bay of Fundy model were adjusted to give a better fit to observations at Beaver Harbour (BHR in Fig. 6), East Quoddy Head (EQH) and West Quoddy Head (WQH), the stations nearest the model open boundary.

Along the outer boundary the tidal amplitude varies from less than 2m to more than 2.6m at the northeastern extreme (Fig. 8). This drives the tide with a 2.5m amplitude, to the inner area north of Campobello Island. The narrow and shallow channel to the southwest of the island, Lubec Channel, has strong currents but has little influence on the tides of the inner model domain. The tides are only slightly amplified within the model, achieving 2.6m in Passamaquoddy and Cobscook Bays, and exceeding 2.7m at the head of the St. Croix River.

There is little variation in phase along the open boundary. The tide is delayed as it moves around Deer Island through Head Harbour Passage, Letete Passage and Western Passage into Passamaquoddy Bay and Cobscook Bay. The tide in Letang Harbour is only slightly behind the tide in the adjacent Bay of Fundy. Passamaquoddy Bay has a fairly uniform phase 8° behind the outer model domain. (A one degree difference in phase lag corresponds approximately to a 2min difference in the arrival of the tide.) There is a progressively increasing phase lag through Cobscook Bay from 5° at the mouth to more than 17° in the upper reaches.

Tidal constants computed from several tidal elevation records are available for model verification. Unfortunately, with the exception of Eastport (Epo), which has a record of over one year, most of the tide stations had record lengths of approximately 1 month, which lowers confidence

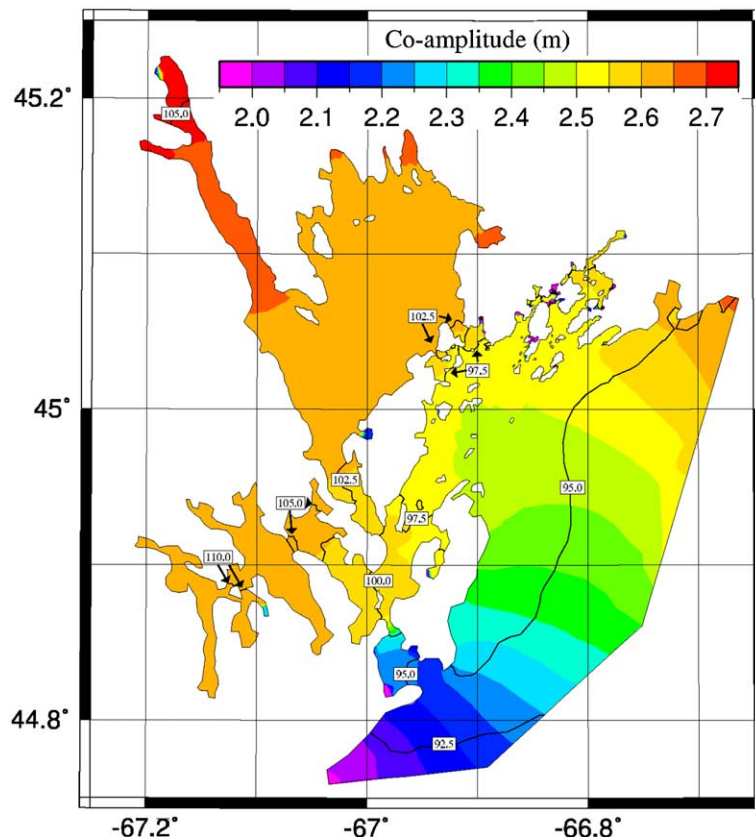


Fig. 8. The M_2 tide co-amplitude contours (metres) and co-phase lines (degrees, UCT) as calculated with the model. The computations of tidal constants are not meaningful in the drying areas.

Table 1

A comparison of the M_2 tidal amplitude and phase statistics for the linear-harmonic model (**FDY**), the fully nonlinear model (**QU**) and the nonlinear drying model (**Qdry**)

	Amplitude (m)			Phase (degrees)		
	Qdry	QU	FDY	Qdry	QU	FDY
Mean error	−0.016	−0.033	−0.039	−0.9	−1.9	−3.8
Mean error	0.043	0.048	0.049	1.3	2.0	3.9

in the tidal constants obtained from data analysis. We have eliminated some stations from the comparison because of gross inconsistencies with the remaining observations. Where multiple analyses are available for a single station, the later records are used for the comparisons, since these were generally longer and more accurate using updated technology and analyses. It is difficult to prove this since original data are often not available, and changes in the tides over time have been noted in the Bay of Fundy (Godin, 1992). We note that some variances between the analyses from single stations were of the same order or greater than the difference between the analyses and the model. Given the limitations of the available data, taken together with the narrow range of amplitude and phase within the model domain, this perhaps limits how definitive we can be in calibration comparisons. The agreement with the three tidal stations in Cobscook Bay—Coffin Point (CPt), Garnet Point (GPt) and Edmunds Point (EPt) is very poor with the model showing large differences in both amplitude and phase with these observations. Since these are more modern observations with somewhat longer record length, we believe that in this bay, the model resolution and the topography available to us are inadequate for accurate modelling of this subregion.

Table 1 gives a comparison between analyses from the available observations, the drying model (*QUODDY_dry*), and two different models: a linear-harmonic model (*FUNDY*) (Lynch et al., 1992; Greenberg et al., 1998) and the fully non-linear model from which the drying model was adapted (*QUODDY*) (Lynch et al., 1996). The latter two models were run with a minimum depth of 10m. All three models use the same mesh, topography and boundary conditions. Generally there was progressive improvement from *FUNDY* to *QUODDY* to *QUODDY_dry*. The average error (model minus data which gives a measure of the bias) and average of the absolute value of the errors (which gives a measure of the variance or spread) shown in Table 1 are less for the drying model than for the other two in both amplitude and phase. The error computations do not include the three Cobscook Bay stations. There was little M_2 phase variation among the comparison stations in *FUNDY* indicating that as expected, nonlinear components of the flow, such as friction and advection, interact with topography and coastlines to influence phase lags. *QUODDY* showed a greater spread in phase while *QUODDY_dry* gave the best agreement with the observations. The differences between the model and observed amplitudes are less systematic, but are generally improved in *QUODDY_dry*.

4.2. Tidal currents

We have compared the analyzed model currents with those measured by acoustic Doppler profiling current meters (ADCPs). Validation with current meter data can be even more challenging

than for tidal elevation data. Small bathymetric features, which might not be resolved by the model, affect both current speed and direction. For instance, if the model depth is different from the actual depth, continuity considerations dictate that the current magnitude could be poor even if the transport is correct. In our simulations, the absence of density gradients (both horizontal and vertical) and wind stress, may miss important influences on vertical current structure. The current records we examined tend to be noisier and of shorter duration than elevation data. In some instances, we have found that where the tidal signal is poorly defined in a current record, the analysis produced a tidal ellipse with a large minor axis; ellipses in areas with small tidal currents, typically less than $0.05 \text{ m} \cdot \text{s}^{-1}$, were almost circular. Such cases were eliminated from comparisons.

M_2 tidal ellipses were computed on model terrain-following levels at nodal points near corresponding ADCP current meter sites. For comparison, the ADCP data were analyzed on equivalent levels. Plots of the ellipse fits are shown for two stations 46_38 and 172_75 in Fig. 9. Station 46_38 shows excellent agreement between model and observation in phase, orientation and magnitude. As we might expect, the current magnitudes and the relative size of the minor axes increase with distance from the bottom due to diminished influence of friction. The model agreement with station 172_75 is not quite as good. The magnitude of the major axis follows the same progression with depth, but in the central water column the observed ellipses are wider and have a slightly

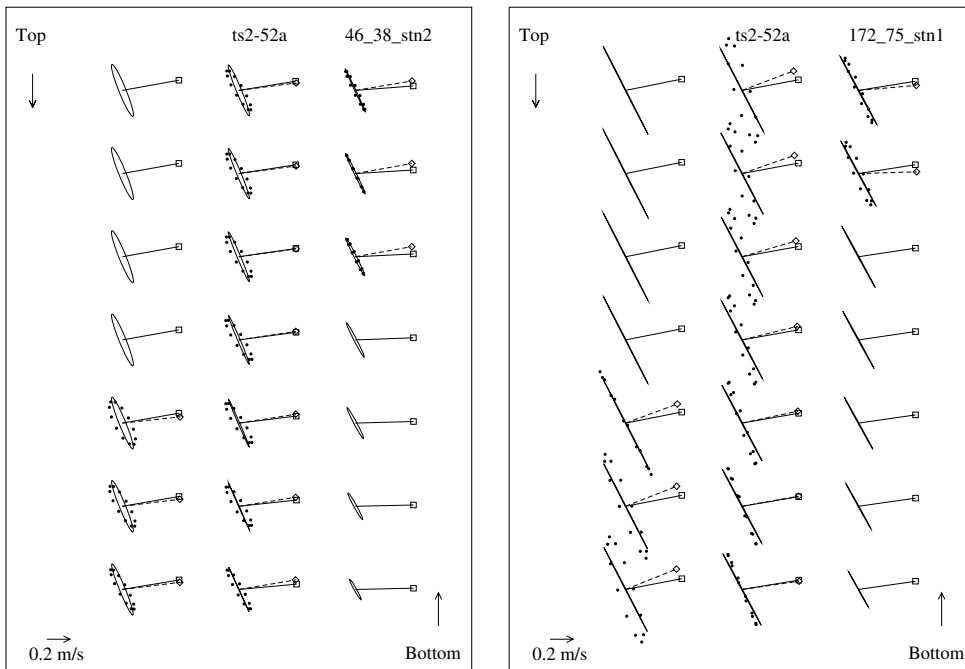


Fig. 9. A comparison of analyzed model and observed M_2 current ellipses and phases of the major axes at stations 46_38 and 172_75 (the stars in Northeastern Passamaquoddy Bay and Northern St. Croix River, respectively, in Fig. 6). Ellipses are oriented relative to north, the positive y -axis. The solid lines are from the model. The broken and dotted lines are from the observations. The straight lines indicate the phase of the ellipse major axis with the angle measured counterclockwise from the positive x -axis.

differing orientation. The phases are close, but again there is a small unexplained variation in the data not seen in the model.

The two stations illustrated above are typical of much of the data, but several stations had anomalies greater than those illustrated. A comparative summary of the different ellipse parameters is shown in Fig. 10. These are from 12 stations covering a total of 138 levels. The problematic cases described above (relating to low magnitude currents) are not included in the plots. Also excluded were comparisons of major axis orientation and phase in cases where the ellipses were close to circular, since almost arbitrary values would come from the analysis. The comparison of the strength of the current along the major axis (Fig. 10a) show good agreement in magnitude and

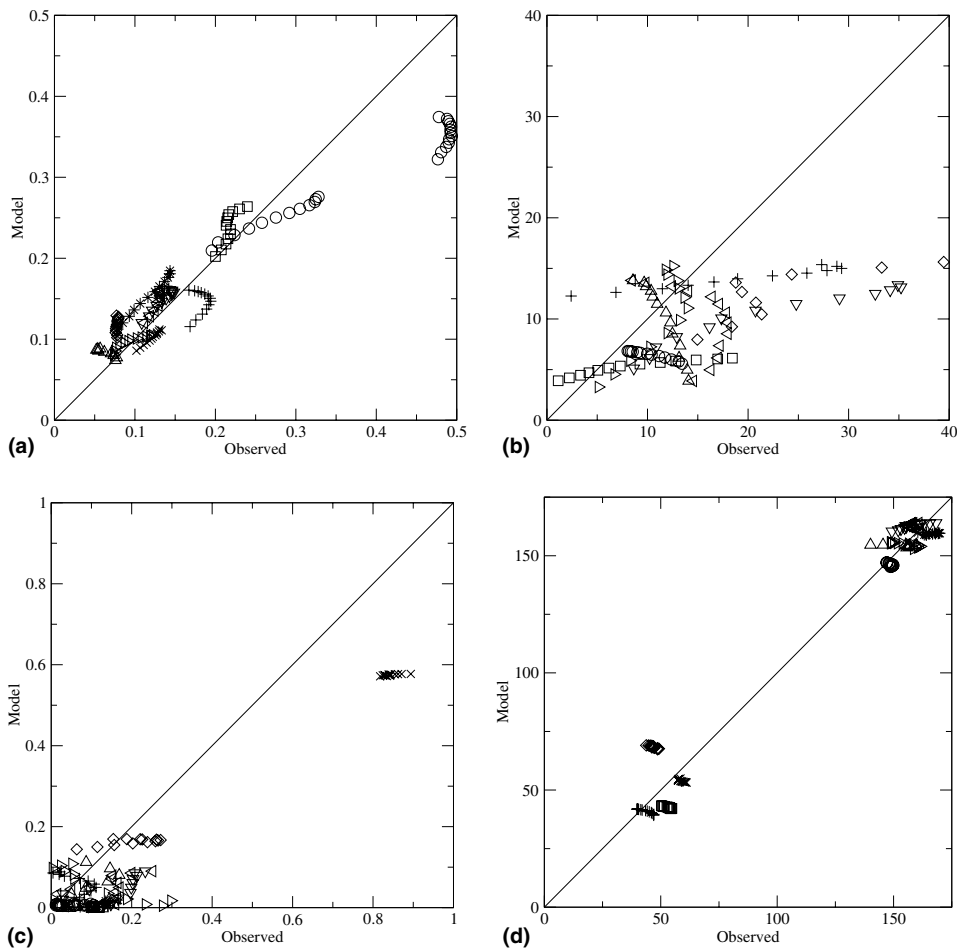


Fig. 10. A comparison of M_2 current ellipse parameters from the model analyzed on terrain-following levels and from ADCP current meters analyzed on equivalent levels. Data from different levels of the same station are plotted with common symbols: (a) the length of the major axis ($\text{m} \cdot \text{s}^{-1}$); (b) the tidal phase of the major axis (degrees, UCT); (c) the ratio of the lengths of the major and minor axes and (d) the major axis orientation angle (degrees from north, positive clockwise).

generally, similar tendency in vertical variation. There are bigger discrepancies in the phase comparisons (Fig. 10b) both in general magnitude and in vertical variation. We think the difference in vertical variation may be due to the missing forcing described above. The reasons for apparent large differences in the phase of all or major parts of a profile are less obvious. LeProvost and Vincent (1986) have noted that velocity computations are less accurate in these models. Noting the limitations of the current meter data as stated above, and that the model has good continuity characteristics with an average phase agreement of $\sim 1^\circ$ in the elevation field, we believe data errors could also be contributing to the apparent inaccuracy. The comparison of ellipticity is given by computing the ratio of the sizes of the major and minor axes (Fig. 10c). In the areas of available observation the ellipses tended to be largely rectilinear. The data tended to have wider ellipses, possibly for the reasons listed above. It is difficult to draw general conclusions about the vertical variation in ellipticity from these data. The model performs well in reproducing ellipse orientation (Fig. 10d), but the narrow range of vertical variation in the data and model profiles again makes it hard to judge the model in this aspect.

5. Discussion and conclusions

We want to re-emphasize that the purpose of including drying areas in a fully nonlinear three-dimensional model is to get useful results in the non-drying areas. This is achieved by better approximating the effects of dynamically constricting and closing off channels and accounting for the proper volume exchanges of water in the nearshore. Although we want qualitatively defensible results, the use and verification of the model in and immediately adjacent to these intertidal areas is not the goal. Observational verification in such areas would be a significant challenge which we are happy to avoid here.

Our tests on the idealized mesh indicate our goals are being met. The progressive flooding and drying over the shallow bathymetry is as we would qualitatively expect. The characteristic shallow water tidal asymmetry in elevation is reproduced. The extreme resolution tests of a minimally resolved (single node width) narrow channel with drying sides and the isolated tidal pool show no anomalous behaviour (with an appropriate choices of the parameter τ_0), without producing the spurious noise that can be found in primitive equation models. The necessity of running the model in an explicit mode necessitates a smaller time step, thus longer computer runs, but some computational demands are reduced because the matrix equation is simplified.

We have applied the model (*QUODDY_dry*) to the Quoddy region of South-west New Brunswick, Canada and compared the results with the associated fully nonlinear model (*QUODDY*) without the drying routines and with a linear harmonic model (*FUNDY*). *FUNDY* computations involve a one step solution and take only seconds to solve on any modern desktop computer. We note that for approximate harmonic solutions, this model is very efficient. The nonlinear and nonlinear-drying models take hours on present day single processor desktop computers. If *QUODDY* is run explicitly with the same time step as *QUODDY_dry*, the computation times are very close. When run implicitly, the time step could be doubled giving half the run time, indicating the stability requirements of the basic implicit model are not greatly different from the drying model. This would suggest that *QUODDY_dry* is definitely more expensive to run, but not prohibitively so.

The three models gave very similar results in calibration to the M_2 tidal elevation data. There were small successive improvements from *FUNDY* to *QUODDY* and *QUODDY_dry*. We believe the minimal phase variation in *FUNDY* demonstrates the importance of nonlinearities in this region. High tidal elevations and currents, the frictional terms, advection and time-varying depth, absent in this linear model, are all significant for these computations.

The further improvement in calibration seen in *QUODDY_dry* over *QUODDY* may also be related to these nonlinearities. The better inclusion of the shallow areas will enhance bottom friction and further emphasize time-varying depth. *QUODDY_dry*'s spatial resolution of the shallow water bathymetry contrasted to the uniform minimum depth of *QUODDY*, will lead to spatial variation in the currents giving rise to larger advective terms. Another significant factor in the improvement could be the better definition of or even complete drying of shallow channels. An example of this, Fig. 11, is seen in the comparison of currents in Back Bay from *QUODDY* and *QUODDY_dry*. Back Bay is separated from Lime Kiln Bay by a shallow area that effectively completely dries at low tide. Even though the elevation from the models (not shown) is almost identical in amplitude and phase, the currents are very different. These current amplitudes are smaller in *QUODDY_dry* by a factor of about two. The difference in the phasing of the tide is about 1 h. Among the intended applications of this model are particle tracking to examine the spread of disease and determination of minimum currents for oxygen resupply to aquaculture farms. The more accurate currents of *QUODDY_dry* will give much more confidence in these computations.

We feel the model is a useful improvement in high resolution tidal modelling of shallow areas. Work is continuing on several fronts. Our application to the Quoddy Region will be further developed. The calibration mismatches will be investigated for several aspects, including: investigating wider parameter ranges, the collection of more calibration data, further increasing resolution in Cobscook Bay and critical channels, and runs that will include multiple tidal constituents. These

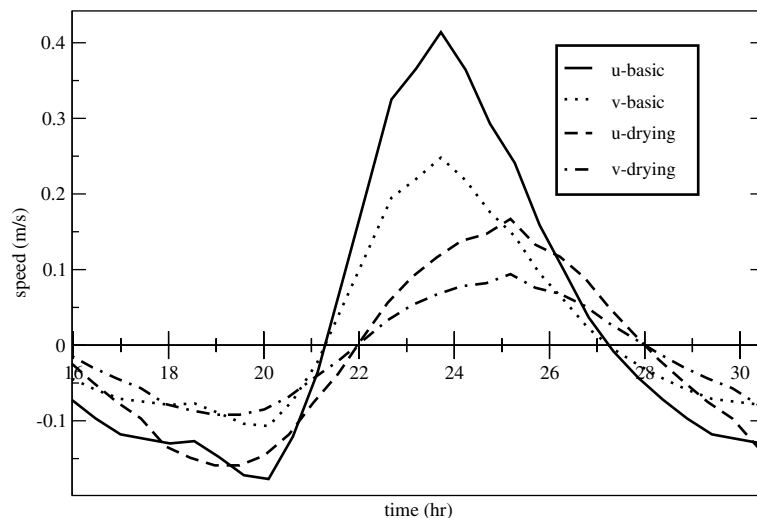


Fig. 11. A comparison of the currents from the drying model, *QUODDY_dry* and the basic model, *QUODDY*, without the drying algorithms, at a location in Back Bay.

will improve our particle tracking ability, and provide for improved bulk measurements of mixing within the Quoddy region (Thompson et al., 2002). The model is also being applied to other areas. The model will be further enhanced to include wind stress, computations in spherical coordinates and prognostic computations of salinity and temperature.

Acknowledgments

We benefited greatly from technical help with data, graphical presentation, analysis and model runs, from Jason Chaffey (Bedford Institute of Oceanography), Randy Losier and Paul McCurdy (St. Andrews Biological Station) and Paul Chapman (now at, Brock University). We have received helpful encouragement and support from the New Brunswick Salmon Growers Association. Important funding for this work was provided by New Brunswick Department of Agriculture, Fisheries and Aquaculture, and the Canadian Department of Fisheries and Oceans Strategic Science Fund and Environmental Strategic Sciences Research Fund.

Appendix A. Aspects of the drying algorithm

The numerical algorithm described in Section 2 involves an integration over the elements to get the elevation field ($\zeta(x, y, t)$) and a point-wise computation to get the velocity field ($\mathbf{v}(x, y, z, t)$). Consistent with this, we remove an element from the computation of ζ if all three of its nodes are *dry* and we use a point-wise check on velocities to set them to zero when they are *dry*. Consider the vertical profile of currents and the corresponding terrain-following level variation over a 12h tidal cycle at a shallow node. The top level always corresponds to the sea surface, ζ . At a shallow node such as this, the bottom level is at h_{\min} (=10m). In water where $h > h_{\min}$, the bottom level is coincident with $-h$. We will refer to a node as *dry* when ζ , falls below $-h$.

The surface elevation, ζ , at point P (Fig. A.1 left) will be frozen in time when ζ at all points, P and N1–N6, are below $-h$. If any one of its neighbours, N1–N6, are still wet, levels at P can continue to vary until all the surrounding points dry. In the case illustrated (Fig. A.1 right), $-h$ is at -0.9m and the surrounding nodes are all dry when ζ_p is at -1.6m . Only the top 8 levels (above the dotted line) rise above $-h$ at some time in the tidal cycle. When, one of the elements surrounding P contain all dry nodes at time t (e.g. element P, N1, N2) then it is not included in the integration that updates ζ_p at time $t + \Delta t$. If just one of P, N1, N2 is wet, then the element is included in the integration, but $\bar{\mathbf{v}}$ and all $\mathbf{v}(z)$ are zero at any dry node.

Because the surface elevation at point P continues to vary only until it and all its connecting points *dry*, it can fall to the level of the shallowest point in the cluster. This behaviour is seen in Fig. 1. If the depths in the cluster are uniform, $\zeta(P)$ would stop moving at a level very close to $-h$. The elevation at P in a cluster with minimal depth range could descend below $-h(P)$ only a small amount reflecting the minimal difference with its neighbours. This would be the case in areas with small gradients in depths or in areas with large depth gradients but high spatial resolution where the gradients are well sampled.

The currents at any level (Fig. A.1 right) will be zero when that level falls below $-h$. Note that these levels can continue to change even after ζ has fallen below this level. As long as node P is

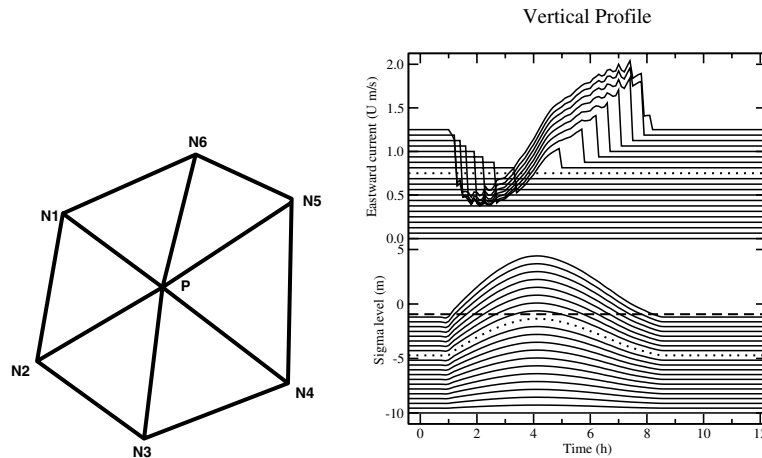


Fig. A.1. (Left) A finite element cluster. (Right) The time evolution of a node that wets and dries over a 12 h cycle, (top) the vertical profile of the u component of current (positive east) and corresponding terrain-following levels of this node (bottom). The dashed line indicates the bottom depth. The dotted lines are at the highest level that does not wet. The current profiles are progressively offset by $0.0625 \text{ m} \cdot \text{s}^{-1}$.

wet, all nodes, P, N1–N6, are included in the computation of $\mathbf{v}(z)$ at P which potentially includes those on levels below $-h$ ($\mathbf{v}(z) = 0$) and those computed normally on levels above. A further restriction sets velocities at all levels to zero when the surface falls below 0.05 m above the bottom ($\zeta < -h + 0.05$).

References

- Atkinson, J.H., Westerink, J.J., Hervouet, J.M., 2004. Similarities between the quasi-bubble and generalized wave continuity equation solutions to the shallow water equations. *International Journal for Numerical Methods in Fluids* 45 (7), 689–714.
- Brooks, D., 1992. Tides and tidal power in Passamaquoddy Bay—a numerical simulation. *Continental Shelf Research* 12 (5-6), 675–716.
- Brooks, D.A., Baca, M.W., Lo, Y.T., 1999. Tidal circulation and residence time in a macrotidal estuary: Cobscook Bay Maine. *Estuarine, Coastal and Shelf Science* 49, 647–665.
- Dorri, B., Kadambi, V., Staub, F.W., Lynch, D.R., 1987. Thermal stress analysis of sintering using a moving grid. *International Journal for Numerical Methods in Engineering* 24, 47–57.
- Flather, R., Heaps, N., 1975. Tidal computations for Morecambe Bay. *Geophysical Journal of the Royal Astronomical Society* 42, 489–517.
- Friedrichs, C., Aubrey, D., 1988. Non-linear tidal distortion in shallow well-mixed estuaries: a synthesis. *Estuarine Coastal and Shelf Science* 27 (5), 521–545.
- Friedrichs, C., Lynch, D., Aubrey, D., 1992. Velocity asymmetries in frictionally dominated tidal embayments: longitudinal. In: Prandle, D. (Ed.), *Dynamics and Exchanges in Estuaries and the Coastal Zone*. American Geophysical Union, Washington, pp. 277–312.
- Garrett, C., 1972. Tidal resonance in the Bay of Fundy and Gulf of Maine. *Nature* 238 (5365), 441–443, August.
- Godin, G., 1992. Possibility of rapid changes in the tide of the Bay of Fundy, based on a scrutiny of the records from Saint John. *Continental Shelf Research* 12 (2/3), 327–338.
- Greenberg, D.A., 1979. A numerical model investigation of tidal phenomena in the Bay of Fundy and Gulf of Maine. *Marine Geodesy* 2 (2), 161–187.

- Greenberg, D.A., Werner, F.E., Lynch, D.R., 1998. A diagnostic finite element ocean circulation model in spherical-polar coordinates. *Journal of Atmospheric and Oceanic Technology* 15, 942–958, August.
- Kinnmark, I.P.E., 1986. The shallow water wave equations: formulation, analysis and application. In: Brebbia, C., Orszag, S. (Eds.), *Lecture Notes in Engineering*, vol. 15. Springer-Verlag, Berlin, p. xxv+187.
- Kolar, R.L., Westerink, M.E., Cantekin, M.E., Blain, C.A., 1994. Aspects of nonlinear simulations using shallow-water models based on the wave continuity equation. *Computers and Fluids* 23 (3), 522–538.
- Lamb, H., 1932. *Hydrodynamics*. Cambridge University Press, New York.
- Leendertse, J.J., Gritton, E.C., 1971. A water quality simulation model for well mixed estuaries and coastal seas: vol 11, computational procedures. Technical Report RM-5294-PR, The Rand Corporation, New York.
- LeHir, P., Roberts, W., Cazaillet, O., Christie, M., Bassoullet, P., Bacher, C., 2000. Characterization of intertidal flat. *Continental Shelf Research* 20, 1443–1459.
- LeProvost, C., Vincent, P., 1986. Some tests of precision for a finite element model of ocean tides. *Journal of Computational Physics* 65, 273–291.
- Lynch, D., Holboke, M., Naimie, C., 1997. The Maine coastal current: Spring climatological circulation. *Continental Shelf Research* 17, 605–634.
- Lynch, D., Ip, J., Naimie, C., Werner, F., 1996. Comprehensive coastal circulation model with application to the Gulf of Maine. *Continental Shelf Research* 16, 875–906.
- Lynch, D.R., 1985. Mass balance in shallow water simulations. *Communications in Applied Numerical Methods* 1, 153–159.
- Lynch, D.R., Gray, W.G., 1979. A wave equation model for finite element tidal computations. *Computers and Fluids* 7, 207–228.
- Lynch, D.R., Holboke, M.J., 1997. Normal flow boundary conditions in 3d circulation models. *International Journal for Numerical Methods in Fluids* 25, 1185–1205.
- Lynch, D.R., Werner, F.E., 1991. Three-dimensional hydrodynamics on finite elements. Part II: Nonlinear time-stepping model. *International Journal for Numerical Methods in Fluids* 12, 507–533.
- Lynch, D.R., Werner, F.E., Greenberg, D.A., Loder, J.W., 1992. Diagnostic model for baroclinic, wind-driven and tidal circulation in shallow seas. *Continental Shelf Research* 12, 37–64.
- McLaughlin, J.W., Bilgili, A., Lynch, D.R., 2003. Numerical modeling of tides in the Great Bay estuarine system: Dynamical balance and spring-neap residual modulation. *Estuarine, Coastal and Shelf Science* 57, 283–296.
- Mellor, G.L., Yamada, T., 1982. Development of a turbulence closure model for geophysical fluid problems. *Reviews of Geophysics Space Physics* 20, 851–857.
- Okubo, A., 1973. Effect of shoreline irregularities on streamwise dispersion in estuaries and other embayments. *Netherlands Journal of Sea Research* 6, 213–224.
- Sidén, G.L.D., Lynch, D.R., 1988. Wave equation hydrodynamics on deforming elements. *International Journal for Numerical Methods in Fluids* 8, 1071–1093.
- Smagorinsky, J., 1963. General circulation experiments with the primitive equations I. the basic experiment. *Monthly Weather Review* 91, 99–164.
- Stigebrandt, A., 1980. Some aspects of tidal interaction with fiord. *Estuarine Coastal Marine Science* 11 (2), 151–166.
- Sullivan, J.M., Lynch, D.R., O'neil, K., 1987. Finite element simulation of planar instabilities during solidification of an undercooled melt. *Journal of Computational Physics* 69 (1), 81–111.
- Thompson, K.R., Dowd, M., Shen, Y., Greenberg, D.A., 2002. Probabilistic characterization of tidal mixing in a coastal embayment: a Markov chain approach. *Continental Shelf Research* 22 (11–13), 1603–1614, July–August.
- Trites, R., Garrett, C., 1983. Physical oceanography. In: Thomas, M. (Ed.), *Marine and Coastal Systems of the Quoddy Region*, New Brunswick, Canada Vol. 64 of Special Publication, Canadian Fisheries and Aquatic Sciences, pp. 9–34.
- Trites, R.W., MacGregor, D.G., 1959. Flow of water in the passages of Passamaquoddy Bay measured by the electromagnetic method (Chapter 4). In: Bumpus, D., Chevrier, J.R., Forgeron, F.D., Forrester, W.D., MacGregor, D.G., Trites, R.W. (Eds.), *Passamaquoddy Fisheries Investigations, Appendix I, Oceanography*. International Joint Commission, Ottawa Ont., Washington, DC.
- Uncles, R., Stephens, J., 2000. Observations of currents, salinity, turbidity and intertidal mudflat characteristics. *Continental Shelf Research* 20, 1531–1549.

- van de Kreeke, J., 1988. Hydrodynamics of tidal inlets. In: Aubrey, D., Weishar, L. (Eds.), *Lecture Notes on Coastal and Estuarine Studies*. Springer-Verlag, New York.
- Werner, F.E., Blanton, J.O., Lynch, D.R., Savidge, D.K., 1993. A numerical study of the continental shelf circulation of the U.S. South Atlantic Bight during autumn of 1987. *Continental Shelf Research* 13, 971–997.



Comparison of advection schemes for high-order h–p finite element and finite volume methods

M. Iskandarani ^{a,*}, J.C. Levin ^b, B.-J. Choi ^b, D.B. Haidvogel ^b

^a *Rosenstiel School of Marine and Atmospheric Science, MPO division, University of Miami, 4600 Rickenbacker Causeway, Miami, FL 33149, USA*

^b *Institute of Marine and Coastal Sciences, Rutgers U., New Brunswick, NJ 08901, USA*

Received 18 December 2003; received in revised form 1 July 2004; accepted 9 September 2004

Available online 2 November 2004

Abstract

We review and compare advection schemes designed for high-order finite element/finite volume methods. The emphasis is on studying, by numerical examples, the properties of these schemes in terms of accuracy, and monotonicity, and their viability for oceanic applications. The schemes reviewed are classical spectral element, Taylor Galerkin Least Square method, the Discontinuous Galerkin method and high-order finite volume method. The latter two schemes exhibit a definite robustness due to their small, but finite, inherent numerical dissipation. They also prove the most flexible since their discontinuous representation of the solution allows easy implementations of flux limiting or adaptive procedure. Finally, an ad-hoc but simple adaptive procedure is presented to illustrate DGM's potential; this procedure proved to be extremely effective at controlling Gibbs oscillations in 1D but was too dissipative on the Hecht problem.

© 2004 Elsevier Ltd. All rights reserved.

1. Introduction

A number of new ocean circulation models based on unstructured-grid finite element (Lynch and Werner, 1991; Iskandarani et al., 1995, 2003; Roux et al., 1998; Danilov et al., 2004; Danilov

* Corresponding author. Tel.: +1 305 361 4045; fax: +1 305 361 4696.

E-mail address: miskandarani@rsmas.miami.edu (M. Iskandarani).

et al., 2005; Ford et al., submitted for publication-a, submitted for publication-b) and on finite volume methods (Casulli and Walters, 2000; Chen et al., 2003) have been developed in the past few years. Their main advantage is the geometric flexibility inherent in their computational grids which allows them to easily handle complicated coastlines, and which endows them with a natural multi-resolution capability. Resolution can be freely distributed and rearranged adaptively to emphasize particular regions and/or critical dynamical features without undue increase in computational cost. Multi-scale and adaptive simulations can thus be carried out within the context of a single model (e.g., coupled simulation of global/basin/coastal circulation).

A number of computational issues remain unresolved with respect to the application of finite element and finite volume methods to oceanic flows. Prominent among these is the issue of tracer advection in finite element models. Oceanic flows are largely determined by density gradients, which in turn depend on the temperature and salt distributions. The evolution of these two tracers is governed by an advection–diffusion equation characterized by a very large Peclet number. Advection is thus the dominant process for the transport of water mass properties.

The numerical solution of advection-dominated problems is complicated by the difficulty in enforcing all the properties of the continuous advective operators in their discrete analogues. Among the desired properties are conservation, monotonicity, shape preservation, accuracy and stability. Last but not least, efficient and scalable schemes are essential if large, multi-scale problems are to be tackled.

In this article we review and evaluate a number of formulations used in solving the advection equation using high-order, h–p type, finite element and finite volume methods. Our aim is to improve the basic advection schemes built into the family of spectral element ocean models (Iskandarani et al., 1995, 2003) As such we focus exclusively on methods that rely on quadrilateral elements for the spatial discretization, and that use relatively high-order polynomials, of degree four to nine, to interpolate the solution within each element. We refer to Hanert et al. (2004) for a review of advection schemes with linear triangular element. The formulations reviewed here are

- the traditional spectral element formulation of the advection equation using continuous basis and weight functions, which we refer to in the following as the Continuous Galerkin method (CGM);
- the Discontinuous Galerkin method (DGM) which uses discontinuous basis and weight functions;
- a Spectral Finite Volume (SFV) formulation that can be made monotonic with a Flux Correct Transport (FCT) limiter; and
- a Taylor Galerkin Least Square formulation (TGLS).

The CGM formulation with its diagonal mass matrix is the most efficient since it allows explicit time-integration schemes to be implemented without requiring the inversion of a system of equations. The CGM solution converges exponentially fast when the solution is infinitely smooth but produces large Gibbs oscillations when the smoothness is finite. The high-order scheme's inherent lack of numerical dissipation allows these oscillations to propagate with little damping, and to eventually pollute the solution everywhere. The typical remedy in such situations is to explicitly include enough dissipation in the form of Laplacian dissipation or filters to damp the noise.

The problem lies in having to anticipate a priori the behavior of the solution, which is not always possible. Furthermore, the interelement continuity requirement of the CGM formulation complicates the implementation of both grid-adaptive procedures and slope/flux limiters.

The DGM formulation (Cockburn, 1998) has become the method of choice for solving hyperbolic and advection-dominated problems in geometrically complex domains. Its most distinguishing feature is the use of discontinuous basis and weight functions. As such, local grid-adaptation and slope limiters are considerably simpler to implement. Furthermore, DGM mass matrices consist of small, element-wise block diagonal matrices that can be easily inverted without resorting to mass lumping. Explicit time stepping is therefore also trivial to implement. (This issue is more of a concern for low-order finite elements.) Here we attempt to assess the performance of DGM with and without slope limiters and adaptivity. The latter is introduced as an illustration of the capability of DGM to implement these algorithms easily thanks to the discontinuous representation of the fields.

The SFV formulation is included here because of the ease with which traditional multi-dimensional limiters can be implemented. If Gibbs oscillations are to be eliminated completely, then limiters are necessary even though they lead to a local loss of convergence order. Here, we have implemented the Flux Corrected Transport (FCT) of Zalesak (1979) to enforce monotonicity of the solution with little modification to Zalesak's original algorithm. The SFV-FCT formulation has been used to develop a shallow water code where the layer thickness is guaranteed to remain non-negative throughout the calculation (Choi et al., 2004).

The only representative of stabilized advection schemes we include here is the Taylor Galerkin Least Square formulation (TGLS; Donea et al., 2000). Our very pragmatic reason for this choice is concerned with the solution of the global matrix equation generated by the stabilization procedure. Since iterative solvers are necessary to avoid memory or parallel scalability bottlenecks in very large problems, it is desirable that the matrix equation be symmetric positive definite so that robust Preconditioned Conjugate Gradient iteration can be used. The least square formulation yields a matrix with the requisite properties. Additionally, the extra terms arising from the least square approach have the same structure as those of the Streamline Upwind Petrov Galerkin (SUPG) stabilization, and provide the necessary upwind dissipation (Jiang, 1998). These extra terms do not require any new adjustable parameter, and depend only on the time step employed in the time integration. Although, we have argued here against the adoption of implicit time-stepping schemes, they may still be the appropriate practical choice, particularly if element sizes vary significantly across the grid. Substantial effort must then be expended in optimizing the iterative solver necessary for large scale applications. The majority of our examples here relies on explicit RK4 time stepping.

Our model advection equation is

$$T_t + \vec{u} \cdot \nabla T = 0, \quad (1)$$

where T stands for one of the prognostic tracers (e.g., temperature). The conservation form of the equation for a divergence-free velocity, $\nabla \cdot \vec{u} = 0$, is

$$T_t + \nabla \cdot (\vec{u}T) = 0. \quad (2)$$

We first outline the different formulations and discuss their distinctive properties. We also propose an ad-hoc adaptation strategy to illustrate the potential of the latter to eliminate oscillations. The

Hecht problem, which consists of advection of a passive tracer in a Stommel Gyre, is considered in the limit of marginal resolution in the western boundary current region. The shearing of the tracer in the swift current leads to small-scale features that are not resolvable on the coarse computational grid. Gibbs oscillations appear and pollute the solution, and differences in the schemes are quite noticeable. Various devices are then explored in order to improve the basic schemes. We finish by comparing CGM and DGM on an active tracer experiment using SEOM-3D.

2. Spatial discretization

We start by describing the common spatial discretization used by the different formulations. We presume the physical domain to have been divided into quadrilateral elements which can be mapped individually to a computational plane (ζ, η) as shown in Fig. 1. The solution within each element is interpolated with a high-order polynomial according to

$$T(\zeta, \eta) = \sum_{i=0}^N \sum_{j=0}^N T_{i,j} \Psi_{ij}(\zeta, \eta), \tag{3}$$

where Ψ_{ij} are the interpolation (or trial) functions, and the $T_{i,j}$ are unknown coefficients that depend on time only. Here we rely exclusively on Lagrangian interpolation so that the coefficients $T_{i,j}$ are the solution values at the collocation points.

In two dimensions the interpolation consists of tensorized Lagrangian polynomials of the form $\Psi_{ij}(\zeta, \eta) = h_i(\zeta)h_j(\eta)$. Two sets of points are commonly used for collocation: the Gauss Lobatto, and the Gauss roots of Legendre polynomials (Boyd, 1989). Both sets of roots cluster near the boundaries to defeat the Runge phenomenon, and to stabilize high order Lagrange interpolation. Legendre polynomials and roots are commonly used because they provide for good interpolation

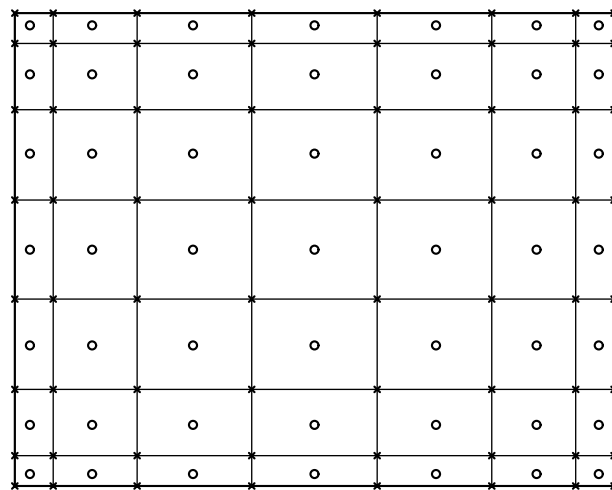


Fig. 1. Sketch of a quadrilateral element and its $N \times N$ cells $\Omega_{kl} = [\zeta_k, \zeta_{k+1}] \times [\eta_l, \eta_{l+1}]$. The Gauss points are indicated by circles.

properties and accurate numerical quadrature for quadrilateral elements (Canuto et al., 1988; Boyd, 1989; Karniadakis and Sherwin, 1999). The Gauss-Lobatto roots include the end points of the interval $[-1, 1]$, and are convenient to enforce function continuity across elements and to impose Dirichlet boundary conditions; they are the collocation points of choice for the CGM formulation. The Gauss roots omit the end points and are, for that reason, used primarily with discontinuous type interpolation such as DGM; they also offer improved integration accuracy over the Gauss-Lobatto points. (A Q -point Gauss quadrature is exact for polynomial of degree $2Q - 1$, whereas a Gauss-Lobatto quadrature is exact for polynomials of maximum degree $2Q - 3$.) Notice that the Gauss and Gauss-Lobatto roots of a given degree Legendre polynomial are staggered. The choice of points for collocation and quadrature will be specified for each formulation.

3. Formulations

3.1. Continuous Galerkin formulation

The weak form of the advection equation amounts to finding a T such that

$$\int_{\Omega} \Phi T_i dA - \int_{\Omega} T \vec{u} \cdot \nabla \Phi dA = - \int_{\partial\Omega_i} \Phi T \vec{u} \cdot \vec{n} dS - \int_{\partial\Omega_o} \Phi T \vec{u} \cdot \vec{n} dS \quad \forall \Phi \in H^1, \quad (4)$$

where the Φ 's are weight functions belonging to the Hilbert space H^1 , and the divergence theorem has been invoked to integrate by parts the divergence term. The boundary integrals on the right hand side of Eq. (4) represents the flux in and out of the domain. The application of the classical (Bubnov) Galerkin procedure leads to a discrete system of ordinary differential equations of the form $MT - DT = f$ where T refers to the vector of unknown coefficients, M is the mass matrix, D represents the discrete divergence operator, and f is the load vector on the system.

The Gauss-Lobatto roots are used for the Lagrangian interpolation within each element to simplify the enforcement of the continuity requirement across elements. The integrals in Eq. (4) are usually evaluated with quadrature given the complicated nature of the integrands. The proper choice of quadrature rule is central to the efficiency and accuracy of the spectral element method, most pertinently for explicit time-stepping schemes. More specifically, choosing the quadrature points to be those associated with the Gauss-Lobatto collocation points leads to a diagonal elemental mass matrix (Ronquist, 1988). The global mass matrix is then also diagonal and its inversion is trivial. Notice that the Gauss-Lobatto quadrature is inexact: the integrand is a polynomial of degree $2N$, possibly $3N$ for a highly distorted element, whereas the quadrature is exact only for polynomials of degree $2N - 1$ or lower. This loss of accuracy is tolerable: first, the gain in computational efficiency is very large, and second the phase degradation of the mass lumped matrix disappears spectrally fast for $N > 2$.

The spectral element CGM formulation is characterized by exponential convergence under p refinement when the solution is infinitely smooth. The convergence rate drops when the solution has finite continuity, and Gibbs oscillations appear when the solution is discontinuous or steep gradients are under-resolved. These oscillations can be non-linearly amplified and lead to a breakdown in the simulation. Fig. 2 illustrates the Gibbs oscillations using the one-dimensional example

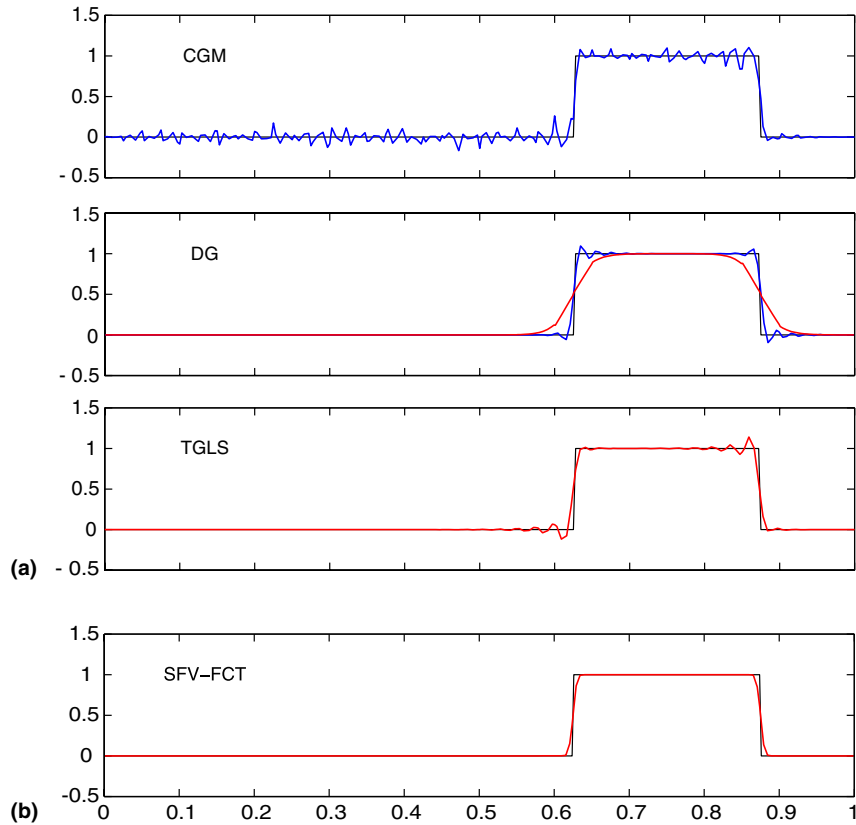


Fig. 2. One dimensional propagation of a square wave. The discretization consists of 40 elements containing six points each. The time step is set to 0.001 and 500 steps are taken. The solid black line shows the analytic solution. The advecting velocity is $u = 1$. The DG solutions were obtained without limiters (blue line) and with limiters (red line).

of a square wave advected by a constant flow field. The CGM solution exhibits the most Gibbs oscillations among the schemes considered because of its “centered” nature, and the absence of numerical dissipation. A further drawback to the classical formulation is its requirement to maintain the continuity of the solution across element edges even though hyperbolic equations such as (2) can lead to discontinuous solutions. The Discontinuous Galerkin Method was developed in order to relax the latter requirement.

3.2. Discontinuous Galerkin formulation

The DG formulation differs from the continuous Galerkin formulation primarily in its choice of function spaces in which to seek the solution. Hyperbolic partial differential equations admit solutions with finite jump discontinuities, and as such the solutions must be sought in the space of square integrable functions. The immediate advantage is that the continuity requirement across elements can be waived, and attention must be paid to the fluxes into and out of each element. The weak formulation leads to an equation similar to Eq. (4) except that Φ is now discontinuous

and the domain of integration is defined element-wise. At interelement boundaries where the solution is discontinuous an upstream-biased choice guarantees stability and convergence (see Cockburn, 1998; Karniadakis and Sherwin, 1999 for more details). We note the following:

- (1) The mass matrix is local to an element and does not require global assembly. Its size is hence $N \times N$ and can be easily inverted. Our implementation here recovers a diagonal mass matrix.
- (2) In our implementation we have collocated the solution on the Gauss roots since they provide for more accurate quadrature than the Gauss-Lobatto roots. The resulting diagonal mass matrix is exact for rectangular elements.
- (3) The ability of DGM to cope with discontinuities is evident in the second panel of Fig. 2. The Gibbs oscillations are confined to the immediate neighborhood of the discontinuity, and have a smaller amplitude than their CGM counterparts.
- (4) Since the solution is discontinuous across elements, local element refinement and/or slope limiters can be easily implemented. These two issues are taken up in the next two sections.

Cockburn and Shu (1989) proposed a limiter for linear elements, $N = 1$, to eliminate Gibbs oscillations from DGM calculations. The scheme limits the slopes of the Legendre spectral interpolation polynomial within an element in comparison with those implied by the variation of the solution-mean across elements. The higher-order Legendre coefficients, if any, are set to zero when the limiter is activated. Biswas et al. (1994) modified the limiter to avoid the drastic step of setting to zero all high-order coefficients. His idea consists of limiting the derivatives of the solution, starting with the highest order coefficient. The process stops if no modification takes place; otherwise the next highest coefficient is limited. This “gradual” application of the slope limiter is meant to preserve accuracy when the solution is smooth.

The blue line in the third panel of Fig. 2 illustrates the impact of the Biswas limiter on the square wave problem. All oscillations have been effectively eliminated at the expense of a somewhat diffused discontinuity. The limiter’s performance, however, deteriorates rapidly as the number of elements decreases: the shape of the initial profile is altered appreciably and its amplitude is substantially dissipated if 10 elements are used instead of 40. Furthermore, while the limiter’s application to smooth problems seems to preserve the *rate* of convergence, the error levels increase substantially. The extension of the Biswas limiter in multiple dimensions represents another impediment to its adoption in general purpose code, as it requires the relative orientation of three neighboring elements to be resolved in an unstructured environment. We do not pursue this limiter further, and focus instead on using adaptive refinement to improve our advection simulation.

3.3. Order adaptation strategy

The poor performance of the DGM slope limiter can be traced to the non-adaptive fixed spatial resolution. Indeed, the effective order in elements where the limiter is active is generally at most linear if not piecewise constant. The situation is exacerbated by the fact that high-order elements are generally chosen larger in size than their low-order counterparts to offset their higher computational cost. The combination of a discontinuous solution and a high-order element with a large foot print makes for a suboptimal spatial discretization. The alternative, which we explore

here in a simple one-dimensional setting, is to modify the resolution locally and adaptively, according to the smoothness of the solution, so as to make optimal use of the computational resources.

Adaptive schemes depend critically on the criteria driving the grid adaptation. The more sophisticated models use a posteriori error analysis (see Prudhomme and Oden, 2003; Süli and Houston, 2003; Adjerid et al., 2002; Adjerid and Massey, 2002) to identify elements where the numerical error is larger than a predetermined threshold; these elements are then tagged for refinement. The implementation of these algorithms hinges on defining acceptable error levels in ocean models, and on sophisticated grid management software to handle the evolving finite element grid.

Our approach here is substantially simpler. The main objective of our adaptive scheme is to prevent the *growth* of Gibbs oscillations, while tolerating their *intermittent* presence. This choice is largely motivated by practical considerations: a strict enforcement of monotonicity is expensive; it will needlessly flatten smooth extrema; and it will in a sense negate the advantages of the high-order representation.

Our adaptive strategy capitalizes on the discontinuous DGM interpolation to enhance the resolution locally with low-order elements when Gibbs oscillations or under-resolution are detected. The high-order representation is retained in regions where the solution is smooth and we revert to a low-order representation when and where the solution becomes rough. The measures of smoothness and roughness, and the rules for how to switch between the representations, may be chosen in many ways. Here, in order to limit the complexity of the adaptation algorithm, and to avoid the need for complicated data structures, we allow only one level of refinement, and fix a priori the number K_L and order N_L of the low-order elements used in the refinement. The adaptive algorithm proceeds as follows:

- (1) The local element-wise extrema of the solution are calculated at time n .
- (2) Both low- and high-order representations are advanced in time. The fluxes passed between elements are those appropriate for the local discretization only, i.e. either low- or high-order fluxes.
- (3) The new extrema at time level $n + 1$ are examined in elements where the high-order representation is active. The element's representation is switched to low-order if these extrema are outside the bounds of the allowable extrema. The bounds on the solution in element e are

$$A_- \min_k(T^k) \leq (T^e)^{n+1} \leq A_+ \max_k(T^k) \quad A_{\pm} = 1 \pm \text{sign}(\min_k(T^k))\epsilon, \quad (5)$$

where the index k refers to the element-number of adjacent elements, and ϵ is a user-defined positive small constant. For $\epsilon > 0$ the solution is allowed to trespass the expected bounds on the solution. The benefit is that smooth peaks in the solution should be preserved, and the adaptation is activated only near “appreciable” oscillations.

- (4) The handling of the solution in elements where the low-order representation is active depends on the order N_L . For $N_L = 0$, we are effectively using a first-order finite volume scheme to advance the solution: this representation is diffusive and guaranteed not to exacerbate Gibbs oscillations. If $N_L > 0$, some sort of limiter must be used to decrease/eliminate the oscillations. We need to test if the (K_L, N_L) solution is representable with the high-order spectral truncation. To this end we perform an \mathcal{L}_2 projection onto the space of Legendre polynomials

and compute the slopes of the Legendre coefficients according to the recipe presented by Mavriplis (1994). If the slope is less than a critical value the solution is switched back to the high-order representation.

A number of numerical experiments were carried out in order to test the performance of the above adaptive scheme. The linear advection equation is solved in a one-dimensional domain for a top hat and for a truncated parabola. The aim of the first experiment is to gauge the model's performance in the presence of strong discontinuities while the other exhibits a smooth extrema and a weaker slope discontinuity. The details of the initial conditions and the spatial discretization can be found in the caption of Fig. 3.

The top panel shows the adaptive scheme using $N_L = 0$, a finite volume scheme, while varying the number of low-order elements K_L used in the refinement. The first remark is that the number of low-order degrees of freedom should exceed the number of degrees of freedom of the parent high-order element in order to avoid excessive numerical errors. The latter arise through the dissipative nature of the finite volume scheme. Nevertheless, as K_L increases the artificial smearing decreases substantially, and becomes more confined to the immediate neighborhood of the discontinuity. Notice that increasing the number of low-order elements from 20 to 40 does not improve the solution much due to the excessive dissipation of the finite volume scheme.

Finally, once the solution is smooth and resolvable on the high-order element, no further smearing takes place as the high-order representation takes over. The second panel repeats the same experiment but for $N_L = 1$, a linear interpolation for the low-order elements. In this case

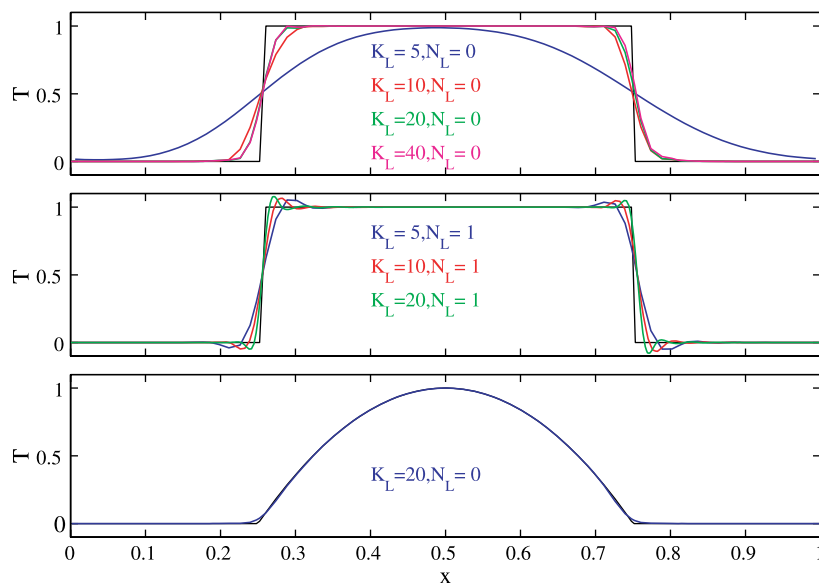


Fig. 3. Adaptive solutions for 1D linear advection. In all cases we have $K = 16$ spectral elements with $N = 6$ points per element. The initial condition for the top two figures is a top hat profile, and for the bottom most figure is $T = \max(0, 1 - 16(x - 1/2)^2)$. The top figure shows the effect of increasing K_L for fixed $N_L = 0$; the middle figure is similar but for $N_L = 1$ (a linear interpolation). The time stepping is third order RK3 and the time step is either $\Delta t = 10^{-3}$ or $\Delta t = 2 \times 10^{-3}$; $\epsilon = 10^{-3}$ in Eq. (5).

the smearing of the solution across the discontinuity is reduced dramatically; Gibbs oscillations, however, persist as no mechanism has been put in place to reduce them (a slope limiter would be needed). Finally the third panel shows the performance of the adaptive scheme for a solution with smooth peak and slope discontinuities only. The preservation of the peak is primarily due to choosing $\epsilon = 10^{-3} > 0$ in Eq. (5), and which prevents round-off errors from activating the low-order representation. Finally, only a very modest amount of dissipation is needed to round the sharp corners of the inverted parabola.

3.4. Spectral Finite Volume-FCT formulation

In this section we present a relatively novel high-order ‘‘Spectral’’ Finite Volume method to solve Eq. (2). The main attraction of a finite volume approach is the straightforward ability to implement slope or flux limiters, and to impose the monotonicity constraint on the numerical solution. Our formulation here attempts to preserve the high-order approximations and geometric flexibility of spectral element methods, while minimizing the complexity of the high-order reconstruction step (see below) in an unstructured grid environment. The scheme formulated here can be viewed as a combination of the FV-FCT schemes proposed in Sidilkover and Karniadakis (1993) and Giannakouros and Karniadakis (1994), and the discontinuous representation found in Kopriva and Kolias (1996), and Kopriva (1996). A similar spectral Finite Volume scheme has been proposed in Wang (2002), Wang and Liu (2002, 2003), and Wang et al. (2004) based on triangular elements. In this section we give a brief overview of the method, concentrating on the high-order aspects, and refer the reader to Choi et al. (2004) for a more detailed description.

The finite volume formulation is obtained simply by setting $\Phi = 1$ in Eq. (4) to obtain:

$$\Omega \frac{\partial \bar{T}}{\partial t} + \oint_{\partial\Omega} T \vec{u} \cdot \vec{n} dS = 0, \quad \bar{T} = \frac{1}{\Omega} \int_{\Omega} T dA, \quad (6)$$

where \bar{T} is the average of T over Ω . The area averages of the solution are the primary unknowns in a finite volume formulation; the function values are needed to calculate the fluxes entering the (yet undetermined) finite volume cells. A reconstruction procedure is then needed to recover solution values from solution averages.

The spatial discretization relies on the spectral element paradigm with its two-level grid structure: the globally unstructured elemental subdivision, and the locally structured cell subdivision shown in Fig. 1. The finite volume Eq. (6) is then enforced on each cell by setting $\Omega = \Omega_{kl}$ where $(k, l) = 1, \dots, N$. In order to take advantage of the interpolation properties of spectral methods, we choose our collocation points for T_{kl} to be the Gauss roots, $\bar{\xi}_k$, of Legendre polynomial of degree N , and the cell edges to be the Gauss-Lobatto roots of the Legendre polynomial of degree N . Thus the cell associated with T_{kl} is defined by the interval $[\bar{\xi}_{k-1}, \bar{\xi}_k] \times [\eta_{l-1}, \eta_l]$. The cell-averages \bar{T}_{kl} can now be computed by integrating the Lagrangian interpolants over the volume of each cell. This is a linear operation that can be recast as a matrix vector product that maps the N^2 values of the functions $T_{i,j}$ into the N^2 cell-averages $\bar{T}_{k,l}$:

$$\bar{T}_{kl} = \sum_{i=1}^N \sum_{j=1}^N A_{kl,ij} T_{i,j}, \quad A_{kl,ij} = \frac{1}{\Omega_{kl}} \int_{\bar{\xi}_{k-1}}^{\bar{\xi}_k} h_i(\bar{\xi}) h_j(\eta) |J| d\bar{\xi} d\eta. \quad (7)$$

The entries of the averaging matrix must be calculated by numerical quadrature: an N -point Gauss quadrature will be exact provided the geometric mapping (i.e. the Jacobian) is bilinear. A similar quadrature is needed for the boundary integrals in Eq. (6).

The T -interpolation is discontinuous at element edges. This simplifies the scheme considerably as it permits the mapping between the function values $T_{i,j}$ and its cell averages $\bar{T}_{k,l}$ to be inverted uniquely and locally. The algorithmic steps for the high-order aspects of the scheme are

- (1) Given the cells averages $\bar{T}_{k,l}^n$, reconstruct the function $T_{i,j}^n = A^{-1}\bar{T}_{k,l}^n$.
- (2) Interpolate the function values $T_{i,j}^n$ to cell-edge quadrature points to evaluate the boundary integrals. The discontinuity on cell edges that coincide with elemental edges is resolved by choosing the upwind value.
- (3) If needed apply the FCT procedure to prevent Gibbs oscillations.
- (4) Integrate the equations in time using a high-order time scheme like AB3, RK3 or RK4 to obtain $\bar{T}_{k,l}^{n+1}$.

The implementation of the Flux Corrected Transport (FCT) algorithm of Zalesak (1979) for our SFV scheme is straightforward thanks to the finite volume formulation and the two-level structure of the elemental grid. The high-order fluxes in our implementation rely on the SFV algorithm presented above, and we follow the prescription laid out in Zalesak, 1979 to define the solution bounds and limiting procedures as they are independent of the spatial discretization details. The low-order fluxes use a donor cell scheme whereby each cell Ω_{kl} is a finite volume in which the solution is interpolated as a piecewise constant; this low-order representation guarantees the monotonicity of the low-order solution. The low- and high-order fluxes, and the solution bounds are the essential ingredients of the FCT algorithm, and we refer the reader to Zalesak (1979) and Choi et al. (2004) for more details. The lower panel of Fig. 2 shows the square wave simulation using the SFV-FCT algorithm. Oscillations have been completely eliminated, and the discontinuity is captured within a few grid cells. The extension of the above algorithm to multi-dimensions is straightforward.

3.5. Taylor Galerkin Least Square formulation

The Taylor Galerkin formulation (Donea, 1984) is an extension of the Lax Wendroff method to finite element discretization. Its principal objective is to transform temporal derivatives into spatial derivatives, using the original partial differential equation, to derive two time-level and high-order temporal schemes. Here we combine the Taylor Galerkin formulation with a least square discretization in space to enhance the method's performance in the advection-dominated regime (Jiang, 1998). Indeed, the least square discretization provides the same upwind-biased weight function as the popular Streamline Upwind Petrov Galerkin (SUPG) method. In addition, the resulting method is parameter-free, and the matrix equations are symmetric positive definite. Pre-conditioned Conjugate Gradient iterative methods can then be used to solve the algebraic system. The Taylor Galerkin Least Square (TGLS) method is the only implicit method we investigate since its matrix equation can be solved with efficient and parallelizable PCG iterations.

A major concern of high-order Taylor Galerkin methods is the presence of second-order or higher spatial derivatives which complicate the finite element formulation. Donea et al. (2000)

have recently proposed a systematic approach to derive higher-order approximations which involves only first-order spatial derivatives at the expense of a larger system of algebraic equations. Here we avoid all these complications by focussing on a Crank-Nicholson discretization of the advection equation using TGLS.

Our TGLS formulation starts with the following second-order temporal Taylor expansion:

$$T^{n+1} + \frac{\Delta t}{2} \nabla \cdot (\vec{u} T^{n+1}) = T^n - \frac{\Delta t}{2} \nabla \cdot (\vec{u} T^n) + O(\Delta t^3), \quad (8)$$

where Eq. (2) has been used to set $T_t = -\nabla \cdot (\vec{u} T)$. The least square formulation seeks to minimize the \mathcal{L}_2 norm of the residual of Eq. (8); it leads to the following variational form:

$$\int_{\Omega} \left(T^{n+1} + \frac{\Delta t}{2} \vec{u} \cdot \nabla T^{n+1} \right) \chi dV = \int_{\Omega} \left(T^n - \frac{\Delta t}{2} \vec{u} \cdot \nabla T^n \right) \chi dV, \quad (9)$$

where the weight function is $\chi = \Phi + \frac{\Delta t}{2} \vec{u} \cdot \nabla \chi$. Comparing the above equation with a straightforward Galerkin formulation of Eq. (8), it is clear that the weight function χ is upstream biased. Jiang (1998) has pointed out the relationship of the least square formulation to SUPG: the integrals involving the weight function $\vec{u} \cdot \nabla \phi$ have a tensorial structure similar to SUPG without involving additional unknown parameters. The least square formulation in Fig. 2 (third panel) produces substantially fewer oscillations than CGM; the amplitude of the oscillations are comparable in the vicinity of the discontinuity, but decreases quickly away from it.

There are a few important remarks to note about this new formulation. First, the least square formulation require the solution of an algebraic system at each time step. The saving grace is that the least square statement leads naturally to a symmetric positive definite matrix solvable by straightforward PCG iterations. Second, the matrix equations changes at each time step when the velocity field is unsteady, and hence must be recomputed and reinverted.

4. Numerical experiments

A number of numerical two-dimensional experiments are presented to compare the performance of the different schemes to oceanographically relevant situations. These tests include the passive tracer advection of Hecht et al. (1995), and the active tracer experiment of a gravitational adjustment in a channel of constant depth (Haidvogel and Beckmann, 1999). The emphasis here is on cases where the solution develops under-resolved features and on assessing the model's response to the ensuing Gibbs oscillations. In addition to these tests we have run simulations for infinitely smooth solutions to confirm that all schemes achieve exponential convergence under h-p grid refinement using the rotating Gaussian hill experiment of Smolarkiewicz (1983). In summary, all schemes achieve their expected high-order convergence rates. At fixed intermediate resolution the DGM solution gave the smallest Gibbs oscillations and dispersive errors, and preserved the shape of the initial pulse best.

4.1. Passive tracer experiments

High-order methods lose their high-order convergence properties when faced with problems whose solution exhibit finite smoothness, e.g., discontinuities of the solution or its derivatives.

Although true discontinuities are rare/non-existent in the ocean, under-resolved features can trigger Gibbs oscillations and lead to a breakdown in the simulation. Here, we revisit the Hecht advection problem (Hecht et al., 1995, 1998, 2000) as it is designed to characterize the behavior of advection schemes in the under-resolved regime. The test consists of advecting a passive tracer in a Stommel Gyre and, most importantly, through its western boundary current where it undergoes severe shearing and straining. The Hecht problem retains only a few essential elements of oceanic flows; its simplicity however allows us to quickly experiment with several advection schemes without having to implement them in a full general circulation model. The emphasis here is on the evaluation of the schemes' performance in a coarse-grid situation; more specifically the boundary current region is about 70 km wide, while the average grid spacing is set to 100 km. For our base experiment we choose a grid of 16×9 elements of order 7 (eight points) to discretize the $10,000 \times 6300 \text{ km}^2$ basin. Although the finite element grid can be easily modified to enhance the resolution in the western boundary region, we refrain from doing so since it is not always possible to predict the regions where grid enhancement is necessary in realistic cases (short of using a dynamically adaptive model). The Hecht problem offers a simple setting on which the behavior of the models can be gauged. The aforementioned does not apply to dynamically adaptive models.

4.1.1. Basic schemes

The initial condition for the tracer is that of a Gaussian Hill centered at $(10,000; 6700)/3 \text{ km}$ from the lower left corner, with a decay length scale of 800 km. The initial evolution of the tracer using the CGM scheme is shown in Fig. 4. The solution remains smooth until the tracer enters the western boundary region and is subject to the severe shearing and straining of the strong currents. Gibbs oscillations, symptomatic of under-resolution, appear, grow and propagate in a south–east direction. At the end of the integration, top left panel of Fig. 5, the extrema of the original tracer field are lost and replaced by large erroneous values (almost a 100 times larger in negative and positive amplitudes). We note that the phase of the solution is captured well in spite of the large amplitude errors.

The results obtained with TGLS are shown in the top right panel of Fig. 5. The least square approach does not eliminate the Gibbs oscillations entirely; it does, however, reduce their

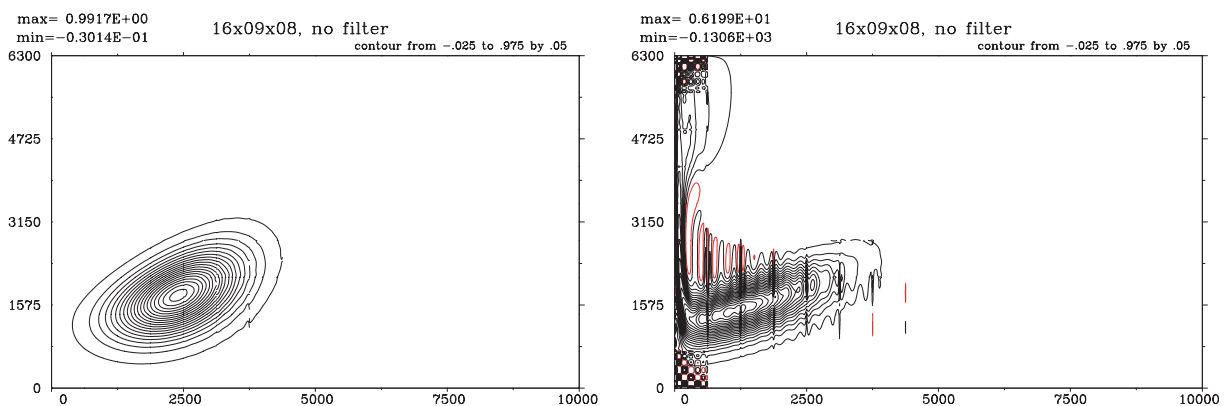


Fig. 4. Tracer evolution using CGM on basic seventh order 16×9 grid, no filtering. The right panel shows the tracer prior to entering the WBC region (time $20 \times 10^6 \text{ s}$), and the left panel during the crossing of the WBC region ($40 \times 10^6 \text{ s}$).

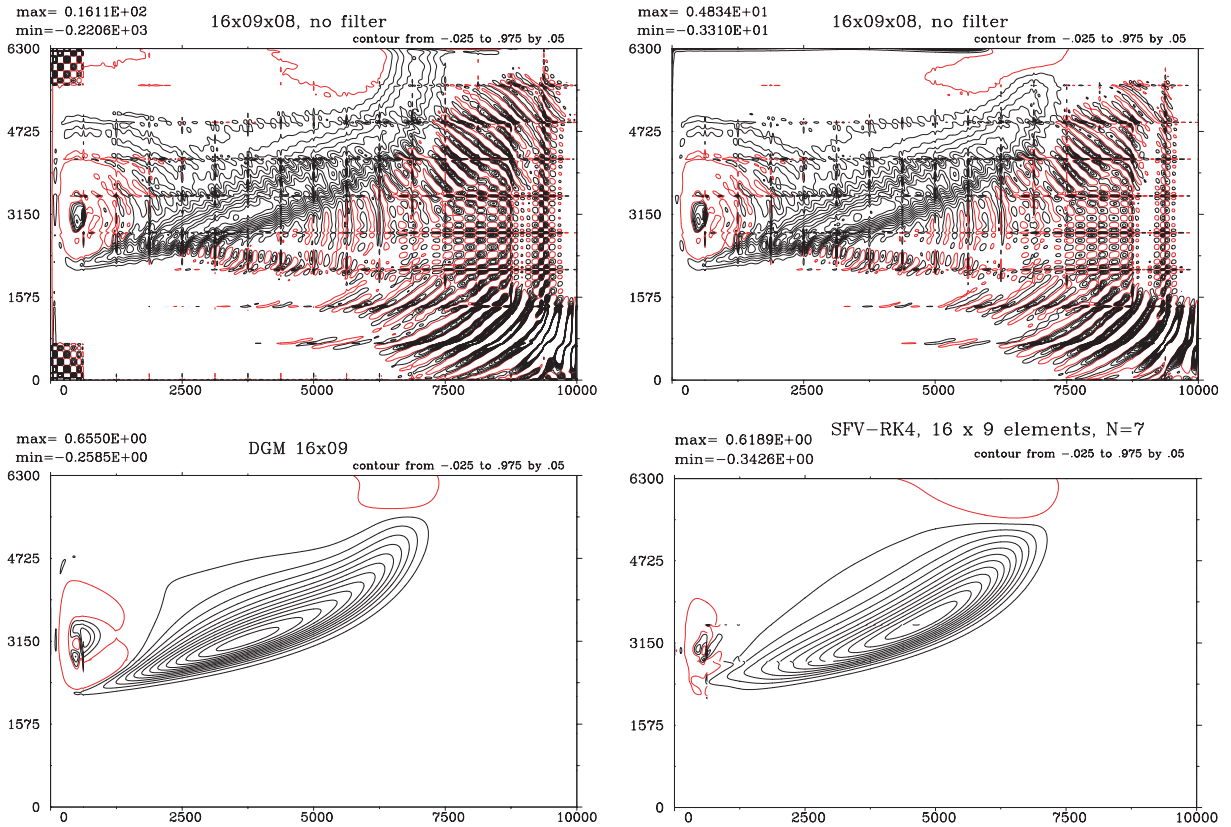


Fig. 5. The tracer distribution at the end of 4.8 year integration. The top panels show the CGM (left) and the TGLS (right) solutions, while the bottom panels show the DGM (left) and SFV (right) solutions.

amplitude greatly. The amplitude of these oscillations decrease with enhanced resolution (not shown); in particular, the TGLS solution exhibits smaller oscillations than a CGM calculation at the same resolution. Finally, the CPU cost, even for this steady flow problem, is substantially higher for the least square approach because of its implicit solver.

The solution obtained with DGM is shown in the lower left panel of Fig. 5. It is apparent that DGM gives the best overall solution. The shape of the tracer concentration is well reproduced, and the extrema within the cone are well preserved. A portion of the tracer is left over in the WBC and seems to be stagnant. Its amplitude, however, is substantially smaller than that found in any of the other schemes, save for the SFV scheme. We note that the present DGM relied on over-integration to achieve the good results shown herein. Thus, the velocity is collocated on 10 Gauss-Lobatto nodes whereas the tracer is collocated on staggered 8 Gauss nodes; and the 10 Gauss-Lobatto nodes are used to integrate the divergence term in the DGM formulation. A similar conclusion can be drawn with respect to the SFV scheme whose solution is depicted in the lower right panel of Fig. 5.

The absence of large oscillations in the DGM and SFV solutions can be traced back to the up-wind treatment at element edges. The latter injects a small amount of numerical dissipation which

prevents the oscillations from growing unchecked. In fact, Cockburn (1998) shows the stabilizing effects of the numerical flux treatment on the DGM solution; no such analysis is available yet for SFV.

4.1.2. Modified schemes

Here we investigate the effectiveness of different approaches at controlling and/or eliminating Gibbs oscillations. The bad performance of the traditional CGM calculations is due to the total absence of dissipation in the model problem. Furthermore, aliasing in the coarse-grid western boundary current leads to a large increase in the amplitude of Gibbs oscillations. Two straightforward mechanisms can be implemented to blunt the growth of these oscillations: dealiasing and inclusion of artificial dissipation. The latter can take the form of spectral filters, and or numerical dissipation induced by dissipative schemes (such as a first-order FV) or flux limiters.

Dealiasing in spectral element calculations amount to calculating the integrals of the advection terms exactly (Kirby and Karniadakis, 2003). For rectangular elements the integrand of the advection term is a polynomial of degree $3N$ and hence requires $(3N + 1)/2$ Gauss quadrature points, or $(3N + 3)/2$ Gauss-Lobatto quadrature points, to be evaluated exactly. The dealiased calculation shown in Fig. 6 shows a substantial decrease in the amplitude of the oscillations; their pattern, however, remains unaffected in the absence of dissipation. There is a minor cost in implementing dealiasing as it requires each of the variables in the integrand to be interpolated to the new quadrature points.

Traditional numerical dissipation based on the Laplace operator is not scale-selective enough to damp the grid scale noise without affecting the larger-scale features. Spectral filters have been proposed to mimic the effect of hyper-viscous dissipation in spectral element calculations; see Boyd (1989) and Levin et al. (1997). The left panel of Fig. 6 shows the filtered CGM solution. The worst of the oscillations have been removed while preserving the large-scale structure of the solution. Spectral filters do present drawbacks however. First, and unlike a Laplacian-like diffusion term, their action is not guaranteed to decrease the variance of the field, and may actually contribute to the generation of oscillations (Boyd, 1994). Furthermore, experimentation is required to adjust the filter frequency and strength to appropriate values. Frequent applications of a weak filter is generally preferable to the infrequent application of a strong filter.

The activation of the FCT limiter for the SFV scheme, bottom left panel of Fig. 6, yields a Gibbs-free solution. The SFV-FCT solution is in fact well suited for the Hecht problem where a coarse-resolution grid is unable to cope with the generation of small-scale structure in the solution. The non-linear nature of the FCT algorithm allows the limiter to act more “forcefully” as the tracer passes through the western boundary region.

Finally, the lower right panel of Fig. 6 shows the solution obtained with an adaptive DGM. The adaptive procedure switched the high-order representation to a finite volume one with 20×20 cells in elements where the solution was not smooth. The smoothness of the solution was calculated using the slope of the spectral coefficients as in Henderson (1999). The solution is for the most part oscillation-free although there are small out-of-range values. The solution is substantially more diffused in the current example since the majority of the tracer is squeezed through the coarsely resolved western boundary region. Our adaptive algorithm, with its reliance on finite volume cells, leads to a substantial amount of numerical diffusion. A more appropriate refinement

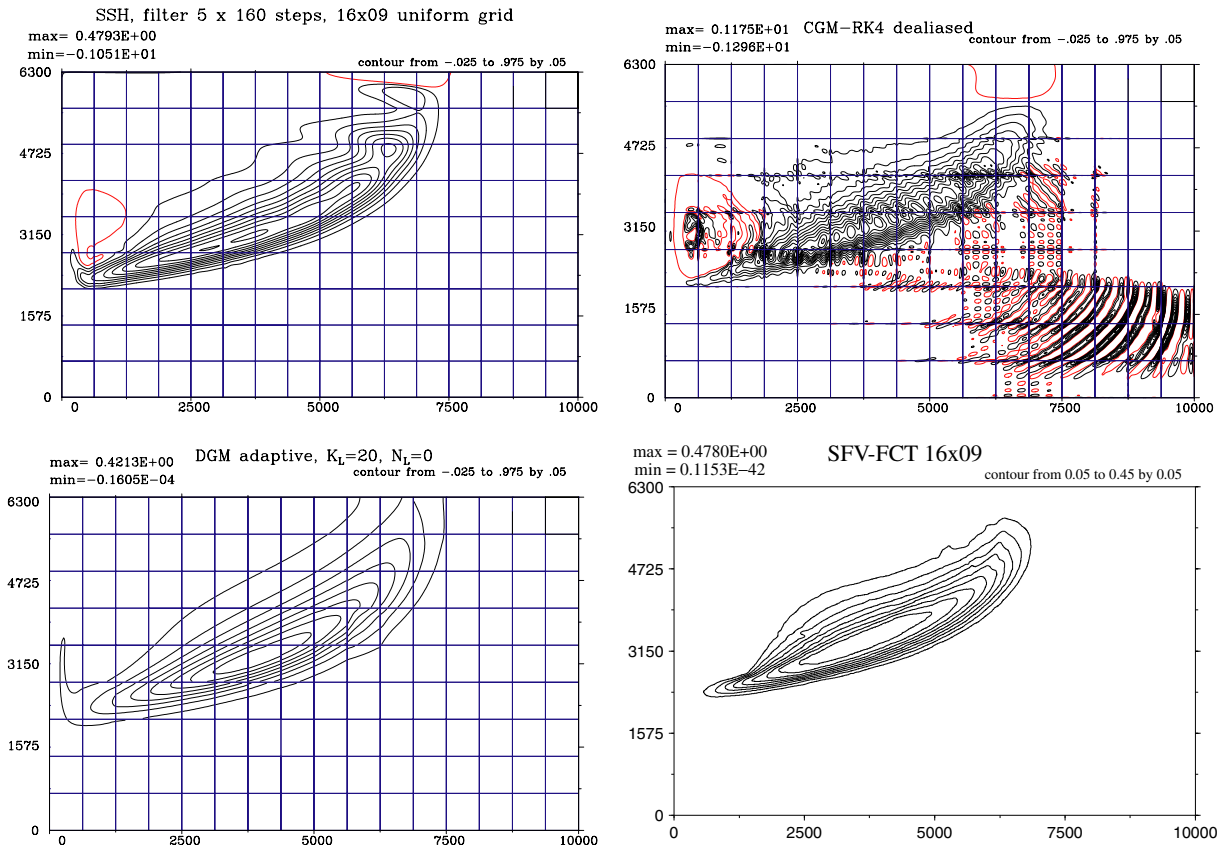


Fig. 6. Hecht test with filtered CGM (top left), dealiased CGM (top right), DGM adaptive (lower left), and the monotone SFV-FCT scheme (lower right).

strategy for the present case would use linear or quadratic elements to minimize the numerical dissipation while further localizing the Gibbs oscillations. We leave this topic for a future article.

We stress that the equations solved are still the linear advection equation. The large differences seen in the solution of the Hecht problem is due primarily to the coarse resolution used in the simulation. Numerical artifacts contaminate the final solution, particularly for the cases with no dissipation. The remedies sought improve the situation marginally since the basic schemes are still severely under-resolved and under-damped.

4.2. Active tracers

The previous tests revolved around passive tracer experiments with no feedback to the dynamics of the flow. Here we investigate the impact of the DGM and CGM formulations when applied to the advection of density in SEOM-3D. The problem setting is that of a gravitational adjustment problem in a rectangular channel 64 km wide and 20 m deep. The initial configuration consists of a two-fluid system at rest separated by a vertical wall and with an initial density contrast of 5 kg/m^3 ;

Table 1

Comparisons of solution extrema for the gravitational adjustment problem for different viscosities ν and Laplacian diffusivities α

α	$\nu = 50 \text{ m}^2/\text{s}$				$\nu = 75 \text{ m}^2/\text{s}$				$\nu = 100 \text{ m}^2/\text{s}$			
	CGM		DGM		CGM		DGM		CGM		DGM	
	ρ_{\min}	ρ_{\max}	ρ_{\min}	ρ_{\max}	ρ_{\min}	ρ_{\max}	ρ_{\min}	ρ_{\max}	ρ_{\min}	ρ_{\max}	ρ_{\min}	ρ_{\max}
0			-1.61	6.79			-1.15	6.07			-0.82	5.71
5			-1.50	6.59			-1.16	6.04	-3.84	39.97	-0.88	5.76
10			-1.36	6.39	-3.76	40.96	-1.11	6.01	-1.03	11.95	-0.88	5.78
25	-7.05	52.3	-0.63	5.71	-1.21	10.37	-0.67	5.65	-0.46	6.79	-0.58	5.56
50	-0.55	6.99	-0.32	5.05	-0.66	5.72	-0.26	5.07	-0.36	5.31	-0.17	5.13
75	-0.12	5.32	-0.06	5.05	-0.12	5.18	-0.06	5.02	-0.08	5.09	-0.05	5.02
100	-0.02	5.04	-0.03	5.04	-0.004	5.004	-0.04	5.02	-0.003	5.004	-0.04	5.01

the wall is lifted and the fluid is allowed to adjust under the influence of gravity. The expected behavior is that of two fronts moving away from each other at the internal gravity speed of 0.5 m/s. The difficulty in this configuration is to maintain the frontal structure in spite of numerical errors and the dissipation required to stabilize the computations. The numerical grid consists of 16 eight-order polynomials elements in the horizontal and five quartic elements in the vertical.

Table 1 compares the CGM and DGM density extrema for different combinations of viscous and diffusion coefficients. Ideally, the density should remain within the original bounds: $0 \leq \rho \leq 5 \text{ kg/m}^3$. Numerical errors and Gibbs oscillations, however, conspire to produce spurious extrema. The frontal structure of the inviscid problem is quite challenging to high-order methods. Experimentation with the CGM formulation has shown that the solution becomes well resolved on the present computational grid for $\alpha = \nu = 100 \text{ m}^2/\text{s}$. The blank entries in Table 1 refers to cases where the simulation was unstable. These cases were isolated to the CGM formulation with weak dissipation, and which resulted in fronts unresolvable on the computational grid. The DGM formulation, however, was stable for these cases. Notice also the very large spurious values for the marginally resolved CGM simulations compared to those of DGM.

5. Conclusion

We have surveyed four different high-order formulations to solve the advection equation using quadrilateral, spectral element type grids. Of the four different formulations considered the straightforward Continuous Galerkin spectral element method is the most efficient provided the solution is well resolved on the computational grid. The lack of numerical dissipation in the scheme requires that dissipation be explicitly prescribed in the form of a Laplacian diffusion or filter. Dealiasing can help reduce the growth of Gibbs oscillations amplitude in under-resolved regions but does not dissipate them. Filtering and dealiasing must then be used in tandem.

The Spectral Finite Volume algorithm presented here provides high-order convergence rates when the solution is smooth. Furthermore, it is readily modified to include an FCT limiter to remove erroneous oscillations. There are two computational drawbacks to the SFV formulation.

First, the flux computations require a relatively expensive, high-order interpolation of the function values to cell edges; this extra cost is mitigated by the tensor-product nature of the interpolation. Second, the variable Jacobian of quadrilateral elements prevents us from rewriting the reconstruction matrix in tensor-product form, and full matrix multiplication is required to reconstruct the solution in two-dimensions; the cost of the reconstruction thus grows as N^4 . For these reasons we recommend using the SFV formulation with moderate degree polynomials in the range of 1–6, only, particularly when the FCT limiter is activated.

The marginal improvement of the TGLS solution over the standard CGM scheme does not justify its higher computational cost. More sophisticated stabilization schemes may prove to be more robust; efforts may then be spent on developing a robust and scalable iterative solver for non-symmetric indefinite systems.

Finally, DGM proved to have a desirable set of properties. Its inherent small dissipative nature damps the grid-scale noise without affecting the large-scale structure. It has a computational cost comparable to the CGM formulation, but requires a bit of extra processing to compute interelement fluxes. Finally, the discontinuous nature of its basis functions makes it possible to implement local h–p adaptive procedures to optimize the solution representation according to its smoothness. The finite volume cell representation turns out to be too diffusive, and we recommend using at least linear interpolation in the low-order elements.

The optimal advection scheme depends largely on the nature of the problem to be solved; the reader is hence urged to carefully consider the circumstances of their target problems before adopting one of the schemes surveyed above. For problems where oscillations are unacceptable, such as negative layer thicknesses in an isopycnal model, the SFV is a rational choice to force the solution to remain monotone throughout the calculations. If small out of range values are tolerable, then DGM becomes competitive with its combination of robustness and efficiency. Most importantly, its discontinuous representation of the solution, simplifies tremendously the implementation of limiters and adaptive solution strategies.

Acknowledgments

The present article benefited from discussion with Dr. Frederic Dupont on adaptive schemes. Support from ONR grants N000140110212, N000140310254, and N000149911066 for Dr. Iskandarani, and N00014-00-1-0230 and N00014-03-1-0254 for Dr. Levin is gratefully acknowledged. This research was also supported by NSF grant 0196444. Mr. B.J. Choi held a graduate student fellowship from the Institute of Marine and Coastal Science, Rutgers University, during the course of this project. We would also wish to thank the reviewers whose comments and suggestions contributed greatly to improving the present manuscript.

References

- Adjerid, S., Devine, K.D., Flaherty, J.E., Krivodonova, L., 2002. A posteriori error estimation for discontinuous Galerkin solution of hyperbolic problems. *Computer Methods in Applied Mechanics and Engineering* 191 (51), 5877–5897.

- Adjerid, S., Massey, T.C., 2002. A posteriori discontinuous finite element error estimation for two-dimensional hyperbolic problems. *Computer Methods in Applied Mechanics and Engineering* 191 (51–52), 1097–1112.
- Biswas, R., Devine, K.D., Flaherty, J.E., 1994. Parallel, adaptive finite element methods for conservation laws. *Applied Numerical Mathematics* 14, 255–283.
- Boyd, J.P., 1989. *Chebyshev and Fourier Spectral Methods*. Lecture Notes in Engineering. Springer-Verlag, New York.
- Boyd, J.P., 1994. Hyperviscous shock layers and diffusion zones: Monotonicity, spectral viscosity, and pseudospectral methods for very high order differential equations. *Journal of Scientific Computing* 9 (1), 81–106.
- Canuto, C., Hussaini, M.Y., Quarteroni, A., Zang, T.A., 1988. *Spectral methods in fluid dynamics*. Springer. Series in computational physics. Springer-Verlag, New York.
- Casulli, V., Walters, R.A., 2000. An unstructured grid, three-dimensional model based on the shallow water equations. *International Journal for Numerical Methods in Fluids* 32, 331–348.
- Chen, C., Liu, H., Beardsley, R.C., 2003. An unstructured grid, finite volume, three-dimensional, primitive equations ocean model: application to coastal ocean and estuaries. *Journal of Atmospheric and Oceanic Technology* 20 (1), 159–186.
- Choi, B.-J., Iskandarani, M., Levin, J.C., Haidvogel, D.B., 2004. A spectral finite volume method for the shallow water equations. *Monthly Weather Review* 132 (7), 1777–1791.
- Cockburn, B., 1998. An introduction to the discontinuous Galerkin method for convection dominated flows. In: Quarteroni, A. (Ed.), *Advanced Numerical Approximation of Nonlinear Hyperbolic Equations*. Springer-Verlag, pp. 151–268.
- Cockburn, B., Shu, C.-W., 1989. TVB Runge-Kutta local projection discontinuous Galerkin finite element method for scalar conservation laws II: general framework. *Mathematics of Computations* 52, 411–435.
- Danilov, S., Kivman, G., Schröter, J., 2004. A finite-element ocean model: principles and evaluation. *Ocean Modelling* 6, 125–150.
- Danilov, S., Kivman, G., Schröter, J., 2005. Evaluation of a an eddy-permitting finite-element ocean model in the north Atlantic. *Ocean Modelling*.
- Donea, J., 1984. A Taylor-Galerkin method for convective transport problems. *International Journal for Numerical Methods in Engineering* 20, 101–119.
- Donea, J., Roig, B., Huerta, A., 2000. High-order accurate time-stepping schemes for convection–diffusion problems. *Computer Methods in Applied Mechanics and Engineering* 182, 249–275.
- Ford, R., Pain, C.C., Piggott, M., Goddard, A., de Oliveira, C.R., Umpleby, A., submitted for publication. A non-hydrostatic finite element model for three-dimensional stratified oceanic flows, Part I: model formulation. *Monthly Weather Review*.
- Ford, R., Pain, C.C., Piggott, M., Goddard, A., de Oliveira, C.R., Umpleby, A., submitted for publication. A non-hydrostatic finite element model for three-dimensional stratified oceanic flows, Part II: model validation. *Monthly Weather Review*.
- Giannakouros, J., Karniadakis, G.E., 1994. A spectral element-FCT method for the compressible Euler equations. *Journal of Computational Physics* 115, 65–85.
- Haidvogel, D.B., Beckmann, A., 1999. *Numerical Ocean Circulation Modeling*. Imperial College Press.
- Hanert, E., Roux, D.Y.L., Legat, V., Deleersnijder, E., 2004. Advection schemes for unstructured grid ocean modelling. *Ocean Modelling* 7 (1–2), 39–58.
- Hecht, M.W., Bryan, F.O., Holland, W.R., 1995. Upwind-weighted advection schemes for ocean tracer transport: an evaluation in a passive tracer context. *Journal of Geophysical Research* 100 (C10), 20763–20778.
- Hecht, M.W., Bryan, F.O., Holland, W.R., 1998. A consideration of four tracer advection schemes in a primitive equation ocean model. *Journal of Geophysical Research* 103 (C2), 3301–3321.
- Hecht, M.W., Wingate, B.A., Kassis, P., 2000. A better, more discriminating test problem for ocean tracer transport. *Ocean Modelling* 2, 1–15.
- Henderson, R.D., 1999. Dynamic refinement algorithms for spectral element methods. *Computer Methods in Applied Mechanics and Engineering* 175 (3–4), 395–411.
- Iskandarani, M., Haidvogel, D.B., Boyd, J.P., 1995. A staggered spectral element model with application to the oceanic shallow water equations. *International Journal for Numerical Methods in Fluids* 20, 393–414.

- Iskandarani, M., Haidvogel, D.B., Levin, J., 2003. A three-dimensional spectral element model for the solution of the hydrostatic primitive equations. *Journal of Computational Physics* 186 (2), 397–425.
- Jiang, B.N., 1998. *The Least Squares Finite Element Method: Theory and Applications in Computational Fluid Dynamics and Electromagnetics*. Springer.
- Karniadakis, G.E., Sherwin, S.J., 1999. *Spectral/hp Element Methods for CFD*. Oxford University Press.
- Kirby, R.M., Karniadakis, G.E., 2003. Dealiasing on non-uniform grids: algorithms and applications. *Journal of Computational Physics* 191 (1), 249–264.
- Kopriva, D.A., 1996. A conservative staggered grid Chebyshev multidomain method for compressible flows. II: A semi-structured approach. *Journal of Computational Physics* 128, 475–488.
- Kopriva, D.A., Kalias, J.H., 1996. A conservative staggered grid Chebyshev multidomain method for compressible flows. *Journal of Computational Physics* 125, 244–261.
- Levin, J., Iskandarani, M., Haidvogel, D.B., 1997. A spectral filtering procedure for eddy-resolving simulations with a spectral element ocean model. *Journal of Computational Physics* 137 (1), 130–154.
- Lynch, D.R., Werner, F.E., 1991. Three-dimensional hydrodynamics on finite elements. part II: nonlinear time-stepping model. *International Journal for Numerical Methods in Fluids* 12, 507–533.
- Mavriplis, C., 1994. Adaptive mesh strategies for the spectral element method. *Computer Methods in Applied Mechanics and Engineering* 116, 77–86.
- Prudhomme, S., Oden, J.T., 2003. Computable error estimators and adaptive techniques for fluid flow problems. In: Barth, T.J., Deconinck, H. (Eds.), *Error Estimation and Adaptive Discretization Methods in Computational Fluid Mechanics*, Lecture Notes in Computational Science and Engineering. Springer, New York, pp. 207–268.
- Ronquist, E.M., 1988. Optimal spectral element methods for the unsteady three-dimensional incompressible Navier-Stokes equations. Ph.D. thesis, Massachusetts Institute of Technology, Cambridge MA.
- Roux, D.Y.L., Staniforth, A., Lin, C.A., 1998. Finite elements for shallow-water equation ocean models. *Monthly Weather Review* 126, 1931–1951.
- Sidilkover, D., Karniadakis, G.E., 1993. Non-oscillatory spectral element Chebyshev method for shock wave calculations. *Journal of Computational Physics* 107, 10–22.
- Smolarkiewicz, P.K., 1983. A simple positive definite advection scheme with small implicit diffusion. *Monthly Weather Review* 111, 479–486.
- Süli, E., Houston, P., 2003. Adaptive finite element approximation of hyperbolic problems. In: Barth, T.J., Deconinck, H. (Eds.), *Error Estimation and Adaptive Discretization Methods in Computational Fluid Mechanics*, Lecture Notes in Computational Science and Engineering. Springer, New York, pp. 269–344.
- Wang, Z.J., 2002. Spectral (finite) volume method for conservation laws on unstructured grids. *Journal of Computational Physics* 178, 210–251.
- Wang, Z.J., Liu, Y., 2002. Spectral (finite) volume method for conservation laws on unstructured grids: II extension to two-dimensional scalar equation. *Journal of Computational Physics* 179, 665–697.
- Wang, Z.J., Liu, Y., 2003. Spectral (finite) volume method for conservation laws on unstructured grids: III one dimensional systems and partition optimization. *Journal of Scientific Computing* 20 (1), 137–157.
- Wang, Z.J., Zhang, L., Liu, Y., 2004. Spectral (finite) volume method for conservation laws on unstructured grids: IV extension to two-dimensional systems. *Journal of Computational Physics* 194 (2), 716–741.
- Zalesak, S.T., 1979. Fully multidimensional Flux-Corrected Transport algorithms for fluids. *Journal of Computational Physics* 31, 335–362.